12-9-2006

Endohedral and Exohedral Complexes of Polyhedral Oligomeric Silsesquioxanes (POSS): Endohedral Clusters of Si12 : a Theoretical Study

Delwar Hossain

ENDOHEDRAL AND EXOHEDRAL COMPLEXES OF POLYHEDRAL OLIGOMERIC SILSESQUIOXANES (POSS). ENDOHEDRAL CLUSTERS OF Si_{12}. A THEORETICAL STUDY

By

Delwar Hossain

A Dissertation
Submitted to the Faculty of
Mississippi State University
in Partial Fulfillment of the Requirements
for the Degree of Doctor of Philosophy
in Chemistry
in the Department of Chemistry

Mississippi State, Mississippi

December , 2006

ENDOHEDRAL AND EXOHEDRAL COMPLEXES OF POLYHEDRAL OLIGOMERIC SILSESQUIOXANES (POSS). ENDOHEDRAL CLUSTERS OF Si_{12}. A THEORETICAL STUDY

By

Delwar Hossain

Approved:

Svein Saebo Professor of Chemistry (Director of Dissertation)	Charles U. Pittman, Jr. Professor of Chemistry, and Research Director of UICRC (Co-Director of Dissertation)
David L. Monts Professor of Physics (Committee Member)	Andrzej Sygula Associate Professor of Chemistry (Committee Member)
Steven Gwaltney Assistant Professor of Chemistry (Committee Member)	Stephen C. Foster Associate Professor of Chemistry (Graduate Coordinator)

Philip B. Oldham
Dean of the College of Arts and Sciences

Name: Delwar Hossain

Date of Degree: December 9, 2006

Institution: Mississippi State University

Major Field: Chemistry

Advisor: Dr. Svein Saebo

Co-advisor: Dr. Charles U. Pittman

Title of Study: ENDOHEDRAL AND EXOHEDRAL COMPLEXES OF POLYHEDRAL OLIGOMERIC SILSESQUIOXANES (POSS). ENDOHEDRAL CLUSTERS OF Si_{12}. A THEORETICAL STUDY.

Pages in Study: 223

Candidate for Degree of Doctor of Philosophy

Two distinct research projects were carried out in this dissertation. In the first project the results of first principle calculations on endo- and exohedral complexes of polyhedral oligomeric silsesqiuoxanes (POSS) with atomic and ionic species were carried out. Detailed studies were performed on structures, stabilities and electronic properties of these complexes. The stabilities of the endohedral T_n-POSS (n = 8, 10 and 12) complexes depends on both the cage size and the nature of the endohedral species. Alkali metal ion encapsulation leads to cage contraction. Halide encapsulation caused the cages to expand. Noble gas encapsulation has minimum effect on the cage structure. Ionization potentials calculated for T_{10}-POSS and T_{12}-POSS endohedral complexes with alkali metals indicate that these complexes have “superalkali” behavior. Several transition metal encapsulations into the T_8-POSS cage gave thermodynamically stable endohedral

complexes. The HOMO-LUMO gaps for the transition metal endohedral complexes were reduced versus that of pure cage. In almost all cases, the exohedral T_n (n = 8, 10, 12) complexes were energetically more stable than their corresponding endohedral counterparts except for the complex with F^-. The exohedral F^- penetrates directly into the T_n-POSS cage forming an endohedral complex.

In the second project ab initio electronic structure calculations based on density functional theory were performed to study small silicon clusters containing an endohedral atoms or ions. The formation of endohedral clusters $M@Si_{12}$ ($Li^{0,1,-1}$, $Na^{0,1,-1}$, K^+, He, F^- and Cl^-) depended on the Si_{12} cage structure and the nature of the embedding species. Only $Li^{0,1,-1}$, $Na^{0,1,-1}$ and He form endohedral clusters with different Si_{12} cage isomers. All observed endohedral clusters are stable and have large HUMO-LUMO gaps (>1eV). The endohedral clusters $Li^-@Si_{12}$ and $Na^-@Si_{12}$ are thermodynamically more stable than their neutral and cationic counterparts. The stability order predicted for the alkali metal series was anionic clusters > neutral clusters> cationic clusters. Encapsulations of halides are completely unfavorable and halide insertions cause the Si_{12} cage rupture.

Encapsulation of two Li atoms into the Si_{18} cage generates the endohedral $Li_2@Si_{18}$ complex. Encapsulating Na atoms into Si_{18} cage leads to an exohedral Na_2Si_{18} cluster. Endohedral $Si_{20}@Li_2$ was also investigated and characterized.

DEDICATION

I would like to dedicate this research to my parents.

ACKNOWLEDGMENTS

I would like to thank my co advisor, Dr. Svein Saebo for his continuous guidance, advice and encouragement throughout my graduate research and preparing of this Dissertation. Without the guidance and encouragement of Dr. Charles Pittman, Jr. the other co-advisor of my Dissertation, I would never have overcome the obstacls, which I confronted during my Ph.D graduate program. Dr. Pittman's advice not only help me to enrich my knowledge in chemistry, but also help to learn how to survive in difficult situations in real life.

I also wish to express my gratitude and thanks to Dr. Frank Hagelberg, Jackson State University and Dr. Steven Gwaltney at MSU for supporting me both academically and financially. Without their generous support, it was impossible for me to finish my studies smoothly. I was fortunate to meet Dr. David Monts of Physics Department at MSU. I was privileged to have audited Dr. Mont's spectroscopy course during my graduate studies. I am also thankful to Dr. Andrzej Sygula for serving on my committee.

My special thanks to Dr. Philip B. Oldham, Dean of Arts and Sciences, Dr. Keith T. Mead, Chairman of Chemistry Department and Dr. Stephen F. Foster for helping me in different issues during my graduate studies.

I wish to thank Dr. Emad El-Giar, Sahar Atwa**,** Arezue Boroujerdi, Ms. Dolly Tompkins and all other staff of the chemistry department for their support and good wishes.

I would like to acknowledge the MCSR for providing use of the supercomputing facility. The receipt of NSF summer fellowships, a Graduate Student Travel Award and an Academic Excellence Award from Dean of Arts and Sciences are all acknowledged.

Finally, I would like to express my deepest gratitude to my brothers, sister, relatives and my wife TOMA for their loving devotion, support and understanding throughout my graduate studies.

TABLE OF CONTENTS

CHAPTER Page

CHAPTER Page

LIST OF TABLES

TABLE Page

TABLE Page

TABLE Page

TABLE Page

LIST OF FIGURES

FIGURE Page

FIGURE Page

FIGURE Page

FIGURE Page

LIST OF ABBREVIATIONS

POSS Polyhedral Oligomeric Silsesquioxanes

LED Light Emitting Diode

PLED Polymer Light Emitting Diode

D4R Defines Double Four Member rings

D5R Defines Double Five Member Rings

HOMO Highest Occupied Molecular Orbital

LUMO Lowest Unoccupied Molecular Orbitals

B3LYP Becke 3-Parameter (Exchange), Lee, Yang and Parr (Hybrid Density Functional Theory)

DFT Density Functional Theory

MP2 Møller-Plesset perturbation theory

BSSE Basis Set Superposition Errors

ZPE Zero Point Energy

$\{6^0 5^2 4^5\}$ Zero Six member Ring Two Five Member Ring and Four Five Member Ring

X@Tn-POSS Endoheral Complex of X and Tn-POSS (n = 8, 10, 12 …)

XTn-POSS Exohedral Complex of X and Tn-POSS

T_8-POSS Octahedral Polyhedral Oligomeric Silsesquioxanes

T_{10}-POSS Decahedral Polyhedral Oligomeric Silsesquioxanes

T_{12}-POSS Do-Decahedral Polyhedral Oligomeric Silsesquioxanes

NBO Natural Bond Orbital

GIAO Gauge-Including Atomic Orbital

ECP Effective Core Potential

TMS Tetramethylsilane

NICS Nuclear Independent Chemical Shift

ABSL Name of a Company

BSSE Basis Set Superposition Errors

CHAPTER I

GENERAL INTRODUCTION

Polyhedral oligomeric silsesquioxane (POSS) molecules were first discovered and isolated in 1946.[1] POSS molecules (Figure 1.1) possess cage like structures (1-3 nm in size) and a hybrid chemical composition ($RSiH_{3/2}$) which is intermediate between silica (SiO_2) and silicones (R_2SiO).[2,3] Many stoichiometrically well- defined POSS frameworks have been reported with synthetically useful functional groups R.[4-9] The R group can be simple alkyl, cycloalkyl, aryl, or reactive/polymerisable groups such as acrylic, α-olefin, styrene, epoxide, carboxylic acid, isocyanate, amine, alcohol or silane functions. Using such functionalization, POSS molecules can be incorporated into polymer systems through blending [10], grafting or copolymerization.[11-14] This enables generation of nanostructured materials whose properties bridge the gaps between organic polymers and ceramics.[15]

Figure 1.1 Structures of T_8, T_{10} and T_{12} POSS Molecule.

Unlike clay nanocomposites, incorporation of POSS derivatives can lead to a reduction in the polymer melt viscosity, which should represent a distinct advantage for many applications.[10,12,16-19] POSS nanofillers can increase the glass transition temperatures (T_g) at higher concentrations.[20,21] This effect hinders molecular or segmental motion versus the pure polymer and reduces its dipole interaction potential. POSS silanols (Si-OH) can be used as coupling agents for fillers and offer a number of advantages over conventional silane coupling agents, including moisture stability, low volatility, no requirement for water addition and no formation of volatile by-products.[3]

Coupar et al has reported dendrimer catalysts based on POSS cores.[22] These materials are expected to combine the traits of homogeneous catalysts with the high activity and precise control of catalytic sites normally associated with homogeneous catalysts. Murfee et al reported that metallodrimers with a diphenylphosphino-POSS core and Ru-based chromophores exhibit unique advantages.[23] Saez et al has synthesized liquid crystalline silsesquioxane dendrimers exhibiting chiral nematic and columnar mesophases.[24]

POSS frameworks are strong electron-withdrawing substituents.[25,2] Consequently, the nonlinear optical properties of H-POSS systems have been explored by Cheng et al.[26] Also, it might be fruitful to explore the incorporation of POSS cages pendant to conjugated polymer chains in order to tune the electronic band-gap. Hence, the light–emitting properties of the conjugated polymer might be tuned. Light emitting diodes (LEDs) based on such inorganic–organic, hybrid, light–emitting polymers could offer

significant performance and lifetime advantages over polymer light emitting diode (PLEDs).[2]

POSS products are attracting interest in a wide range of materials applications, including aerospace, sporting goods, medical applications and electronics.[2,27,28] Other potential proposed applications of functionalized POSS frameworks are: membranes for gas separations; resists for EB lithography; and optical waveguides-leading to advances in multi component composite material systems.[29-31]

The discovery, design and development of new materials are of high priority in material science. Small structural modifications can change material properties significantly. Computer modeling and simulation play key roles in the design of many novel materials. In recent efforts to generate new materials, computational chemistry has been used to predict promising energetic systems, assess their stability and guide efficient synthesis of selected candidates.

Recently it has been found, both theoretically[32-41] and experimentally[32-46], that atoms and ions can be incorporated into the cage like molecules. The properties of these cage molecules were changed significantly after incorporation of different atoms or ions. POSS molecules are cages. The cage cavity size of the smallest T_8-POSS cage is 0.87 Å. This size is large enough to enclose many atoms or ions. This prediction is backed up experimentally by the recent synthesis of fluoride encapsulation within a silsesquioxane cage.[47] Both T_{10}-POSS and T_{12}-POSS are larger than T_8-POSS. Thus it can be predicted that T_{10}-POSS and T_{12}-POSS will be able to encapsulate atoms and ions more readily than T_8-POSS. Although synthesis and theoretical[26,48-52] investigations of

silsesquioxanes, $(HSiO_{3/2})_n$ with n = 8, 10, 12, 14 and 16 have been reported, there is a lack of information about the exohedral or endohedral complexes of POSS with different elements. The major questions regarding the endohedral POSS complexes are:

I) Can POSS cages act as a host to atoms or ions?

II) What interactions may exist between an incorporated atoms or ions with the atoms of the POSS cages?

III) What properties might these endohedral complexes exhibit?

If POSS cages can incorporate atoms or ions many technical applications might result. For example, lithium incorporation into the POSS cage may be useful for rechargeable lithium batteries as a reusable storage sites. Endohedral POSS/metal complexes might be superb singlet oxygen protection barriers. Radiation degradation of coatings is a problem associated with the space shuttle upon entry into the earth's atmosphere. POSS polymers with encapsulated heavy atoms may provide radiation protection or reduce the rate of damage. Therefore, the task of investigating endohedral and exohedral complexes of POSS as well as measuring and understanding their electronic properties has become increasingly interesting.

In this dissertation, two distinct research projects were pursued. The first project (Chapters II, III, IV, V and VI) describe *ab initio* investigations of endoheral and exohedral complexes of polyhedral oloigomeric silsesquioxane (POSS) molecules $(HSiO_{3/2})_8$, $(HSiO_{3/2})_{10}$, and $(HSiO_{3/2})_{12}$ with different atomic and ionic species. We perform first principle calculations on the individual building units of polyhedral hydrogen-silsesquioxanes (HSQ) with and without atomic and ionic species present. The

objectives were to determine the stabilities of exohedral and endoheral complexes and determine the relative stabilities of the exohedral and endohedral complexes as well as predicting and interpreting electronic properties of various endo- and exohedral complexes. Chapter II, will discuss the results of endohedral and exohedral complexes of T_8-POSS with different alkali metal ions, halides and noble gases. Chapter III, presents the results of an investigation of the endo and exohedral complexes of T_8-POSS with transition metals and their cations. In Chapter IV, the endohedral and exohedral complexes of T_{10}-POSS with different alkali metal and their ions, halides and noble gases are discussed. Chapter V, described the exohedral and endohedral complexes of T_{12}-POSS with alkali metal ions, halides and noble gases . Finally in Chapter VI, exohedral and endohedral complexes of T_{12}-POSS with alkali metal ions, halides and noble gases are described.

The second project is an *ab initio* investigation of endohedral clusters of Si_{12} cage with different atomic and ionic species. Nanosized materials are of great interest because their properties can be manipulated by changing size, shape and composition. Since silicon is the most widely used material in microelectronic industries, silicon clusters have attracted extensive theoretical and experimental interest. Recently, small silicon clusters containing a single transition metal impurity have been the subject of extensive research[53-77] to elucidate their equilibrium geometries, growth patterns, and electronic structures. Although recent computational studies have focused on silicon clusters incorporating different transition metal atoms, the study of silicon clusters with endrohedral alkali metals, halides and noble gas impurities is still in its infancy.

Three isomers D_{6h}, D_{2d} and I_h of Si_{12} cage were used as a host for a variety of guests. The guests included alkali metals and their ions, halides and the noble gases, He and Ne as a guest. Their structures, stabilities and electronic properties will be discussed in Chapter VII. In the last Chapter VIII, the results of these investigations are summarized and future directions for this work are suggested.

We used density functional theory through out our research. Density functional theory is very successful for describing ground state properties of molecules, solids or in polymers. [78,79] But DFT is not suitable to use for excited states and long-range interaction like Van der Waals interactions (VdW). The weak but long range VdW interactions dominates, the interaction between e.g. atoms, molecules, and surfaces at large separations, and affects the properties of a large number of systems such as molecular solids and liquids, membranes, and polymers. The calculation of structural properties of such systems poses a special problem for DFT, since they enclose large regions of very low electron density. The large differences in the absolute values of electron density strain the basic assumption of adopting the uniform electron gas as a reference system.[78,79,80] In endohedral POSS complexes, the systems are bound. For exohedral systems, a long-range dispersion force may be all that exists between a POSS cage and an exohhedral atom or molecules. Hence special care should be used to interpreting DFT results these systems.

References

(1) Scott, D. W. *J. Am. Chem. Soc.* **1946**, *68*, 356.

(2) http://www.azonano.com/details.asp?ArticleID=1342.

(3) http://www.hybridplastics.com/posstech.html.

(4) Agaskar, P. A. *Inorg Chem.* **1991**, *30*, 2707.

(5) Feher, F. J.; Newman, D. A.; Walzer, J. F. A. *J. Am.Chem. Soc.* **1989**, *111*, 1741.

(6) Voronkov, M. G.; Lavrent'yev, V. I. *Top. Curr. Chem.* **1982**, *102*, 199.

(7) Sellinger, A. L., R.M. *Macromolecules* **1996**, *29*, 2327.

(8) Murugavel, R. e. a. *Acc. Chem. Res.* **1996**, *29*, 183.

(9) Baney, R. H. e. a. *Chem. Rev.* **1995**, *95*, 1409.

(10) Fu, B. X.; Yang, L.; Somani, R. H.; Zong, S. X.; Hsiao, B. S.; Phillips, S.; Blanski, R.; Ruth, P. *J. Polym. Sci., Part B: Polym. Phys.*, *39*, 2727.

(11) Zhang, W.; Fu, B. X.; Schrag, E.; Mather, P. T.; Yang, N.-L.; Xu, D.; Ade, H.; Rafailovich, M.; Sokolov, J.; Seo et, a. *Macromolecules, 35*, 8029.

(12) Fu, B. X.; Hsiao, B. S.; White, H.; Rafailovich, M.; Mather, P. T.; Jeon, H. G.; Phillips, S.; Lichtenhan, J.; Schwab, J. *Polym. Int.* **2000**, *49*, 437.

(13) Kim, G.-M.; Qin, H.; Fang, X.; Sun, F. C.; Mather, P. T. *J. Polymr Sci., Part B: Polym. Phys.*, *41*, 3299.

(14) Romo-Uribe, A.; Mather, P. T.; Haddad, T. S.; Lichtenhan, J. D. *J. Polym. Sci., Part B: Polym. Phys.* **1998**, *36*, p 1857.

(15) Silsesquioxanes, B. t. G. b. P. C. Silsesquioxanes, Bridging the Gap between Polymers & Ceramic. In *ChemFiles*, 2001; Vol. 1.

(16) Shigenori Egusa, T. S., Miyuki Hagiwara,. *J. Appl. Polym. Sci.* **1987**, *34*, 2163.

(17) Shigenori Egusa, T. S., Miyuki Hagiwara,. *J. Appl. Polym. Sci.* **1987**, *34*, 2177.

(18) Pittman, C. U., Jr.; Li, G.-Z.; Ni, H. *Macromolecular Symposia* **2003**, *196*, 301.

(19) Liang, K.; Toghiani, H.; Li, G.; Pittman, C. U., Jr. *J. Polym. Sci., Part A: Polym. Chem.* **2005**, *43*, 3887.

(20) Zhao, Y.; Schiraldi, D. A. *Polymer* **2005**, *46*, 11640.

(21) Xu, H.; Kuo, S.-W.; Lee, J.-S.; Chang, F.-C. *Macromolecules* **2002**, *35*, 8788.

(22) Coupar, P. e. a. *J. Chem. Soc., Dalton Trans.* **1999**, 2183.

(23) Murfee, H. J. e. a. *Inorg. Chem.* **2000**, *39*, 5209.

(24) Saez, I. M. e.; al. Chemistry (Weinheim an Der Bergstrasse, G., 7, 2758. *Chemistry (Weinheim an Der Bergstrasse, Germany)* **2001**, *7*, 2758.

(25) Feher, F. J. B., T.A. *J. Organomet. Chem.* **1989**, *33*.

(26) Cheng, W.-D.; Xiang, K.-H.; Pandey, R.; Pernisz, U. C. *J. Phys. Chem.* **2000**, *104*, 6737.

(27) http://www.reade.com/products/Polymeric/poss.html.

(28) McCusker, C.; Carroll, J. B.; Rotello, V. M. *Chem. Communi. (Cambridge, United Kingdom)* **2005**, 996.

(29) Symposium on "3-D Silicon-Oxygen Cages: Materialsfor the 21st Century", American Chemical Society, 222nd National Meeting, Aug. 26-30, 2001; Primary sponsor: Materials Chemistry Secretariat.

(30) Hybrid Organic/Inorganic Materials, Proceedings of the Materials Research Society Spring 2000 Meeting; Lane, R. M., Sanchez, C., Giannelis, E., Brinker, C.J., Eds.; Vol. 628.

(31) Hybrid; Inorganic-Organic Polymers. In Polymer Preprints; Stoney, R. F., Ed.; American Chemical Society: Washington D.C., 2000; Vol. 41, pp 502-625.

(32) Charkin, O. P.; Klimenko, N. M.; Moran, D.; Mebel, A. M.; Charkin, D. O.; Schleyer, P. v. R. *Inorg. Chem.* **2001**, *40*, 6913.

(33) Charkin, O. P.; Klimenko, N. M.; Moran, D.; Mebel, A. M.; Charkin, D. O.; Schleyer, P. V. R. *J. Phys. Chem. A* **2002**, *106*, 11594.

(34) Chen, Z.; Jiao, H.; Moran, D.; Hirsch, A.; Thiel, W.; Schleyer, P. v. R. *J. Phys. Chem. A* **2003**, *107*, 2075.

(35) Jemmis, E. D.; Balakrishnarajan, M. M. *J. Am. Chem. Soci.* **2000**, *122*, 7392.

(36) Irle, S.; Rubin, Y.; Morokuma, K. *J. Phys. Chem. A* **2002**, *106*, 680.

(37) Jemmis, E. D.; Jayasree, E. G. *Collect. Czechoslovak Chem. Communi.* **2002**, *67*, 965.

(38) Moran, D.; Stahl, F.; Jemmis, E. D.; Schaefer, H. F., III;; Schleyer, P. v. R. *J. Phys. Chem. A* **2002**, *106*, 5144.

(39) Schleyer, P. v. R.; Najafian, K.; Mebel, A. M. *Inorg. Chem.* **1998**, *37*, 6765.

(40) Sun, Q.; Wang, Q.; Yu, J. Z.; Ohno, K.; Kawazoe, Y. *J. Phys.: Condensed Matter* **2001**, *13*, 1931.

(41) Ternansky, R. J.; Balogh, D. W.; Paquette, L. A. *J. Am. Chem. Soc.* **1982**, *104*, 4503.

(42) Rose, H. R.; Dance, I. G.; Fisher, K. J.; Smith, D. R.; Willett, G. D.; Wilson, M. A. *Org. Mass Spect.* **1994**, *29*, 470.

(43) Weiske, T.; Schwarz, H.; Hirsch, A.; Groesser, T. *Chem. Phys. Lett.* **1992**, *199*, 640.

(44) Saunders, M.; Cross, R. J.; Jimenez-Vazquez, H. A.; Shimshi, R.; Khong, A. *Science (Washington, D. C.)* **1996**, *271*, 1693.

(45) Shinohara, H. *Report Prog. Phys.* **2000**, *63*, 843.

(46) Heath, J. R.; O'Brien, S. C.; Zhang, Q.; Liu, Y.; Curl, R. F.; Tittel, F. K.; Smalley, R. E. *J. Am. Chem. Soc.* **1985**, *107*, 7779.

(47) Bassindale, A. R.; Pourny, M.; Taylor, P. G.; Hursthouse, M. B.; Light, M. E. *Angew. Chem., Int. Ed. Engl.* **2003**, *42*, 3488.

(48) Mattori, M.; Mogi, K.; Sakai, Y.; Isobe, T. *J. Phys. Chem. A* **2000**, *104*, 10868.

(49) Earley, C. W. *J. Phys. Chem.* **1994**, *98*, 8693.

(50) Tejerina, B.; Gordon, M. S. *J. Phys. Chem. B* **2002**, *106*, 11764.

(51) Xiang, K.-H.; Pandey, R.; Pernisz, U. C.; Freeman, J. *J. Phys. Chem. B* **1998**, *102*, 8704.

(52) Tossell, J. A. *J. Phys. Chem.* **1996**, *100*, 5025.

(53) Kumar, V.; Y. Kawazoe. *Phys. Rev. Lett.* **2001**, *87*, 045503.

(54) Kumar, V.; Y. Kawazoe. *Phys. Rev. B* **2002**, *65*, 073404.

(55) Kumar, V.; Majumder, C.; Kawazoe, Y. *Chem. Phys. Lett.* **2002**, *363*, 319.

(56) Kumar, V.; Kawazoe, Y. *Appl. Phys. Lett.* **2002**, *80*.

(57) Kumar, V.; Kawazoe, Y. *Rev. Modern Quantum Chem.* **2002**, *2*, 1421.

(58) Kumar, V.; Kawazoe, Y. *Phys Rev Lett* **2003**, *90*, 05550.

(59) Kumar, V.; Kawazoe, Y. *Physical Review Letters* **2003**, *91*, 199901/1.

(60) Kumar, V. *Comp. Mater. Sci.* **2004**, *30*,, 260.

(61) Kumar, V.; Singh, A. K.; Kawazoe, Y. *Nano Lett.* **2004**, *4*, 677.

(62) Khanna, S. N.; Rao, B. K.; Jena, P. *Phys. Rev. Lett.* **2002**, *89*, 016803/1.

(63) Jackson, K.; Nelleermore, B. *Chem. Phys. Lett.* **1996**, *254*, 249.

(64) Menon, M.; Subbaswamy, K. R. *Chem. Phys. Lett.* **1994**, *219*, 219.

(65) Menon, M.; Andriotis, A. N.; Froudakis, G. *Nano Letters* **2002**, *2*, 301.

(66) Mitas, L.; Grossman, J. C.; Stich, I.; Tobik, J. *Phys. Rev. Lett.* **2000**, *84*, 1479.

(67) Mittelbach, V. T.; Fritsche, H. G.; Mueller, H. *Zeitschrift fuer Physikalische Chemie (Muenchen, Germany)* **1994**, *187*, 45.

(68) Ray, U.; Jarrold, M. F.; Creegan, K. M.; Bower, J. E. *Int. J Mass Spect. and Ion Processes* **1990**, *100*, 625.

(69) Q. Sun; Q. Wang; P. Jena; B.K. Rao; Y. Kawazoe. *Phys. Rev. Lett.* **2003**, *90*, 135503.

(70) Scherer, J. J.; Paul, J. B.; Collier, C. P.; Saykally, R. J. *J. Chem. Phys.* **1995**, *102*, 5190.

(71) Scherer, J. J.; Paul, J. B.; Collier, C. P.; Saykally, R. J. *J. Chem. Phys* **1995**, *103*, 113.

(72) Scherer, J. J.; Paul, J. B.; Collier, C. P.; O'Keefe, A.; Saykally, R. J. *J. Chem. Phys.* **1995**, *103*, 9187.

(73) Hagelberg, F.; Xiao, C.; Lester, W. A. *Phys. Rev. B: Condensed Mater and Mater. Phys.* **2003**, *67*, 035426/1.

(74) A. N. Andriotis, A. N.; Mpourmpakis, G.; Froudakis, G.; Menon, M. *New J. Phys.* **2002**, *4*, 78.

(75) Beck, S. M. *J. Chem. Phys.* **1989**, *90*, 6306.

(76) Beck, S. M. *Adv. Met. Semicond. Clusters* **1993**, *1*, 241.

(77) Beck, S. M. *J. Chem. Phys.* **1987**, *87*, 4233.

(78) Lima, N. A. and Caldas, M. J. *Phys. Rev.* B 2005, **72**, 033109.

(79) Adamson, R. D. Dombroski, J. P. and Gill, P. M. W. *J. Comput. Chem.* **1999**, *20*, 921 .

(80) Leininger, T. Stoll, H. Werner, H.-J. and Savin, A. Chem. Phys. Lett. ,**1997**, *275*, 151.

CHAPTER II

ENDOHEDRAL AND EXOHEDRAL COMPLEXES OF T_8-POLYHEDRAL OLIGOMERIC SILSESQUIOXANE $(HSIO_{3/2})_8$ WITH ATOMS AND IONS

Introduction

Octahydridosilsesquioxane, $(HSiO_{3/2})_8$, or Polyhedral Oligomeric Silsesquioxane (POSS) T_8 cage systems and its derivatives have attracted considerable interest.[1-10] The T_8 cage POSS monomer consists of silicon atoms occupying the vertices of a cube, and oxygen atoms bridging each pair of silicon atoms. In the parent octahydridosilsesquioxane a single hydrogen atom is attached to each silicon atom. In general, POSS derivatives exhibit the composition $(RSiO_{3/2})_n$, where R denotes an organic ligand and n = 8, 10, and 12. POSS derivatives incorporated into organic polymers, dendrimers, and zeolites have attracted substantial attention due to their applications in material science and catalysis.[1-10] One interesting feature of these cages is that atoms or ions can probably be encapsulated into them. Several studies, including the present study, have focused on this property. Most experimental and theoretical studies[1-10]reported in the literature have focused on the pure or metal-substituted parent POSS

cage with or without encapsulated species. Throughout this chapter $X@(HSiO_{3/2})_8$ will be used to denote endohedral and $X(HSiO_{3/2})_8$ for exohedral complexes with T_8-POSS.

The structure of the parent T_8-cage molecule $(HSiO_{3/2})_8$ has been characterized by IR and NMR in solution as well by X-ray and neutron diffraction in the solid state and mass spectrometry in the gas phase.[1-10] Matsuda et al[11]and Päch et al.[12] studied the double four membered ring (D4R) silicate cage with an encapsulated hydrogen atom by ESR spectroscopy. Taylor et al. synthesized the endohedral T_8-POSS complexes, octaphenyl octasilsesquioxane fluoride, as a quarternary ammonium salt. It's structure was confirmed by ^{1}H NMR, ^{29}Si NMR, negative-ion Fast Atom Bombardment (FAB) mass spectrometry, and X-ray diffraction.[13]

The properties of POSS and it's derivatives and the reaction path that leads to the incorporation of foreign atomic or ionic species into the POSS cage can be predicted from computational studies. Such studies also may predict novel complexes for future experimental examination. Thus, Mattori et al. reported computational results on the trapping and release transition states (TS) of atomic hydrogen in an octasilsesquioxane host cage.[14] Sodium cations form exohedral complexes with POSS according to ion mobility studies and molecular mechanics (MM) calculations.[15,16] Encapsulation of Na^+, F^- or OH^- inside $[(OH)SiO_{3/2}]_8$ have been investigated by local density functional (LDF) techniques.[17] The geometric structures of these composites, as well as the charge redistribution among the host cage and the endohedral ionic species, were predicted.

Computational results have been reported for the structures and reaction mechanisms of the endohedral complexes $X@(HSiO_{3/2})_8$ ($X = N_2$ and O_2)[18], as well as

H@$(HSiO_{3/2})_{8.}$[14] However, very little information exists about the complexes arising from the combination of noble gas atoms, halides, or alkali metal ions with $(HSiO_{3/2})_8$ cage. Nothing is known about the formation process of these endohedral and exohedral complexes beyond the pioneering synthetic encapsulation of F^- by Taylor et al.[13] These issues, however, are of relevance both for a systematic understanding of POSS and POSS analogs, as well as for the possible fabrication of both exohedral and endohedral D4R[34] unit complexes.

In this study, the question addressed is to what extent the geometric, energetic, and electronic properties of $(HSiO_{3/2})_8$ can be influenced by endohedral or exohedral complexation of atomic and ions with POSS cages. More specifically, the exohedral $X(HSiO_{3/2})_8$ and endohedral $X@(HSiO_{3/2})_8$ [X = He, Ne, Ar, Li^+, Na^+, K^+, F^-, Cl^-, Br^-,] complexes were investigated (Figure 2.1). The most likely direct insertion mechanism is assumed to be the passage of impurities through a square face of the cubic POSS structure. This work should contribute to understanding the design and control of these molecular systems and to support ongoing endeavors to create new polyhedral sphero-atomic-oxide materials with novel properties.

Computational Details

All calculations were performed using the Gaussian03[19] and PQS[20] suite of programs. For all species the geometries and the harmonic vibrational frequencies were determined with density functional (DFT) calculations employing the B3LYP[21,33] potential. It has been demonstrated that this method combined with a basis set of at least a double zeta plus polarization quality yields reasonable molecular structures and

frequencies for many systems.[22] The vibrational frequencies were calculated for all optimized structures to allow classification of the various structures as minima or transition states; in addition it allowed corrections of calculated energy differences[17,23] for differences in zero-point vibrational energies.

Initially, all structures were studied using the 6-31G(d) basis set, and subsequently, refined calculations were carried out employing the 6-311++G(2d,2p) basis. For the host cage $(HSiO_{3/2})_8$, however, the geometry optimizations and frequency computations were also performed at the B3LYP/6-311++G(2d,p) level to resolve small structural differences between experimentally detected isomers. For the parent $(HSiO_{3/2})_8$ cage additional calculations using the cc-pVDZ and cc-pVTZ basis sets[18,24] were carried out for comparison. The agreement of the B3LYP/6-311++G(2d,2p) results with those obtained with the c-pVTZ basis set are within 0.5%..

Application of a method that explicitly includes electron correlation would have been preferable for a study of this nature; however, even the least expensive correlation method (MP2) turned out to be too time consuming for this study. However, the geometry of the parent POSS-cage was optimized at the MP2/6-311G(d,p) level and the geometry was found to be similar to the geometry obtained at the B3LYP level. The LYP-potential does incorporate some correlation effects and the B3LYP method was chosen as a cost-effective compromise for these studies. The systems investigated are illustrated in Figure 2.1. The binding energies, BE_{exo} (kcal/mol), of the exohedral clusters were evaluated by taking the energy difference of $X(HAO_{3/2})_8$ (E_{exo}) and the sum of the energies of the isolated components, E_x and E_{pure}. The binding energies for the

endohedral complexes, BE_{inc} (kcal/mol), were calculated in an analogous manner. The counterpoise method[25,26] was used to estimate the size of BSSE on the inclusion energies BE_{inc} and BE_{exo}. These calculations yield a slight modification of the endohedral binding energies without affecting their trends. For the exohedral binding energies, the BSSE were small.

Adiabatic ionization potentials (IP) were computed for the pure host cages $(HSiO_{3/2})_8$ as the difference between the total energies of the optimized cations and the optimized neutrals. For the treatment of the open shell species an unrestricted formalism was used.

Results and Discussion

This section is organized in the following way: The geometrical features will be discussed first starting with the pure host cages, followed by the endohedral and exohedral complexes, and finally the transition states separating the exohedral and endohedral complexes. In the last section of this part the energetics, i.e. the binding energies and activation barriers will be discussed.

Geometrical Features

Host Cages: The geometric parameters of the host cages calculated with the B3LYP method, are summarized in Figure 2.2. Only symmetry-unique parameters are shown. Table 2.1 contains the lowest vibational frequency, the adiabatic ionization potentials (IP), the cavity radii (see footnote c of Table 2.1), as well as energy differences between the O_h and T_h isomers. It should be noted that the global minimum exhibits T_h

symmetry in each case. This is consistent with experimental findings which yielded O_h symmetry for $(HSiO_{3/2})_8$ in solution[27] and T_h in the gas phase. The respective O_h and T_h structures also turned out to be very similar as can be seen in Figure 2.2. While these two isomers are near degenerate for the silicate cage, their energies are well separated from each other for the analogous carbonate and germanate cages. From Figure 2.2, it is also seen that the geometric differences between the host cages and their cations are small.

The radii of the host cavity Si: 0.986 Å is sufficient to encapsulate both ionic and atomic species. Ideally, if O_h symmetry is assumed, the SiOSi angle should be close to 148°.[28] However, if the symmetry is reduced to T_h (Figure 2.2) the SiOSi bond angles are smaller for T_8-POSS.

The isosurface plots of the HOMO and the LUMO are presented in Figure 2.3 for the host cage. For all cages, the HOMO is preceded by a threefold degenerate HOMO-1 and, in reverse order, the LUMO followed by a threefold degenerate LUMO+1. The HOMO consists mainly of an oxygen lone pair. The LUMO and the LUMO+1 contain mainly Si contributions, which are antibonding in Si-H and Si-O.

Endohedral Complexes

Despite the considerable variations in the sizes of the atomic and ionic endohedral species, stable endohedral geometries were obtained for all complexes investigated in this study. The geometric deformations induced by the encapsulated species were small. Table 2.2 contains the total energies, point groups, endohedral binding energies, and optimized bond lengths for the endohedral complexes $X@(HSiO_{3/2})_8$ with X = Li^+, Na^+, K^+, F^-, Cl^-, Br^-, He, Ne, Ar.

Endohedral complexes with alkali metal ions: Most of the endohedral complexes retain the symmetry of the respective pure host cage, i.e. O_h or T_h. However, this is not observed for $Li^+@(HSiO_{3/2})_8$. The former turns out to be a stationary point as O_h symmetry is imposed on the system. Frequency analysis results in five imaginary frequencies for both these structures. Deforming the systems along their triply and doubly degenerate unstable coordinates, we find minima with both D_{2d} and D_{4h} symmetry for $Li^+@(HSiO_{3/2})_8$. The coordination of the lithium cation is tetrahedral for the D_{2d} geometry and tetraplanar for the D_{4h} (Figure 2.4). For both systems the D_{2d} structures are more stable than the D_{4h} 3.4 kcal/mol, for $Li^+@(HSiO_{3/2})_8$ The bond distances between Li and its nearest O atom neighbors for the most stable structures is 2.045 Å $[Li^+@(HSiO_{3/2})_8]$ (D_{2d}) as seen in Table 2.2.

The distance $r_{X\text{-}O}$ of the host cage (using the convention that 'X' denotes the geometric center of the pure cage) shrinks considerably as Li^+ is inserted into $(HSiO_{3/2})_8$. The Li-Si bond lengths, $r_{X\text{-}Si}$, connecting the Li^+ ion with the vertices, is 2.745 Å $[Li^+@(HSiO_{3/2})_8]$. The lithium ion was the smallest endohedral ion considered, and when this ion is inserted into the cage, the original T_h symmetry of the cage is reduced to D_{2d} in order to maximize the electrostatic interaction between the cation and the cage. This is analogous to the solvation/complexation of alkali ions by crown ethers.[25]

The $Na^+@(HSiO_{3/2})_8$ minima exhibit O_h symmetry. Clearly, the symmetry of the endohedral complexes depends on the relative size of the inserted cation. For Li^+, the smallest alkali cation the distortion of the cage was insignificant and no distortion occurred for the cages when the largest alkali metal ion, K^+, was inserted. It should be

noted that in the cases where no cage distortion was observed D_{2d} structures were not stationary points on the potential surfaces.

The Si-O bond distances of all the endohedral cationic metal complexes are longer than the respective distances in the pure host cages and lengthen as the size of the endohedral cations (X = Li^+, Na^+, K^+) increase. Natural charge analysis[26,29], as shown in Table 2.3, reveals that the cationic species induce not only the transfer of electron density from the Si-H bonds to the Si–O bonds of the $(HSiO_{3/2})_8$ host cages but also accept electron density from the host cages (see Table 3 for numerical details). The amount of charge transfer decreases in the order $Li^+ > Na^+ > K^+$. The endohedral $K^+@(HSiO_{3/2})_8$ complexes have the shortest Si-H bond lengths 1.454Å, while the $Li^+@(HSiO_{3/2})_8$ complexes have the longest 1.456Å.

Endohedral complexes with halides: The endohedral halide (X = F^-, Cl^-, Br^-) complexes all retain the high symmetry of the parent cage (O_h or T_h). All endohedral halide complexes exhibit O_h symmetry, with the exception of $F^-@(HSiO_{3/2})_8$ which had a T_h symmetry. Geometries with lower symmetries (e. g. D_{2d}) were also considered, but these structures revert to the more symmetrical T_h or O_h structures.

In contrast to the alkali metal ions, the halides transfer electron density to the host cages. Electron donation occurs from endohedral halides to both the Si–O bonds and the hydrogen sites with a slight irregularity for X = F. Both the Si-O and Si-H distances elongate as a consequence of halide implantation. The amount of electron donation from the anionic halide to the host cage increases in the order $F^- < Cl^- < Br^-$.

$F^-@(HSiO_{3/2})_8$ has the longest Si-H (1.472 Å) and the shortest X-Si bond length (2.693 Å) among the octahydridosilsesquenoxane derivatives discussed here. The Si-O and Si-H bond lengths are longer and the X-Si bond lengths are shorter in the halide endohedral complexes compared to the alkali ion counterparts with $X = Na^+, K^+$ (Table 2). The experimental distances between the silicon atoms and the cage center in $F^-@[(Ph)SiO_{3/2}]_8$ and $[(Ph)SiO_{3/2}]_8$[13] (Figure 2.5), are a little shorter in the endohedral F^- species (2.653 Å) than in the isolated host cage (2.691 Å), and the experimental X-O distance is longer in the endohedral species (2.707 Å) than in the isolated host cage (2.643 Å). Furthermore, the Si-O bonds (1.625 Å) are longer and ∠SiOSi angles (141.2°) are smaller in $F^-@[(Ph)SiO_{3/2}]_8$ than in $[(Ph)SiO_{3/2}]_8$ (Si-O = 1.612, ∠SiOSi = 149.2°). These experimental trends are consistent with our calculated results.

Endohedral complexes with noble gases: For endohedral complexes $X@(HSiO_{3/2})_8$ where X is a neutral noble gas atom (He, Ne, or Ar), the geometric changes are almost negligible for He and Ne, but significantly larger when X = Ar. Details can be found in Table 2.2.

Exohedral Complexes

Table 2.5 summarizes selected geometric parameters and binding energies for the optimized exohedral D4R complexes involving alkali metal cations, $X(HSiO_{3/2})_8$ ($X = Li^+$, Na^+, K^+). The bond designations used in Table 2.5 are illustrated in Figure 2.6. In all of these complexes, the alkali metal cation is attached to a face of the cage. Clearly, an exohedral impurity will destroy the high symmetry of the host cage system; specifically, all exohedral complexes have C_{2v} or C_{4v} symmetry. The X-O bond lengths for

$X(HSiO_{3/2})_8$ with $X = Li^+$, Na^+ are similar to the distances in the respective endohedral systems; the same holds for the X-Si bond lengths when $X = Li^+$. In both types of complexes the Li^+ ion interacts with four oxygen atoms. Both the exohedral and the endohedral addition of a Li^+ ion to the pure D4R cages are exothermic processes (see below). Only minor changes, in the range of ±0.04Å, occur in the Si-O bond lengths (r_1 to r_4) in the face adjacent to the alkali ion and in the opposite face (see Figure 2.6 and Table 2.5).

Halide complexes were also investigated and the results are shown in the Table 2.5. The $HSiO_3F^-$ subunit adopts a regular trigonal bipyramidal structure. The main geometric difference between the isomers shown in Figures 2.7a and 2.7b is that F^- occupies an axial position within this bipyramid in Figure 2.7a and an equatorial position in Figure 2.7b. The location of F^- is in sharp contrast to the face location adopted by alkali metal ions in the exohedral complexes discussed above. The axial fluoride (Figure 2.7a) exhibits a longer Si-F distance (1.709 Å) than the equatorial fluoride (1.652 Å), and the axial Si-F bond length is significantly longer than the S-F bond found in tetracoordinated SiF_4 (Exp.:1.56 Å, Theo.: 1.57 Å), and also longer than the axial pentacoordinated silyl fluoride (1.67 Å).[29] However, this 1.709 Å bond length is shorter than those reported for pentacoordinated silicon in the SiO_4F^- (1.74 Å) subunit of zeolite. As expected, the Si-O and Si-H bonds of the pentacoordinated silicon atoms that are connected to the exohedral F^- ions are longer than the corresponding bonds in the pure $(HSiO_{3/2})_8$ cage that contains tetracoordinated Si.

No exohedral isomers are included for the noble gas complexes. The respective structures were found to involve large distances in the order of 5 to 6 Å between the host face and the noble gas atom. Thus, they were hardly distinguishable from the separated species. These very weakly bonded complexes could be artifacts caused by basis set superposition errors.

Energetics

We will first discuss the binding energies for formation of the endohedral and exohedral complexes and then discuss the barriers for the insertion processes. Table 2.4 summarizes the ZPE-corrected endohedral (BE_{endo}) and exohedral (BE_{exo}) binding energies for the species $X@(HSiO_{3/2})_8$ and $X(HSiO_{3/2})_8$, respectively. These binding energies were calculated as the energy difference between a complex and the sum of the energies of X and the isolated host cage. A negative BE thus indicates that the complex is favored compared to the separated species. All exohedral complexes listed in Table 2.4 are preferred over the separated species. In contrast, the formation of most of the endohedral complexes was found to be endothermic, except the systems $F^-@(HSiO_{3/2})_8$ and $Li^+@(HSiO_{3/2})_8$ which all had lower energies than the separated species (see Table 2.4 for details).

As is seen from the values of BE_{inc} in Table 2.4, the bonding between the encapsulated impurity X and the cage strengthens as the atomic number of X decreases within a group of the periodic table which should simply be a manifestation of the size of the guest species. The impurities F^-, Ne, and Na^+ are isoelectronic. Furthermore, F^- and Na^+ as well as He and Li^+ have approximately equal radii.[30] However, the binding

energies of these complexes differ significantly. Thus, the size is of the guest species is only one of the factors that impact the endohedral binding energies. The large differences between the natural charges of guests that are similar in size, as indicated in Table 2.3, suggest that charge transfer from the impurity to the host cage determines BE_{endo} in the absence of size effects.

It is interesting to compare the energetic properties of $X@(HSiO_{3/2})_8$ with those of the hydrocabon analogs $X@C_{20}H_{20}$.[31] The endohedral binding energies of $X@(HSiO_{3/2})_8$ (X = He: 12.3; Ne: 24.2; Ar :95.9 kcal/mol) are lower (i.e. the complexes are more stable) than those of $X@C_{20}H_{20}$ (X = He: 37.9; Ne: 102.9; Ar: 320.2 kcal/mol). The same hierarchy of stabilities as established in this work for $X@(HSiO_{3/2})_8$ ($X = Li^+, Na^+, K^+$) was found by Sun et al in computations on fullerene C_{32} as the host for Li^+ ($Li^+@C_{32}$: -53.1 kcal/mol), Na^+ ($Na^+@C_{32}$: -26.9 kcal/mol), and K^+ ($K^+@C_{32}$: 13.7 kcal/mol), using the GGA DFT procedure.[32] Consistently, the Li^+ incorporating system emerges as most stable, while the K^+ containing unit is of lowest stability.

The exohedral binding energies (BE_{exo}) show a similar charge and size dependence as the endohedral binding energies (E_{inc}, Table 2.2). Adsorption of the small Li^+ ion turns out to be the most exothermic process for all three $(HSiO_{3/2})_8$ cages, followed by Na^+ and K^+. The energy differences between the exohedral and endohedral structures (the "relative energy", E_{iso}, listed in Table 2.4), demonstrate that the exohedral species are usually energetically more favorable than the endohedral alternatives. Among the alkali ion-containing complexes, E_{iso} is smallest for Li^+ encapsulated in $(HSiO_{3/2})_8$.

Its E_{rel} is only 4.7 kcal/mol, which may be close to the uncertainty of the calculated energy differences in this study.

Conclusions

The D4R cage geometries for $(HSiO_{3/2})_8$ exhibit either T_h or O_h symmetry. The cavities of these cages are sufficiently large to accommodate atomic and ionic guests.

The endohedral complexes, $X@(HSiO_{3/2})_8$ (X = Li^+, $Na,^+$, K^+, F^-, Cl^-, Br^-, He, Ne, Ar) were found to have either T_h or O_h symmetry with exception of the $Li^+@(HSiO_{3/2})_8$, which favor D_{2d} symmetry. Encapsulated noble gas atoms (He, Ne, Ar) expand the cage roughly in proportion to their radii, elongating the Si-O bond lengths of the host cages. These calculations predict markedly different features for encapsulated halogen anions than for their isoelectronic nobel gas and alkali metal cations. Thus, for the isoelectronic series F^-, Ne, and Na^+, the Si-O bond lengths increase, while the Si-H bond lengths change in the reverse order. This behavior is understood as the result of charge redistribution between the Si–O and the Si–H bonds of the host cage, as induced by the presence of the guest species.

Several guest/host combinations were identified for which guest inclusion is energetically favorable. Charge polarization between the host and the guest turned out to be the principal cause for the stability of these complexes. All endohedral complexes enclosing alkali cations have higher energy than their exohedral counterparts, as suggested by ion mobility studies on various silsesquioxanes cationized by addition of Na^+.[15,16] The endohedral complexes $F^-@(HSiO_{3/2})_8$, is preferred over the exohedral alternatives, in accord with experiment.[13]

Based on our work, we hope that novel host cages composed of D4R units may be synthesized in conjunction with endohedral as well as exohedral alkali metal ion or halide guests.

Acknowledgments

This work has been published in the Journal of Physical Chemistry, Part A in 2004. Park, S. S.; Xiao, C.; Hagelberg, F.; Hossain, D.; Pittman, C. U., Jr.; Saebo, S. J. Phys. Chem. A 2004, 108, 11260.

References

(1) Brown, J. F., Jr.; Vogt, L. H., Jr. *J. Am. Chem. Soc.* 1965, *87*, 4313.

(2) Feher, F. J.; Wyndham, K. D. *Chem. Communi.* 1998, 323

(3) Maxim, N.; Abbenhuis, H. C. L.; Stobbelaar, P. J.; Mojet, B. L.; van Santen, R. A. *Phys. Chem. Chem. Phys.* 1999, *18*, 4473.

(4) Maxim, N.; Magusin, P. C. M. M.; Kooyman, P. J.; van Wolput, J. H. M. C.; van Santen, R. A.; Abbenhuis, H. C. L. *Chem. Materials* 2001, *13*, 2958.

(5) Wada, K.; Yamada, K.; Kondo, T.; Mitsudo, T.-A. *Chem. Lett.* 2001, 12.

(6) Lamm, M. H.; Chen, T.; Glotzer, S. C. *Nano Lett.* 2003, *3*, 989.

(7) Zheng, L.; Waddon, A. J.; Farris, R. J.; Coughlin, E. B. *Macromolecules* 2002, *35*, 2375.

(8) Li, G. Z.; Wang, L.; Toghiani, H.; Daulton, T. L.; Koyama, K.; Pittman, C. U., Jr. *Macromolecules* 2001, *34*, 8686.

(9) Li, G.; Wang, L.; Ni, H.; Pittman, C. U., Jr. *J. Inorg. Organomet. Polym.* 2002, *11*, 123.

(10) Li, G.-Z.; Wang, L.; Ni, H.; Pittman, C. U., Jr. *J. Inorg. Organomet. Polym.* 2001, *11*, 123.

(11) Sasamori, R.; Okaue, Y.; Isobe, T.; Matsuda, Y. *Science (Washington, DC, United States)* 1994, *265*, 1691.

(12) Päch, M.; Stösser, R. *J. Phys. Chem. A* 1997, *101*, 8360.

(13) Bassindale, A. R.; Pourny, M.; Taylor, P. G.; Hursthouse, M. B.; Light, M. E. *Angew. Chem., Int. Ed.* 2003, *42*, 3488.

(14) Mattori, M.; Mogi, K.; Sakai, Y.; Isobe, T. *J. Phys. Chem. A* 2000, *104*, 10868.

(15) Gidden, J.; Kemper, P. R.; Shammel, E.; Fee, D. P.; Anderson, S.; Bowers, M. T. *Int. J. Mass Spect.*2003, *222*, 63.

(16) Baker, E. S.; Gidden, J.; Fee, D. P.; Kemper, P. R.; Anderson, S. E.; Bowers, M. T. *Int. J. Mass Spect.* 2003, *227*, 205.

(17) George, A. R.; Catlow, C. R. A. *Chem. Phys. Lett.* 1995, *247*, 408.

(18) Tejerina, B.; Gordon, M. S. *J. Phys. Chem. B* 2002, *106*, 11764.

(19) Frisch, M. J. T., G. W.; Schlegel, H. B.; Scuseria, G. E.; Robb, M. A.; Cheeseman, J. R.; Montgomery, Jr., J. A.; Vreven, T.; Kudin, K. N.; Burant, J. C.; Millam, J. M.; Iyengar, S. S.; Tomasi, J.; Barone, V.; Mennucci, B.; Cossi, M.; Scalmani, G.; Rega, N.; Petersson, G. A.; Nakatsuji, H.; Hada, M.; Ehara, M.; Toyota, K.; Fukuda, R.; Hasegawa, J.; Ishida, M.; Nakajima, T.; Honda, Y.; Kitao, O.; Nakai, H.; Klene, M.; Li, X.; Knox, J. E.; Hratchian, H. P.; Cross, J. B.; Bakken, V.; Adamo, C.; Jaramillo, J.; Gomperts, R.; Stratmann, R. E.; Yazyev, O.; Austin, A. J.; Cammi, R.; Pomelli, C.; Ochterski, J. W.; Ayala, P. Y.; Morokuma, K.; Voth, G. A.; Salvador, P.; Dannenberg, J. J.; Zakrzewski, V. G.; Dapprich, S.; Daniels, A. D.; Strain, M. C.; Farkas, O.; Malick, D. K.; Rabuck, A. D.; Raghavachari, K.; Foresman, J. B.; Ortiz, J. V.; Cui, Q.; Baboul, A. G.; Clifford, S.; Cioslowski, J.; Stefanov, B. B.; Liu, G.; Liashenko, A.; Piskorz, P.; Komaromi, I.; Martin, R. L.; Fox, D. J.; Keith, T.; Al-Laham, M. A.; Peng, C. Y.; Nanayakkara, A.; Challacombe, M.; Gill, P. M. W.; Johnson, B.; Chen, W.; Wong, M. W.; Gonzalez, C.; and Pople, J. A.; Gaussian, Inc., Wallingford CT, 2004. Gaussian 03; Gaussian 03 ed., 2004.

(20) PQS version 3.1, P. Q. S., 2013 Green Acres Road, Fayetteville, AR 72703.

(21) Becke, A. D. *J. Chem. Phys.* 1993, *98*, 5648.

(22) Foresman, J. B.; Frisch, M. J. *Exploring Chemistry with Electronic Structure Methods*, 1996, 2nd ed.; Gaussian, Inc.: Pittsburgh, PA, 1996.

(23) Hehre, W. J.; R. F. Stewart, R. F.; J.A, P. *J. Chem. Phys.* 1969, *51*, 2657.

(24) Woon, D. E.; Dunning, T. H., Jr. *J. Chem. Phys.* 1993, *98*, 1358.

(25) Frisch, M. J.; Del Bene, J. E.; Binkley, J. S.; Schaefer, H. F., III. *J. Chem. Phys.* 1986, *84*, 2279.

(26) Schwenke, D. W.; Truhlar, D. G. *J. Chem. Phys.* 1985, *82*, 2418.

(27) Agaskar, P. A.; Klemperer, W. G. *Inorg. Chim. Acta* 1995, *229*, 355.

(28) Li, H.; Yaghi, O. M. *J. Am. Chem. Soc.* 1998, *120*, 10569.

(29) Foster, J. P.; Weinhold, F. *J. Am. Chem. Soc.* 1980, *102*, 7211.

(30) Huheey, E. J.; Keiter, A. E.; Keiter , L. R. *Inorganic Chemistry : Principles of Structure and Reactivity*; HarperCollins,: New York, USA, 1993.

(31) Moran, D.; Stahl, F.; Jemmis, E. D.; Schaefer, H. F., III;; Schleyer, P. v. R. *J. Phys. Chem. A* 2002, *106*, 5144.

(32) Sun, Q.; Wang, Q.; Yu, J. Z.; Ohno, K.; Kawazoe, Y. *J. Phys.: Conden. Matter* 2001, *13*, 1931.

(33) Lee, C.; Yang, W.; Parr, R. G. *Phys. Rev. B: Condens. Matter and Materials Phys.* **1988**, *37*, 785.

(34) D4R is used to define the each surface of T_8-POSS cage in which four silicon atoms are inter connected with each othe by oxygen atoms.

Table 2.1 Magnitudes of the Lowest Vibrational Frequencies (ω_1), Adiabatic Ionization Potentials (IP), Cage Radii, and Relative Energy (ΔE) Between O_h and T_h Isomers at B3LYP/6-311++G(d,p)[a]

	Si (T_h)
ω_1 (cm^{-1})[b]	74[a]
IP (eV)	10.02
Cavity radius (Å)[c]	0.986
ΔE (kcal/mol)[d]	0.7[a]

[a]at B3LYP/6-311++G(2d,p) optimized structures. [b]lowest frequency. [c]Cavity radius = [distance between cage center and edge – anionic oxygen radius]. [d]ΔE = Total Energy (O_h) - Total Energy (T_h).

Table 2.2 Total Energies (in Hartree), Zero-point Energies (ZPE), Molecular point Groups, Lowest Vibrational Frequencies ω_1 (cm^{-1}), Zero-point Corrected Inclusion Energies (kcal/mol), and Optimized Bond Lengths (Å) for Endohedral Minima of $X@(HSiO_{3/2})_8$ Calculated at the B3LYP/ 6-311++G(d,p) Level.

X	Energy	ZPE	*Sym.*	ω_1	E_{inc}	r_{X-A}	r_{X-O}	r_{A-O}	r_{A-H}
Pure	-3225.16019	87.7	O_h	51		2.746	2.679	1.644	1.460
Li^+	-3232.47633	88.8	D_{2d}	96	-18.5	2.745	2.045	1.651	1.456
Na^+	-3387.22991	87.8	O_h	58	11.3	2.804	2.633	1.655	1.454
K^+	-3824.81416	88.2	O_h	110	67.6	2.821	2.656	1.667	1.454
F^-	-3325.16466	89.2	O_h	80	-71.2	2.693	2.746	1.648	1.472
Cl^-	-3685.41998	88.2	O_h	125	28.0	2.724	2.791	1.671	1.470
Br^-	-5799.27129	87.2	O_h	143	79.0	2.738	2.814	1.683	1.469
He	-3228.05663	89.3	O_h	69	12.3	2.751	2.682	1.647	1.460
Ne	-3354.08419	89.1	O_h	84	24.2	2.757	2.690	1.651	1.461
Ar	-3752.56249	88.6	O_h	125	95.9	2.781	2.725	1.669	1.460

Table 2.3. Natural Charge Analysis of Endohedral Minima at the B3LYP/6-31G(d) Level

X	Q_X[a]	ΣQ_{SiO}[b]	ΣQ_H
Pure		1.92	-1.92
Li^+	0.86	1.71	-1.57
Na^+	0.83	1.74	-1.57
K^+	0.91	1.60	-1.52
F^-	-0.71	1.95	-2.24
Cl^-	-0.58	1.69	-2.11
Br^-	-0.44	1.52	-2.08
He	0.04	1.86	-1.90
Ne	0.07	1.82	-1.89
Ar	0.16	1.66	-1.82

[a]Q_X = Charge on impurity X. The symbols Q_{Si}, Q_H and Q_O are defined analogously; [b]$\Sigma Q_{SiO} = \Sigma Q_{Si} + \Sigma Q_O$.

Table 2.4 Inclusion Energies for Formation of Endohedral (E_{inc}) and Binding for Exohedral (E_{exo}) Complexes, and Isomerization Energies (E_{iso}[a]) for $(HSiO_{3/2})_8$ Calculated at the B3LYP/6-311++G(d,p) Level.

X	E_{inc}	E_{exo}	E_{iso}
Li^+	-18.5	-46.7	28.2
Na^+	11.3	-29.6	40.9
K^+	67.6	-18.0	85.6
F^-	-71.2	-58.4	-12.8
Cl^-	28.0	-14.2	42.2
Br^-	79.0	-9.5	88.5
He	12.3		12.3
Ne	24.2		24.2
Ar	95.9		95.9

[a]$E_{iso} = E_{endo} - BE_{exo}$. All energies are in kcal/mol

Table 2.5 Total Energies (in Hartree), Lowest Frequencies ω_1 (cm^{-1}), Molecular point Groups, Binding Energies (kcal/mol), Optimized Bond Lengths (Å), and Natural Charges on Metal Atoms (Q_X) for Exohedral Minima of Cationic Metal Complexes Calculated at the B3LYP/6-311++G(d,p) Level.

X	Energy	ω_1	Sym.	BE_{exo}	r_{X-A}	r_{X-O} (r'_{X-O})	r_1 (r'_1)	r_2	r_3	r_4 (r'_4)
Li^+	-3232.52175	78	C_{4v}	-46.7	2.730	2.087	1.678	1.611	1.663	1.640
Na^+	-3387.29599	75	C_{4v}	-29.6	3.125	2.501	1.672	1.614	1.660	1.640
K^+	-3824.95055	69	C_{4v}	-18.0	3.553	2.955	1.666	1.617	1.658	1.641

[a]At the B3LYP/6-31G(d) level

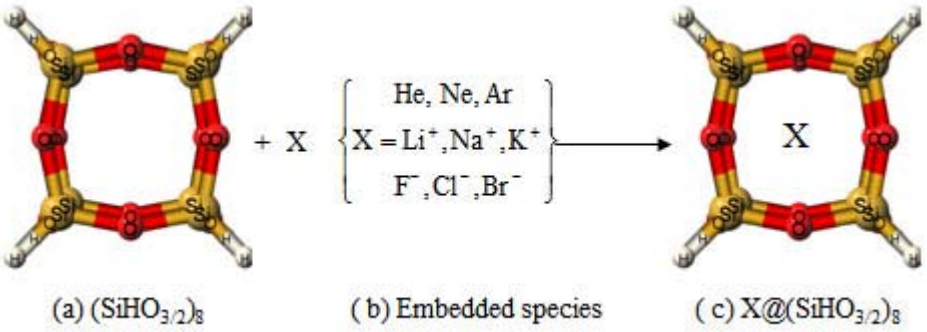

Figure 2.1 Schematic Representation of Host Cage with D4R units and Embedded Species; (a) Host cage with O_h or T_h Symmetries, (b) Embedded Species and (e) Endohedral Complexes.

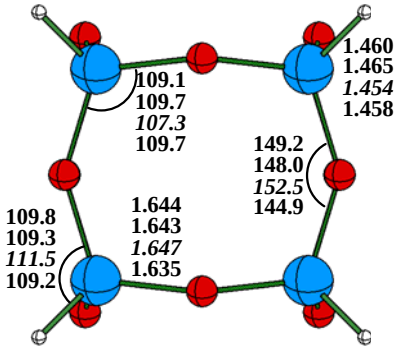

(b) $(HSiO_{3/2})_8$;, O_h or T_h

Figure 2.2 Optimized Geometries (Å and degrees) and Molecular point Groups of $(HAO_{3/2})_8$ Molecules Calculated with the B3LYP Method, using two Different Basis Sets. The Order is (from above): 6-311++G(d,p) and 6-31G(d). Data Referring to the Structures of the Cations are Printed in Italics; the Respective Results are Obtained on the B3LYP/6-311++G(d,p) Level. For $(HSiO_{3/2})_8$, Data Pertaining to T_h Symmetry, Obtained at the B3LYP/6-311++G(2d,p) Level, are Included as the Fourth Entry in Each Column.

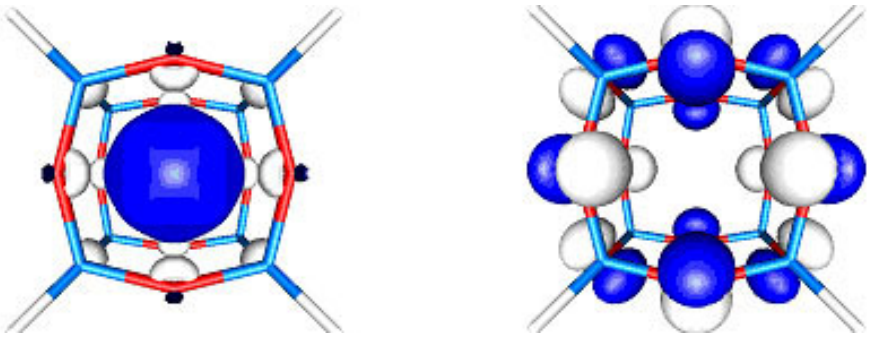

Figure 2.3 Isosurfaces (dark: positive; light; negative values) for the HOMO and LUMO of the Host Cages Considered in this Work (upper row: LUMOs, lower row: HOMOs; isosurface parameter: 0.04 e/Å^3).

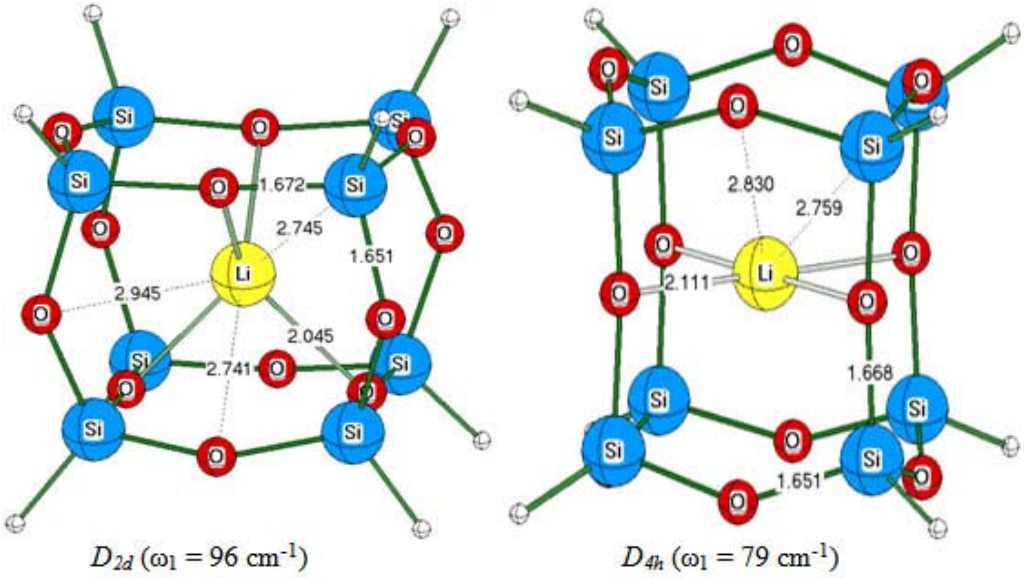

Figure 2.4 Optimized Geometries of $Li^+@(HSiO_{3/2})_8$ at the B3LYP/6-311++G(2d,2p) Level.

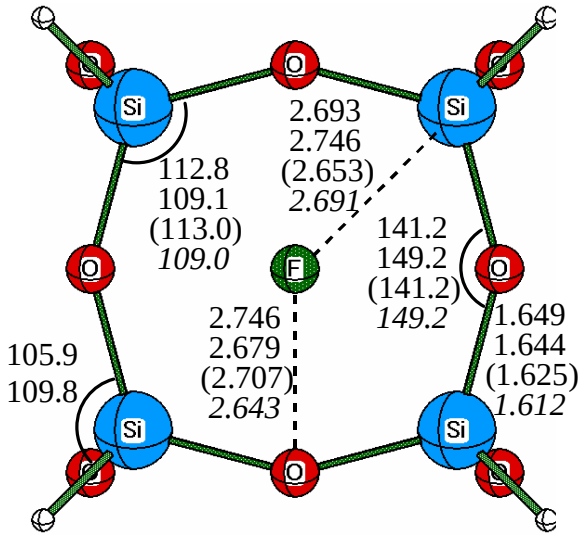

Figure 2.5 Otimized Geometry of $F^-@(HSiO_{3/2})_8$ with O_h Symmetry at the B3LYP/6-311++G(2d,2p) Level. For Comparison, the Structural data of the Pure $(HSiO_{3/2})_8$ Cage are Included in the Second Entry of Each Column. The Experimental Values of $F^-@[(Ph)SiO_{3/2}]_8$ and $[(Ph)SiO_{3/2}]_8$ are Printed in Parenthesis and in Italics, Respectively.

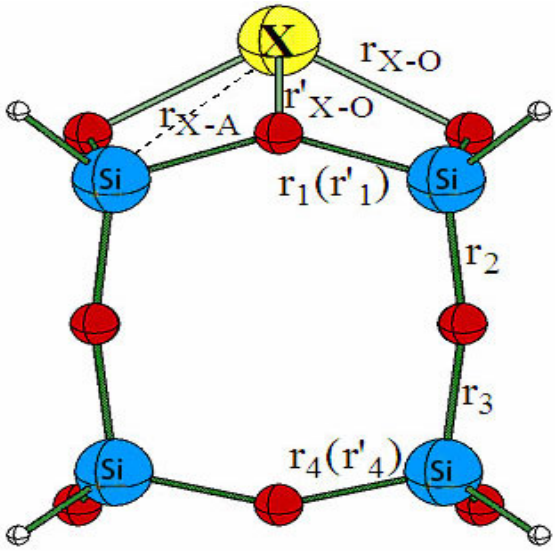

Figure 2.6 Schematic Geometry for the $X^+(HSiO_{3/2})_8$ Complex with X = Alkali Metal Species. The Primed Symbols Refer to C_{2v}, the Unprimed to C_{4v} Symmetry (see text).

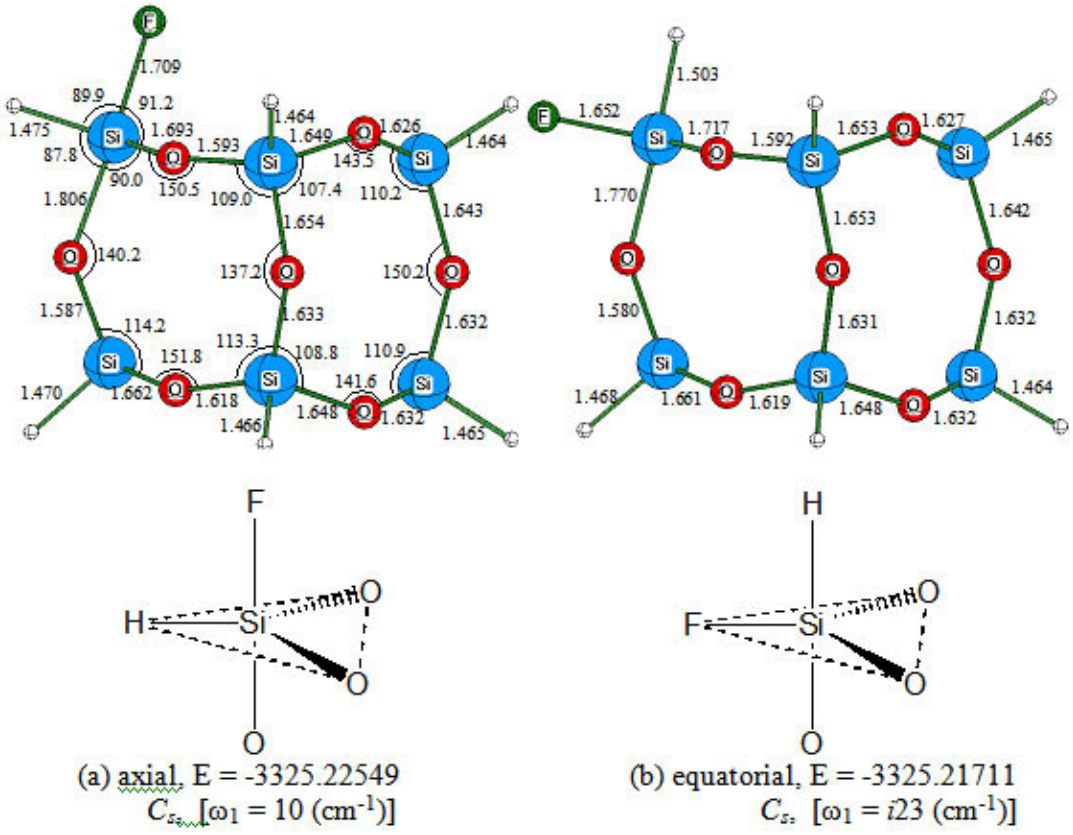

Figure 2.7 Optimized Geometries of Two Isomers of Exohedral $F^-(HSiO_{3/2})_8$ with C_s Symmetry at the B3LYP/6-311+G(2d,p) Level.

CHAPTER III

ENDOHEDRAL AND EXOHEDRAL COMPLEXES OF T_8-POLYHEDRAL OLIGOMERIC SILSEQUIOXANE (POSS) WITH TRANSITION METAL ATOMS AND IONS

Introduction

Polyhedral Oligomeric Silsesquioxanes (POSS) are cage molecules comprised of a silicon and oxygen core, exhibiting the composition $(RSiO_{3/2})_{2n}$, where R denotes a hydrogen, organic or inorganic ligand. Octahydridosilsesquioxane, $(HSiO_{3/2})_8$, (designed as T_8-POSS) consists of silicon atoms occupying the vertices of a cube, oxygen atoms bridging each pair of silicon atoms and a single hydrogen atom attached to each silicon atom. T_8-POSS and its derivatives incorporated into organic polymers, dendrimers, and zeolites have received substantial attention due to their applications in material science and catalysis.[1-14] POSS has also emerged as a viable filler in high performance nanocomposites.[15] POSS polymer nanocomposites are substantially harder than the unfilled polymers.[16] POSS cage incorporation into the polymeric materials enhances properties such as glass transition temperatures, decomposition temperatures and mechanical strength.[17-20] In POSS-PEO-based polymer electrolytes, POSS acts as an inhibitor to polyethylene oxide (PEO) crystallization.[21] Cationic polyhedral oligomeric

silsesquioxane (POSS) units can serve as carriers and potential drug delivery agents.[22] Because of their nanostructured nature and their ceramic like properties (creep oxidation resistant), POSSs are being used for synthesis of polymer-derived ceramics.[23]

Metal containing siloxanes, and oligomettalla-silosesquioxanes are used as catalytic converters for homogeneous catalysts in olefin processing. Epoxidation of alkene is easily accomplished with certain POSS catalysts.[24-28] POSS is also used as a supporter for Ziegler-Natta catalysts.[29] Coupar et al[30] has reported dendrimer catalysts based on POSS cores. These materials are expected to combine the traits of homogeneous catalysts with the high activity and precise control of catalytic sites normally associated with homogeneous catalysts. Murfee et al[31] reported that metallodrimers with a diphenylphosphino-POSS core and Ru-based chromophores exhibit unique advantages. A liquid crystalline silsesquioxanes dendrimer exhibiting chiral nematic and columnar mesophases has been synthesized by Saez et al.[32]

The cage-like structures of POSS chemicals makes them useful for separating gas mixtures as in siloxanes and silicon-based capillary membranes.[33,34] Silicon rubber, poly(dimethylsiloxane), is more permeable to oxygen.[35] than to nitrogen and is used to separate N_2/O_2 mixtures.[36] Cationic polyhedral oligomeric silsesquioxane (POSS) units can serve as carriers and potential drug delivery agents.[22] Most experimental and theoretical studies[37-43] reported in the literature describe pure or metal-substituted parent POSS cages without encapsulated species. However, a few studies of endohedral T_8-POSS have appeared.[44-46] The parent T_8-cage molecule $(HSiO_{3/2})_8$ structure has been characterized by IR and NMR in solution as well as X-ray

and neutron diffraction in the solid state, and mass spectrometry in the gas phase.[47-53] Matsuda et al.[54] and Päch et al.[55] studied the double four-membered ring (D4R) silicate cage with an encapsulated hydrogen atom by ESR spectroscopy. Taylor et al.[45] synthesized an endohedral fluoride ion complex, octaphenyl octasilsesquioxane fluoride, as its quaternary ammonium salt. This structure was confirmed by ^{1}H NMR and ^{29}Si NMR, negative-ion Fast Atom Bombardment (FAB) mass spectrometry, and X-ray diffraction.[45] Endohedral analog complexes analog of octaphenyl octasilsesquioxane fluoride also exist. For example, Morris et al.[56,57] prepared molecular fluoride-encapsulated octaspherogermante, $F^{-}@[(OH)GeO_{3/2}]_8$, confirming its structure by NMR and X-ray diffraction experiments.

The properties of POSS and its derivatives and the reaction path that leads to endohedral incorporation of atomic or ionic species can be obtained from computational studies. These studies also may predict novel complexes for future experimental examination. Mattori et al. reported computational results on the trapping and detrapping mechanism of atomic hydrogen in an octasilsesquioxane host cage.[58] Ion mobility studies and molecular mechanics (MM) calculations predicted that sodium cations form exohedral complexes with POSS.[59,60] Encapsulation of Na^{+}, F^{-} or OH^{-} inside $[(OH)SiO_{3/2}]_8$ has been investigated by local density functional (LDF) techniques. [46] The geometrical structures and the charge redistribution among the host cage and the endohedral ionic species were predicted.

Computational results have been reported for the structures and encapsulation mechanisms of the endohedral complexes $X@(HSiO_{3/2})_8$ ($X = N_2$ and O_2)[61],

$H@(HSiO_{3/2})_8$[58] and $X@(HSiO_{3/2})_8$[44] ($X = Li^+, Na^+, K^+$, He, Ne, Ar, F^-, Cl^-, Br^-) However, very little information exists about the structures arising from the combination of transition metal atoms or ions with $(HSiO_{3/2})_8$ cages. Is the T_8-POSS cage stable when different transition metal or their cations are incorporated into the cage? What kind of interactions occurs between the incorporated ion (or atom) with the T_8-POSS skeleton? To address these questions, we optimized the structure of the complexes formed between transition metal atoms and their +1 ions with T_8-POSS. Alternatively, someone may synthesize T_8-POSS someday in a manner where the cage assembles and closes around a transition metal (TM) or its cation as found for $F^-(PhSiO_{3/2})_8$.[45] In this chapter, we address to what extent are the geometric, energetic, and electronic properties of $(HSiO_{3/2})_8$ influenced by addition of transition metal (TM) atoms or ions. Specifically, we report the endohedral $X@(HSiO_{3/2})_8$ and exohedral $X(HSiO_{3/2})_8$ ($X = Sc^{0,+}$, $Cr^{0,+}$, $Fe^{0,+}$, $Co^{0,+}$, $Ni^{0,+}$, $Cu^{0,+}$, $Zn^{0,+}$, $Mo^{0,+}$, $W^{0,+}$, $Ru^{0,+}$, $Os^{0,+}$) systems (Figure 3.1). The direct insertion mechanism is assumed to be the passage of impurities through a D4R face of the cubic POSS structure. This work may contribute to understanding the design and control of these molecular systems and to support ongoing endeavors to create new polyhedral sphero-atomic-oxide materials with novel properties.

Computational Details

All calculations were performed using the Gaussian 03[62] suite of programs. For all species the geometries and the harmonic vibrational frequencies were determined with density functional (DFT) calculations employing the B3LYP[63,82] potential. It has been demonstrated that this method combined with a basis set of at least a double zeta plus

polarization yields reasonable molecular structures and frequencies for many systems.[17c] The vibrational frequencies were calculated for all optimized structures using the same levels of theory to characterize the stationary points as minima (zero imaginary frequencies) saddle points (one maginary frequency). The frequency calculation allowed the calculated energy differences[17] to be corrected for differences in zero-point vibrational energies. The NMR shielding tensors for selected systems were calculated using B3LYP/6-311G (d,p) and GIAO methods.[64,65] The electronic properties and atomic charges were evaluated using natural bond orbital analysis (NBO).[66]

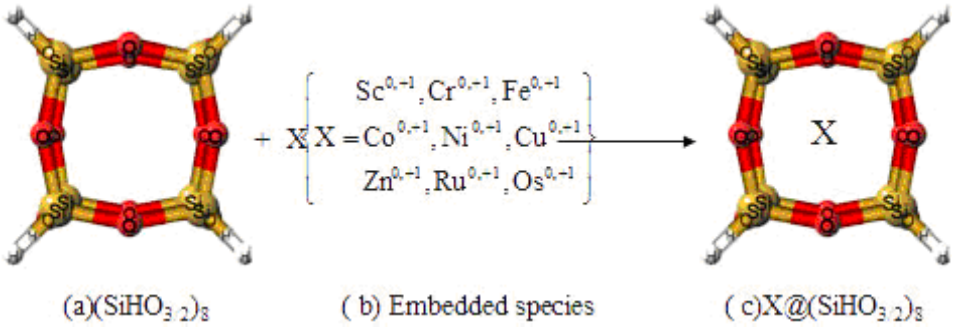

Figure 3.1 Schematic Representation of Host Cage Species $(HSiO_{3/2})_8$ with D5R units and Impurities; (a) Host Cage with O_h Symmetry (b) Identity of X (c) Endohedral Species of $X@(HSiO_{3/2})_8$.

Initially, all structures were studied using the LanL2MZ[67-69] basis set. Subsequently, refined calculations were carried out employing the LanL2DZ basis set.[67-70] Geometry optimizations and frequency computations for the host $(HSiO_{3/2})_8$ were also performed at the B3LYP/6-311G(2d,p) level to resolve small structural differences between experimentally detected isomers. For the parent $(HSiO_{3/2})_8$ cage, additional

calculations using the cc-pVDZ and cc-pVTZ basis sets[18] were carried out for comparison. The LanL2DZ basis set slightly over-estimates the bond lengths and bond angles. However, due to availability of basis sets for transition metals, we used LanL2DZ basis set throughout our calculations. For NMR calculations, however, LanL2DZ is a poor choice. The NMR for selected systems were calculated using the 6-311G(d,p) basis set.

Explicitly including electron correlation would have been preferable however, even the least expensive correlation method (MP2) turned out to be too time consuming and expensive for this study. However, the geometry of the parent T_8-POSS cage was optimized at the MP2/6-311G(d,p) level and the geometry was found almost the same as that almost the same as that obtained at the B3LYP level. The LYP-potential does incorporate some correlation effects and the B3LYP method was chosen as a cost-effective compromise for our studies.

The inclusion energies, E_{inc} (kcal/mol), of the endohedral clusters were defined as the energy difference between $X@(HSiO_{3/2})_8$ and the sum of the energies of the isolated components, E_x and E_{cage}. The counterpoise method[19,71] is used for estimating the size of basis set superposition errors BSSE on the inclusion energies (E_{incl}) and binding energies (E_{bind}). The BSSE has been found to be significant for endohedral complexes. However, the general trends of the complexes still remain same. For exohedral complexes it is small.[44] Hence, the extensive and expensive calculation of basis set superposition errors (BSSE) was neglected.

Adiabatic ionization potentials (IP) were computed for the $X@(HSiO_{3/2})_8$ complexes (where X = $Sc^{0,+}$, $Fe^{0,+}$, $Co^{0,+}$, $Ni^{0,+}$, $Cu^{0,+}$, $Zn^{0,+}$, $Ru^{0,+}$, $Os^{0,+}$) as the difference between the total energies of the optimized cationic and the optimized neutral transition metal complexes of ($HSiO_{3/2}$).

Results and Discussion

This section is organized to discuss the geometrical features first, starting with the pure host cage, followed by the neutral and cationic endohedral and exohedral complexes, the ionization potentials and finally the NMR chemical shifts of selected endohedral complexes. Finally the inclusion and binding energies will be discussed.

Geometrical Features

Host Cage: The $(HSiO3/2)_8$ cage's geometric parameters calculated at the B3LYP/LanL2DZ level are summarized in Table 3.1. The calculated structure has O_h symmetry and this is consistent with O_h symmetry of $(HSiO_{3/2})_8$ in solution[72] and T_h symmetries in the gas phase.[48] In solution, both ^1H and ^{29}Si NMR spectra give unique signals indicating an octahedral structure for $(HSiO_{3/2})_8$. Both O_h and T_h structures are very similar and have near-degenerate silicate cages. Tejrina and Gordon[61] theoretically predicted that the possible T_8-POSS symmetry in the gas phase are C_{4v}, D_{4h}, T_d and O_h. All of these isomers converged to the same O_h symmetry.

A comparison of the predicted and experimental $(HSiO_{3/2})_8$ geometries is given in Table 3.1. The agreement between theoretically predicted and the experimental geometries are very good. De Man and Sauer[73] predicted a Si-O distances of 1.64 Å by

using a HF split-valence plus polarization basis set. Tossel obtained a Si-O distance of 1.619 Å at the HF /6-31G* level.[74] Pasquarello et al[75] predicted an Si-O distance of 1.62 using LDA-DFT with effective core potentials (ECP). Earley[76] predicted the Si-O distance was 1.630Å, the Si-H distance equaled 1.457 Å and angles of 149° for SiOSi and 109° for OSiO. Xiang et al[77] predicted the Si-O distance t0 be 1.64 and 1.68 Å using DFT-local and nonlocal and double-ξ basis sets, respectively. The analogous bond lengths and angles for hexamethyl disiloxane and $(HSiO_{3/2})_8$ are known from experiment[23,24] and turn out to be very similar. Disiloxane, exhibits ∠SiOSi = 144.1° and r_{Si-O} = 1.634 Å.[24] The respective values for $(HSiO_{3/2})_8$ are ∠SiOSi = 141.7° and r_{Si-O} = 1.649 Å[23]. These findings suggest that our geometry of $(HSiO_{3/2})_8$ will be very close to with experimental geometry.

Endohedral Neutral and Cation Complexes X@$(SiHO_{3/2})_8$

The optimized endohedral complex structures of the neutral transition metals and their +1 cations obtained at the B3LYP/LanL2DZ level are shown in Figure 3.2. Stable endohedral geometries were obtained for all the neutral and ionic complexes, except $Sc^{0,+}$,$Mo^{0,+}$ and $W^{0,+}$ despite considerable variations in the sizes of the embedded atoms or cations. The geometric deformations induced by the encapsulated species, $Cr^{0,+}$, $Fe^{0,+}$, $Co^{0,+}$, $Ni^{0,+}$, $Cu^{0,+}$, $Zn^{0,+}$, $Ru^{0,+}$, $Os^{0,+}$ were small. However, the geometric deformation for $Sc^{0,+}$,$Mo^{0,+}$ and $W^{0,+}$ are quite large. Table 3.2 contains the total optimized energies, point groups, endohedral inclusion energies, isomerization energies and bond lengths for the endohedral complexes X@$(HSiO_{3/2})_8$ complexes (X = $Sc^{0,+}$,$Cr^{0,+}$, $Fe^{0,+}$, $Co^{0,+}$, $Ni^{0,+}$, $Cu^{0,+}$,

$Zn^{0,+}$, $Mo^{0,+}$, $W^{0,+}$, $Ru^{0,+}$, $Os^{0,+}$) . It is worth to note that $Sc^{0,+}$, $Mo^{0,+}$, $W^{0,+}$ are actually not a endohedral complex in their optimized structure.

If O_h symmetry was imposed most of the endohedral complexes had several imaginary frequencies. Consequent reoptimization of these structures without employing O_h symmetry lead to minima on the potential energy surface. Most of these minima had C_1 symmetry except for the ground state structure of $Cu@(HSiO_{3/2})_8$ and $Ru@(HSiO_{3/2})_8$ which both have T_h symmetry.

Four of the oxygen atoms in the D4R faces of the endohedral $X@T_8$-POSS complexes (where, X= Fe, Fe^+, Co and Co^+) are drawn inward toward the metal by equal amounts, while the remaining eight oxygens have moved outward, away from the metal. The four Fe-O internuclear distances in $Fe@(HSiO_{3/2})_8$ have the same 2.080 Å length and the remaining eight Fe-O distances are each 2.992 Å. All the Fe-Si distances are equal (2.765 Å). The Si-O_b (O_b = oxygen joining Si atoms of D4R surface) and Si-O distances are 1.691 and 1.740 Å, respectively. All the OSiO angles are 106.1° and SiO_bO[83] all angles are 131.6°. Similarly, four short Co-O distances in each $Co@(HSiO_{3/2})_8$ are each 2.259 Å and the remaining eight Co-O distances are all 2.9388 Å. The Co-Si distances are all 2.788 Å. The Si-O and Si-O_b distances are 1.693 and 1.687 Å, respectively. All the OSiO angles are 106.8° and all Si-O-Si angles are 136.1° respectively. In $Co^+@(HSiO_{3/2})_8$ complexes the four shorter Co^+-O distances are 2.207 Å and the other eight are each 2.851 Å. All the Si-Co^+ distances are 2.843 Å. Each Si-O distance is 1.711 Å and all the Si-O_b distances are 1.680 Å. The OSiO and SiOSi angles are 106.8° and 144.8°, respectively. The OSiO angles in the endohedral metal cation complexes were

significantly smaller than those in the neutral metal encapsulated complexes. In contrast, the SiO_bSi angles were larger in the metal ion endohedral complexes compared to their neutral metal analogs.

The structure of $Ni@(HSiO_{3/2})_8$ is different than that of $Ni^+@(HSiO_{3/2})_8$. The Ni atom in $Ni@(HSiO_{3/2})_8$ is attached to eight Si atoms and two oxygen atoms. These two-oxygen atoms are drawn inward (Ni-O = 2.021 Å) and the remaining ten-oxygen atoms move outward (2.887 Å). This deformation created two distinct Ni-Si distances (four at 2.732 Å and the remaining four at 2.848 Å). The Si-O and $Si-O_b$ distances in this complex are 1.676 Å and 1.697 Å, respectively. Two distinct OSiO angles (112.7° and 102.3°) are present. All the SiO_bSi angles are 139.2° and the HSiO angles are 114.0°. In contrast, four oxygen atoms are drawn inward (Ni-O = 1.980 Å) in $Ni^+@(HSiO_{3/2})_8$ and the remaining eight oxygen atoms moved outward (Ni-O = 2.918 Å). The Ni^+ is coordinated to the four inner oxygens and eight Si atoms of the cage. This structure is analogous to those of the Fe and Co encapsulated complexes. All the $Si-Ni^+$ distances are 2.794 Å. The Si-O distances are 1.724 Å and 1.676 Å.

The encapsulated metal atom or cation is attached to all eight cage Si atoms in the endohedral $X@(HSiO_{3/2})_8$ (X = Zn, Cu, Cu^+, and Ru). All the metal-oxygen distances of each complex are equal: 2.820 Å (Ru), 2.746 Å (Cu), 2.649 Å (Cu^+) and 2.768 Å (Zn). The X-O distances are 2.777 Å (Ru) 2.819 Å (Cu), 2.853 Å (Cu^+) and 2.841 Å (Zn), respectively, the Si-O distances are 1.697 Å (Ru), 1.678 Å (Cu), 1.746 Å (Cu^+) and 1.695 Å (Zn) complexes, respectively, and the Si-H distances are 1.459 Å (Ru), 1.461 Å (Cu), 1.457 Å (Cu^+), and Zn (1.461 Å) respectively.

The optimized structure of $Ru^{+}@(HSiO_{3/2})_8$ is reminiscent of thetructure of the endohedral complexes $X@(HSiO_{3/2})_8$ (X = Fe, Co, Co^{+} and Ni^{+}). There are two types of Si and O present. Four Si-Ru^{+} distances are 2.838 Å and the other four distances are slightly longer (2.841 Å). Four oxygens move inward and are bonded to Ru^{+} (2.195 Å). The remaining eight oxygens move outward (Ru-O = 2.901 Å). The Si-O distances are 1.725 Å, 1.726 Å, 1.687 Å and 1.688 Å respectively. All Si-H distances are 1.457 Å despite the fact that two types of non-equivalent types of silicon are present. In the $Zn^{+}@(HSiO_{3/2})_8$ complex, both Si and O are attached to Zn^{+}. The eight Si-Zn^{+} distances are each 2.875 Å and all twelve O-Zn^{+} distances are equivalent (2.677Å). The Si-O distances are 1.687 Å and the Si-H distances are 1.457 Å.

The shape of the T_8-POSS cage is completely distorted in $Os@(HSiO_{3/2})_8$. All the bond angles and lengths are different from each other in the $Os@(HSiO_{3/2})_8$ ground state optimized structure. In contrast, in $Os^{+}@(HSiO_{3/2})_8$, six oxygen atoms are pulled inward toward Os^{+} (Os^{+}-O = 2.202-2.665 Å) and joined with Os^{+}. The remaining six oxygen atoms distort outward (2.921-3.063 Å). The Si-H distances are 1.458 Å. The Si-O distances vary in the range 1.693-1.733 Å. The Si-O distances for all the endohedral neutral metals or cations T_8-POSS complexes are longer than the respective distances in the pure host cages. The Si-O distances lengthen as the size of the endohedral transition metal or their cations increase. Every endohedral metal cation complex hadalways have shorter Si-O and Si-H distances than their corresponding neutral metal complex.

Exohedral complexes

Table 3.3 summarizes selected geometric parameters, total energies, zero point energies, lowest frequencies, and binding energies optimized at the B3LYP/LanL2DZ level for exohedral $X(HSiO_{3/2})_8$ complexes of the neutral transition metals and their +1 cations. The bond designations used in Table 3.3 are illustrated in Figure 3.4. The host cage's high symmetry (O_h) is removed upon exohedral metal coordination. The Si-X lengths for the neutral $X(HSiO_{3/2})_8$ exohedral complexes (X= Cr, Fe, Co, Ni, Os, Ru) are 3.034 Å, 3.021 Å, 3.564 Å, 3.026 Å, 3.133 Å and 3.076 Å, respectively. The Si-X distances in these exohedral complexes are remarkably longer (ranging from 3.021 to 3.564 A°) than their endohedral counterparts. The O-X lengths for the these exohedral complexes (X= Cr, Fe, Co, Ni, Os, Ru) are 2.207 Å, 2.084 Å, 3.564 Å, 2.252 Å, 2.191 Å and 2.202 Å, respectively. The exohedral Cu and Zn exhibit very long Si-X and O-X distances from host cage 4DR surface (for Cu Si-X = 4.113 and O-X = 3.674 and for Zn, Si-X = 6.329 A° and O-X = 5.931 A°). Thus they are hardly distinguishable from the separated species. Only a very weak attractive force might exists between the D4R framework atoms and Zn or Cu, which could be artifacts, caused by basis set superposition errors.

The exohedral complexes of $X(HSiO_{3/2})_8$ (X= Cr^+, Fe^+, Co^+, Ni^+, Cu^+, Zn^+, Ru^+) are shown in Figure 3.6. The exohedral complexes structure of Cr^+, Cu^+ and Zn^+ differ from their neutral exohedral counterparts. In $Cr^0(HSiO_{3/2})_8$, the Cr^0 atom form bridging bonds between two oxygen atoms on one of the D4R surfaces. In contrast, the exohedral Cr^+ in $Cr^+(HSiO_{3/2})_8$ is attached four oxygen and four silicons on D4R surface. The Cr^+-O

and Cr^{+}-Si distances are slightly shorter than the Cr^{0}-O and Cr^{0}-Si distances (Table 3.3). Although the Cu^{0} and Zn^{0} do not form exohedral complexes both Cu^{+} and Zn^{+} form exohedral complexes with $(HSiO_{3/2})_8$. Exohedral $Cu^{+}(HSiO_{3/2})_8$ and $Cr^{+}(HSiO_{3/2})_8$ have almost the same structure (Table 3.3 and Figure 3.5(d)). Zn^{+} is attached to four oxygen on one of the D4R surfaces in $Zn^{+}(HSiO_{3/2})_8$ (Figure 3.5(f)). These O-Zi^{+} distances are 2.339 Å and while the Si-Zn^{+} distances to the same D4R face are 3.143Å. The exohedral complexes of $(HSiO_{3/2})_8$ with $Fe^{0,+}$, $Ni^{0,+}$ and $Ru^{0,+}$ are all structurally similar. In these exohedral complexes the metal atoms or their ions each form a bridging bond with two oxygen atoms on one of the D4R surfaces. The Si-X and O-X distances are shorter than that of their exohedral neutral counterparts (Table 3.3) in all of these exohedral transition metal ion complexes of $(HSiO_{3/2})_8$

Energetics

The ZPE-corrected endohedral inclusion energies (E_{inc}) for the endohedral $X@(HSiO_{3/2})_8$ and $X^{+}@(HSiO_{3/2})_8$ complexes are summarized in Table 3.2. The inclusion energy is defined as the energy difference between the energy of a complex and the sum of the energies of isolated X and the isolated host cage. A negative E_{inc} value shows that the endohedral complex is more stable than the isolated components. The inclusion energies obtained in calculations at the B3LYP/LanL2dz level for $Cr@(HSiO_{3/2})_8$, $Fe@(HSiO_{3/2})_8$, $Ni@(HSiO_{3/2})_8$, and $Ru@(HSiO_{3/2})_8$ were -163.1 kcal/mol, –10.8 kcal/mol, –7.6 kcal/mol and for –7.1 kcal/mol respectively. Encapsulating these metals in T_8-POSS is predicted to thermodynamically favorable. Unlike these endohedral Cr, Fe, Ni and Ru T_8-POSS complexes, all the other endohedral

complexes were less stable than the separated species. The inclusion energies are related to both size and charge of the endohedral species (more details are in Table 3.2). Inclusion energies of the neutral metal complexes become more positive as the atomic radius increases going from left to right across a period or down a group in the periodic table. For example, the inclusion energies of the first row transition metal follow the stability trend: Cr > Fe > Ni > Cu > Zn. The stability of endohedral complexes decreases going from left to right across the periodic table. Going down a group in periodic table stabilities also decreases as indicated by endohedral Fe, Ru, and O_S which follow the stability order Fe > Ru > Os. $Cr@(HSiO_{3/2})_8$ is the most stable of the neutral endohedral complexes.

The inclusion energies of the endohedral cationic complexes $X^+@(SiHO_{3/2})_8$ (X = Fe^+, Co^+, Ni^+, Cu^+, Ru^+ and Os^+) are all exothermic (Table 3.2). The inclusion energy of Zn^+ is endothermic. The cation inclusion energies follow the order Os^+ (-48.9 kcal/mol) > Ru^+(-40.8 kcal/mol) > Fe^+(-39.4 kcal/mol) > Co^+(-30.7 kcal/mol) > Cu^+(-29.4 kcal/mol) > Zn^+(13.0 kcal/mol).

Complexes of Sc^0, Mo^0 and W^0 are also formed exothermically. However, these are not endohedral complexes. Instead, Sc^0, Mo^0 or W^0 inclusion causes the cage to rupture. The metal atoms emerge and become part of the cage surface. The global minima structures of these Sc^0, Mo^0 and W^0 complexes are shown in Figure 3.2. These three structures are all exothermic relative to the sum of the energies of $(HSiO_{3/2})_8$ and M^0.

Table 3.2 summarizes the total energy of exohedral neutral and cationic $X(HSiO_{3/2})_8$ complexes, their binding energies (E_{exo}) and isomerization energies (E_{isom}).

All exohedral neutral and ionic complexes are energetically favorable except Zn^0 and Cu^0. The exohedral Cu^0 and Zn^0 atoms are so far away from D4R surface of $(HSiO_{3/2})_8$ they essentially not bound with $(HSiO_{3/2})_8$. The exohedral binding energies for Cu and Zn are only –1.7 and 0.1 kcal/mol, respectively, which are negligible and may be artifacts caused by basis set superposition errors. In exohedral ionic transition metal complexes are energetically more favorable with respect to their neutral counter part except Cr. The exohedral $Cr^0(HSiO_{3/2})_8$complex is –92.3 kcal/mol stable than the exohedral $Cr^+(HSiO_{3/2})_8$ complex. The exohedral Cr^0 complex is energetically more favorable compare to other exohedral neutral and cationic complexes (Table 3.2).

The energy differences between exohedral and endohedral complexes are called the isomerization energies (ΔE_{isom}). The isomerization energies are summarizes in Table 3.3. All exohedral neutral and ionic transition metal complexes are energetically more favorable than their corresponding endohedral neutral and ionic transition metal complexes. The isomerization energies, favoring exohedral over endohedral complexes are very low for Cr (-0.5 kcal/mol), Fe (-0.3 kcal/mol) and Ni (-2.6 kcal/mol). These values are less than the uncertainties in the calculated energy differences. The low isomerization values indicate that the endohedral and exohedral complexes of these metals have almost equal energy.

Electronic properties

The electronic properties depend on the nature of the metal atoms embedded inside the T_8-POSS cage (see atomic charges in Table 3.4). The endohedral metal atoms Fe^0, Ru^0 and Os^0 acquire electron density from the T_8-POSS cage.

In contrast, endohedral Cr^0, Co^0, Ni^0, Cu^0, and Zn^0 provide electron density to the host cage. Electron donation occurs from endohedral Co, Cu and Zn metal atoms into the Si–O bonds. The Si-O distances lengthen. The isosurface plots of HOMO and the LUMO of ($HSiO_{3/2}$) are presented in Figure 3.7 together with the selected $X@(SiHO_{3/2})_{10}$ (X= Cr, Co, Fe, Cu, Ru, Os). Both HOMO and LUMO of the empty cage is threefold degenerate. The HOMO consists mainly of oxygens lone pair. The LUMO contain mainly Si contributions, which are mainly antibonding in Si-H and Si-O. These agree with previous predicted results.[77] The isosurface HOMO and LUMO plots for selected endohedral complexes are shown in Figure 3.7. The HOMO is mainly comprised of a metal d orbital and an oxygen p orbital for every M^0 except Cu. The HOMO of $Cu(HSiO_{3/2})_8$ is a hybrid of a Cu *s* orbital and an oxygen *p* orbital. Its LUMO is comprised of a Cu *p* orbital and oxygen *p* orbital and a hydrogen *s* orbital. In $Co(HSiO_{3/2})_8$ the LUMO is a combination of a Co *s* orbital, an oxygen *p* orbital and the H *s* orbital. In Ru and Os endohedral complexes the both HOMOs and LUMOs consists of metal d orbitals and oxygen *s* orbitals. The HOMO-LUMO gaps for different endohedral complexes are presented in Table 3.4. The HOMO-LUMO gap of $(HSiO_{3/2})_8$ is very large (8.12 eV). Hence the pure T_8-POSS cage is not suitable for an optoelectronic material. However, inclusion of metal atoms into the cage reduces these gaps and optoelectronic properties appear in different region of absoption band. The HOMO-LUMO gaps vary over the range of 1.18-4.96 eV. These large HOMO-LUMO gaps indicate that the endohedral complexes $X@(SiHO_{3/2})_8$ are stable. The predicted electronic absorption bands of these $X@T_8$-POSS complexes vary over a wide range (1051 nm to 250 nm).

Ionization Potentials

The ionization potentials for $X@(SiHO_{3/2})_8$ (X= Sc^0, Sc^+, Co^0, Co^+, Ni^0, Ni^+, Cu^0, Cu^+, Zn^0, Zn^+, Ru^0, Ru^+, and Os^0, Os^+,) calculated at the B3LYP/LanL2DZ level are summarized in Table 3.5. The calculated ionization potentials of the free metal differ with the experimental free metal experimental values by only ≤1.3% for all transition metal atoms with atomic numbers higher than ≥ 29. However, transition metal atoms with atomic numbers ≤29 exhibited much larger deviations. The ionization potentials of encapsulated Sc^0, Co^0, Ni^0, Cu^0, Zn^0, Ru^0, and Os^0, are considerably lower than those of the free metal. This is consistent with the computational predictions for alkali metal encapsulated with the T_{10}-POSS and T_{12}-POSS cages and with dodecahedrane endrohedral complexes of alkali and alkaline earth metals.[78] Boldyrev and coworkers[79-81] defined species with first ionization potential less than that of atomic Cs (90.0 kcal/mol; 3.9 eV) as "superalkalies". The first ionization potentials for T_8-POSS encapsulated Sc^0, Co^0, Ni^0, Cu^0, Zn^0, Ru^0, and Os^0 range from 110.3 kcal/mol to 230.1 kcal/mol. These values are significantly higher than that of cesium and do not qualify as "superalkalies" behavior. This is in contrast to the predicted ionization potentials endohedral alkali metal complexes of T_{10}-POSS, T_{12}-POSS and dodecahedrane[78] which were that of "superalkalies".

Conclusions

These *ab intio* calculations predicted that the cavity of the T_8-POSS cage is sufficiently large (cavity radius 0.986 Å) to accommodate many transition metal atoms or

their cations. Several endohedral host-guest combinations were observed where inclusion of the metal or its cation was energetically favorable. The zero-point corrected inclusion energies of the endohedral $X@(SiHO_{3/2})_8$ (X = $Cr^{0,+}$, $Fe^{0,+}$, Co^{+}, $Ni^{0,+}$, Cu^{+}, $Ru^{0,+}$, Os^{+}) suggest that these complexes are more stable than their isolated components. Exohedral species are formed with the T_8-POSS cage by (X = $Cr^{0,+}$, $Fe^{0,+}$, Co^{+}, $Ni^{0,+}$, $Cu^{0,+}$, $Ru^{0,+}$, Os^{+}) and these complex were more stable than their corresponding endohedral T_8-POSS complexes. The relative isomerization energies (E_{iso}) for Cr and Fe systems were very small, so we cannot predict whether the endohedral or exohedral complex is more stable with anyconfidence.

Ru^0, Os^0, Zn^0 and Ni^0 exhibit both attractive and repulsive interactions with the cage oxygen atoms in their endohedral complexes. The Si-O and Si-H bond lengths were shortened when hosting a cation versus their corresponding neutral transition metal atoms. This is due to the donation of electron density from the cage framework to the metal cation.

The cage properties changed quite distinctly upon encapsulating a transition metal atom or ion. For example, upon encapsulation of Cr^0, Ni^0, Cu^0, and Zn^0 into T_8-POSS, electron density is transferred from the metal to the cage. In contrast, encapsulation of Fe^0, Ru^0 and Os^0 leads to donation of electron density from the cage to the encapsulated metal.

The ionization potentials of endohedral $X@(SiHO_{3/2})_{10}$ (X = Sc^0, Ti^0, Cr^0, Fe^0, Co^0, Ni^0, Cu^0, Zn^0, Mo^0, W^0, Ru^0, Os^0) species are lower than those of the isolated metal. However, the drop in ionization potential is not sufficient to classify any of these species as superalkalis. The HOMO-LUMO gaps of the endohedral transition metal T_8-POSS

complexes are smaller than that of the pure cage. The predicted HOMO-LUMO gaps suggest that various endohedral TM complexes can be used to absorb light over wide range of absorption bands. Overall, the present work suggests a new research direction. The transition metal T_8-POSS complexes are unknown experimentally. All the endohedral cage complexes $X@(SiHO_{3/2})_8$ that were predicted to be more stable than their isolated components appear to be viable synthetic targets.

References

(1) Brown, J. F., Jr.; Vogt, L. H., Jr. *J. Am. Chem. Soc.* **1965**, *87*, 4313.

(2) Feher, F. J.; Wyndham, K. D. *Chem. Commun.* **1998**, 323

(3) Li, G.; Wang, L.; Ni, H.; Pittman, C. U., Jr. *J. Inorg. Organomet. Polym.* **2002**, *11*, 123.

(4) Li, G. Z.; Wang, L.; Toghiani, H.; Daulton, T. L.; Koyama, K.; Pittman, C. U., Jr. *Macromolecules* **2001**, *34*, 8686.

(5) Li, G. Z.; Wang, L.; Toghiani, H.; Daulton, T. L.; Pittman, C. U. *Polymer* **2002**, *43*, 4167.

(6) Maxim, N.; Abbenhuis, H. C. L.; Stobbelaar, P. J.; Mojet, B. L.; van Santen, R. A. *Phys. Chem. Chem. Phys.* **1999**, *18*, 4473.

(7) Maxim, N.; Magusin, P. C. M. M.; Kooyman, P. J.; van Wolput, J. H. M. C.; van Santen, R. A.; Abbenhuis, H. C. L. *Chem. Mater.* **2001**, *13*, 2958.

(8) Zheng, L.; Waddon, A. J.; Farris, R. J.; Coughlin, E. B. *Macromolecules* **2002**, *35*, 2375.

(9) Wada, K.; Yamada, K.; Kondo, T.; Mitsudo, T.-A. *Chem. Lett.* **2001**, 12.

(10) Dance, B. *Semiconduct. Int.* **2001**, *24*, 46.

(11) Lamm, M. H.; Chen, T.; Glotzer, S. C. *Nano Lett.* **2003**, *3*, 989.

(12) Li, G.-Z.; Wang, L.; Ni, H.; Pittman, C. U., Jr. *J. Inorg. Organomet. Polym.* **2001**, *11*, 123.

(13) Li, G.-Z.; Wang, L.; Toghiani, H.; Pittman, C. U., Jr.; ; Daulton, T. L.; Koyama, K. *Macromolecules* **2001**, *34*, 8686.

(14) Li, G.-Z.; Wang, L.; Toghiani, H.; Pittman, C. U., Jr.;; Daulton, T. L. *Polymer* **2002**, *43*, 4167.

(15) Fu, B. X.; Hsiao, B. S.; Pagola, S.; Stephens, P.; White, H.; Rafailovich, M.; Sokolov, J.; Mather, P. T.; Jeon, H. G.; Philips, S.; Lichtenhan, J.; Schwab, J. *Polymer* **2001**, *42*, 599.

(16) Romo-Uribe, A.; Mather, P. T.; Haddad, T. S.; Lichtenhan, J. D. *J. Polym. Sci. B-Polym. Phys.* **1998**, *36*, 18571872.

(17) Fu, B. X.; Hsiao, B. S.; White, H.; Rafailovich, M.; Mather, P. T.; Jeon, H. G.; Phillips, S.; Lichtenhan, J.; Schwab, J. *Polym. Int.* **2000**, *49*, 437.

(18) Lee, A.; Lichtenhan, J. D. *J. Appl. Polym. Sci.* **1999**, *73*, 1993.

(19) Haddad, T. S.; Lichtenhan, J. D. *Macromolecules* **1996**, *29*, 7302.

(20) Schwab, J. J.; Lichtenhan, J. D. *Appl. Organomet. Chem.* **1998**, *12*, 707.

(21) Maitra P.; Wunder, S. L. *Electrochem Solid-State Lett* **2004**, *7*, A88.

(22) McCusker, C.; Carroll, J. B.; Rotello, V. M. *Chem. Communi. (Cambridge, United Kingdom)* **2005**, 996.

(23) Raj, R.; Riedel, R.; Soraru, G. D. *J. Am. Ceram. Soc.* **2001**, *84*, 2158.

(24) Abbenhuis, H. C. L. *Chem. Eur. J.* **2000**, *6*, 25.

(25) Ducateau, R.; Cremer, U.; Harmsen, R. J.; Mohamud, S. I.; C. L. Abbenhuis, C. L.; Avan Saten, R.; Meetsma, A.; Thiele, S. K.-H.; F. F. H. van Tol, F. F. H.; Kranenburg, M. *Organometallics* **1999**, *18*, 5447.

(26) Klunduk, M. C.; Maschmeyer, T.; Thomas, J. M.; Johnson, F. G. *Chem. Eur. J.* **1999**, *5*, 1481.

(27) Pescarmona, P. P.; Waal, J. C. v. d.; Maxwell, I. E.; Maschmeyer, T. *Angew. Chem., Int. Ed.* **2000**, *40*, 740.

(28) Xiao, F. S.; Han, Y.; Yu, Y.; Meng, X.; Yang, M.; Wu, S. *J. Am. Chem. Soc.* **2002**, *124*, 888.

(29) Liu, J. C. *Appl. Organomet. Chem.* **1999**, *13*, 295.

(30) Coupar, P. et. al. *J. Chem. Soc., Dalton Trans.* **1999**, 2183.

(31) Murfee, H. J. et. al. *Inorg. Chem.* **2000**, *39*, 5209.

(32) Saez, I. M. et. al. Chemistry (Weinheim an Der Bergstrasse, G., 7, 2758. *Chemistry (Weinheim an Der Bergstrasse, Germany)* **2001**, *7*, 2758.

(33) de Vos, R. M.; Verweij, H. *J. Membr. Sci.* **1998**, *143*, 37.

(34) Suzuki, F.; Nakane, K.; Yasuo, H. *J. Mem. Sci.* **1995**, *104*, 183.

(35) Shanbhag, P. V.; Sirkar, K. K. *J. Appl. Polym. Sci.* **1998**, *69*, 1263.

(36) Feng, X.; Shao, P.; Y. M. Huang, Y. R.; Jiang, G.; Xu, -. X., R.;. *Seperation and Purification Technology*, **2002**, *27*, 211.

(37) Maxim, N.; Overweg, A.; Kooyman, P. J.; van Wolput, J. H. M. C.; Hanssen, R. W. J. M.; van Santen, R. A.; Abbenhuis, H. C. L. *J. Phys. Chem. B* **2002**, *106*, 2203.

(38) Murugavel, R.; Davis, P.; Shete, V. S. *Inorg. Chem.* **2003**, *42*, 4696.

(39) Uzunova, E. L.; St. Nikolov, G. *J. Phys. Chem. B* **2000**, *104*, 7299.

(40) Pescarmona, P. P.; Van der Waal, J. C.; Maxwell, I. E.; Maschmeyer, T. *Ange. Chem., Int. Ed.* **2001**, *40*, 740.

(41) Feher, F. J.; Newman, D. A.; Walzer, J. F. *J. Am. Chem. Soc.* **1989**, *111*, 1741.

(42) Thomas, J. M.; Sankar, G.; Klunduk, M. C.; Attfield, M. P.; Maschmeyer, T.; Johnson, B. F. G.; Bell, R. G. *J. Phys. Chem. B* **1999**, *103*, 8809.

(43) Kudo, T.; Gordon, M. S. *J. Phys. Chem. A* **2001**, *105*, 11276.

(44) Park, S. S.; Xiao, C.; Hagelberg, F.; Hossain, D.; Pittman, C. U., Jr.; Saebo, S. *J. Phys. Chem. A* **2004**, *108*, 11260.

(45) Bassindale, A. R.; Pourny, M.; Taylor, P. G.; Hursthouse, M. B.; Light, M. E. *Angew. Chem, Int. Ed.* **2003**, *42*, 3488.

(46) George, A. R.; Catlow, C. R. A. *Chem. Phys. Lett.* **1995**, *247*, 408.

(47) Auf der Heyde, T. P. E.; Buergi, H. B.; Buergy, H.; Toenroos, K. W. *Chimia* **1991**, *45*, 38.

(48) Törnroos, K. W. *Acta Crystallogr.* **1994**, *C50*, 1646.

(49) Frye, C. L.; Collins, W. T. *J. Am. Chem. Soc.* **1970**, *92*, 5586.

(50) Bärtsch, M.; Bornhauser, P.; Calzaferri, G.; Imhof, R. *J. Phys. Chem. A* **1998**, *1994*, 2817.

(51) Bornhauser, P.; Calzaferri, G. *J. Phys. Chem.* **1996**, *100*, 2035.

(52) Muller, R.; Dathe, C.; Heinrich, L. *J. de Physiologie (Paris, 1946-1992)* **1959**, *9*, 71.

(53) Agaskar, P. A. *Inorg. Chem.* **1991**, *30*, 2707.

(54) Sasamori, R.; Okaue, Y.; Isobe, T.; Matsuda, Y. *Science (Washington, DC, United States)* **1994**, *265*, 1691.

(55) Päch, M.; Stösser, R. *J. Phys. Chem. A* **1997**, *101*, 8360.

(56) Villaescusa, L. A.; Lightfoot, P.; Morris, R. E. *Chem. Communi. (Cambridge, United Kingdom)* **2002**, 2220.

(57) Villaescusa, L. A.; Wheatley, P. S.; Morris, R. E.; Lightfoot, P. *Dalton Transactions* **2004**, 820.

(58) Mattori, M.; Mogi, K.; Sakai, Y.; Isobe, T. *J. Phys. Chem. A* **2000**, *104*, 10868.

(59) Gidden, J.; Kemper, P. R.; Shammel, E.; Fee, D. P.; Anderson, S.; Bowers, M. T. *Int. J. Mass Spect.*. **2003**, *222*, 63.

(60) Baker, E. S.; Gidden, J.; Fee, D. P.; Kemper, P. R.; Anderson, S. E.; Bowers, M. T. *Int. J. Mass Spect.*. **2003**, *227*, 205.

(61) Tejerina, B.; Gordon, M. S. *J. Phys. Chem. B* **2002**, *106*, 11764.

(62) Frisch, M. J. T., G. W.; Schlegel, H. B.; Scuseria, G. E.; Robb, M. A.; Cheeseman, J. R.; Montgomery, Jr., J. A.; Vreven, T.; Kudin, K. N.; Burant, J. C.; Millam, J. M.; Iyengar, S. S.; Tomasi, J.; Barone, V.; Mennucci, B.; Cossi, M.; Scalmani, G.; Rega, N.; Petersson, G. A.; Nakatsuji, H.; Hada, M.; Ehara, M.; Toyota, K.; Fukuda, R.; Hasegawa, J.; Ishida, M.; Nakajima, T.; Honda, Y.; Kitao, O.; Nakai, H.; Klene, M.; Li, X.; Knox, J. E.; Hratchian, H. P.; Cross, J. B.; Bakken, V.; Adamo, C.; Jaramillo, J.; Gomperts, R.; Stratmann, R. E.; Yazyev, O.; Austin, A. J.; Cammi, R.; Pomelli, C.; Ochterski, J. W.; Ayala, P. Y.; Morokuma, K.; Voth, G. A.; Salvador, P.; Dannenberg, J. J.; Zakrzewski, V. G.; Dapprich, S.; Daniels, A. D.; Strain, M. C.; Farkas, O.; Malick, D. K.; Rabuck, A. D.; Raghavachari, K.; Foresman, J. B.; Ortiz, J. V.; Cui, Q.; Baboul, A. G.; Clifford, S.; Cioslowski, J.; Stefanov, B. B.; Liu, G.; Liashenko, A.; Piskorz, P.; Komaromi, I.; Martin, R. L.;

Fox, D. J.; Keith, T.; Al-Laham, M. A.; Peng, C. Y.; Nanayakkara, A.; Challacombe, M.; Gill, P. M. W.; Johnson, B.; Chen, W.; Wong, M. W.; Gonzalez, C.; and Pople, J. A.; Gaussian, Inc., Wallingford CT, 2004. Gaussian 03; Gaussian 03 ed., 2004.

(63) Becke, A. D. *J. Chem. Phys.* **1993**, *98*, 5648.

(64) Cheeseman, J. R.; Trucks, G. W.; Keith, T.; Frisch, M. J. *J. Phys. Chem.* **1996**, *104*, 5497.

(65) Schreckkenbach, G., ;; Ziegler, T. *J. Phys. Chem.* **1995**, *99*, 606.

(66) Glendening, E. D.; Reed, A. E.; Carpenter, J. E.; Weinhold, F. *NBO 4.M University of Wisconson: Madison* **1993**.

(67) Hay, P. J.; Wadt, W. R. *J. Chem. Phys.* **1985**, *82*, 299.

(68) Hay, P. J.; Wadt, W. R. *J. Chem. Phys.* **1985**, *82*, 270.

(69) Wadt. W. R.; Hay, J. P. *J. Chem. Phys.* **1985**, *82*, 284.

(70) Abbenhuis, H. C. L.; van Herwijnen, H. W. G.; van Santen, R. A. *Chem.. Commun.* **1996**, 1941.

(71) Woon, D. E.; Dunning, T. H., Jr. *J. Chem. Phys.* **1993**, *98*, 1358.

(72) Agaskar, P. A.; Klemperer, W. G. *Inorg. Chim. Acta* **1995**, *229*, 355.

(73) de Man, A. J. M.; Sauer, J. *J. Phys. Chem.* **1996**, *100*, 5025.

(74) Tossell, J. A. *J. Phys. Chem.* **1996**, *100*, 5025.

(75) Pasquarello, A.; Hybertsen, M. S.; Car, R. *Phys. Rev. B* **1996**, *54*, R2339.

(76) Earley, C. W. *J. Phys. Chem.***1994**, *98*, 8693.

(77) Xiang, K.-H.; Pandey, R.; Pernisz, U. C.; Freeman, J. *J. Phys. Chem. B* **1998**, *102*, 8704.

(78) Moran, D.; Stahl, F.; Jemmis, E. D.; Schaefer, H. F., III;; Schleyer, P. v. R. *J. Phys. Chem. A* **2002**, *106*, 5144.

(79) Rehm, E.; Boldyrev, A. I.; Schleyer, P. v. R. *Inorg. Chem.* **1992**, *31*, 4831.

(80) Gutsev, G. L.; Boldyrev, A. I. *Chem. Phys. Lett.* **1982**, *92*, 262.

(81) Gutsev, G. L.; Boldyrev, A. I. *Adv. Chem. Phys.* **1985**, *61*, 169.

(82) Lee, C.; Yang, W.; Parr, R. G. *Phys. Rev. B: Condens. Matter and Materials Phys.* **1988**, *37*, 785.

(83) Oxygen joining the two D4R surface is indicated as O_b.

Table 3.1 Selected Optimization Structural Parameters of $(HSiO_{3/2})_8$: Bond lengths (in Å) and Bond Angles (in degrees).

Basis Set	HF		DFT	
	Bond length	Bond angle	Bond length	Bond angle
6-31G** (point group=O_h)	Si-O 1.626 Si-H 1.453	Si-O-Si 149.4 O-Si-O 109.0 H-Si-O 110.0	Si-O 1.644 Si-H 1.464	Si-O-Si 148.1 O-Si-O 109.6 H-Si-O 109.3
6-311G** (point group=O_h)	Si-O 1.622 Si-H 1.453	Si-O-Si 150.7 O-Si-O 108.3 H-Si-O 110.6	Si-O 1.642 Si-H 1.460	Si-O-Si 149.4 O-Si-O 109.0 H-Si-O 110.0
cc-pVDZ (point group=O_h)	Si-O 1.650 Si-H 1.462	Si-O-Si 149.0 O-Si-O 109.2 H-Si-O 109.8	Si-O 1.668 Si-H 1.473	Si-O-Si 147.2 O-Si-O 110.1 H-Si-O 108.9
cc-pVTZ (point group=O_h)	Si-O 1.615 Si-H 1.456	Si-O-Si 149.3 O-Si-O 109.0 H-Si-O 109.9	Si-O 1.637 Si-H 1.462	Si-O-Si 148.1 O-Si-O 110.1 H-Si-O 109.3
LanL2DZ			Si-O 1.668 Si-H 1.463	Si-O-Si 152.3 O-Si-O 107.5 H-Si-O
Expet	Si-H 1.461 Si-O 1.625	Si-O-Si 147.3 O-Si-O 109.4		

Table 3.2 Total Energies (in Hartrees), Zero-point Energies (ZPE, kcal/mol), Molecular point Groups, Lowest Vibrational Frequencies ω_1 (cm^{-1}), Zero-point Corrected Inclusion Energies (E_{inc}, kcal/mol), and Optimized Bond Lengths (Å) for Endohedral Complex of $X@(HSiO_{3/2})_8$.

X	Energy	ZPE	*Sym.*	ω_1	E_{inc}	r_{X-Si}	r_{X-O}	r_{Si-O}	r_{Si-H}
Pure	-939.514309	87.4	O_h	92.01				1.668	1.463
Sc	-985.995970	85.5	C_1	68.60	-76.3	2.841	1.921	1.671	1.466
Sc^+	-985.808346	85.2	C_1	76.01	-140.4	2.979	2.228	1.763	1.530
							2.269	1.689	
Cr	-1025.585447	84.8	C_1	64.29	-163.1	3.008	3.113	1.687	1.463
						2.765			
						/	2.080	1.691	
Fe	-1062.782056	85.6	C_1	120.72	-10.8	2.992	2.992	1.704	1.464
							1.985	1.673	
Fe^+	-1062.592079	85.9	C_1	127.62	-39.4	2.803	2.942	1.681	1.458
								1.694	
Co	-1084.461681	85.2	C_1	50.5634	35.6	2.789	3.180	1.688	1.318
								1.711	
Co^+	-1084.201992	86.0	C_1	43.13	-30.7	2.843	3.155	1.680	1.458
Ni	-1108.716166	86.1	C_1	100.03	-7.6	2.732	2.021	1.697	1.463
							2.918	1.724	
Ni^+	-1095.225045	83.0	C_1	122.19	83.6	2.794	1.980	1.676	1.541
Cu	-1135.563057	85.6	T_h	124.04	41.0	2.819	2.746	2.746	1.461
Cu^+	-1135 .387300	85.5	T_h	i83.39(5)	-29.4	2.853	2.649	1.678	1.457
Zn	-1004.957308	85.7	C_1	144.12	94.2	2.841	2.768	1.695	1.461
Zn^+	-1004.749652	85.6	C_1	112.77	13.0	2.875	2.677	1.687	1.457
						2.450	2.015		
Mo	-1006.872348	85.0	C_1	51.75	-70.7	2.846	2.262	1.771	1.461
W	-1007.162911	88.3	C_1	86.59	-75.3	2.529	1.996	1.721	1464
Ru	-1033.2226 97	84.3	*Th*	112.49	-7.1	2.823	2.777	1.697	1.461
							2.195	1.725	
Ru^+	-1033.028462	106.0	C_1	98.91	-40.8	2.838	2.901	1.687	1.457
Os	-1030.307446	84.3	C_1	103.85	16.1	2.872	2.229	1.732	1.463
							2.665		
Os^+	-1030.085401	89.9	C_1	98.91	-48.9	2.883	3.005	1.720	1.457

Table 3.3 Total Energies (in Hartrees), Zero-point Energies (ZPE, kcal/mol), Molecular point Groups, Lowest Vibrational Frequencies ω_1 (cm^{-1}), Zero-point Corrected Binding Energies (E_{exo}, kcal/mol), Optimized Bond Lengths (Å) and Isomerization Energies (E_{isom}, in kcal/mol) for Exohedral Complexes of $X@(HSiO_{3/2})_8$.

X	Energy	ZPE	ω_1[a]	E_{exo}	r_{X-Si}	r_{X-O}	r_{Si-O}	r_{Si-O}	r_{Si-O}	r_{Si-O}	r_{Si-H}	E_{iso}
Cr	-1025.588718	86.4	72.88	-163.6	3.034	2.207	1677	1.664	1.671	1.660	1.461	-0.5
Cr^+	-1025.491333	87.3	i65.70(1)	-71.3	2.959	2.200	1.706	1.637	1.684	1.662	1.460	
Fe	-1062.784176	86.7	54.58	-11.0	3.021	2.084	1.674	1.665	1.672	1.668	1.462	-0.3
Fe^+	-1062.642458	87.3	i47.24(1)	-70.7	3.001	2.069	1.736	1.637	1.662	1.663	1.458	-31.3
Co	-1084.524106	87.3	7.40	-1.4	3.995	3.564	1.670	1.666	1.668	1.668	1.642	-37.0
Co^+	-1084.256289	87.7	50.19									-42.6
Ni	-1108.720921	86.7	i129.37(1)	-10.0	3.026	2.252	1.671	1.667	1.671	1.668	1.462	-2.4
Ni^+	-1108.580715	87.3	91.74	-64.9	3.008	2.089	1.684	1.637	1.662	1.663	1.460 1.468	
Cu	-1135.634018	87.5	14.88	-1.7	4.113	3.674	1.671	1.667	1.667	1.667	1.462	-42.6
Cu^+	-1135.440625	87.3	48.88	-61.0	2.974	2.241	1.702	1.637	1.684	1.663	1.466 1.458	-31.7
Zn	-1005.110110	87.4	54.58	0.1	6.329	5.931	1.668	1.668	1.668	1.668	1.462	-94.2
Zn^+	-1004.857550	87.2	68.79	-53.1	3.143	2.372 2.339	1.697	1.635	1.685	1.662	1.460	-66.1
Ru	-1033.244701	86.5	9.76	-18.7	3.076	2.191	1.672	1.670	1.673	1.669	1.462	-11.6
Ru^+	-1033.075463	87.3	78.15	-68.9	2.198	3.250	1.681	1.638	1.685	1.664	1.460 1.458	-28.1
Os	-1030.353360	86.6	39.11	-10.5	3.133	2.209	1.666	1.673	1.668	1.671	1.460	-27.1

[a]Values in the brackets indicates the number if imaginary frequencies.

Table 3.4 Natural Charge Analysis and HOMO and LUMO Gaps (eV) of X@ T_8-POSST_8 at the B3LYP/LanL2DZ Level.

X	Q_X[a]	Q_{Si}	Q_o	Q_{o1}	Q_H	HOMO-LUMO
Pure		2.200	-1.31	-1.31	-0.24	8.12
Fe	-0.04	2.140	-1.28	-1.28	-0.22	3.58
Co	0.66	1.065	-0.65	-0.65	-0.11	4.73
Ni		2.144		-1.38	-0.22	
	0.12	2.156	-1.29	-1.30	-0.23	4.35
Cu	0.17	2.151	-1.30	-1.30	-0.22	3.82
Zn	0.32	2.142	-1.31	-1.31	-0.22	4.96
Ru	-0.08	2.158	-1.28	-1.29	-0.22	1.18
Os	-0.11	2.139	-1.28	-1.22	-0.22	3.97

[a]Q_X = Charge on impurity X. The symbols Q_{Si}, Q_H and Q_O are defined analogously.

Table 3.5 Ionization Potential (IP in kcal/mol) of Free Atom and Metal Encapsulated Complexes of (X@ T_8-POSS) at the B3LYP/LanL2DZ Level.

Ionization process	IP adiabatic	expt IP	ΔIP
$Sc \rightarrow Sc^+ + e$	18.5	156.1	
$Sc@(SiHO_{3/2})_8 \rightarrow Sc^+@(SiHO_{3/2})_8 + e^-$	17.7		0.8
$Fe \rightarrow Fe^+ + e$	149.2	182.2	
$Fe@(SiHO_{3/2})_8 \rightarrow Fe^+@(SiHO_{3/2})_8 + e^-$	119.2		3.0
$Co \rightarrow Co^+ + e^-$	230.1	187.7	
$Co@(SiHO_{3/2})_8 \rightarrow Co^+@(SiHO_{3/2})_8 + e^-$	163.0		67.2
$Ni \rightarrow Ni^+ + e^-$	143.5	176.2	
$Ni@(SiHO_{3/2})_8 \rightarrow Ni^+@(SiHO_{3/2})_8 + e^-$			
$Cu \rightarrow Cu^+ + e^-$	180.5	178.2	
$Cu@(SiHO_{3/2})_8 \rightarrow Cu^+@(SiHO_{3/2})_8 + e^-$	110.2		70.2
$Zn \rightarrow Zn^+ + e^-$	211.4	216.6	
$Zn@(SiHO_{3/2})_8 \rightarrow Zn^+@(SiHO_{3/2})_8 + e^-$	130.3		81.1
$Os \rightarrow K + e^-$	204.9	200.8	
$Os@(SiHO_{3/2})_8 \rightarrow Os^+@(SiHO_{3/2})_8 + e^-$	139.3		65.6
$Ru \rightarrow Ru^+ + e^-$	132.1	147.5	
$Ru@(SiHO_{3/2})_8 \rightarrow Ru^+@(SiHO_{3/2})_8 + e^-$	121.9		10.1

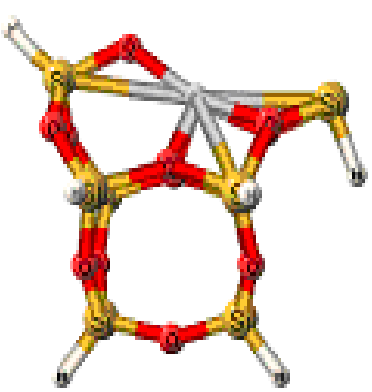

$Sc@(SiHO_{3/2})_8$

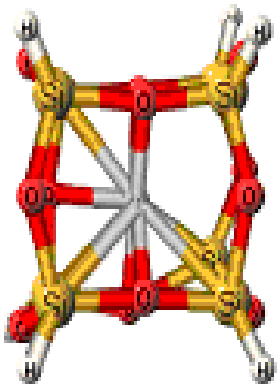

$Cr@(SiHO_{3/2})_8$

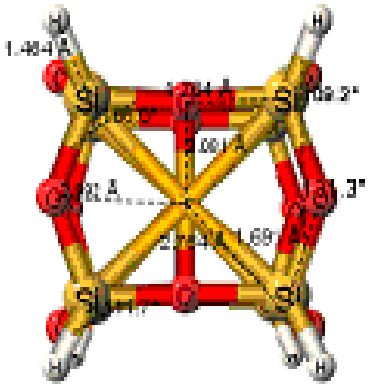

$Fe@(SiHO_{3/2})_8$

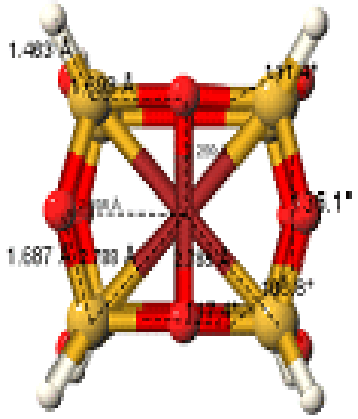

$Co@(SiHO_{3/2})_8$

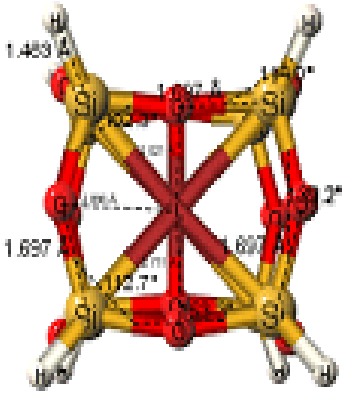

$Ni@(SiHO_{3/2})_8$

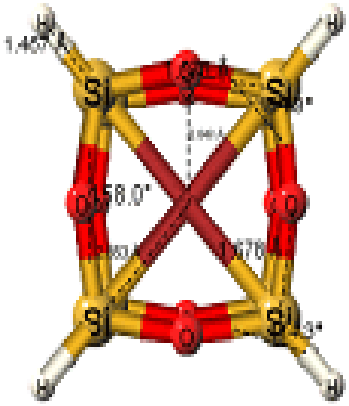

$Cu@(SiHO_{3/2})_8$

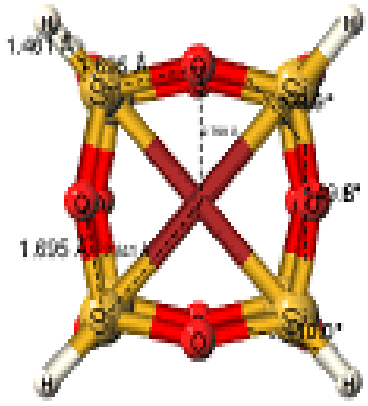

$Zn@(SiHO_{3/2})_8$

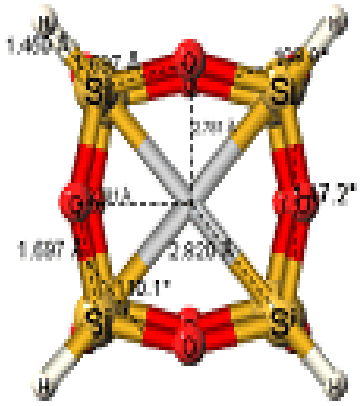

$Ru@(SiHO_{3/2})_8$

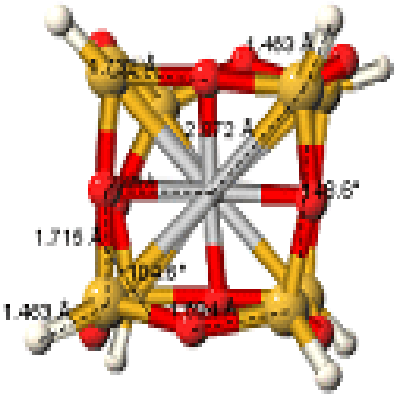

$Os@(SiHO_{3/2})_8$

Figure 3.2 Optimized Geometries of Endohedral $X@(HSiO_{3/2})_8$ Complexes at the B3LYP/LanL2DZ Level

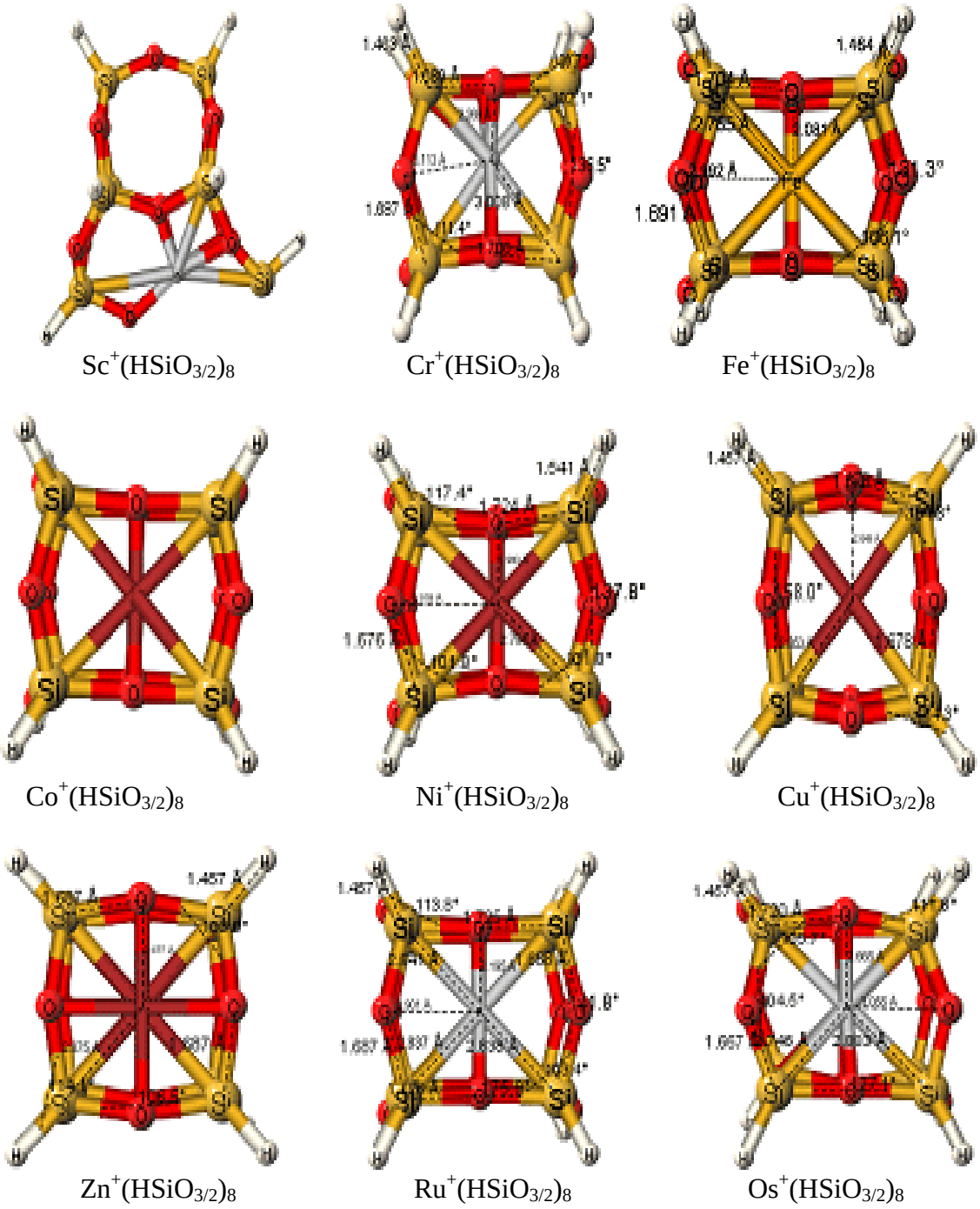

Figure 3.3 Optimized Geometries of Endohedral $X^{+}@(HSiO_{3/2})_8$ Complexes at the B3LYP/LanL2DZ Level.

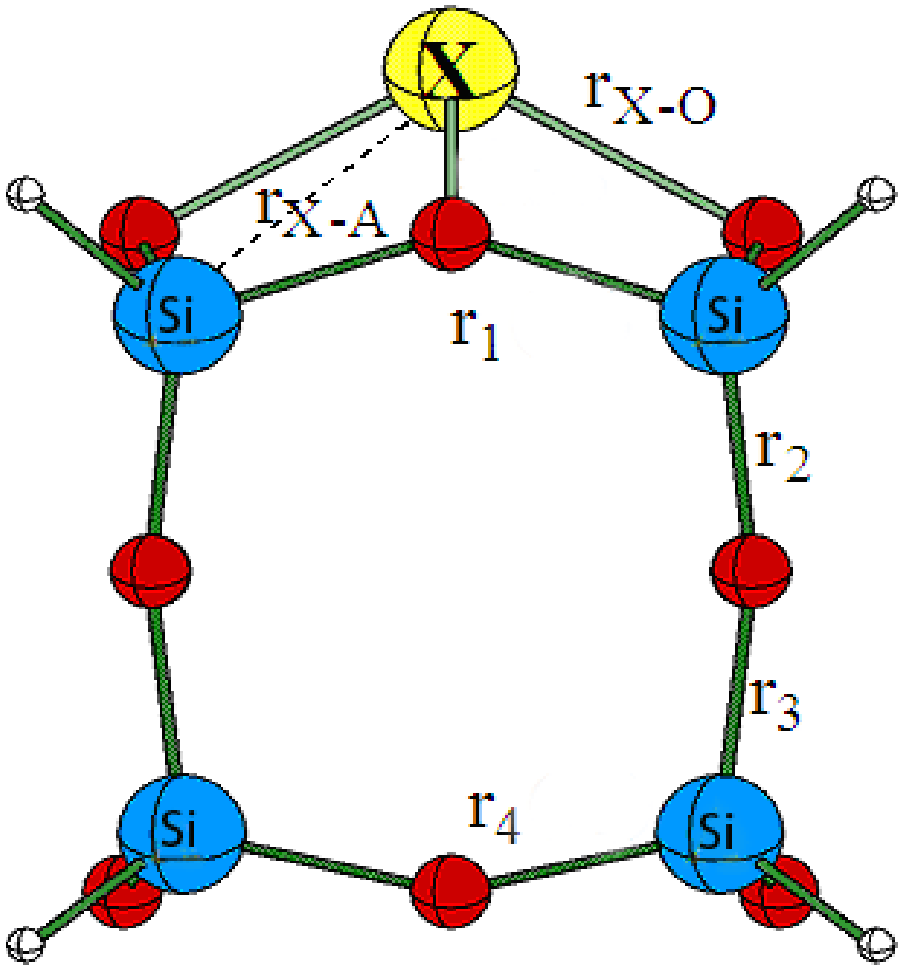

Figure 3.4 Schematic Geometries for the Exohedral $X(HSiO_{3/2})_8$ Complex. Where X = Transition Metals and their Ions.

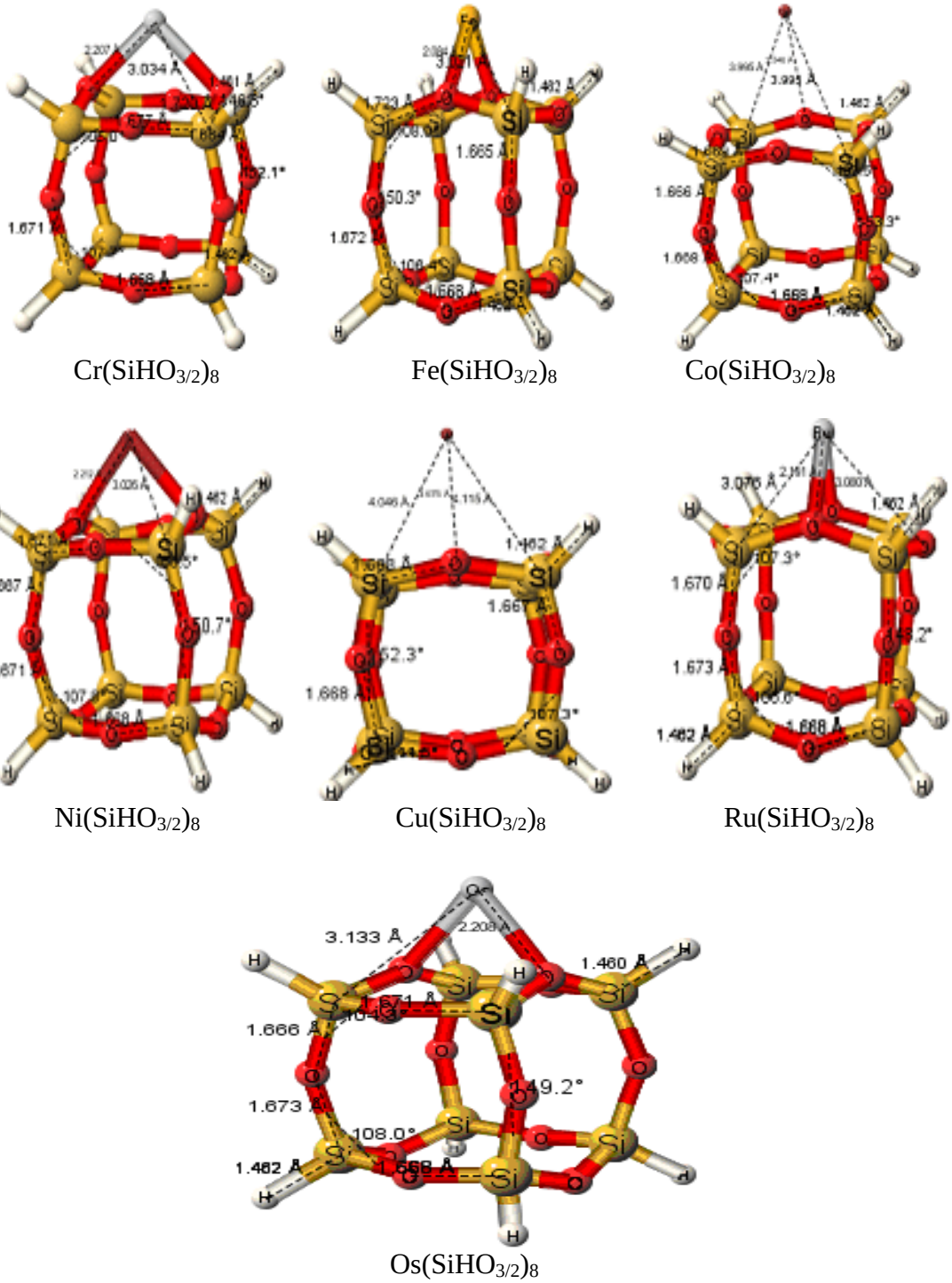

Figure 3.5 Optimized Geometry of Exohedral $X(HSiO_{3/2})_8$ Complexes at the B3LYP/LanL2DZ Level.

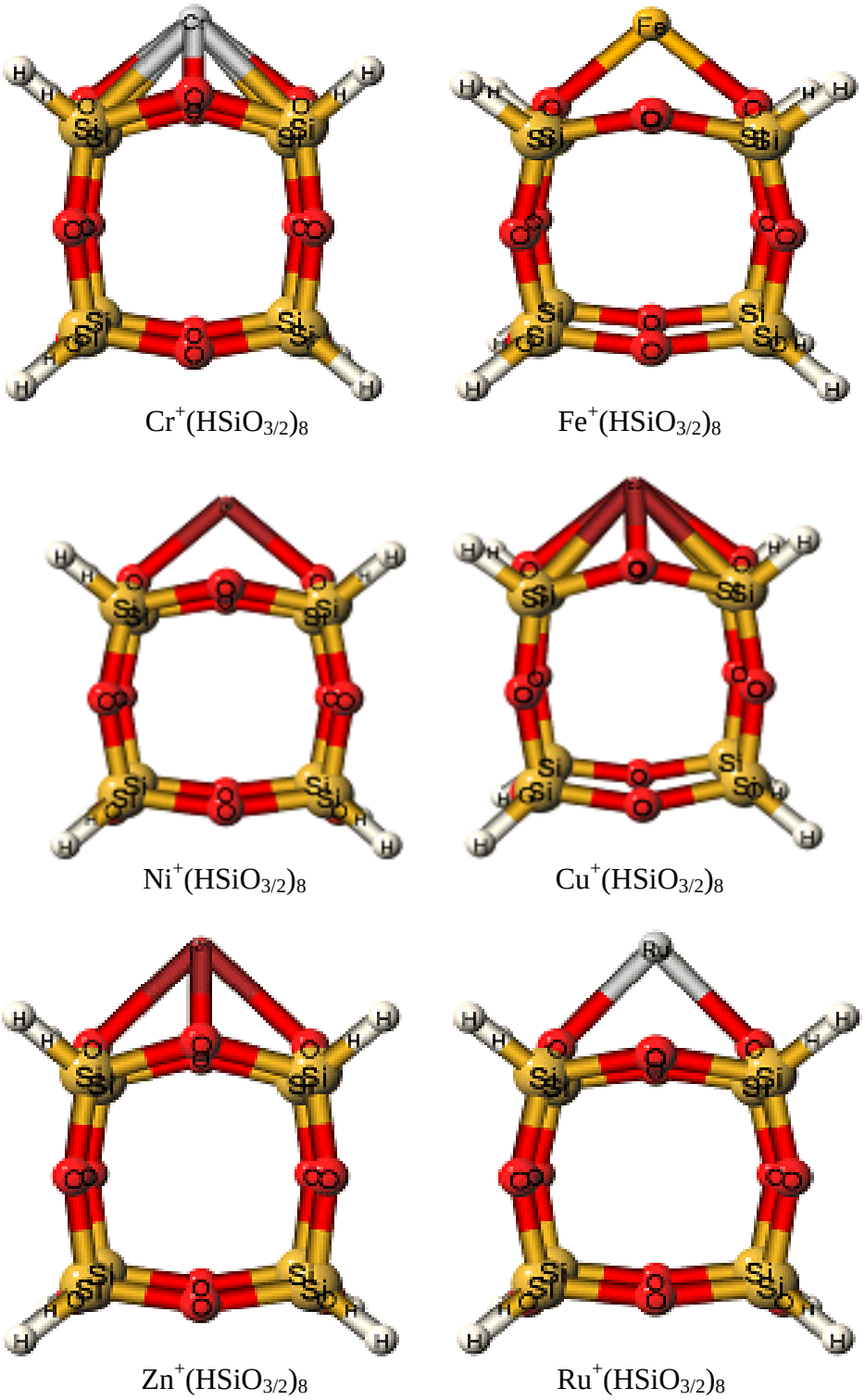

$Cr^{+}(HSiO_{3/2})_8$ $Fe^{+}(HSiO_{3/2})_8$

$Ni^{+}(HSiO_{3/2})_8$ $Cu^{+}(HSiO_{3/2})_8$

$Zn^{+}(HSiO_{3/2})_8$ $Ru^{+}(HSiO_{3/2})_8$

Figure 3.6 Structures of Exohedral $X^{+}(HSiO_{3/2})_8$ with Transition Metal Ions.

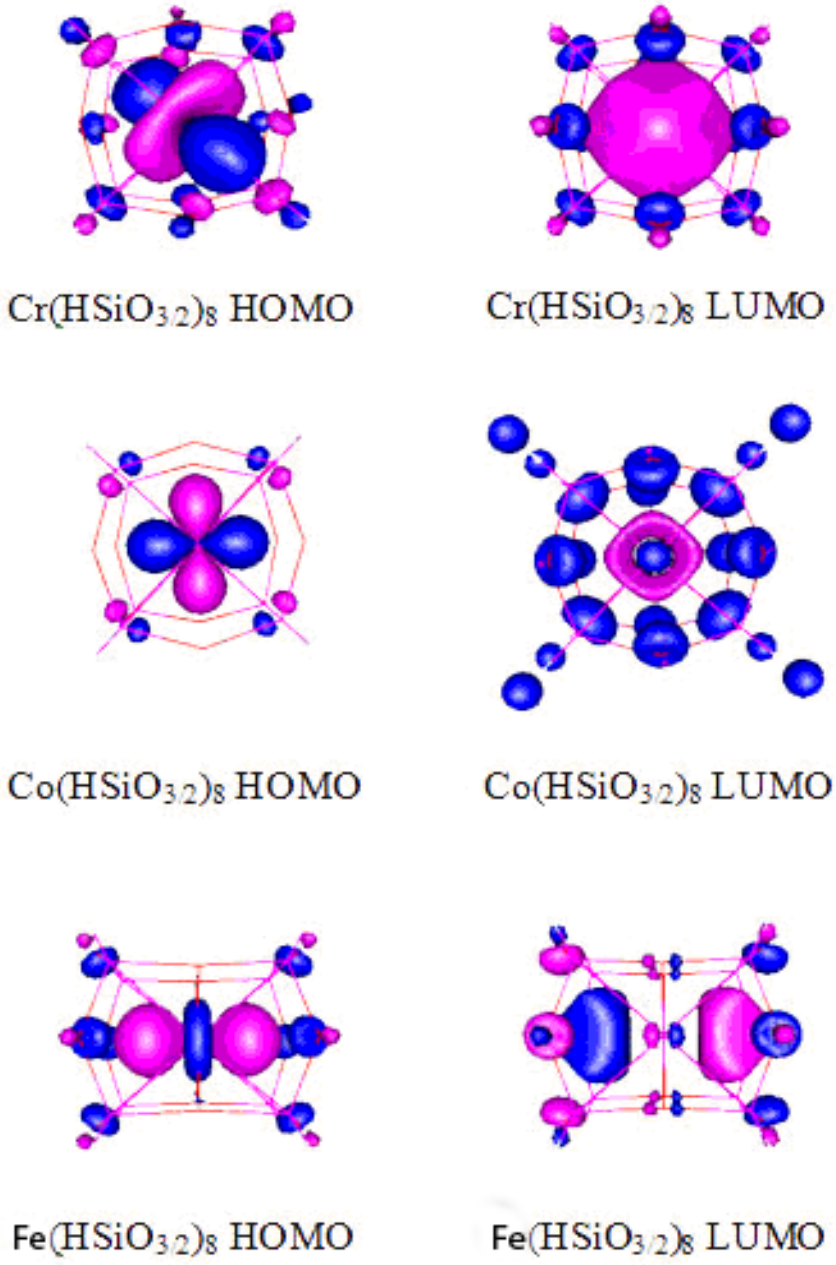

Figure 3.7 Molecular Orbital Pictures (dark: positive; light; negative values) for the HOMO and LUMO of the Host Cage $(SiHO_{3/2})_8$ and Representative Endohedral Complexes.

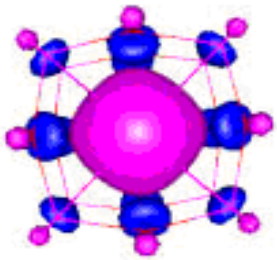

$Cu(HSiO_{3/2})_8$ HOMO

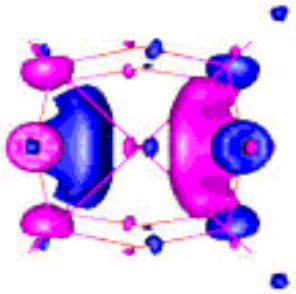

$Cu(HSiO_{3/2})_8$ LUMO

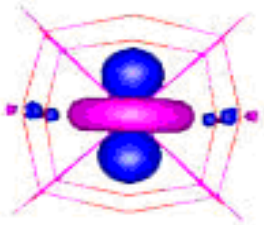

$Ru(HSiO_{3/2})_8$ HOMO

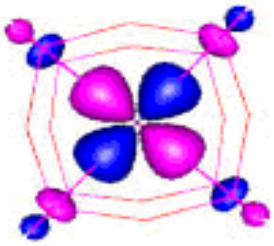

$Ru(HSiO_{3/2})_8$ LUMO

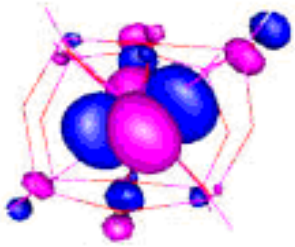

$Os(HSiO_{3/2})_8$ HOMO

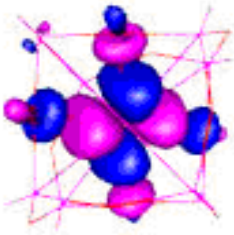

$Os(HSiO_{3/2})_8$ LUMO

Figure 3.7 (continued)

CHAPTER IV

STRUCTURES, STABILITIES, IONIZATION POTENTIALS AND ELECTRONIC PROPERTIES OF ENDO- AND EXOHEDRAL COMPLEXES OF $(HSiO_{3/2})_{10}$ T_{10}-POSS CAGES

Introduction

Polyhedral oligomeric silsesquioxane (POSS) nanostructured chemicals have been widely investigated in hybrid inorganic/organic polymers and nanocomposites. The building block of the H-silesquioxanes is the trifunctional monomer unit ($HSiO_{3/2}$) and the letter T is used to describe this unit.[1-4] If a POSS molecule comprised n numbers of ($HSiO_{3/2}$) units then the POSS is defined as T_n. The cage structures are formed from the ($HSiO_{3/2}$) building block. For example, the T_{10} cage contains 10 silicon and 15 oxygen atoms with each silicon attached to one hydrogen outside the cage. According to Agaskar and Klemperer[5] the nomenclature of a POSS is given by a topological descriptor $\{r^s.....t^u\}$, which indicates the number of s- and r-membered rings (faces) that comprise the polyhedron T_n. For example, T_{10}-POSS cage D_{5h} isomer is defined as $\{6^0 5^2 4^5\}$(no six membered two five membered and five four membered rings). POSS derivatives incorporated into organic polymers, dendrimers, and zeolites

have a variety of applications in materials science and catalysis.[4,6-15] POSS has also emerged as viable filler in high performance nanocomposites.[1] POSS polymer nanocomposites are substantially harder than the unfilled polymers.[3] Incorporation of POSS cages into the polymeric materials enhance certain properties such as glass transition temperatures, decomposition temperatures and mechanical strength.[16-19] In POSS-PEO-based polymer electrolytes, POSS acts as an inhibitor to polyethylene oxide (PEO) crystallization.[2] POSSs are being used for synthesis of polymer-derived ceramics because of their nano-sized structure and ceramic like composition.[20] Metal containing siloxanes, and oligometalla-silosesquioxanes are used as catalysts in olefin processing. For example, metathesis and epoxidation of alkenes have been accomplished with POSS derivatives.[21-25] POSS are also used to support Ziegler-Natta catalysts.[26] The cage structure of POSS makes them useful substances for separating gas mixtures with silicon-based capillary membranes.[27,28] Cationic polyhedral oligomeric silsesquioxane (POSS) units can serve as carriers and potential drug delivery agents.[29]

Xiang et al[30] studied the structural and electronic properties of different H-silsesquioxanes and Cheng et al[31] reported the linear and non-linear optical properties of H-silsesquioxanes. Space filling models of such cages indicate there is a void at the center of the cube, but it is questionable whether this space could be filled with an atomic species. Pach and Stosser[32] suggested that γ-irradiation of octaalkyl(T_8)silsesquioxane or octatrialkylsiloxy(T_8)silsesquioxane leads to encapsulated hydrogen. ESR spectroscopy showed that a hydrogen atom had migrated from a peripheral organic substitutent into the cage.

The presence of extra framework (a larger cage) can play a decisive role in both the structural and catalytic behavior of microporous solids. [33] What might happen upon total incarceration of atoms, ions, or molecules within an enclosed molecular framework? Previous experimental and theoretical studies have been largely limited to T_8-POSS. Bassindale et al[34] recently synthesized the fluoride-ion encapsulated T_8-POSS cage. Catlow and George[33] investigated electronic structure of Na^+, F^- and OH^- ion incorporation into hydroxy-substituted double four membered ring (D4R) silsesquioxanes using local density (LDR) techniques. Gordon and Tejerina[35] investigated the insertion mechanism of N_2 and O_2 into T_n-POSS (n = 8, 10, 12)-silsesquioxane framework theoretically. Very recently we[36] investigated the behavior and properties of both endoheral and exohedral complexes of T_8-POSS. Allen and Beers [37] investigated the binding strength of T_8-POSS cationic complexes by *ab initio* methods. In contrast to T_8-POSS complexes studies of endrohedral or exohedral complexes of T_{10}-POSS with atoms and ions have only been quite recently.

In the discussion below the following questions will be addressed: Is the T_{10}-POSS cage stable when different cations and anions are incorporated into the cage? What kind of interactions occurs between the incorporated ion (or atom) and the T_{10}-POSS skeleton? Since very little is known about these questions, T_{10}-POSS, with a larger cavity than its T_8 analog is an ideal candidate for study. In this report we present results of theoretical studies of the stabilities and geometric, energetic, and electronic properties of the endohedral complexes with Li^0, Li^+, Li^-, Na^0, Na^+, Na^-, K^0, K^+, K^-, F^-, Cl^-, Br^-, He,

Ne, and Ar (Figure 4.1). Thoughout this paper the endohedral complexes are denoted by X@T_{10}-POSS and exohedral by XT_{10}POSS.

$(HSiO_{3/2})_{10}$ can, in principle, have several isomers. The most stable isomer has D_{5h} symmetry with $\{4^2 5^2\}$ topology and this is also the only isomer known experimentally.[5] The existence of two additional isomers of $(HSiO_{3/2})_{10}$ has been suggested by theoretical calculations. These have C_{2V} symmetry with $\{3^2 4^3 6^2\}$ topology or C_{2V} symmetry with $\{3^4 4^1 7^2\}$ topology.[35,38] The D_{5h} symmetrical species is predicted to be more stable than the two C_{2V} isomers ($\{3^2 4^3 6^2\}$ and $\{3^4 4^1 7^2\}$ topologies) by 18.0 kcal/mol and 42.7 kcal/mol, at the MP2 level, respectively.[35] Hence, in this work the D_{5h} structure was used as a starting point in all the model calculations.

Computational Details

All the calculations were performed using density functional theory (DFT/B3LYP).[39,40] B3LYP was chosen over Hartree-Fock since part of the correlation energy is included in the exchange–correlation potential. However, an explicitly correlated method like MP2 would have been desirable but it was found too expensive for this study. For all systems reported here the 6-311G(d,p)[41] was employed. Preliminary calculations on the T_{10}-POSS cage and selected endohedral complexes were carried out at both the Hartree-Fock and B3LYP levels with several smaller and larger basis sets. The results did not differ significantly for the B3LYP/6-311G(d,p) results and they will not be discussed here. For all structures discussed here complete optimization the geometries as well calculation of the vibrational frequencies were performed. For open shell species

the unrestricted formalism was used. Gaussian 03[42] and PQS[43] *ab initio* programs were used to perform the calculations

Three relative energies will be discussed. The inclusion energy for endohedral complexes, E_{inc}, the binding energy for exoheral complexes, E_{bind}, and the isomerization energy E_{isom} defined as

$$E_{inc} = E_{endo} - (E_{cage} + E_x)$$

$$E_{bind} = E_{exo} - (E_{cage} + E_x)$$

$$E_{isom} = E_{exo} - E_{endo}$$

All energies reported have been corrected using the unscaled zero point vibrational energies.

As mentioned, the vibrational harmonic frequencies were computed for all optimized structures using the same levels of theory as for the optimization, to characterize the stationary points as minima (zero imaginary frequencies) or saddle points (one imaginary frequency). Nuclear magnetic shielding tensors for selected systems were calculated using B3LYP/6-311G(d,p) and GIAO methods.[44-47] The electronic properties, atomic charges and electronic configurations were evaluated using natural bond orbital analysis (NBO).[48]

The magnitude of the basis set superposition errors (BSSE) was estimated by the Boys-Bernardi counterpoise method.[49] The BSSE correction for endohedral $X@(HSiO_{3/2})_{10}$ ($X=Li^+$, Na^+, K^+, F^-, Cl^-, Br^- He, Ne and Ar) was calculated at the B3LYP/6-311(d,p) level. The results are shown in Table 4.11. These are quit significant. For the Br- and Ne complexes the BSSE are actually higher than the inclusion energies.

Previously we have found that the basis set superposition errors were small for endohedral T_8-POSS complexes.[36] and counterpoise calculations showed that for the exohedral POSS-T_{10} complexes the BSSE were negligible.

Throughout this paper total energies are given in Hartrees, relative energies in kcal/mole; bond lengths in Angstroms, and bond angles in degrees.

Results and Discussion

Geometric Features

The optimized geometrical parameters for the parent D_{5h} form of the POSS-T_{10} cage as well as the endohedral complexes are summarized in Table 4.1.

Host cage: The POSS-T_{10} cage in it's stable D_{5h} geometry consist of two (-SiH-O-)$_5$ rings bridged by 5 oxygen atoms. The bridging oxygens are denoted O_b while the D5R oxygen are denoted by O throughout this text. Our calculated geometrical parameters (Table 4.1) are consistent with previous experimental[50] and theoretical[35,51] results. Typical Si-O bond lengths in the D5R and D4R[52] frames are 1.64 **Å**. de Man and Sauer calculated a Si-O distance of 1.64 Å using the Hartee-Fock method with split-valence plus polarization basis sets.[53] Using HF/6-31G(d) method, Tossell predicted Si-O distance of 1.64 Å. Xiang et al[54] have studied the molecular and electronic structures of Tn-POSS (n even, 4-16) using DFT with double-ξ basis set and predicted Si-O distances of 1.64 Å. Pasquarello et al.[55] used LDA-DFT with effective core potential (ECP) and found that the Si-O distance was 1.62 Å. This agrees with the experimental X-ray diffraction values (Si-O 1.62 Å).

Endoheral $(SiHO_{3/2})_{10}$ alkali metal complexes: The endoheral complexes of the alkali metal ions Li^+, Na^+ and K^+ and the POSS-T_{10} cage as well as neutral complexes which could be described as endohedral complexes of Li, Na, and K, respectively were investigated. Negatively charge complexes with the same three alkali metals were also considered. These complexes could formally be considered as endohedral complexes of Li^-, Na^- and K^- even though negative oxidation states of alkali metals are highly unlikely. Among the endohedral complexes of alkali metals the D_{5h} symmetry of the parent cage was conserved only for X=Na^-, K^+, K and K^-. (see Figure 4.2). The D_{5h}-structures of the endohedral complexes with Li, Li^+, Li^-, Na^+, and Na had between one and seven imaginary frequencies. When the symmetry constrains of these structures were removed, subsequent optimization of the structures resulted in structures which were minima on the molecular potential surface (no imaginary frequencies). All these structures had no symmetry. The distortion from the initial D_{5h} structures were quite significant for all three endohedral lithium complexes while the geometry change differed only slightly from D_{5h} symmetry for the sodium complexes (see Figure 4.2).

Naturally, the bond distances and bond angles change after insertion of different atoms or ions into the T_{10}-cage. In each of the cationic systems (Li^+, Na^+, K^+), different oxygen to cation internuclear distances exists. The ten D5R frame oxygens (O) were closer to the cation than the five bridging oxygen and the bridging oxygens have moved slightly outward compared to the empty cage. The calculated geometrical trends for the endohedral alkali metal complexes are complicated by the fact that the Li^+ complex is distorted significantly from D_{5h} symmetry. The Si-H bond distance of 1.462 Å in the

parent cage shortens for the Li^+, Na^+, and K^+ endohedral complexes, respectively. The Si-O-Si angles are 155.9° for the T_{10}-POSS cage. After cation insertion, the corresponding bond angles decrease for the Li^+, Na^+ complexes and increase for K^+ encapsulated complexes (Table 4.1). However, the O-Si-O of 110.0° angle in the POSS-cage decrease to 108.9° for Na^+ and 106.8° for K^+ endohedral complexes, respectively. The SiO_bSi angle of 152.0° in the parent cage decrased significantly for Li^+, Na^+ and K^+ encapsulated complexes. The 109.6° OSiH angle increased to 112.5° and 113.0° for Na^+ and K^+ endohedral complexes respectively. Endohedral cations increase the Si-O bond lengths and the Si-O-Si angles while decreasing the O-Si-O angles.

Endoheral $(SiHO_{3/2})_{10}$ halide complexes: The D_{5h} symmetry was conserved for both the endohedral Cl^- and Br^- complexes while the fluoride complex distorted to a system with Cs symmetry and this makes direct comparison of the geometry of the fluoride complex with the chloride and bromide complexes difficult. The framework oxygen to halide distances (X-O) have values 3.004Å, 3.130Å, and 3.148Å for $X=F^-$, Cl^-, and Br^- respectively. The X-Si distances increase from (2.757-2.859)Å going from F^- to Br^-(Table 4.1). The changes are smaller than the changes in anion size. The Si-O_b distance in $(HSiO_{3/2})_{10}$ is 1.642. After halide insertion the Si-O distance (originally 1.637 Å) become 1.636 Å (F^-), 1.645 Å (Cl^-) and 1.650 Å (Br^-). Both Si-O and Si-H bonds lengthen significantly due to insertion of anions. Pronounced changes occur in bond angles. The Si-O-Si angles for the T_{10}-POSS cage are 155.9° and 152.0.

After halide insertion, the corresponding bond angles decreased to 147.8° and 150.6° (F^-), 148.3° and 149.2° (Cl^-) and 148.2° and 148.6° (Br^-). Furthermore, the O-Si-

O angles, 110.0° in T_{10}-POSS expand to 112.2° for F^-, 111.9° for both Cl^- and Br^-. Halide encapsulation causes the T_{10}-POSS cages, Si-O bond lengths, O-Si-O bond angles to increase and the Si-O-Si bond angles to decrease. The cage size increases as the size of encapsulated anion increases due to cage atom-halide ion repulsions.

Endoheral $(SiHO_{3/2})_{10}$ noble gas complexes: The changes in the geometry of the POSS-T_{10} cage upon insertion of noble gases are remarkably small. The Si-O_b distance in the parent POSS-T_{10} cage is 1.637Å while these distances are 1.638 Å, 1.639 Å, and 1.645 Å , for the He-, Ne- , and Ar-complexes, respectively (Table 4.1). Insertion of He, Ne or Ar has almost no effect on the Si-H bond lengths, however, the Si-O bond lengths increase slightly. One of the Si-O-Si bond angles remains almost unchanged while the other Si-O-Si bond angles decrease slightly for He endohedral noble gas POSS-T10 complexes indicate that negligible electron transfer occurs between the cage atoms and the encapsulated He, Ne and Ar atoms. This is also evident from the electronic charge and electronic configurations. The OSiO 110.0° angle in $(HSiO_{3/2})_{10}$, changed to 109.2° for both He and Ne and 109.1° for Ar in X@$(HSiO_{3/2})_{10}$. The SiO_bSi angle of 152.0° increases to 152.3° for He@$(HSiO_{3/2})_{10}$, 152.5° for Ne@$(HSiO_{3/2})_{10}$, and 113.9° for He@$(HSiHO_{3/2})_{10}$. The HSiO angles in $(HSiO_{3/2})_{10}$ decrease to 109.7°, 109.6° and 109.3° for the endohedral (X=He, Ne, Ar) complexes, respectively (Table 4.1).

Exohedral Clusters $X(HSi3/2)_{10}$: Table 4.2 summarizes selected geometric parameters, total energies, zero point energies, lowest vibrational frequencies, and binding energies for the exohedral $X(HSiO_{3/2})_{10}$ complexes of the alkali metal cations, halides and noble gases. The bond designations used in Table 4.2 are shown in Figure

4.3. The optimized geometry for the exohedral complexes are given in Figure 4.4. Exohedral complexation removes the host cage's high D_{5h} symmetry. The Si-X bond lengths for the exohedral complexes (X = Li^+,Na^+, K^+) are 2.903 Å, 2.710 Å, 3.169 Å and 3.567 Å respectively, similar to those predicted in the corresponding endohedral systems. In contrast to alkali cations, the Si-X and O-X distances in these exohedral Cl^- and Br^- complexes are markedly longer (3.452 Å and 4.966 Å). In the exohedral complexes with He, Ne, Ar the Si-X and O-X distances were also quite long (ranging from 3.997-4.242 Å). This indicates that a weekly attractive force only joins the 5DR framework atoms and exohedral noble gases.

Inclusion and Isomerization Energies

The total energies and the zero-point corrected endohedral inclusion energies (E_{inc}) for X@$(HSiO_{3/2})_{10}$ (X= He, Ne, Ar, Li^+, Li, Li^-, Na^+, Na, Na^-, K^+, K, K^-, F^-, Cl^-, Br^-), obtained at the B3LYP/6-311(d,p) level and B3LYP/6-311++G(2d,2p) are shown in Tables 4.3 and 4.4, respectively. The inclusion energies reveal that the $Li^{+,-}$@$(HSiO_{3/2})_{10}$, Na^+@$(HSiO_{3/2})_{10}$, F^-@$(HSiO_{3/2})_{10}$ and Cl^-@$(HSiO_{3/2})_{10}$ endohedral complexes are more stable than the respective separated ion and the empty cage. All the remaining complexes are less stable than the respective separated ion and the empty cage. Including diffuse functions in the 6-311G(d,p) basis set, (i.e. 6-311++G(d,p)) did not change the results significantly. The endohedral F^- complex is exceptionally stable. The values of E_{inc} in Tables 4.3 and 4.4 show that the endohedral complexes become more stable as the size of X decreases within its periodic table group. Na^+ and K^+ cation inclusion is energetically more favorable than their neutral metals and anions while the K^+ analog is energetically

unfavorable compared to the separated species. For Na and K the inclusion energy follow the trends $M^+ > M^0 > M^-$ while the order for lithium is $Li^+ > Li^- > Li^o$.

F^-, Ne, and Na^+ are isoelectronic. However, the inclusion energies of these complexes differ significantly. Besides size effects, large differences exist between the natural charges of similar sized included species (see Tables 4.3 and 4.4). This demonstrates that charge transfer from the encapsulated species to the host cage contributes to the values of E_{inc}.

For all ions and elements, except Ar, all the exohedral complexes, are more stable then their isolated components. The binding energy for $Ar(HSiO_{3/2})_{10}$ is only -0.1 which is smaller than the uncertainty in the calculated energy difference. Exohedral F^- ions exhibit a remarkable behavior, different from all other exohedral complexes. Exohedral F^- ions spontaneously penetrate into the center of the cage forming endohedral $F^-@(HSiO_{3/2})_{10}$ (identical to the endohedral complex formed by initially placing F^- at the center of the cage). Similar behavior was also predicted for fluoride ion and T_8-POSS cage.[36] The exohedral binding energies (E_{exo}) show charge and size dependence similar to the endohedral inclusion energies (E_{inc}, Tables 4.3 and 4.4). Adsorption of the small Li^+ ion turns out to be the most exothermic process for $(HSiO_{3/2})_{10}$ cage, followed by Na^+ and K^+.

The ZPE-corrected energy difference between the exohedral and endohedral structures is defined as the isomerization energy.[56] The isomerization energies, E_{isom} (kcal/mol), calculated at the B3LYP/6-311G(d,p) level summarized in the Table 4.3 demonstrate that the exohedral complexes $X(HSiO_{3/2})_{10}$ ($X=Li^+$, Na^+, K^+, He, Ne, Ar, Cl^-

, Br^-) are more stable than the corresponding endroheral complexes, but the unfavorable thermodynamics are not sufficiently prohibitive that it would prevent formation of the endohedral complex. For example, $He@C_{20}H_{20}$ have been prepared despite its large isomerization energy (35.4 kcal/mol).[57] Among the noble gas-containing complexes, E_{isom} is smallest for Ne. Its E_{isom} is only –4.1 kcal/mol, which may be close to the uncertainty of the calculated energy differences in this study.

The energies of $X@(HSiHO_{3/2})_{10}$ may be compared with those of endrohrdral dodecahedrane complexes $X@C_{20}H_{20}$[56] and endoheral T_8-POSS[36] complexes. The endoheral complexes of Li^+ and Na^+ with T_{10}-POSS are considerably more stable (inclusion energy X = Li^+: -47.1 kcal/mol; Na^+: -23.8 kcal/mol) than the corresponding T_8-POSS analogs. (X = Li^+: -18.5 kcal/mol; Na^+: 11.3 kcal/mol). They are more stable than those of dodecahedran $C_{20}H_{20}$ (Li^+: -12.7, Na^+: 55.3 kcal/mol).[56] Furthermore, the noble gas inclusion energies of $X@(HSiO_{3/2})_{10}$ (X=He: -16.3 kcal/mol, Ne:-14.0, Ar: 14.0 kcal/mol) are lower (more stable) than those of $X@C_{20}H_{20}$[56] (X= He:37.9 kcal/mol, Ne:102.9 kcal/mol, Ar:320.2 kcal/mole) and $X@(SiHO_{3/2})_8$ (X=He:12.3 kcal/mol; Ne:24.2 kcal/mol; Ar:95.9 kcal/mole)[36]. The same stability order predicted for alkali metal cation complexes $X@(HSiO_{3/2})_{10}$ (X = Li^+>Na^+>K^+) in this work was also found by Sun et al[58] in computations on endohedral C_{32} cage complexes of M^+ for Li^+ ($Li^+@C_{32,}$ -53.1 kcal/mol), Na^+ ($Na^+@C_{32}$, -26.9 kcal/mol), and K^+ ($K^+@C_{32}$, 13.7 kcal/mol), using the generalized gradient approximation (GGA) DFT procedure. The smaller Li^+ ion complexes emerge as most stable, while the larger K^+ containing complexes exhibit the lowest stability.

Electronic Properties

In this section, the electronic properties of T_{10}-POSS cage and $X@(HSiO_{3/2})_{10}$ complexes are discussed using natural population analysis (NBO), and the HOMO-LUMO gaps.

The calculated charges of the endohedral complexes, (Table 4.5), provide insights into the electronic distribution in these systems. Natural population analysis (NPA) gives a measure of the charge on atoms. The charge densities depend on the basis set used and they are some times less realistic when a diffuse orbital on one atom strongly overlaps with the orbitals of other atoms. NPA depends strongly on the adapted density functional scheme in DFT and should be used with care. However, charge densities can be helpful in semi-quantitative interpretations of ionic/covalent interactions or guest-host electron transfer. Recognizing these deficiencies in the population analysis, atomic populations were only used to estimate the relative trends in charge transfer. Core electrons usually do not participate in the bonding process. However, the behavior of the valence orbitals varies from structure to structure. The charges computed on the individual atoms and ions at the B3LYP/6-311G(d,p) level are given in Table 4.5.

For Li^+, Na^+ and K^+ encapsulation into the $(HSiO_{3/2})_{10}$, the average charge at alkali ion decrease from +1.0 in the free state to 0.87 (Li^+), 0.88 (Na^+) and 0.89 (K^+) respectively. Electron density has been transferred from the framework to the cation. The variation in charge distributions on oxygen is complex. In the presence of Li^+, some oxygens gain electron density and some lose electron density. In the Na^+ and K^+ complexes, negative charge on all the oxygens increase. The terminal H atom donates

electron density to the Si atoms for Li^+, Na^+ and K^+ complexes. The overall back donation from cage to the alkali cation is more pronounced in the $K^+@(HSiO_{3/2})_{10}$ complex. Electron flows from the cage atoms to encapsulated metal cations.

Negative charge on the central metal atom increases with an increase in its size (see Table 4.5). In contrast, encapsulation of neutral and anionic alkali metals into T_{10}-POSS cage increases the electron density donated to the cage framework. The computed amounts of electronic charge that resides on different atoms are given in Table 4.7.

The calculated charge on the endohedral He shows this atom is neutral. Similar behavior was previously predicted for $X@C_{20}H_{20}$ (where X = He, Ne).[56] Ne and Ar are much larger than He. Thus, Ne and have greater host guest interactions than He. The charge on encapsulated Ne and Ar atoms is +0.02 and +0.06 respectively, reflecting a small amount of charge transfer from Ne or Ar to the host cage. Although the charge transfer between encapsulated noble gases and T_8-POSS cage is negligible, encapsulation of the noble gases caused considerable charge redistribution among the cage framework atoms. The positive charge increases on Si when He is encapsulated but decreases when Ne and Ar are embedded. Negative charge on oxygen increased while that for hydrogen decreased.

We next consider how endohedral anion cages alter the bonding by transferring electron density to and from the $(HSiO_{3/2})_{10}$ cage. Upon encapsulation of F^-, Cl^- and Br^- anion, the charge on the anion is reduced to approximately –0.8 for all three halides. A small amount of charge transfer appears to occur from the encapsulated halide to the cage. The positive charge increased on Si, and negative charge on oxygen and hydrogen

atoms increased. Upon F^- or Cl^- encapsulation in to the $(HSiO_{3/2})_8$ cage the amount of negative charge on the oxygens in D5R ring decreases compared to empty cage. Upon encapsulation of Br^-, charge is transferred from oxygen and hydrogen to the silicon atoms. Adding a halide to the T_{10}-POSS cage clearly reduced the ionic bonding character in the cage framework. Upon incorporation of atomic and ionic species the T_{10}-POSS framework, silicon atom acts as an electron density 'sink' in all cases. George and Catlow observed the similar behavior for encapsulation of Li^+ and Na^+ into T_8-POSS cage.[33]

HOMO-LUMO gaps: The spatial extent and shape of HOMOs and LUMOs of T_{10}-POSS and its endrohedral complexes X@T_{10}-POSS are shown in the Figure 4.5. In the T_{10}-POSS-cage the HOMO is mainly composed of oxygen (lone pair) *p* orbitals with small contribution from silicon *p* and hydrogen s orbitals (Si = 2%, O = 96% and H = 2%). The LUMO is formed mainly from Si *p*-orbitals with small contributions from H s orbitals (Si =95% and H = 5%). The HOMO-LUMO gaps for different endohedral X@$(HSiO_{3/2})_{10}$ complexes are given in Table 4.6. In Li^+@$(HSiO_{3/2})_{10}$ complex the HOMO is derived mainly from oxygen *p* orbitals (98%) with a small contributions from Si *P* orbital (2%). In Na^+@$(HSiO_{3/2})_{10}$ and K^+@$(HSiO_{3/2})_{10}$ HOMO is made up mainly from oxygen *p* orbitals with small contribution from Si and H. The LUMO is from the Li^+ *p* orbital (81%) with a small contribution from Si (19%). The LUMO in Li^+@$(HSiO_{3/2})_{10}$ and Na^+@$(HSiO_{3/2})_{10}$ is composed of Li^+ and Na^+ *p* orbital H s orbital. However, in K^+@$(HSiO_{3/2})_{10}$, the LUMO is mostly the K^+ *p* orbitals with small contributions from Si *p* orbitals and and the H s orbitals.

In $Cl^-@(HSiO_{3/2})_{10}$ and $Br^-@(SiHO_{3/2})_{10}$ complexes the HOMO is formed mainly from Si *p* orbitals followed by chloride or bromide *p* orbitals with small contribution from oxygens *p* orbitals and hydrogen s orbitals . In $Cl^-@(HSiO_{3/2})_{10}$ the LUMO is composed from Si *p* orbitals with small contribution from oxygen *p* orbitals. But in $Br^-@(SiHO_{3/2})_{10}$ the LUMO is mainly from Si $_P$ orbitals (75%) with a small contribution from hydrogen *s* orbitals (26%). In $He@(HSiO_{3/2})_{10}$ and $Ne@(HSiO_{3/2})_{10}$, complexes the HOMO is mainly from oxygen p orbital with small contribution from Si *p* and H s orbital. In $Ar@(HSiO_{3/2})_{10}$ HOMO is mainly oxygen p orbital. The LUMO is mainly from Si p orbital with small contribution from oxygen p orbital and hydrogen s orbital. However, in $Ne@(HSiO_{3/2})_{10,}$ Ne s orbital also contribute in LUMO. The large HOMO-LUMO energy gaps of endohedral complexes indicate the stability of the complexes.

To understand the bonding nature of the endohedral complexes, the Kohn-Sham energy states of the $(HSiO_{3/2})_{10}$ cage and the endohedral complexes $X@(HSiO_{3/2})_{10}$ shown in Figure 4.6. This energy level diagram demonstrated that both occupied and unoccupied orbitals level are shifted to lower energies when $X=Li^+$, Na^+, and K^+, compared to the pure $(HSiO_{3/2})_{10}$ cage. Furthermore, both occupied and unoccupied orbitals energy states moved to higher energies when $X= F^-$, Cl^-, and Br^-. This indicates that charge transfer occurs between the cage and the encapsulated atoms or ions. However, no significant changes occurred in energy levels when X = He, Ne, and Ar, indicating little or no charge transfer takes place between the cage framework and the noble gases.

Ionization Potentials

The adiabatic ionization potentials and electron affinities for endohedral $X@(HSiO)_{10}$ ($X=Li^-$, Li^0, Li^+, Na^- , Na^0, Na^+, K^- , K^0 and K^+) derivatives calculated at the B3LYP/6-311(d,p) level are summarized in Table 4.8 The difference between calculated and experimental values are within a reasonable range. The ionization potentials of encapsulated Li^0, Na^0 and K^0 are considerably lower than those of the free metal. Boldyrev and coworkers [59-61] defined species with first ionization potentials less than the Cesium atom (90.0 kcal/mol; 3.9 eV) as "superalkalies". The first ionization potential for encapsulated Li^0, Na^0, and K^0 range from 54.7 kcal/mol to 34.5 kcal/mol. These values are significantly smaller than the IP of Cesium. Thus, $X@(HSiO_{3/2})_{10}$ (X = Li, Na, and K) are superalkalis. Moran et al observed similar behavior for the dodecahedrane endrohedral complex of alkali and alkaline earth metals.[56]

NMR Chemical Shifts

Table 4.9 summarizes the chemical shifts for the parent $(HSiO_{3/2})_{10}$ cage and for $X@(HSiO_{3/2})_{10}$ (where guests are X= He, Li^+ and F^-) calculated at the B3LYP/6-311G(d,p) level using the GIAO method.[44-47] The chemical shifts for encapsulated Li^+, F^- , and He were obtained by taking the difference between the isotropic shielding of the free species and the isotropic shielding of the encapsulated ones. Silicon and hydrogen chemical shifts are relative to TMS. We also calculated Li^+ chemical shifts referenced against LiCl. The He atom is slightly deshielded (0.75 ppm) by the $(HSiO_{3/2})_{10}$ cage. This is in sharp contrast with the large calculated shielding obtained by Buhl et al. [62] for $He@C_{60}H_{60}$ (-5.2 ppm) but reminiscent of the deshielding of He in $He@C_{20}H_{20}$ (1.51

ppm) predicted by Jimenez-Vazquez et al.[63] The nuclear independent chemical shift (NICS) calculated at the center of the $(HSiO_{3/2})_{10}$ cage is –0.15 ppm. For comparison the NICS valcule calculated at the center of the benzene ring is -11.5 ppm and -2.1 ppm for cyclohexane.[64] Since the NICS value of –0.15 ppm for T_{10}-POSS cage, no evidence exists for either aromaticity or antiaromaticity for the empty T_{10}-POSS cage.

Overall, the effects of encapsulating of He and F^- on the NMR spectra of $(HSiO_{3/2})_{10}$ are small. The ^{29}Si chemical shifts in $He@(HSiO_{3/2})_{10}$, $Li^+@(HSiO_{3/2})_{10}$ and $F^-@(HSiO_{3/2})_{10}$ chemical shifts are shifted relative to $(HSiO_{3/2})_{10}$ by 9.7 ppm, -7.3 to -23.2 ppm and -0.2 to 0.3 ppm, respectively. The ^1H chemical shifts in $Li^+@(HSiO_{3/2})_{10}$ and $F^-@(HSiO_{3/2})_{10}$ are displaced by 0.4 ppm and -0.2 to –0.3 ppm respectively, relative to $(HSiO_{3/2})_{10}$. The proton chemical shift in $He@(HSiO_{3/2})_{10}$ (4.7 ppm) is almost the same as that exhibited by the protons of the pure cage (4.8 ppm). Therefore, ^1H NMR will be a useful tool to detect and identify $Li^+@(HSiO_{3/2})_{10}$ and $F^-@(HSiO_{3/2})_{10}$ while ^{29}Si NMR can be used to characterize $He@(HSiO_{3/2})_{10}$ and $Li^+@(HSiO_{3/2})_{10}$.

Presence of a Counter Ion

Experimentally, alkali metals would most likely be inserted into T_{10}-POSS cage as a cation. Therefore, an anion must be present. One could envision incorporating both ions inside the cage or one ion could be endoheral and the counterion could be exohedral. The effect of a counterion was investigated using LiF as an example. Initially, a structure was generated by placing both Li^+ and F^- ion 1 Å apart inside the cage. A second geometry was generated where F^- ion was placed at the center of the cage and a Li^+ outside the D5R surface. The second geometry is reminiscent of the ammonium $F^-@T_8$-

POSS salt synthesized and characterized by Taylor. [65] The geometries were optimized at the B3LYP/6-311G(d,p) level. Table 4.10 summarizes energies, zero-point energies, zero-point corrected binding energies bond lengths and charge on encapsulated Li^+ and F^- . The calculated bond lengths are given in Figure 7(a) and Figure 7(b) for the first and second types of geometries, respectively. Both structures (Figure 7(a) and 7(b)) are similar. In both cases (7(a) and 7(b)) the F^- ion remained inside the cage and the Li^+ ions bonded five Si, five oxygens on the cage D5R surface. In the optimized structure, the F^- ion from the cage center moves towards lithium ion. The shape of the optimized structures look like an umbrella (Figures 7(a) and 7(b)). The binding energies are essentially identical for the two structures (–255.4 kcal/mol). The $F^-@Li^+(HSiO_{3/2})_{10}$ complex is –154.0 kcal/mole lower in energy compared to $F^-@HSiO_{3/2})_{10}$ ($F^-@HSiO_{3/2})_{10}$ complex without counterion). The exohedral Li^+ counterion stabilizes the $F^-@Li^+(HSiO_{3/2})_{10}$ complex system significantly. The distance between Li^+ and F^- in the $F^-@(Li^+(HSiO_{3/2})_{10}$ complex is 1.741 Å. The distance between Li^+ and F^- in gaseous LiF calculated at the B3LYP/6-311G(d,p) level is 1.55 Å. Hence the distance between Li^+ and F^- in the $F^-@Li^+(HSiO_{3/2})_{10}$ complex is larger than the distance in free LiF. This enables us to suggest the presence of partial chemical bonding between the F^- and Li^+ in the $F^-@Li^+(HSiO_{3/2})_{10}$ complex. The charge distributions on the Li^+ and F^- ions as given in Table 4.10 indicates the dipolar nature of the LiF species in the $F^-@Li^+(HSiO_{3/2})_{10}$ complexes. An interesting observation is that the bonding in LiF in $F^-@Li^+(HSiO_{3/2})_{10}$ is less ionic or dipolar than the isolated species gaseous LiF .

To assess the feasibility of ions penetrating into the cage, the F^- ion is placed inside and the Li^+ ion situated outside of the D4R surface of the T_{10}-POSS cage. The optimized structure is shown in Figure 7(c). The Li^+ attached both oxygen and Si atoms on the D4R surface. In the optimized structure F^- moved from the cage center towards the Li^+ ion. In contrast to the cases discussed above, Li^+ and F^- do not form chemical bond, but attract each other by weak interactions. The distance between F^- and Li^+ is 2.738 **Å**. The binding energy in $F^-@Li^+(HSiO_{3/2})_{10}$ (Li^+ on D4R surface) is –229.6 kcal/mole. The energy difference between the complex $F^-@Li^+(HSiO_{3/2})_{10}$ (Li^+ on D5R surface) and $F^-@Li^+(HSiO_{3/2})_{10}$ (Li^+ on D4R surface) is –25.8 kcal/mol. The Li^+ ion approaching in to the cage is energetically more favorable to interact with F^- or penetrate into the cage thought the (D5R) surface versus the D4R surface.

Conclusions

The following conclusions can be drawn from these theoretical calculations.

The formation of the endohedral complexes $Li^+@(HSiO_{3/2})_{10}$, $Na^+@(HSiO_{3/2})_{10}$, $K^+@(HSiO_{3/2})_{10}$, $F^-@(HSiO_{3/2})_{10}$, $Cl^-@(HSiO_{3/2})_{10}$ from their isolated components are energetically favorable. These ions are thermodynamically stable within the $(HSiO_{3/2})_{10}$ cage. Encapsulation of Ar is thermodynamically unfavorable. The exohedral $X(HSiO_{3/2})_{10}$ ($X=Li^+$, Na^+, K^+, He, Ne, Cl^- and Br^-) complexes are energetically more favorable than their endohedral counterparts except for F^-. Instead of forming an exohedral complex, the F^- ion penetrates into the cage center with no energy barrier.

Exohedral X@ $(HSiO_{3/2})_{10}$ compounds ($X=Li^0$, Na^0, K^0) have smaller first ionization potentials (IP) than the IP of atomic Cesium and can thus be considered as "superalkalis ".

Upon encapsulation of an alkali metal cation, halide or noble gas into the center of the $(SiHO_{3/2})_{10}$, the framework properties changed distinctly. The electron density was transferred from the F^-, Cl^- and Br^- onto the silicon atoms in $X(HSiO_{3/2})_{10}$ ($X = F^-$, Cl^- and Br^-).

Upon inclusion of cations, the silicon atoms donate electron density to the cations. Encapsulation of noble gases generates negligible charge transfer.

Calculated NMR chemical shifts of endohedral He (0.8 ppm) , Li^+ (5.1 ppm) and F^- (195.3 ppm) nuclei indicate considerable deshielding compare to their corresponding isolated ions. The NICS computed at the center of the $(HSiO_{3/2})_{10}$ cage shows no evidence for any aromaticity or antiaromaticity in the cage molecule.

In summary, the present work represents a new direction in the investigation of T_{10}-POSS clusters via accurate theoretical calculations. Subtle aspects of the structure and bonding were investigated for systems of considerable complexity. Among the salient points of this work is the significant amount of charge redistribution around the cage framework and at the incorporated ionic and atomic species. This effect is subtly different for anions, cations and noble gases. The framework silicon atoms act as an electron density sink, which can easily be changed depending on the nature of the particle incorporated.

References

(1) Fu, B. X.; Hsiao, B. S.; Pagola, S.; Stephens, P.; White, H.; Rafailovich, M.; Sokolov, J.; Mather, P. T.; Jeon, H. G.; Philips, S.; Lichtenhan, J.; Schwab, J. *Polymer* **2001**, *42*, 599.

(2) Maitra P.; Wunder, S. L. *Electrochem Solid-State Lett* **2004**, *7*, A88.

(3) Romo-Uribe, A.; Mather, P. T.; Haddad, T. S.; Lichtenhan, J. D. *J. Polym. Sci. B-Polym. Phys.* **1998**, *36*, 18571872.

(4) Li, G.; Wang, L.; Ni, H.; Pittman, C. U., Jr. *J. Inorg. Organomet. Polym.* **2002**, *11*, 123.

(5) Agaskar, P. A.; Klemperer, W. G. *Inorg. Chimi. Acta* **1995**, *229*, 355.

(6) Brown, J. F., Jr.; Vogt, L. H., Jr. *J. Am. Chem. Soc*.**1965**, *87*, 4313.

(7) Feher, F. J.; Wyndham, K. D. *Chem. Commun.* **1998**, 323

(8) Li, G. Z.; Wang, L.; Toghiani, H.; Daulton, T. L.; Koyama, K.; Pittman, C. U., Jr. *Macromolecules* **2001**, *34*, 8686.

(9) Li, G. Z.; Wang, L.; Toghiani, H.; Daulton, T. L.; Pittman, C. U. *Polymer* **2002**, *43*, 4167.

(10) Maxim, N.; Magusin, P. C. M. M.; Kooyman, P. J.; van Wolput, J. H. M. C.; van Santen, R. A.; Abbenhuis, H. C. L. *Chem. Mater.* **2001**, *13*, 2958.

(11) Maxim, N.; Overweg, A.; Kooyman, P. J.; van Wolput, J. H. M. C.; Hanssen, R. W. J. M.; van Santen, R. A.; Abbenhuis, H. C. L. *J. Phys. Chem.B* **2002**, *106*, 2203.

(12) Zheng, L.; Waddon, A. J.; Farris, R. J.; Coughlin, E. B. *Macromolecules* **2002**, *35*, 2375.

(13) Wada, K.; Yamada, K.; Kondo, T.; Mitsudo, T.-A. *Chem. Lett.* **2001**, 12.

(14) Dance, B. *Semiconduct. Int.* **2001**, *24*, 46.

(15) Lamm, M. H.; Chen, T.; Glotzer, S. C. *Nano Lett.* **2003**, *3*, 989.

(16) Fu, B. X.; Hsiao, B. S.; White, H.; Rafailovich, M.; Mather, P. T.; Jeon, H. G.; Phillips, S.; Lichtenhan, J.; Schwab, J. *Polym. Int.* **2000**, *49*, 437.

(17) Lee, A.; Lichtenhan, J. D. *J. Appl. Polym. Sci.* **1999**, *73*, 1993.

(18) Haddad, T. S.; Lichtenhan, J. D. *Macromolecules* **1996**, *29*, 7302.

(19) Schwab, J. J.; Lichtenhan, J. D. *Appl. Organomet. Chem.* **1998**, *12*, 707.

(20) Raj, R.; Riedel, R.; Soraru, G. D. *J. Am. Ceram. Soc.* **2001**, *84*, 2158.

(21) Abbenhuis, H. C. L. *Chem. Eur. J.* **2000**, *6*, 25.

(22) Ducateau, R.; Cremer, U.; Harmsen, R. J.; Mohamud, S. I.; C. L. Abbenhuis, C. L.; Avan Saten, R.; Meetsma, A.; Thiele, S. K.-H.; F. F. H. van Tol, F. F. H.; Kranenburg, M. *Organometallics* **1999**, *18*, 5447.

(23) Klunduk, M. C.; Maschmeyer, T.; Thomas, J. M.; Johnson, F. G. *Chem. Eur. J.* **1999**, *5*, 1481.

(24) Pescarmona, P. P.; Van der Waal, J. C.; Maxwell, I. E.; Maschmeyer, T. *Angew. Chem., Int. Ed.* **2001**, *40*, 740.

(25) Xiao, F. S.; Han, Y.; Yu, Y.; Meng, X.; Yang, M.; Wu, S. *J. Am. Chem. Soc.* **2002**, *124*, 888.

(26) Liu, J. C. *Appl. Organomet. Chem.* **1999**, *13*, 295.

(27) de Vos, R. M.; Verweij, H. *J. Membr. Sci.* **1998**, *143*, 37.

(28) Suzuki, F.; Nakane, K.; Yasuo, H. *J. Mem. Sci.* **1995**, *104*, 183.

(29) McCusker, C.; Carroll, J. B.; Rotello, V. M. *Chemical Communications (Cambridge, United Kingdom)* **2005**, 996.

(30) Zahang, C.; Babonneau, F.; Bonhomme, C.; Laine, R. M.; Soles, C. L.; Hristov, A. H.; Yee, F. A. *J. Am. Chem. Soc.* **1998**, *120*, 8380.

(31) Cheng, W.-D.; Xiang, K.-H.; Pandey, R.; Pernisz, U. C. *J. Phys. Chem.* **2000**, *104*, 6737.

(32) Päch, M.; Stösser, R. *J. Phys. Chem. A* **1997**, *101*, 8360.

(33) George, A. R.; Catlow, C. R. A. *Chem. Phys. Lett.* **1995**, *247*, 408.

(34) Bassindale, A. R.; Pourny, M.; Taylor, P. G.; Hursthouse, M. B.; Light, M. E. *Angew. Chem., Int. Ed.* **2003**, *42*, 3488.

(35) Tejerina, B.; Gordon, M. S. *J. Phys. Chem. B* **2002**, *106*, 11764.

(36) Park, S. S.; Xiao, C.; Hagelberg, F.; Hossain, D.; Pittman, C. U., Jr.; Saebo, S. *J. Phys. Chem. A* **2004**, *108*, 11260.

(37) Allen, E. C., ;; Beers, K. J. *Polymer* **2005**, *46*, 569.

(38) Earley, C. W. *J. Phys. Chem.* **1994**, *98*, 8693.

(39) Lee, C.; Yang, W.; Parr, R. G. *Phys. Rev. B: Condens. Matter and Materials Phys.* **1988**, *37*, 785.

(40) Becke, A. D. *J. Chem. Phys.* **1993**, *98*, 5648.

(41) Frisch, M. J.; Pople, J. A.; S., B. J. *J.Chem.Phys.* . **1984**, *80*, 3265.

(42) Frisch, M. J. T., G. W.; Schlegel, H. B.; Scuseria, G. E.; Robb, M. A.; Cheeseman, J. R.; Montgomery, Jr., J. A.; Vreven, T.; Kudin, K. N.; Burant, J. C.; Millam, J. M.; Iyengar, S. S.; Tomasi, J.; Barone, V.; Mennucci, B.; Cossi, M.; Scalmani, G.; Rega, N.; Petersson, G. A.; Nakatsuji, H.; Hada, M.; Ehara, M.; Toyota, K.; Fukuda, R.; Hasegawa, J.; Ishida, M.; Nakajima, T.; Honda, Y.; Kitao, O.; Nakai, H.; Klene, M.; Li, X.; Knox, J. E.; Hratchian, H. P.; Cross, J. B.; Bakken, V.; Adamo, C.; Jaramillo, J.; Gomperts, R.; Stratmann, R. E.; Yazyev, O.; Austin, A. J.; Cammi, R.; Pomelli, C.; Ochterski, J. W.; Ayala, P. Y.; Morokuma, K.; Voth, G. A.; Salvador, P.; Dannenberg, J. J.; Zakrzewski, V. G.; Dapprich, S.; Daniels, A. D.; Strain, M. C.; Farkas, O.; Malick, D. K.; Rabuck, A. D.; Raghavachari, K.; Foresman, J. B.; Ortiz, J. V.; Cui, Q.; Baboul, A. G.; Clifford, S.; Cioslowski, J.; Stefanov, B. B.; Liu, G.; Liashenko, A.; Piskorz, P.; Komaromi, I.; Martin, R. L.; Fox, D. J.; Keith, T.; Al-Laham, M. A.; Peng, C. Y.; Nanayakkara, A.; Challacombe, M.; Gill, P. M. W.; Johnson, B.; Chen, W.; Wong, M. W.; Gonzalez, C.; and Pople, J. A.; Gaussian, Inc., Wallingford CT, 2004. Gaussian 03; Gaussian 03 ed., 2004.

(43) PQS version 3.1, P. Q. S., 2013 Green Acres Road, Fayetteville, AR 72703. PQS version 3.1, Parallel Quantum Solutions, 2013 Green Acres Road, Fayetteville, AR 72703 ed.

(44) Wolinski, K.; Hinton, J. F.; Pulay, P. *J. Am. Chem. Soc.* **1990**, *112*, 8251.

(45) Schreckkenbach, G., ;; Ziegler, T. *J. Phys. Chem.* **1995**, *99*, 606.

(46) Cheeseman, J. R.; Trucks, G. W.; Keith, T.; Frisch, M. J. *J. Phys. Chem.* **1996**, *104*, 5497.

(47) Ditchfield, R. *J. Chem. Phys.* **1976**, *65*, 3123.

(48) Glendening, E. D.; Reed, A. E.; Carpenter, J. E.; Weinhold, F. *NBO 4.M University of Wisconson: Madison* **1993**.

(49) Boys, S. F.; Bernardi, F. *Mol. Phys.* **1970**, *19*, 553.

(50) Heyde, T. P. E.; Burgi, H., -B.;; Burgi, H.; Tornroos, K. W. *Chimia* **1991**, *45*, 38.

(51) de Man, A. J. M.; Sauer, J. *J. Phys. Chem.* **1996**, *100*, 5025.

(52) D5R defined the surface of the cage comprised five Si and five oxygen atoms. The two surface of T_{10}-POSS cage are joined with each other through by joining Si aom by oxygen.

(53) Tossell, J. A. *J. Phys. Chem.* **1996**, *100*, 5025.

(54) Xiang, K.-H.; Pandey, R.; Pernisz, U. C.; Freeman, J. *J. Phys. Chem. B* **1998**, *102*, 8704.

(55) Pasquarello, A.; Hybertsen, M. S.; Car, R. *Phys. Rev. B* **1996**, *54*, R2339.

(56) Moran, D.; Stahl, F.; Jemmis, E. D.; Schaefer, H. F., III;; Schleyer, P. v. R. *J. Phys. Chem.A* **2002**, *106*, 5144.

(57) Cross, R. J.; Saunders, M.; Prinzbach, H. *Org. Lett.* **1999**, *1*, 1479.

(58) Sun, Q.; Wang, Q.; Yu, J. Z.; Ohno, K.; Kawazoe, Y. *J. Phys.: Condens. Matter* **2001**, *13*, 1931.

(59) Rehm, E.; Boldyrev, A. I.; Schleyer, P. v. R. *Inorg. Chem.* **1992**, *31*, 4831.

(60) Gutsev, G. L.; Boldyrev, A. I. *Chem. Phys. Lett.* **1982**, *92*, 262.

(61) Gutsev, G. L.; Boldyrev, A. I. *Adv. Chem. Phys.* **1985**, *61*, 169.

(62) Buhl, M.; Thiel, W.; Jiao, H.; Schleyer, P. v. R.; Saunders, M.; Anet, F. A. L. *J. Am. Chem. Soc.* **1994**, *116*, 6005.

(63) Jimenez-Vazquez, H. A.; Tamariz, J.; Cross, R. J. *J. Phys. Chem. A* **2001**, *105*, 1315.

(64) Jiao, H.; Nagelkerke, R.; Kurtz, H. A.; Williams, R. V.; Borden, W. T.; Schleyer, P. v. R. *J. Am. Chem. Soc.* **1997**, *119*, 5921.

(65) Bassindale, A. R.; Baukov, Y. I.; Borbaruah, M.; Glynn, S. J.; Negrebetsky, V. V.; Parker, D. J.; Taylor, P. G.; Turtle, R. *J. Org. Chem.* **2003**, *669*, 154.

(66) Huheey, E. J.; Keiter, A. E.; Keiter , L. R. *Inorganic Chemistry : Principles of Structure and Reactivity*; HarperCollins,: New York, USA, 1993.

(67) James, M. A.; Lord, P. M. *Macmillan's Chemical and Physical Data*; Macmillan: London, UK, 1992.

Table 4.1 Selected Bond Lengths (Å) and Bond Angles (in Degrees) of the $(HSiO_{3/2})_{10}$ Cage and Endohedral $X@(HSiO_{3/2})_{10}$ Complexes at the B3LYP/6-311G(d,p) Level.

	X-Si	X-O	X-O_b	Si-O	Si-O_b	Si-H	OSiO	SiOS_b	OSiO	HSiO
Cage				1.637	1.642	1.162	110.0	152.0	155.9	109.6
Li^+	2.980	3.051	3.462	1.684	1.639	1.457	108	130.6	143.0	112.1
Li	2.522-3.220	3.220-3.239	3.220-3.239	1.663	1.636-1.655	1.463	105.9	150.4	125.5	111.4
Li^-	2.741	3.133	3.133	1.679	1.621	1.466	108.3	140.3	126.7	109.7
Na^+	3.223 3.198	2.411	3.376	1.667	1.667	1.458	108.9	136.6	153.6	113.0
Na^0	2.795	2.361	2.361	1.666 1.639	1.662 1.631	1.462	108.0	147.4	155.0	107.0
Na^-	3.140	3.085	3.207	1.654	1.657	1.470	112.4	145.3	149.2	146.8
K^+	3.201	2.875	3.224	1.649	1.649	1.456	106.8	148.8	164.8	112.5
K	3.199	2.843	3.299	1.647	1.652	1.456	106.5	143.8	167..8	113.0
K^-	3.194	2.824	3.341	1.645	1.656	1.456	106.1	140.9	170.1	113.3
F^-	3.027 3.162	3.004	3.008	1.636	1.470	1.472	112.2	150.6	147.8	106.9
Cl^-	3.126	3.130	3.130	1.645	1.648	1.471	111.9	149.2	148.3	105.8
Br^-	3.183	3.148	3.148	1.650	1.652	1.471	111.9	148.6	148.2	105.6
He	3.157	2.982	2.982	1.638	1.642	1.462	109.2	152.3	155.9	109.7
Ne	3.158	2.987	2.987	1.639	1.643	1.462	109.2	152.5	155.7	109.6
Ar	3.168	3.031	3.031	1.645	1.647	1.462	109.7	153.7	154.9	109.3

Table 4.2. Total Energies (in Hartrees), Lowest Frequencies ω_1 (cm^{-1}), Molecular point Groups, Binding Energies E_{bind} (kcal/mol), and Selected Bond Lengths (Å), of Exohedral $X(HSi_{3/2})_{10}$ Complexes Calculated at the B3LYP/ 6-311G(d,p) Level

X	Energy	ZPE	ω_1	Sym.	E_{bind}	r_{X-Si}	r_{X-O} (r'_{X-O})	r_1,r_2(r_6)	r_3	r_4	r_7(r_8)
Li^+	-4038. 812964	111.0	i82.85(2)	C_{5v}	-63.0	2.903	2.212	1.663,1.663 (1.674)	1.618	1.660	1.457 (1.458)
Na^+	-4193.587173	110.8	33.90	C_{5v}	-44.7	3.169	2.479	1.664(1.634)	1.617	1.658	1.459/1.458
K^+	-4631.235679	110.6	34.29	C_{5v}	-29.2	3.567	2.888	1.660(1.634)	1.618	1.655	1.460/1.458
Cl^-	-4491.741693	109.4	i45(4)	C_{5v}	-8.4	4.028	3.617	1.628 (1.640)	1.668	1.636	1.462/1.467
Br^-	-6605.674932	110.3	18.68	C_1	-8.7	4.966-3.452	3.927-3.297	1.629-1.639 (1.638-1.641)	1.655 1.683	1.631 1.637	1.464-1.468
He	-4034.372779	109.7	10.42	C_1	-20.7	4.590/ 4.630	4.047-4.076	1.637(1.63	1.642	1.642	1.462
Ne	-4160.381548	110.4	25.89	C_{5v}	-1.8	3.813	3.259	1.637(1.637)	1.642	1.642	1.442
Ar	-4558.980727	110.4	10.02	C_{5v}	0.1	4.773	4.242	1.637(1.637)	1.642	1.642	1.462

*The notation used for define bond lengths is illustrated in Figure 4.3.

Table 4.3 Total Energies (in Hartrees), Zero-point Energies (ZPE) (in kcal/mol), Molecular point Groups, Lowest Vibrational Frequencies ν_1 (cm^{-1}), Zero-point Corrected Inclusion Energies E_{inc} (kcal/mol), and Isomerization Energies (kcal/mol) for Endohedral Complexes $X@(HSiO_{3/2})_{10}$ Calculated at B3LYP/6-311G(d,p) Level.

X	Energy	ZPE	*Sym.*	ω_1	E_{inc}	E_{iso}
Pure	-4031.427632	110.3	D_{5h}	25.76		
Li^+	-4038.789806	111.8	C_1	76.18	-47.1	-16.0
Li^0	-4038.893495	109.1	C_1	61.72	14.7	
Li^-	-4038.948852	109.1	C_1	69.25	-10.2	
Na^+	-4193.553367	110.5	C_1	16.53	-23.8	-20.6
Na^0	-4193.646499	108.4	D_{5h}	67.29	40.6	
Na^-	-4193.639109	106.3	D_{5h}	27.89	53.5	
K^+	-4631.177345	110.2	D_{5h}	68.0	7.0	-22.2
K^0	-4631.242685	108.9	D_{5h}	76.43	68.3	
K^-	-4631.220251	109.3	D_{5h}	78.07	92.8	
F^-	-4131.412207	111.3	*Cs*	26.70	-101.5	0.0
Cl^-	-4491.760210	111.3	D_{5h}	96.6	-19.0	
Br^-	-6650.651373	110.0	D_{5h}	107.3	2.4	-10.0
He	-4034.335469	111.2	D_{5h}	50.1	4.1	-24.1
Ne	-4160.376129	111.1	D_{5h}	61.7	2.3	-4.1
Ar	-4558.926895	111.4	D_{5h}	92.7	34.9	-35.0

Table 4.4. **T**otal Energies (in Hartrees), Zero-point Energies (ZPE), Molecular point Groups, Lowest Vibrational Frequencies ω_1 (cm^{-1}), Zero-point Corrected Inclusion Energies E_{incl} (kcal/mol), and Optimized Bond Lengths (Å) for Endohedral Complex of $X@(HSiO_{3/2})_{10}$ at the B3LYP/6311++G(2d,2p) Level.

X	Energy	ZPE	*Sym.*	ω_1	E_{incl}	r_{X-Si}	r_{X-O}	r_{Si-O}	r_{si-ob}	r_{A-H}
pure	-4031.459079	109.5	D_{5h}	7.59				1.637	1.642	1.462
						3.178-		1.622-	1.644-	
Li^0	-4038.922276	109.6	C1	54.53	17.8	2.534	2.817	1.634	1.657	1.464
Li^+	-4038.841475	110.8	C_1	20.85	-59.8	3.178	2.727	1.646		1.457
						2.736	1.870	1.814	1.627	1.477
						2.835	2.136	1.612	1.814	1.486
						2.895	2.162	1.623	1.662	1.470
Li^-	-4038.981878	108.6	C_1	75.17	-7.8	2.946	3.142	1.707		1.467
Na^0	-4193.676396	107.6	D_{5h}	i79.81(1)	41.6	2.795	2.950	1.666	1.666	1.461
Na^+	-4193.580726	110.0	C_1	15.13	-20.9	3.186	2.763	1.648	1.648	1.457
Na^-	-4193.673547	105.8	D_{5h}	28.81	55.2	3.146	3.077 (3.212)	1.655	1.658	1.468
K^0	-4631.276512	107.5	D_{5h}	55.82	66.3	3.211	2.893 (3.211)	1.650	1.649	1.458
K^+	-4631.206260	109.6	D_{5h}	71.14	8.8	3.201	2.875 (3.22)	1.51	1.649	1.458
K^-	-4631.277534	108.5	D_{5h}	63.86	78.7	3.201	2.855 (3.278)	1.649	1.653	1.457
						3.112	3.073	1.637		1.472
F^-	-4131.451682	110.7	*Cs*	27.05	-64.1	3.112	(3.073)	1.637	1.642	1.472
					-18.9		3.090		1.649	
Cl^-	-4491.794647	110.6	D_{5h}	94.34		3.129	(3.136)	1.647		1.471
					7.3		3.101		1.654	
Br^-	-6605.686121	110.0	D_{5h}	105.60		3.137	(3.154)	1.652		1.470
					4.3		2.987		1.644	
He	-4034.367217	110.5	D_{5h}	49.40		3.159	(3.123)	1.639		1.462
					6.6		3.000		1.644	
Ne	-4160.410345	110.4	D_{5h}	60.93		3.159	(3.100)	1.640		1.462
Ar	-4558.959173	110.5	D_{5h}	90.50	34.8	3.171	3.017 (3.112)	1.647	1.649	1.462

Table 4.5 Natural Charge Analysis and HOMO-LUMO Gaps (eV) of X@POSST$_{10}$ at the B3LYP/6-311G(d,p) Level.

X	Q_X[a]	Q_{Si}	Q_o	Q_{o1}	Q_H	HOMO-LUMO
Pure		2.14	-1.27	-1.27	-0.24	8.97
		2.10	-1.26	-1.24	-0.19	9.16
		2.09		-1.31	-0.20	
Li^+	0.87	2.11				
		2.13	-1.26	-1.27	-0.21	4.12
Li°	0.75	1.50	-1.22	-1.23	-0.23	
		2.10	-1.26	-1.26	-0.26	
Li^-	-0.51	2.10	-1.26	-1.26	-0.26	
Na^+	0.88	2.11	-1.29	-1.22	-0.20	
		2.10	-1.26	-1.26	-0.23	2.23
Na°	0.15	2.10	-1.26		-0.23	
	-0.46	2.09	-1.27	-1.27	-0.24	1.30
Na^-			-1.27			
K^+	0.89	2.109	-1.28	-1.25	-0.19	9.34
K°	0.08	2.10	-1.28	-1.25	-0.20	0.58
K^-	-0.80	2.09	-1.28	-1.25	-0.21	
F^-	-0.83	2.16	-1.26	-1.27	-0.28	2.79
Cl^-	-0.80	2.14	-1.26	-1.27	-0.27	8.23
Br^-	-0.76	2.06	-1.24	-1.25	-0.21	7.90
He	0.01	2.14	-1.27	-1.27	-0.24	9.67
Ne	0.02	2.14	-1.27	-1.27	-0.24	9.59
Ar	0.06	2.12	-1.26	-1.27	-0.23	9.60

[a]Q_X = Charge on impurity X in atomic units. The symbols Q_{Si}, Q_H and Q_O are defined analogously.

Table 4.6 Natural Electron Configurations of the Cage Elements, Free Atoms and Ions.

Atoms/ions	Configuration
Si	[core]$3s^{0.67}3p^{1.15}3d^{0.04}$
O	[core]$2s^{1.71}2p^{5.55}$
	[core]$2s^{1.72}2p^{5.54}$
H	$1s^{1.23}$
Li^+	[core]$1s^0$
Na^+	[core]$1s^0$
K^+	[core]$1s^0$
F^-	[core]$2s^{2.00}2p^{6.00}$
Cl^-	[core]$3s^{2.00}3p^{4.00}$
Br^-	[core]$4s^{2.00}4p^{2.00}$
He	$1s^{2.00}$
Ne	[core]$2s^{2.00}2p^{6.00}$
Ar	[core]$3s^{2.00}3p^{6.00}$

Table 4.7 Natural Electron Configuration of both the Cage Atoms and the Embedding Atoms and Ions in $X@(HSiO_{3/2})_{10}$.

	X	Si	O	H
Cage		[core]$3s^{0.67}3p^{1.15}3d^{0.04}$	[core]$2s^{1.71}2p^{5.55}$	$1s^{1.23}$
			[core]$2s^{1.72}2p^{5.54}$	
Li^+	[core]$2s^{0.10}2p^{0.01}3d^{0.01}$	[core]$3s^{0.70}3p^{1.16}3d^{0.04}4p^{0.01}$	[core]$2s^{1.73}2p^{5.49}$	$1s^{1.19}$
			[core]$2s^{1.73}2p^{5.51}$	
			[core]$2s^{1.71}2p^{5.54}3p^{0.01}$	
Na^+				
K^+	[core]$3d^{0.03}4p^{0.01}6s^{0.10}$	[core]$3s^{0.69}3p^{1.16}3d^{0.04}$	[core]$2s^{1.71}2p^{5.56}$	$1s^{1.19}$
			[core]$2s^{1.72}2p^{5.53}$	
F^-	[core]$2s^{1.99}2p^{5.84}$	[core]$3s^{0.65}3p^{1.15})3d^{0.04}4p^{0.01}$	[core]$2s^{1.722}p^{5.54}$	$1s^{1.27}$
			[core]$2s^{1.72}2p^{5.55}$	
Cl^-	[core]$3s^{1..97}3p^{5.83}$	[core]$3s^{0.65}3p^{1.15}3d^{0.04}4p^{0.01}$	[core]$2s^{1.72}2p^{5.53}$	$1s^{1.26}$
			[core]$2s^{1.72}2p^{5.55}$	
Br^-	[core]$4s^{1.97}4p^{5.79}$	[core]$3s^{0.70}3p^{1.23}4p^{0.01}$	[core]$2s^{1.73}2p^{5.51}$	$1s^{1.21}$
He	[core]$1s^{1.99}$	[core]$3s^{0.67}3p^{1.15}3d^{0.04}$	[core]$2s^{1.71}2p^{5.55}$	$1s^{1.23}$
Ne	[core]$2s^{2.00}2p^{5.98}$	[core]$3s^{0.67}3p^{1.15}3d^{0.04}$	[core]$2s^{1.71}2p^{5.55}$	$1s^{1.23}$
			[core]$2s^{1.72}2p^{5.55}$	
Ar	[core]$3s^{1.99}3p^{5.95}$	[core]$3s^{0.67}3p^{1.15}3d^{0.04}4p^{0.01}$	[core]$2s^{1.71}2p^{5.54}$	$1s^{1.23}$
			[core]$2s^{1.72}2p^{5.55}$	

Table 4.8 Ionization Potentials (IP, kcal/mol) of Free atoms and Metal Encapsulated ($X@POSST_{10}$) Complexes Calculated at the B3LYP/6-311G(d,p) Level.

Ionization process			IPCalculated	expt IP[a]	ΔIP [b]
Li^-	→	$Li + e^-$	11.6		
$Li^-@(HSi_{3/2})_{10}$	→	$Li@(HSi_{3/2})_{10} + e^-$	34.7		25.0
Li	→	$Li^+ + e^-$	129.5	124.3	
$Li@(HSi_{3/2})_{10}$	→	$Li^+@(HSi_{3/2})_{10} + e^-$	65.1		74.8
Na^-	→	$Na + e^-$	10.3		
$Na^-@(HSi_{3/2})_{10}$	→	$Na@(HSi_{3/2})_{10} + e^-$	2.6		7.7
Na	→	$Na^+ + e^-$	125.0	118.5	
$Na@(HSi_{3/2})_{10}$	→	$Na^+@(HSi_{3/2})_{10} + e^-$	60.6		64.4
K^-	→	$K + e^-$	10.1		
$K^-@(HSi_{3/2})_{10}$	→	$K@(HSi_{3/2})_{10} + e^-$	14.1		3.4
K	→	$K^+ + e^-$	113.7	100.1	
$K@(HSi_{3/2})_{10}$	→	$K^+@(HSi_{3/2})_{10} + e^-$	41.0		52.7

[a] Reference 66, and 67 [b] Reduction in IP by encapsulation into POSS-T_{10} cage.

Table 4.9 Chemical Shifts[a] (in ppm) for T_{10}-POSS and Endohedral T_{10}-POSS Complexes Calculated at the B3LYP/6-311G(d,p) Level

System	^{29}Si	^{1}H	X
T_{10}-POSS Cage	-93.3, -86.255[1]	4.8, 4.244[1]	
$He@(SiHO_{3/2})_{10}$	-103.0	4.7	0.8
$Li^{+}@(SiHO_{3/2})_{10}$	-77.2, -79.0, -84.5, -70.1, -71.6	5.3, 5.1	5.1, -2.0[2]
$F^{-}@(SiHO_{3/2})_{10}$	-93.1, -93.6	4.4	195.3

[a] the ^{1}H and ^{29}Si chemical shifts are relative to TMS. Li^{+}, F^{-} and He chemical shifts obtained by subtracting the absolute isotropic shielding of encapsulated Li^{+}, F^{-}, and He from the corresponding unencapsulated species.
[1] the experimental chemical shifts of ^{1}H and ^{29}Si relative to TMS.
[2] the Li^{+} chemical shift relative to LiCl.

Table 4.10 B3LYP/6-311G(d,p) Calculated Properties of Compexes of LiF with T_{10}-POSS. Total Energies (Hatrees) Zero point Energies (ZPE in kcal/mol), Binding Energies (E_{bind} in kcal/mol) and Bond Lengths (r_{Li-F} in Å), Natural Charges is e^-.

System	Total Energy	Sym	ZPE	E_{bind}	r_{Li-F}	Natural charge
$LiF@POSST_{10}$	-4138.945508	Cs	113.2	-255.4	1.741	Li 0.21 F -0.59
$F^-@Li^+POSST_{10}$ (D5R)	-4138.945443	C_{5V}	113.2	-255.4	1.742	Li 0.21 F -0.59
$F^-@Li^+POSST_{10}$ (D4R)	-4138.895918	C_{2v}	112.7	-229.6	2.738	Li 0.20 F -0.59

Table 4.11 BSSE (in kcal/mol) for Endohedral $X@T_{10}$ –POSS Complexes Calculated at the B3LYP/6-311G(d,p) Level.

System	Energy
$Li^+@POSST_{10}$	5.96
$Na^+@POSST_{10}$	4.81
$K^+@POSST_{10}$	4.11
$F^-@POSST_{10}$	4.35
$Cl^-@POSST_{10}$	6.38
$B^-@POSST_{10}$	11.45
$He@POSST_{10}$	0.60
$Ne@POSST_{10}$	6.69
$Ar@POSST_{10}$	2.86

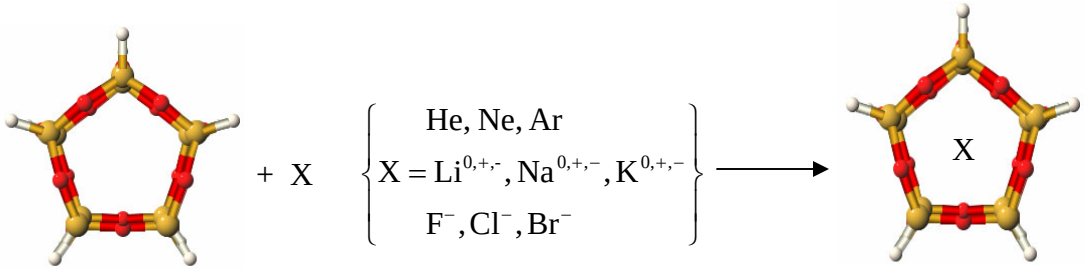

(a) $(SiHO_{3/2})_{10}$ (b) (c)X@$(SiHO_{3/2})_{10}$

Figure 4.1 Schematic Representation of Host Cage Species $(SiHO_{3/2})_{10}$ with D5R units and Impurities; (a) Host Cage with D_{5h} Symmetry (b) Identity of X (c) Endohedral Species of X@$(SiHO_{3/2})_{10}$

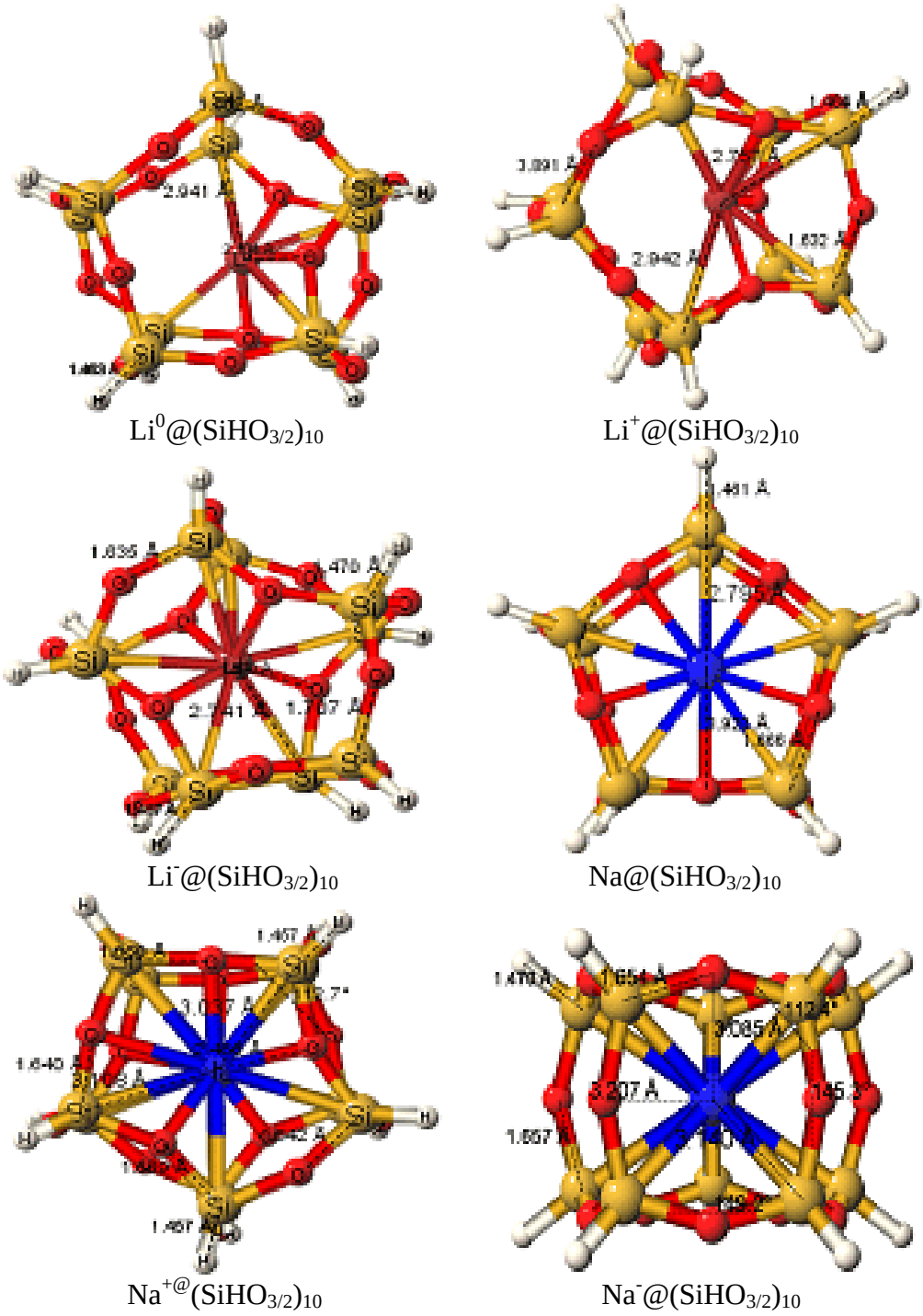

Figure 4.2 Optimized Geometries of Endohedral X@(HSiO$_{3/2}$)$_{10}$ Complexes at the B3LYP/6-311G(d,p) Level.

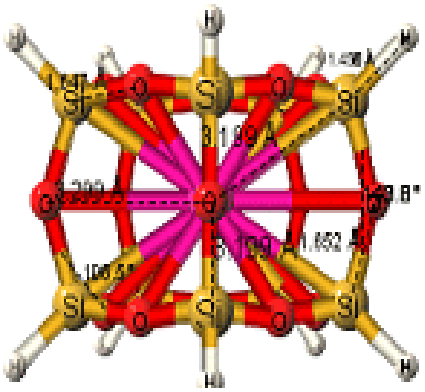

$K@(SiHO_{3/2})_{10}$

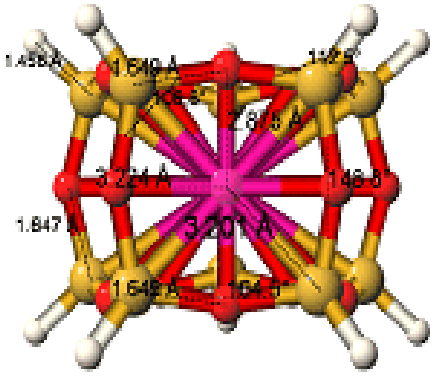

$K^{+}@(SiHO_{3/2})_{10}$

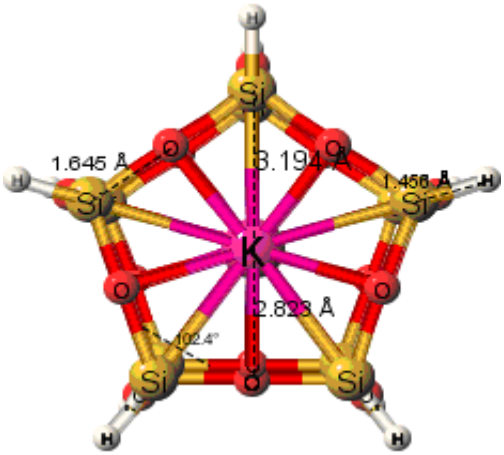

$K^{-}@(SiHO_{3/2})_{10}$

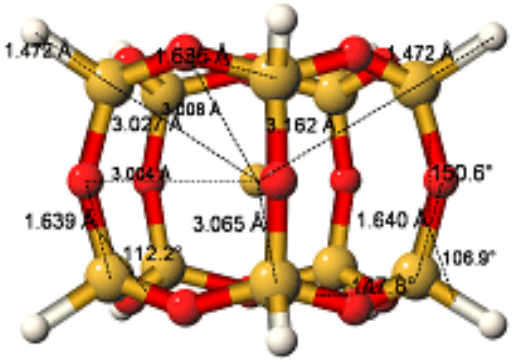

$F^{-}@(SiHO_{3/2})_{10}$

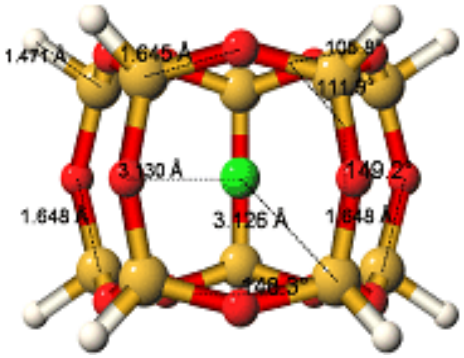

$Cl^{-}@(SiHO_{3/2})_{10}$

Figure 4.2 (continued)

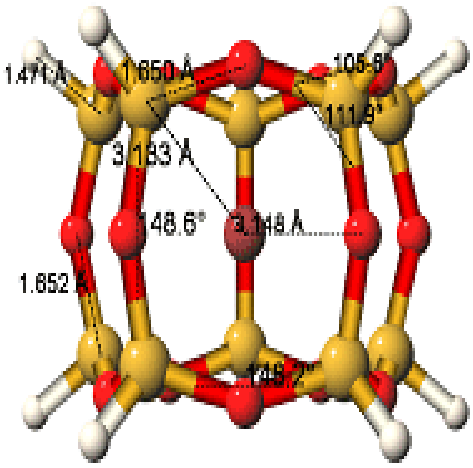

$Br^-@(HSiO_{3/2})_{10}$

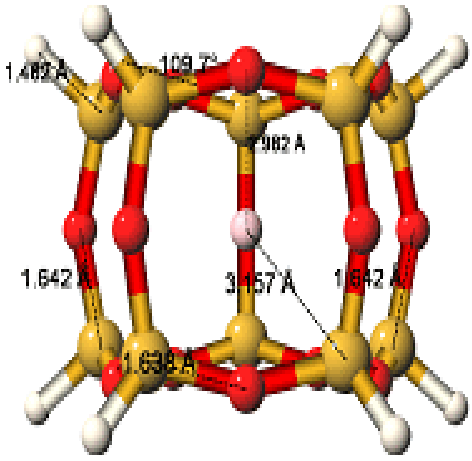

$He@(HSiO_{3/2})_{10}$

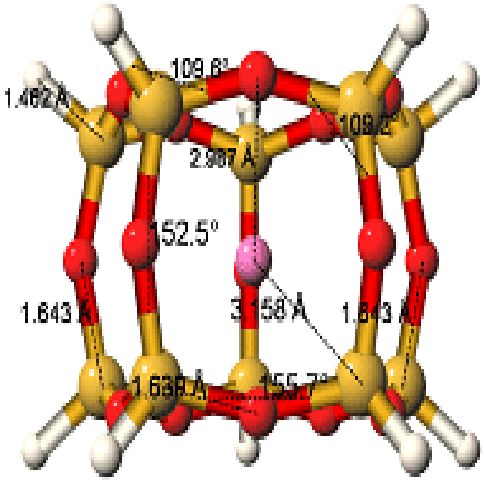

$Ne@(SiHO_{3/2})_{10}$

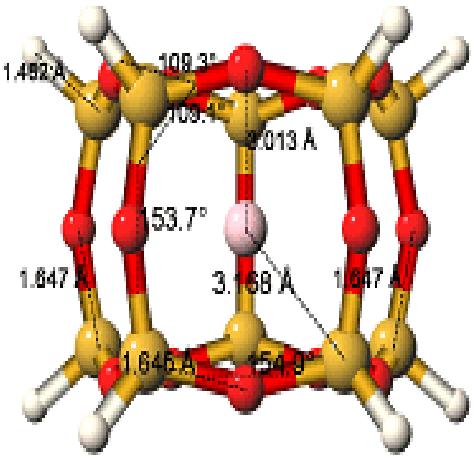

$Ar@(SiHO_{3/2})_{10}$

Figure 4.2 (continued)

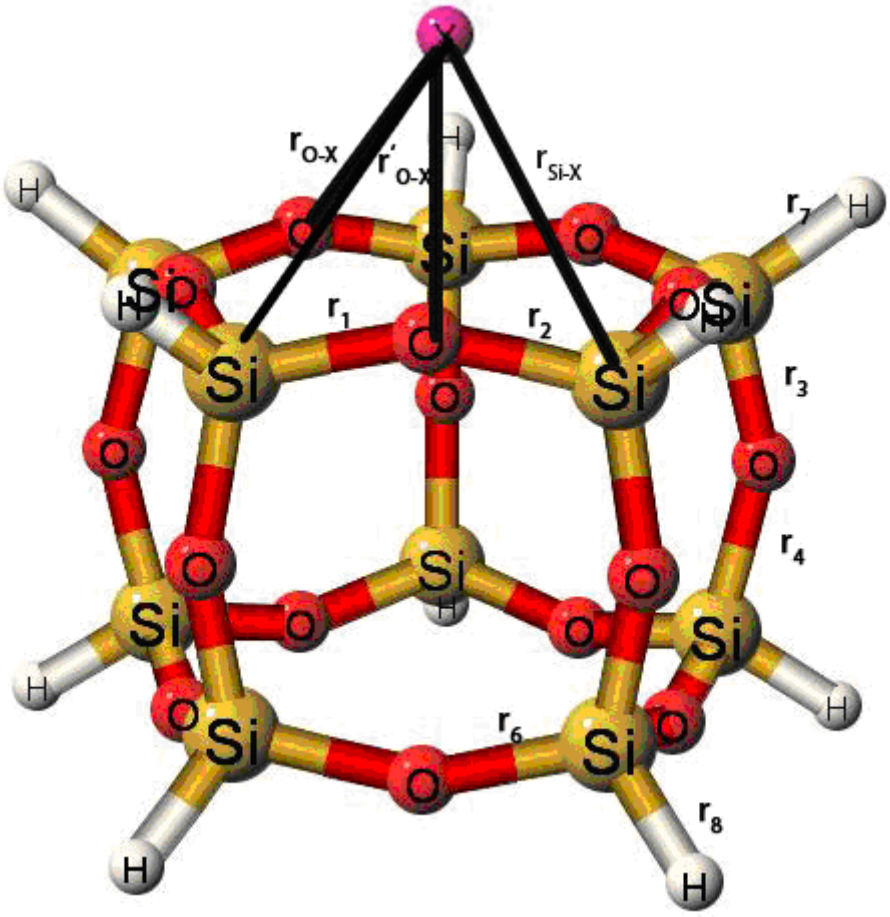

Figure 4.3 Schematic Representation of Exohedral $X(HSiO_{3/2})_{10}$ with D_{5h} Symmetry.

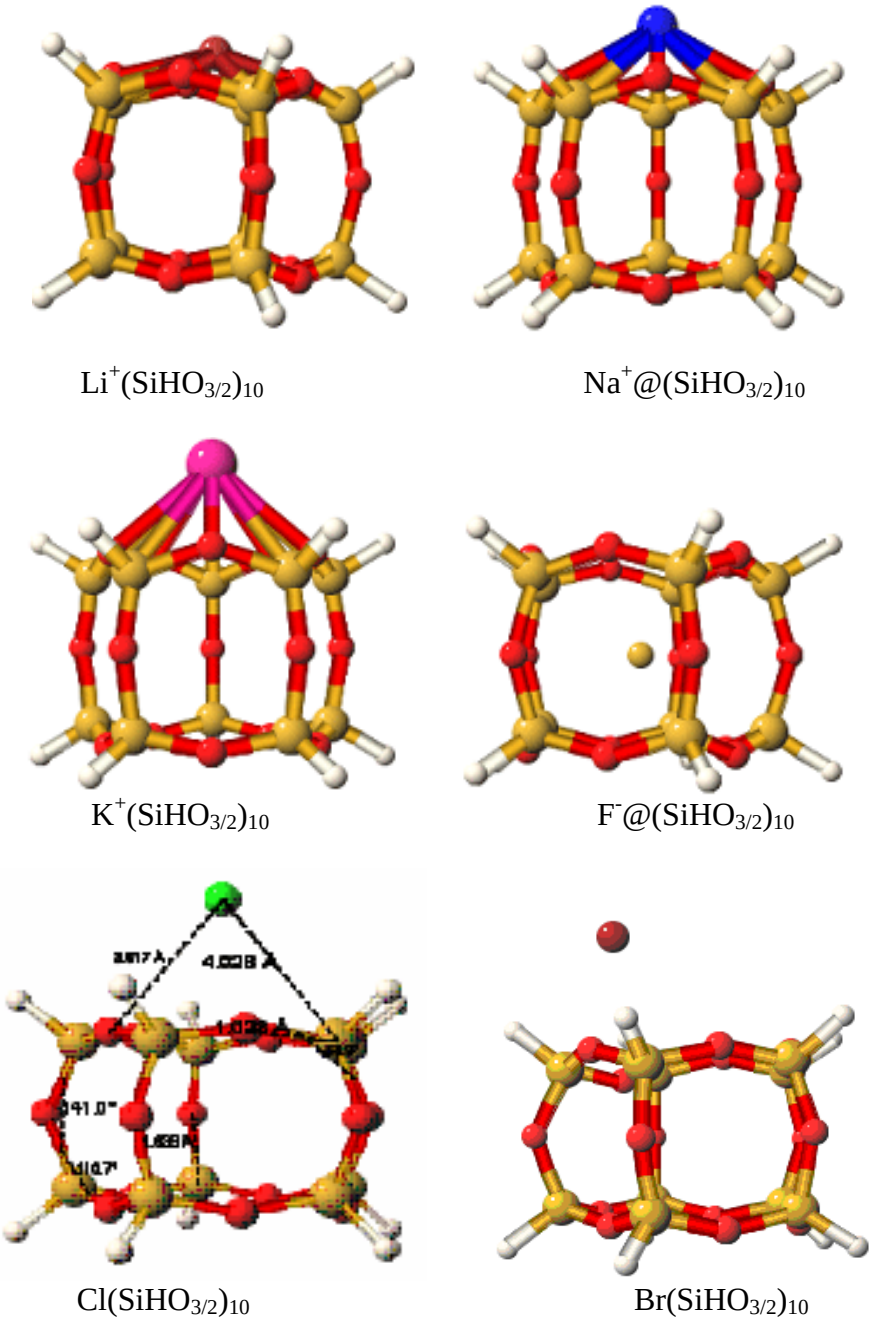

Figure 4.4 Optimized Geometry of Exohedral $X(HSiO_{3/2})_{10}$ with D_{5h} Symmetry at the B3LYP/6-311G(d,p).

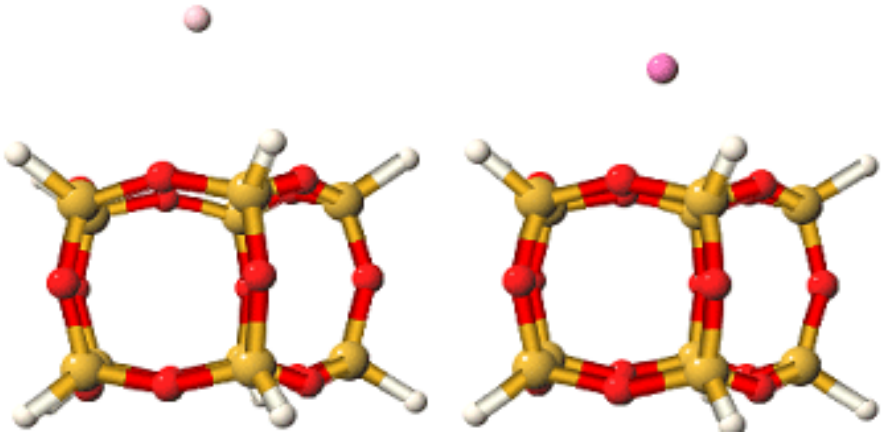

$He(SiHO_{3/2})_{10}$ $Ne@(SiHO_{3/2})_{10}$

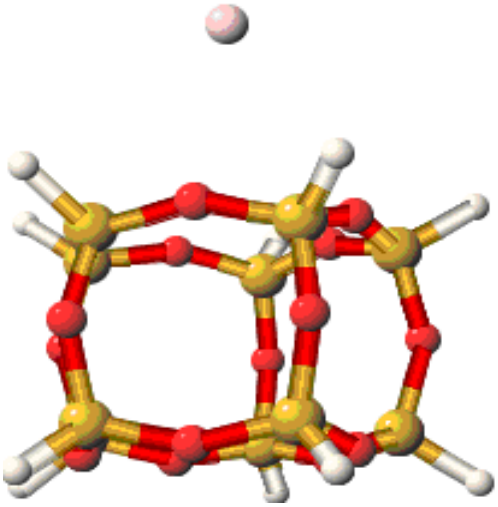

$Ar(SiHO_{3/2})_{10}$

Figure 4.4 (continued)

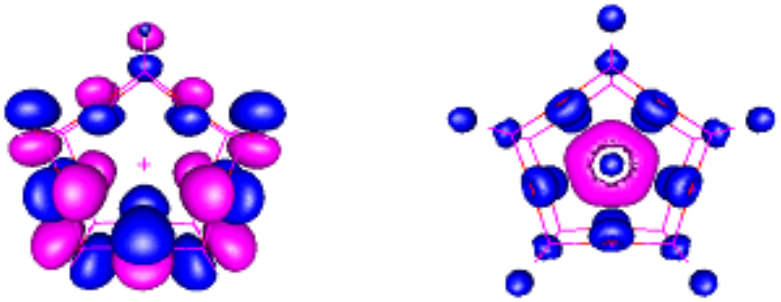

$Li^+@(SiHO_{3/2})_{10}$ HOMO $Li^+@(SiHO_{3/2})_{10}$ LUMO

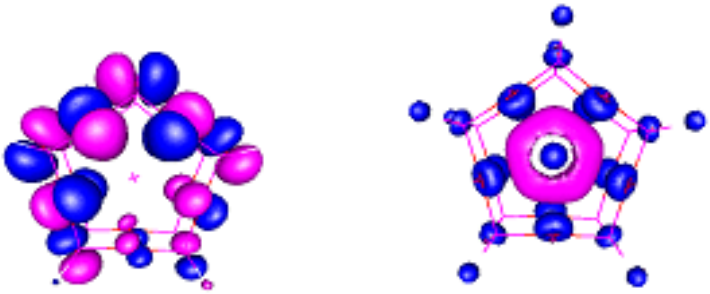

$Na^+@(SiHO_{3/2})_{10}$ HOMO $Na^+@(SiHO_{3/2})_{10}$ LUMO

$K^+@(SiHO_{3/2})_{10}$ HOMO $K^+@(SiHO_{3/2})_{10}$ LUMO

Figure 4.5. Orbital Pictures (dark: positive; light; negative values) for the HOMO and LUMO of the Host Cage $(SiHO_{3/2})_{10}$ and Representative Endohedral Complexes.

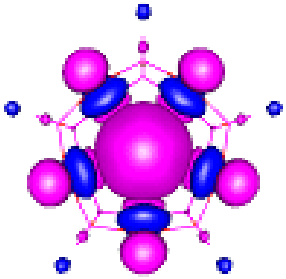

$Cl^-@(SiHO_{3/2})_{10}$ HOMO

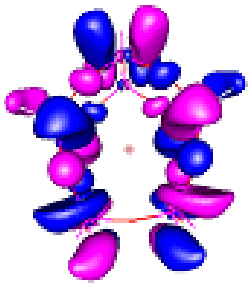

$Cl^-@(SiHO_{3/2})_{10}$ LUMO

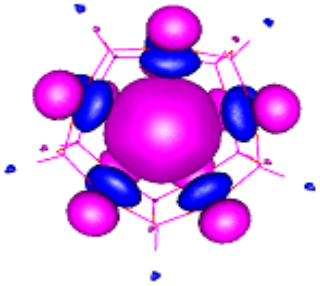

$Br^-@(SiHO_{3/2})_{10}$ HOMO

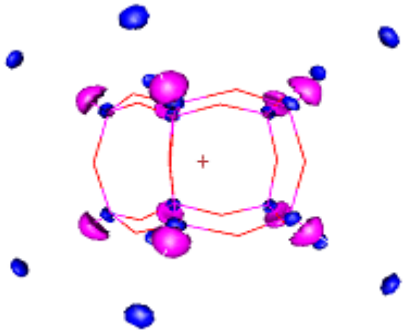

$Br^-@(SiHO_{3/2})_{10}$ LUMO

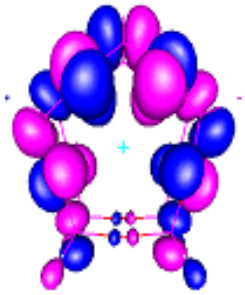

$He@(SiHO_{3/2})_{10}$ HOMO

$He@(SiHO_{3/2})_{10}$ LUMO

Figure 4.5. (Continued)

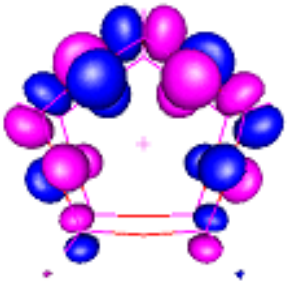

$Ne@(SiHO_{3/2})_{10}$ HOMO

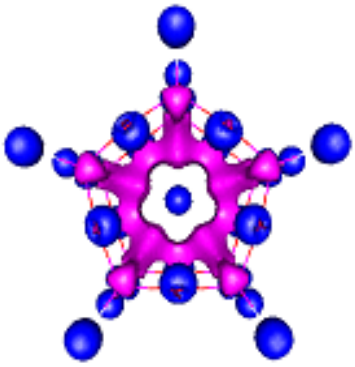

$Ne@(SiHO_{3/2})_{10}$ LUMO

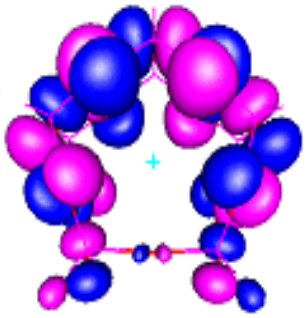

$Ar@(SiHO_{3/2})_{10}$ HOMO

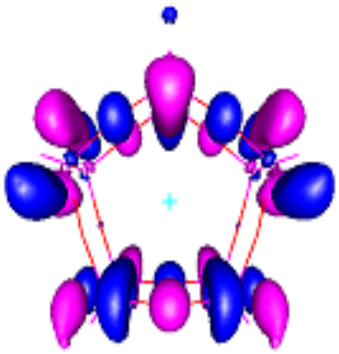

$Ar@(SiHO_{3/2})_{10}$ LUMO

Figure 4.5. (continued)

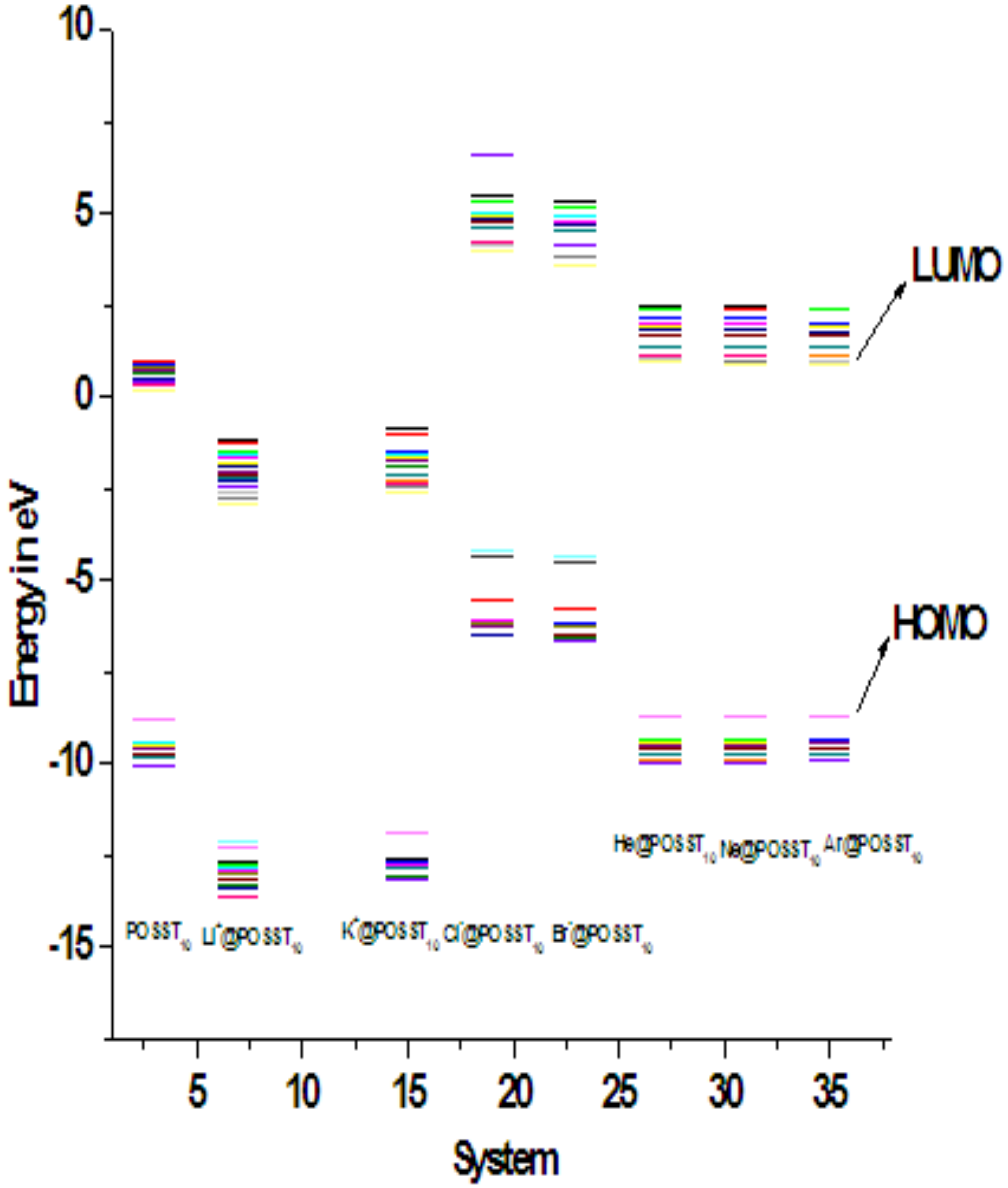

Figure 4.6 Khon-Sham Orbital Energy Diagram for $(HSiO_{3/2})_{10}$ and Endohedral Complexes. Only the Partial Orbital Energy Levels is Shown.

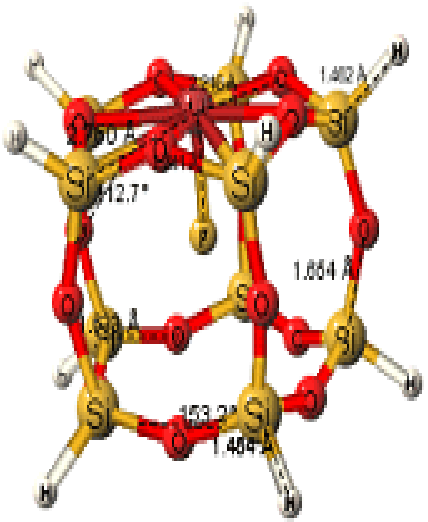

(a) $F^-@Li^+(SiHO_{3/2})_{10}$

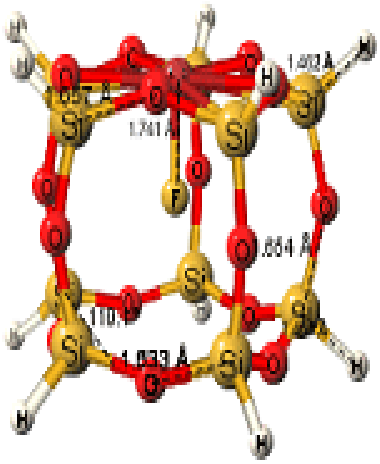

(b) $F^-@Li^+(SiHO_{3/2})_{10}$ (D5R)

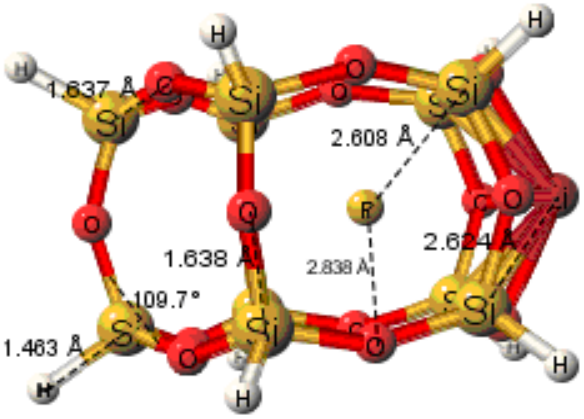

(c) $F^-@Li^+(SiHO_{3/2})_{10}$(D4R)

Figure 4.7 Optimized Geometries of $F^-@ Li^+(HSiO_{3/2})_{10}$ Ion pair at the B3LYP/ 6-311(d,p) Level. (a) $F^-@ Li^+(HSiO_{3/2})_{10}$, Placing both Li^+ and F^- Inside the Cage Center. b) $F^-@ Li^+(HSiO_{3/2})_{10}$, Placing Li^+ on D5R Surface and F^- Inside the Cage Center. (c) $F^-@ Li^+(HSiO_{3/2})_{10}$, Placing Li^+ on D4R Surface and F^- Inside the Cage Center.

CHAPTER V

STRUCTURES AND STABILITIES OF ENDO- AND EXO-DODECAHEDRAL SILSESQUIOXANE (T_{12}-POSS) COMPLEXES

Introduction

The polyhedral oligomeric silsesquioxanes (POSSs) are important nanostructured hybrid inorganic-organic chemicals. The building block of H-silesquioxanes is the monomer unit ($HSiO_{3/2}$), which is designated by the letter T. The structures of POSS compounds are based on siloxane-containing cages that are formed from ($HSiO_{3/2}$) or ($RSiO_{3/2}$) units. The general formula of POSS is defined as $(RSiO_{3/2})_{2n}$ where R denotes a hydrogen, organic or inorganic ligands. [1] Dodecasilsesquoixane, $(HSiO_{3/2})_{12}$ (denoted as T_{12}-POSS) consists of 12 silicon atoms that are connected to each other through intervening oxygen atoms and a single hydrogen is attached to each silicon. According to Agaskar and Klemperer[2] the nomenclature of a POSS is given by a topological descriptor $\{r^s.....t^u\}$, which indicates the number of s- and r-membered rings (faces) that comprise the polyhedron T_n. For example, the T_{12}-POSS cage D_{6h} isomer is defined as $\{6^2 5^0 4^6\}$(two six-membered no five-membered and six four-membered rings). Polyhedral oligomeric silsesquioxanes (POSSs) and their derivatives have been widely incorporated

into organic polymers, dendrimers, and zeolites over the last decade because of the

variety of applications in materials science and catalysis.[1,3-12] POSS has also emerged as a viable filler in high performance nanocomposites.[13] POSS polymer nanocomposites are substantially harder than the unfilled polymers.[14] POSS cage incorporation into the polymeric materials enhances certain properties such as glass transition temperatures (T_g), decomposition temperatures and mechanical strengths.[15-18] In POSS-PEO-based polymer electrolytes, POSS acts as an inhibitor of polyethylene oxide (PEO) crystallization. Because of their nanostructured nature and their ceramic-like properties (creep, oxidation resistance), POSSs are being used for synthesis of polymer-derived ceramics.[19] Metal containing siloxanes, and oligomettalla-silosesquioxanes are used homogeneous catalysts in olefin processing. Metathesis and alkene epoxidation are easily accomplished with certain POSS catalysts.[20-24] POSS is also used as a support for Ziegler-Natta catalysts.[25] Coupar et al[26] has reported dendrimer catalysts based on POSS cores. These materials are expected to combine the traits of homogeneous catalysts with the high activity and precise control of catalytic sites normally associated with homogeneous catalysts. Murfee et al[27] reported that metallodendrimers with a diphenylphosphino-POSS core and Ru-based chromophores exhibit unique advantages. Liquid crystalline silsesquioxane dendrimers exhibiting both chiral nematic and columnar mesophases has been synthesized by Saez et al.[28]

The cage-like structures of POSS chemicals makes them useful for separating gas mixtures as has been observed in siloxanes and and silicon-based capillary membranes.[29,30] Poly(dimethylsiloxane) is more permeable to oxygen[31] than to nitrogen

and is used to separate N_2/O_2 mixtures.[32] Cationic polyhedral oligomeric silsesquioxane (POSS) units can serve as carriers and potential drug delivery agents.[33]

Xiang *et al*[34] studied the structural and electronic properties of different polyhedral H-silsesquioxanes (T_n-POSS, n = 8, 10, 12). Cheng *et al*[35] reported the linear and non-linear optical properties of H-silsesquioxanes. Space filling models of such cages indicate there is a void at the center of these molecules. Could this space be filled with endohedral atomic or molecular species? Pach and Stosser[36] have suggested that γ-radiation of octaalkyloctasilsesquioxane $(RSiO_{3/2})_8$ or octatrialkylsiloxyoctasilsesquioxane $(R_3SiO_{3/2})_8$ leads to hydrogen-encapsulated within the T_8 cage. ESR spectroscopy showed that the endohedral hydrogen originated from the peripheral substituents.

The presence of exohedrally or endohedrally captured cations can play a decisive role in both the structural and catalytic behavior of microporous solids.[37] Hence, physical scientists have been fascinated with the concept of incarcerating atoms, ions, and or molecules within a molecular framework. Cage molecules with endoheral atoms and ions are important both theoretically[38-43] and practically.[44-47] Endohedral cage complexes have potential applications as magnetic resonance imaging contrast agents,[48] semiconductors and ferromagnets.[49] Saunders et al used helium atoms and NMR to probe the internal electronic and magnetic environments of fullerene cages.[50]

Most of the previous experimental studies have been limited to studies of the T_8-POSS cage. Bassindale *et al*[51] recently synthesized the fluoride-ion encapsulated T_8-silsequioxane complex. Using local density (LDR) techniques Catlow and George[37]

investigated theoretically the electronic and structural effects of Na^+, F^- and OH^- incorporation into the hydroxyl group-substituted D4R silsesquioxanes. Gordon and Tejerina[52] investigated the mechanism for inserting N_2 and O_2 into T_n-POSS (n = 8, 10, 12)-silsesquioxane framework theoretically. Allen and Beers[53] investigated the binding strengths of T_8-POSS-cation complexes by *ab initio* methods. Recently, we[54] investigated the structural and electronic properties of endohedral $X@(SiHO_{3/2})_n$ and exohedral $X(SiHO_{3/2})_n$ (n = 8 and 10; X= Li, Na, K, F^-, Cl^-, Br^-, He, Ne and Ar) complexes.[54] Encapsulation of alkali metals, their ions, halide anions or noble gases into the POSS cage can change the POSS cage properties significantly.

The internal cavity of the T_{12}-POSS cage is larger than that of the T_8-POSS or T_{10}-POSS cages. While theoretical and experimental reports on endohedral and exohedral T_8-POSS and T_{10}-POSS complexes exist, studies of endrohedral or exohedral complexes of T_{12}-POSS are still in the preliminary stage. Is the T_{12}-POSS stable when different cation or anions are incorporated into this cage? What interactions may exist between an incorporated ion or atom with the atoms of the T_{12}-POSS skeleton? Little information exists regarding these questions. Thus, T_{12}-POSS is an ideal candidate for theoretical studies to compare with T_8 and T_{10}-POSS since all these are now commercially available. Herein, we present our *ab initio* computations of the geometries, energies, stabilities and the electronic properties of the endohedral $X@(HSiO_{3/2})_{12}$ and exohedral $X(HSiO_{3/2})_{12}$ complexes with different atomic and ionic species.

T_{12}-POSS compounds might exist as several isomers. Tejerina et al [55] investigated the twelve possible T_{12}-POSS structures. The most stable isomers have D_{2d}, D_{6h} and T_d

symmetries. The D_{2d}, D_{6h} and T_d structures are denoted as $\{4^55^4\}$, $\{4^66^2\}$ and $\{3^46^4\}$ topologies, respectively. The T_d isomer contains three-member rings and was predicted to be unstable.[56] Hence the possible stable isomers for T_{12}-POSS are D_{2d} and D_{6h}. The energy difference between D_{2d} symmetry with $\{4^55^4\}$ topology and D_{5h} and T_d isomers, with $\{4^66^2\}$ and $\{3^46^4\}$ topologies, obtained at the HF level theory are 4.7 kcal/mole and 16.3 kcal/mole respectively. [55] Using the HF level of theory, Earley [56] estimated the energy difference between D_{2d} and D_{6h} isomers to be 2.6 kcal/mole. The D_{2d} isomer was found to be 1 kcal/mol stable than that of D_{6h} isomer using MP2 theory. The only experimental structure of T_{12}-POSS has D_{2d} symmetry, determined by X-ray diffraction. [57] The only isomer detected in solution had D_{2d} symmetry ($\{4^55^4\}$ topology) based on ^1H and ^{29}Si NMR studies.[2,58,59] The D_{6h} isomer can be described as a double six-member ring and is observed as a secondary building block in solid-state geolites. In the present investigation, the D_{2d} isomer is predicted to be more stable (5.3 kcal/mol) than the D_{6h} isomer at the B3LYP/6-311G(d,p) level of theory. This finding is consistent with previous experimental and theoretical results. Hence, structure with D_{2d} symmetry is considered to be the realistic one and all the model calculations were based on D_{2d} symmetry with $\{4^55^4\}$ topology and D_{6h} symmetry with $\{4^66^2\}$ topology.

Computational Details

All the calculations were performed using density functional theory (DFT/B3LYP).[60,61] We used 6-311G(d,p) and 6-311++G(2d,2p), basis sets to optimize the geometry and calculate the vibrational frequencies for the T_{12}-POSS system. These basis sets are also used for the geometry optimization and frequency calculation of the

endohedral X@T_{12}-POSS complexes (X= Li^+, Na^+, K^+, He, Ne, Ar, F^-, Cl^-, Br^-). Including diffusion functions in the basis set 6-311G(d,p) i.e. 6-311++G(2d,2p) did not change the results significantly. Hence, all calculations on the exohedral complexes (XT_{12}-POSS) were performed using the 6-311G(d,p) basis set. Considering ease of use, error tolerance and energy discrepancies among the different basis sets, both 6-311G(d,p) and 6-311++G(2d, 2p) are considered a good choice. Gaussian 03[63] and PQS[64] programs were used to perform the calculations.

The atoms or ions were introduced into the center of T_{12}-POSS cage and geometry optimizations were performed (Figures 5.1 and 5.2). The atoms and ions were situated outside of the 6DR (D_{6h}) and the 5DR (D_{2d}) faces for optimizations of the exohedral complexes geometries. NBO calculations were performed to obtain the electronic properties. The optimized energy of the cation or anion was calculated in order to obtain the inclusion and binding energies. The sum of the energies of the atom or ions, E_x, plus the optimized energy of $(HSiO_{3/2})_{12}$, E_{cage}, was subtracted from the optimized energy of the exohedral complexes, E_{exo}, to give the binding energy, E_{bind}. The same level of theory was used to obtain E_x and E_{cage}. The inclusion energies, E_{inc} (kcal/mol), of the endoheral complexes were evaluated by substracting the sum of the energies of the isolated species from the energy of X@$(HSiO_{3/2})_{12}$ (E_{endo}). The isomerization energy ΔE_{iso} was defined as the energy difference between the exohedral complex's energy and that of its corresponding endohedral complex. The values of E_{inc}, E_{bind} and E_{iso} are represented by:

$$E_{inc} = E_{endo} - (E_{cage} + E_x)$$

$$E_{bind} = E_{exo} - (E_{cage} + E_x)$$

$$\Delta E_{iso} = E_{exo} - E_{endo}$$

All energies were corrected using the unscaled zero point energy.

The vibrational harmonic frequencies of $(HSiO_{3/2})_{12}$, $X@(HSiO_{3/2})_{12}$ and $X(HSiO_{3/2})_{12}$ were computed for all optimized structures using the same levels of theory, to characterize the stationary points as minima (zero imaginary frequencies) or saddle points (one imaginary frequency). The NMR shielding tensors for selected systems were calculated using B3LYP/6-311G (d,p) and GIAO methods.[65-68] The electronic properties, atomic charges and electronic configurations were evaluated using natural bond orbital analysis (NBO).[69]

The BSSE was checked by the Boys-Bernardi counterpoise method.[70] The BSSE energy was only 0.03 kcal/mole for $He@(HSiO_{3/2})_{12}$ system using B3LYP/6-311(d,p). This is negligible. Previously we found that the basis set superposition errors were significant for endohedral T_8-POSS complexes[54] but this did not change the general trends. Hence, the calculation of basis set superposition errors (BSSE) was ommited to avoid expensive and time-consuming computations.

Results and Discussions

Geometries

POSS cage: Table 5.1 and 5.4 summarizes the results of geometries, the optimized bond lengths and bond angles for the D_{2d} isomer of T_{12}-POSS and its endohedral $X@T_{12}$-POSS complexes, calculated at the B3LYP/6-311(d,p) and B3LYP/6-311++G(2d,2p) level. The accuracy of the calculated geometries of $(HSiO_{3/2})_{12}$ molecule in the can be assessed by

comparison the x-ray crystal structure of the D_{2d} isomer.[57,71] The molecule was found to have approximate D_{2d} symmetry, with Si-O bond lengths ranging 1.582-1.617 Å. In the calculations conducted herein, the Si-O bond lengths range from 1.630 to 1.642 Å.

Comparison of the calculated structure of the D_{6h} $(HSiO_{3/2})_{12}$ isomer with experimental results is not possible because D_{6h} isomer has never been isolated. However, the calculated structures of both D_{2d} and D_{6h} isomers can be compared with other theoretical results. The bond lengths and angles obtained here agree well with previous experimental[71] and theoretical[52,72] results. de Man and Sauer calculated a Si-O distance of 1.64 Å using HF split-valence plus polarization.[72] Tossell predicted a Si-O distance of 1.64 Å using HF/6-31G* calculations.[73] Xiang *et al*. have studied the molecular and electronic structure of T_n-POSS compounds (n even, 4-16) using DFT with a double-ζ basis set and predicted a Si-O distance of 1.64.[34] Using LDA-DFT with an effective core potential(ECP), Pasquarello et al.[74] obtained a Si-O distance of 1.62 Å, the same as experimental X-ray diffraction values (Si-O, 1.62 Å). The Si-O distances in both D_{2d} and D_{6h} isomers (Tables 5.1 and 5.2) obtained by the B3LYP/6-311G (d,p) method are in good agreement with previous experimental and calculated values.

Endohedral T_{12}-POSS complexes

The alkali metals Li, Na, K and their ions were placed at center of the D_{2d} $(HSiO_{3/2})_{12}$ isomer and then optimized (Figure 5.1). Geometry optimizations were performed enforcing D_{2d} symmetry, and the optimized geometries of these complexes are shown in Figure 5.2. These geometries are minima except for $K^+@(HSiO_{3/2})_{12}$ and $F^-@(HSiO_{3/2})_{12}$. The D_{2d} form of the $K^+@(HSiO_{3/2})_{12}$ complex has four imaginary

frequencies and $F^-@(HSiO_{3/2})_{12}$ has one imaginary frequency. No further attempts were made to obtain minima for these structures.

The optimized D_{6h} structure of the endohedral complexes are shown in Figure 5.5. The optimized structure of the endohedral $X@(HSiO_{3/2})_{12}$ (X= Cl^-, Br^-, He, Ne and Ar) complexes are minima. However, D_{6h} form of $Li^+@(HSiO_{3/2})_{12}$ has nine, $Na^+@(HSiO_{3/2})_{12}$ has seven, $K^+@(HSiO_{3/2})_{12}$ has three, and $F^-@(HSiO_{3/2})_{12}$ has two imaginary frequencies. Changing the coordinate in certain directions in the $Li^+@(HSiO_{3/2})_{12}$ and $Na^+@(HSiO_{3/2})_{12}$ gives structures which were minima on the potential energy surface (Figure 5.5).

Tables 5.1 and 5.4 show selected X-Si and X-O distances for Li^+, Na^+, and K^+ encapsulated complexes of T_{12}-POSS D_{2d} isomer at the B3LYP/6-311G(d,p) and B3LYP/6-311++G(2d,2p), respectively. Upon insertion of alkali metal ions, the cage size is contracted. The X-Si and X-O distances increase in the order $K^+ > Na^+ > Li^+$. The 1.636 Å Si-O distances in $(HSiO_{3/2})_{12}$ increased to 1.648 Å, 1.646 Å and 1.644 Å after insertion of Li^+, Na^+, K^+, respectively, into the $(HSiO_{3/2})_{12}$. The two different Si-O lengths, 1.637 Å and 1.642 Å, of $(HSiO_{3/2})_{12}$ decreased in the $X^+@(HSiO_{3/2})_{12}$ (Li^+, Na^+) complexes but remain unchanged in the $K^+@(HSiO_{3/2})_{12}$ complex. The 1.463 Å Si-H distances in $(HSiO_{3/2})_{12}$ decreased to 1.456 Å in $Li^+@(HSiO_{3/2})_{12}$ and 1.457 Å in $X@(HSiO_{3/2})_{12}$ (Na^+, K^+). The Si-H distance of 1.464 Å in $(HSiO_{3/2})_{12}$ decreased to 1.459 Å in both $Li^+@(HSiO_{3/2})_{12}$ and $Na^+@(HSiO_{3/2})_{12}$ and to 1.458 Å $K^+@(HSiO_{3/2})_{12}$. The changes in bond distances and angles depend on the endohedral cation's size. The cage size contracts upon cation insertion because of the attractive interaction. In addition, the Si-O and Si-H

bond lengths shorten when hosting an alkali metal cation versus its corresponding neutral metal. For example, The Si-H bond lengths in endohedral Li@$(HSiO_{3/2})_{12}$ are 1.461° while that of Li^+@$(HSiO_{3/2})_{12}$ is 1.457A°. The Si-H bond shortens in Li^+@$(HSiO_{3/2})_{12}$ because the electron donation from cage atoms to alkali cations causes an increase in *s* character in the Si-H bonds. Selected bond angles of $(HSiO_{3/2})_{12}$ and its Li^+, Na^+ and K^+ endohedral complexes are shown in Table 5.1. In almost all endohedral cation complexes, the bond angle decreased relative to the parent $(HSiO_{3/2})_{12}$ cage bond angles. However, the 109.3° OSiO bond angle in $(HSiO_{3/2})_{12}$ increased to 109.7° in Li^+@$(HSiO_{3/2})_{12}$ and 109.6° in K^+@ $(HSiO_{3/2})_{12}$ but decreased to 109.1° in Na^+@ $(HSiO_{3/2})_{12}$.

Encapsulation of alkali metal ions into the D_{6h} $(HSiO_{3/2})_{12}$ isomer pulls the oxygen atoms inwards strongly. The Si atoms move slightly outwards. The Si-O bond lengths are increased. However, the Si-H bond lengths decreased compared to the pure cage. The 109.3º OSiO angle in pure cage decreased significantly due to Li^+, Na^+ and K^+ encapsulation (Tables 5.2 and Table 5.6). Overall, the cage shriks for alkali metal encapsulation into the D_{6h} $(HSiO_{3/2})_{12}$ isomer.

Anions: Insertion of halide anions into $(HSiO_{3/2})_{12}$ changes bond lengths and bond angles (Tables 5.2 and 5.4). The framework oxygen to halide distances (X-O) increased as the size of the halide increases. For example, the (X-O) distance have values 3.182A°, 3.216A°, 3.229A° for X=F^-, Cl^-, and Br^- inclusion into the D_{2d} isomer respectively. The X-Si distances increased with an increase in the endohedral anion's size. These bond lengths range from 2.757 to 2.859 Å going from F^- to Br^-. The X-O distances also

increased with increasing halide size. The Si-O distance in $(HSiO_{3/2})_{12}$ (1.636A°) changed slightly to 1.630A° (F^-), 1.634A° (Cl^-) and 1.635A° (Br^-), respectively, after halide insertion. The Si-H bonds lengthen slightly due to insertion of anions. The lengthening of Si-H bonds indicates that the *s* character of the bond decreased. After halide insertion, bond angle effects are more pronounced and mixed. Insertion of halides caused the five different Si-O-Si angles, 109.3°, 107.4°, 109.6°, 109.2°, 109.3° of T_{12}-POSS cage to increase to 112.7°, 111.4°, 113.9°, 110.5°, 111.9° for $F^-@(HSiO_{3/2})_{12}$ and to 113.7°, 111.1°, 114.8°, 110.3°, 112.1° for $Cl^-@(HSiO_{3/2})_{12}$. Finally, these Si-O-Si angles were 113.9°, 110.9°, 114.9°, 110.2°, 112.2° for $Br^-@(HSiO_{3/2})_{12}$ complexe. Furthermore, the Si-O-Si angle 150.9° in T_{12}-POSS closed to 148.4°, 148.7° and 149.1° for $X@(HSiO_{3/2})_{12}$ (X = F^-, Cl^-, Br^-) complexes, respectively. Halide encapsulation caused the T_{12}-POSS cage's Si-O bond lengths and O-Si-O bond angles to increase. The Si-O-Si bond angles decreased. The cage size increases as the size of encapsulated anion size increases due to cage atom-halide ion repulsions.

Encapsulation of halides into the D_{6h} $(HSiO_{3/2})_{12}$ isomer pushes the oxygen atoms outwards and pushes the Si atoms inwards. Effect on the Si-O bond lengths is negligible. However, the Si-H bond lengths increase significantly compare to the pure cage (Table 5.2 and 5.6). The 109.3° OSiO angle in pure cage increased to 112.7, 113.2 and 113.6° for F^-, Cl^- and Br^- encapsulation, respectively (Table 5.2).

Noble Gases: The optimized geometries of the endohedral $X@(HSiO_{3/2})_{12}$ (X = He, Ne, Ar) complexes obtained from D_{2d} isomer are shown in Table 5.2. The X-Si distances increase in the order Ar > Ne > He. The X-O distances are 3.570Å, 3.570Å and

3.574 Å, for He, Ne, and Ar, respectively (Tables 5.1 and 5.4). The larger the radius of the noble gas, the greater the internal repulsions become. But the resulting cage expansions are not large in this series. Insertion of He, Ne or Ar has almost no effect on the Si-H bond lengths. The Si-O bond distances in $X@(HSiO_{3/2})_{12}$ (X= He, Ne) are almost the same as the parent cage. However, Si-O distances increase slightly in $Ar@H_{12}Si_{12}O_{18}$ complexes. Encapsulation of noble gases changes some of the cage bond angles significantly. The OSiO angle of 109.3° in $(HSiO_{3/2})_{12}$ changed to 109.7° (He), 109.8° (Ne), 110.2° (Ar). The OSiO angle of 104.4° in $X@(HSiO_{3/2})_{12}$ (X = He and Ne) remain unaltered but increased to 109.9° in $Ar@(HSiO_{3/2})_{12}$ complex. The Si-O-Si angle, 150.9°, in $H_{12}Si_{12}O_{18}$ decreased to 150.2° in the $X@(HSiO_{3/2})_{12}$ (X=He, Ne) complexes and to 148.6° in $Ar@(HSiO_{3/2})_{12}$. The parent cage's OSiO angle (109.6°) increased slightly to 109.7° in $X@(HSiO_{3/2})_{12}$ (X=He, Ne) complexes and to 110.4° in $Ar@(HSiO_{3/2})_{12}$. The Si-H bond lengths were constant at 1.64Å in the $X@T_{12}$-POSS (X = He, Ne, Ar) complexes, demonstrating negligible electron transfer had occurred between the guest He, Ne and Ar atoms and the cage framework. This was also evident from the atomic charges and electronic configurations.

Encapsulation of He, Ne and Ar into the D_{6h} T_{12}-POSS isomer has no significant effects on the $(HSiO_{3/2})_{12}$ cage structure (Tables 5.2 and 5.6). There is no strong interaction between He (or Ne) and the cage framework as evident from the charge on encapsulated He and Ne atoms and the bond lengths and bond angles. The small changes in the cage size and geometric parameters for Ar encapsulation are due to the small polarization of charge between Ar and cage framework and the large size of Ar.

Exohedral Clusters X@$(HSiO_{3/2})_{12}$

Tables 5.9 and 5.10 summarize selected geometric parameters, total energies, zero-point energies, lowest frequencies and zero-point corrected exohedral binding energies for the optimized exohedral $(HSiO_{3/2})_{12}$ D_{2d} and D_{6h} complexes, respectively. The guests were alkali metal cations, halides and noble gases. The bond designations used in Table 5.9 and 5.10 are illustrated in Figures 5.7 and 5.8 respectively. The optimized structures for exohedral complexes are shown in Figure 5.5 and 5.6 respectively. Exohedral complexation removes the high host cage D_{2d} symmetry. The optimized structures of exohedral complexes of D_{2d} $(HSiO_{3/2})_{12}$ with $Na^{+,}$ K^+ and Ne have C_s symmetry. All the remaining exohedral complexes of D_{2d} $(HSiO_{3/2})_{12}$ in their optimized structure has C_1 symmetry.

In the Li^+, Na^+ and K^+ exohedral complexes of D_{2d} $(HSiO_{3/2})_{12}$ the alkali cation is attached to a D5R face of D_{2d} $(HSiO_{3/2})_{12}$ Figure (5.5). The X-Si and X-O distances in endohedral X@$(HSiO_{3/2})_{12}$, where X = Li^+, Na^+ and K^+, are nearly equal to the distances in the corresponding exohedral systems. In the $Li^+(HSiO_{3/2})_{12}$ complex the Li^+ is joined four oxygen and five silicon atoms on a D5R face. Whereas in the $Na^+(HSiO_{3/2})_{12}$ and $K^+(HSiO_{3/2})_{12}$ complexes, both the Na^+ and K^+ ions are joined with five oxygen and five silicon atoms on a D5R face of D_{2d} $(HSiO_{3/2})_{12}$ isomer, respectively. The Si-O distances in the face adjacent to the alkali ion and in the opposite face change slightly.

The geometrical features of the exohedral complexes $X^-(HSiO_{3/2})_{12}$ (X = F^-, Cl^- and Br^-) obtained from the D_{2d} $(HSiO_{3/2})_{12}$ isomer differ from each other significantly. $F(HSiO_{3/2})_{12}$ and $Br^-(HSiO_{3/2})_{12}$ complexes both have the halide attached to one of the Si

atoms of the host cage. The $F^-@(HSiO_{3/2})_{12}$ structure changed slightly compared to the original $(HSiO_{3/2})_{12}$. However, the $Br^-(HSiO_{3/2})_{12}$ structure deformed significantly as shown in Figure 5.4. In contrast to the exohedral F^-, and Br^- complexes the chloride in exohedral $Cl^-(HSiO_{3/2})_{12}$ did not bond directly to Si atoms of the host cage. The Cl^--Si and Cl^-O distances are 3.313 and 3.861Å respectively. The Cl^- and a host cage's D5R face appear to the bound to each other by a weak attractive force.

The exohedral complexes of the D_{2d} $(HSiO_{3/2})_{12}$ isomer with noble gases guests, He, Ne and Ar, are shown in Figure 5.4. The X-O and X-Si distances in $X(HSiO_{3/2})_{12}$ with X = He and Ne are nearly similar to the distances in their corresponding endohedral systems. The Ar-O and Ar-Si distances in $Ar(HSiO_{3/2})_{12}$ are considerably larger than the distances in $Ar@(HSiO_{3/2})_{12}$. The He, Ne and Ar did not bind to the host cage's D5R face directly. The interaction between the host cage D5R face and Ar is weak and has no significant effects on host cage geometry. On the other hand the interaction between host cage's D5R face and He and Ne are strong. In the $He(HSiO_{3/2})_{12}$ complex no significant changes occur in the cage's geometrical structure compared to the parent cage. However, a significant change in cage shape occurred in $Ne(HSiO_{3/2})_{12}$. Some of the cage framework oxygen atoms pull inward. The cage is deformed slightly and shrinks.

Exohedral complexation removes the host cage high D_{6h} symmetry. Specifically, the initial geometry of exohedral complexes of the D_{6h} T_{12}-POSS isomer had C_{6v} symmetry. The exohedral complexes of D_{6h} $(HSiO_{3/2})_{12}$ with Na^+, K^+, Ne and Ar retain C_{6v} symmetry in the optimized structure. However, the optimized structure in $X(HSiO_{3/2})_{12}$ (X = Li^+, Cl^-, Br^- and He) has C_1 symmetry. The Si-X bond lengths in the

exohedral $X(HSiO_{3/2})_{12}$ complexes are X = Li^+(2.781 Å), Na^+(3.341 Å) and K^+ (3.633 Å) (Table 5.10). These distances are similar to those predicted in the respective endohedral complexes. The Si-X and O-X distances, respectively, are much longer (from 3.452 to 4.966 Å) for the exohedral halide complexes. The exohedral Si-X and O-X distances to He, Ne, Ar were also very large (3.236-5.076 Å) demonstrating that the D6R face of host cage and noble gases are only weekly bound. These weak interactions are probably caused by BSSE. The exohedral complex of He is hardly distinguishable from its isolated species.

Inclusion Energies

The total energy and the ZPE-corrected endohedral inclusion energies (E_{inc}) for the $X@(HSiO_{3/2})_{12}$ complexes (X= He, Ne, Ar, Li^+, Li, Li^-, Na^+, Na, Na^-, K^+, K, K^-, F^-, Cl^-, Br^-) obtained from the D_{2d} isomer are reported in Tables 5.3 and 5.4. Those from the D_{6h} isomer appear in Tables 5.5 and 5.6. The inclusion energies obtained from both B3LYP/6-311G(d,p) and B3LYP/6-311++(2d,2p) level calculations reveal that $Li^+@(HSiO_{3/2})_{12}$, $Na^+@(HSiO_{3/2})_{12}$, $K^+@(HSiO_{3/2})_{12}$, $F^-@(HSiO_{3/2})_{12}$, $Cl^-@(HSiO_{3/2})_{12}$, $Br^-@(HSiO_{3/2})_{12}$, $He@(HSiO_{3/2})_{12}$ and $Ne@(HSiO_{3/2})_{12}$ have lower energy than the corresponding separated species. These endohedral complexes are more stable than their precursors. Including the diffusion function into 6-311G(d,p), i.e. 6-311++(2d,2p) basis set, did not improve the results significantly.

The inclusion energies for the endohedral complexes prepared from the D_{2d} and D_{6h} $(HSiO_{3/2})_{12}$ isomers with halides follow the trend $F^- > Cl^- > Br^-$. The stability order for encapsulation of alkali metal ions and noble gases into the D_{2d} and D_{6h} isomers of

$(HSiO_{3/2})_{12}$ are $Li^+ > Na^+ > K^+$ and He > Ne > Ar respectively. The size of the embedding ion is an important factor inflencing the stability of the endohedral complexes. The strain energy increases upon increasing the size of the embedded ions or atoms. Values of E_{inc} (Tables 5.3, 5.4 5.5 and 5.6) increase as the atomic number (hence size) of X decreases within its periodic table group. Large differences between the atomic charges of similar sized guests exist and these are shown in Tables 5.7 and 5.8. This suggests that charge transfer from the encapsulated species to the host cage determines the magnitude of E_{inc} in the absence of size effects. It is worthwhile mentioning that the endoheral complexes obtained from D_{6h} isomer are thermodynamically more stable than the corresponding complexes obtained from the D_{2d} isomer. These results are in contrast to the stability of respective parent cages where the D_{2d} cage is more stable than the D_{6h} cage.

The exohedral complexes obtained from the D_{6h} isomer are more stable than their isolated components for all ions and elements studied. The exohedral complexes of the D_{2d} isomer are also more stable than their corresponding endohedral counterparts, except the exohedral complexes $X(HSiO_{3/2})_{12}$ of He and Ar. The endothermic binding energy values for these two exohedral complexes are only 0.22 kcal/mol ($He@(HSiO_{3/2})_{12}$) and 0.08 kcal/mol ($Ar(HSiO_{3/2})_{12}$). These values are so small that the computational error is larger. The endothermic encapsulation energy for $He@(HSiO_{3/2})_{12}$ is only 2.09 kcal/mol (B3LYP/6-311(d,p)), while that for $Ne@(HSiO_{3/2})_{12}$ is 1.95kcal/mole (B3LYP/6-311++(2d,2p) starting from the D_{2d} T_{12}-POSS isomer. The corresponding endothermic encapsulation energy for $He@(HSiO_{3/2})_{12}$ is only 1.31 kcal/mol (B3LYP/6-311(d,p) when

employing the D_{6h} isomer. All these values are so small that they may be less than the uncertainty in the calculated energy differences.

Exohedral F^- ions located outside the cage along a line from the cage center through the midpoint of the D6R face exhibit a remarkable behavior, different from all other exohedral complexes starting with the D_{6h} isomer. An exohedral F^- ion spontaneously penetrates into the center of the cage forming the endohedral $F^-@(HSiO_{3/2})_{12}$ species that is identical to the corresponding complex formed by initially placing F^- at the center of the cage followed by optimization. In contrast, identical placement of exohedral F^- outside of the D5R face of the D_{2d} isomer did not lead to F^- penetration into the cage. Instead the F^- ion became attached exohedrally to one of the Si atoms forming a pentacoordinated silicon.

The exohedral binding energies (E_{bind}) exhibit charge and size dependences on X similar to those of the endohedral inclusion energies (E_{inc}, Tables 5 and 6). Exohedral adsorption of the small Li^+ ion yielded the largest inclusion energy, followed by Na^+ and K^+.

The ZPE-corrected energy difference between the exohedral and endohedral structure is defined as the isomerization energy.[39] The isomerization energies, ΔE_{iso} (kcal/mol), in Tables 5.3 and 5.5 illustrated that the exohedral complexes $X(HSiO_{3/2})_{12}$ ($X=Li^+$, Na^+, K^+, He^+, Ne, Ar, Cl^-, Br^-) are energetically more favorable than the corresponding endohedral complexes. However, formation of the endohedral complexes should not be prohibited just because the exohedral complexes are more stable. For example, $He@C_{20}H_{20}$ has been prepared despite its large isomerization energy (35.4

kcal/mol).[75] E_{iso} is smallest for Li^+ encapsulated in $(HSiO_{3/2})_{12}$ of all the alkali ion-containing complexes, Its E_{iso} is only 4.7 kcal/mol, which may be close to the uncertainty of the calculated energy differences in this study.

It is interesting to compare the inclusion energies of $X@(HSiO_{3/2})_{12}$ with those of endohedral dodecahedrane complexes $X@C_{20}H_{20}$[39], T_8-POSS[54] complexes and T_{10}-POSS complexes. The endohedral complexes of Li^+ and Na^+ in $(HSiO_{3/2})_{12}$ are considerably more stable (X= Li^+:-53.0, Na^+: -35.3, K^+: -12.4 kcal/mol) than the corresponding endohedral composites of $(HSiO_{3/2})_8$ (X = Li^+: -18.5; Na^+: 11.3 kcal/mol) or dodecahedrane $C_{20}H_{20}$ (Li^+: -12.7, Na^+: 55.3 kcal/mol).[39] Furthermore, the noble gas inclusion energies of $X@(HSiO_{3/2})_{12}$ (X=He = -2.9, Ne = 2.0, Ar = 16.2 kcal/mol) are lower (more stable) than those of $X@C_{20}H_{20}$ (X= He = 37.9, Ne = 102.9, Ar = 320.2 kcal/mole) and $X@(SiHO_{3/2})_{10}$ (X = He = 12.3; Ne = 24.2; Ar = 95.9 kcal/mole). The same hierarchy of stabilities that were established for alkali metal cation complexes $X@(HSiO_{3/2})_{12}$ (X = Li^+, Na^+, K^+) in this work was also found by Sun et al[76] in Generalized gradient approximation (GGA) DFT computations for the endohedral fullerene C_{32} complexes $Li^+@C_{32}$, -53.1 kcal/mol, $Na^+@C_{32}$, -26.9 kcal/mol, and $K^+@C_{32}$, 13.7 kcal/mol. Consistently, the small Li^+ ion complexes emerge as most stable, while the larger K^+-containing complexes exhibit the lowest stability.

Electronic Properties

The charges on the endohedral guests were obtained by using the natural population analysis (NPA). These values are given in Tables 5.6 and 5.7. The population analysis gives a measure of the charge on atoms. Charge densities are very helpful in the

interpretation of electronic structure. The nature of ionic/covalent interactions or guest-host electron transfer is better examined after obtaining these charges. The core electrons usually do not participate in bonding processes. However, the behavior of the valence orbitals is markedly different and varies from structure to structure.

The average charges on each of the two types of nonequivalent Si atoms are +2.4 and +2.2 in the empty D_{2d} T_{12}-POSS isomer. The charges on these cage Si atoms decreased upon encapsulation of Li^+, Na^+ and K^+. The +1 electronic charge in Li^+, Na^+ and K^+ decreased to 0.9 for all three systems. Careful inspection reveals that electrons are transferred from oxygen 2*p* orbital to encapsulated Li^+, Na^+, and K^+ 2*s*, 3*s* and 4*s* orbitals respectively and also from H *s* orbitals to silicon 3*p* orbital. The charge distributions on oxygens are more complex. In the presence of alkali metal cations, the negative charge on the six bridging oxygens decreased and the amount of negative charge on the remaining oxygens increased. The negative charge on all the H-atoms decreased. All the hydrogens donate electron density to the Si atoms. Back donation of electron density from the cage to alkali ions is more pronounced in the case of the Na^+ ion. Li^+, Na^+ and K^+ are essentially ionic after encapsulation into the T_{12}-POSS cage. Electrons are donated from the cage atoms to encapsulated metal ions. Consequently, electronic density on the Si, and H in the cage framework decreases.

The He and Ne atoms encapsulated in T_{12}-POSS are essentially neutral. No significant charge transfer occurs between the cage and the encapsulated He and Ne. Similar behavior was observed for endohedral complexes of X@T_8-POSS, X@T_{10}-POSS and X@$C_{20}H_{20}$ when X = He or Ne. The charge +0.1 on encapsulated Ar reflect a very

small charge transfer between the Ar atom and the atoms of cage atoms. However, noble gas encapsulations lead to charge redistributions among the cage framework atoms. The positive charge on the Si atoms increased and the negative charge on H atoms decreased slightly. Negative charge on O atoms also increased slightly.

Halide ions inserted into the $(HSiO_{3/2})_{12}$ cage center alter the bonding by transferring electron density to the cage. The natural charge present on an isolated halide, –1.0, is lowered to –0.9, –0.9 and -0.8 respectively when F^-, Cl^- and Br^- are inside the cage. Charge transfer occurs from the halide to the cage framework atoms. The amount of positive charge on Si always increases while the amount of negative charge on H increased.

The encapsulation of alkali metal ions, halides and noble gases into the D_{6h} isomer of $(HSiO_{3/2})_{12}$ shows the same behavior as that of D_{2d} isomer. Alkali metal cations caused transfer of electron density from the cage framework to the alkali metal cations. In contrast, F^-, Cl^- and Br^- lose electron density while the framework atoms gain electrons. The halides –1.0 charge in the isolated state changes to –0.85, –0.88 and –0.83 for F^-, Cl^- and Br^-, respectively, upon encapsulation into the cage. The amount of negative charge on the hydrogens and six of the oxygens (oxygen joining the Si atoms of two D6R faces) increased. The electron density on both of the D6R ring oxygens decreased upon F^-, Cl^- and Br^- incarceration. Noble gases induce little electron transfer. He, Ne and Ar encapsulated into T_{12}-POSS (D_{6h}) are almost neutral.

Ionization Potentials

The ionization potentials calculated at the B3LYP/6-311(d,p) level for endohedral $X@(HSiO_{3/2})_{12}$ derivatives where $X=Li^-$, Li^0, Na^-, Na^0, K^- and $K^0$are summarized in Table 5.11. The calculated ionization potentials for isolated Li^0, Na^0 and K^0 metal atoms differ from the respective experimental values only by 4%. The ionization potentials of T_{12}-POSS encapsulated Li^0, Na^0 and K^0 are considerably lower than those of the free metal. Boldyrev and coworkers[77-79] defined species with first ionization potentials less than the cesium atom (90.0 kcal/mol; 3.9 eV) as "superalkalis". The first ionization potential for encapsulated Li^0, Na^0, and K^0 are 65.7 kcal/mol to 65.5 kcal/mol and 56.3 kcal/mol, respectively. These values are significantly smaller than the IP of cesium. Thus, $X@(HSiO_{3/2})_{12}$ (X = Li, Na, and K) are "superalkalis". Similar behavior was observed for the dodecahedrane-containing endrohedral alkali and alkaline earth metals [39] and endohedral alkali T_{10}-POSS complex.

NMR Chemical Shifts

Table 5.12 summarizes the calculated chemical shifts for the parent $(HSiO_{3/2})_{12}$ cage D_{2d} isomer and the endohedral complexes $X@(HSiO_{3/2})_{12}$ (X= Li^+, Na^+, He, Ne, Ar and F^-, Cl^- and Br^-). These chemical shifts are referenced against TMS and unencapsulated X. All calculation were preformed at the B3LYP/6-311G(d, p) level using the GIAO method.[65-68] The chemical shifts for the embedded atoms or ions were obtained by subtracting the isotropic shielding of the unencapsulated X (X= Li^+, Na^+, He, Ne, Ar, F^-, Cl^- and Br^-) from that of encapsulated X in $X@(HSiO_{3/2})_{12}$. The computed ^{29}S chemical shifts of the empty pure cage $(HSiO_{3/2})_{12}$ cage were –89.65 and –93.23 and for

the ^{1}H shifts were 4.82 and 4.72 ppm respectively. These values agree well with the experimental values (Si = -85.784, -87.760; H = 4.263, 4.294 ppm).[2]

The $(HSiO_{3/2})_{12}$ cage deshields all of the encapsulated atomic and ionic species. He atom is slightly deshielded (0.79 ppm) by the $(HSiO_{3/2})_{12}$ cage. This is in sharp contrast with the large calculated shielding obtained by Buhl et al. [46] for $He@C_{60}H_{60}$ (-5.2ppm) but reminiscent of the deshielding of He in $He@C_{20}H_{20}$ (1.51 ppm) predicted by Jimenez-Vazquez *et al* [62] and $He@T_{10}$-POSS (0.75 ppm) (in this Dissertation, Chapter IV). Li^{+} is also slightly deshielded (4.48 ppm) inside the $(HSiO_{3/2})_{12}$ cage . As the size of the ions or atoms increased the deshielding becomes more pronounced (Table 5.12).

The NICS at the $(HSiO_{3/2})_{12}$ cage center is –0.56 ppm. The NICS calculated at the D5R ring center is –0.24 ppm. This may be compared to the NICS value at the center of benzene (-11.5 ppm) or cyclohexane (-2.1 ppm),[81] to illustrate the lack of cyclic electron delocalization in the cage. Since the NICS value of $(HSiO_{3/2})_{12}$ at the cage center or D5R ring center is extremely small, no evidence exists for either aromaticity or Encapsulation of He, Ne, Ar, Li^{+}, Na^{+}, F^{-}, Cl^{-} and Br^{-} into the $(HSiO_{3/2})_{12}$ (D_{2d}) cage antiaromaticity in the empty $(HSiO_{3/2})_{12}$ cage. This conclusion is the same as that made for $(HSiO_{3/2})_{10}$ in this ddissertation.

Encapsulation of He, Ne, Ar Li^{+}, Na^{+}, F^{-}, Cl^{-} and Br^{-} causes the ^{29}Si chemical shifts upfield relative to $(HSiO_{3/2})_{12}$ by 7.62-11.27 ppm (He), 0.43-5.12 ppm (Ne), 0.25-1.16 ppm (Ar), 16.19-23.30 ppm (Li^{+}), 9.03-14.58 ppm (Na^{+}) , 0.18-0.25 ppm (F^{-}), 0.72 - 1.31,ppm (Cl^{-}) and 0.4-1.32 ppm (Br^{-}). The ^{29}Si chemical shifts are changed significantly for He, Li^{+}, and Na^{+} inclusion. The ^{1}H chemical shifts in Li^{+}, Na^{+}, Ne, Ar, F^{-}, Cl^{-} and Br^{-}

are displaced by 0.26-0.55 ppm (Li^+), 0.33-0.31 ppm (Na^+), 0.06-0.01 ppm (Ne), 0.16-0.57 ppm (Ar), 0.40-0.29 ppm (F^-), 0.21-0.23 ppm (Cl^-) and 0.06-0.01 ppm (Br^-) relative to the ^1H in $(HSiO_{3/2})_{12}$. The proton chemical shift in He@$(HSiO_{3/2})_{12}$ is almost unchanged versus that of the pure cage. Thus, ^1H NMR spectroscopy could be used to detect and differentiate among the Li^+, Na^+, Ar, F^-, and Cl^- complexes. The calculated chemical shifts suggest that ^{29}Si NMR spectroscopy could be used to characterize all the endohedral complexes.

D_{6h} isomer and its endohedral complexes: Table 5.13 summarizes the calculated chemical shifts for the parent D_{6h} $(HSiO_{3/2})_{12}$ cage and for X@$(HSiO_{3/2})_{12}$ (X= He, Ne, Ar, F^-, Cl^- and Br^-). These calculated were the same procedure as those for the D_{2d} isomer. Since, the D_{6h} isomer of $(HSiO_{3/2})_{12}$ is not known to exist, the computed ^1H and ^{29}Si chemical shifts in $(HSiO_{3/2})_{12}$ cannot be compared with experimental values. The endohedral He atom is slightly deshielded (0.75 ppm) versus free He while Ne and Ar are strongly deshielded (Ne ; 28.5 ppm; Ar ; 107.08 ppm) versus free Ne and Ar by the $(HSiO_{3/2})_{12}$ cage. Encapsulated F^-, Cl^- and Br^- are each strongly deshielded. The nuclear independent chemical shift (NICS) calculated at the $(HSiO_{3/2})_{12}$ cage center is –0.68 ppm. For comparison the NICS value calculated at the center of the benzene ring is -11.5 ppm and -2.1ppm for cyclohexane. Since the NICS value of –0.68 ppm for T_{12}-POSS cage, no evidence exists for either aromaticity or antiaromaticity for the empty T_{12}-POSS cage.

Overall, encapsulating of He, Ne, Ar and F^- in to the D_{6h} $(HSiO_{3/2})_{12}$ isomer have no significant effect on ^1H and ^{29}Si NMR spectra. The ^1H and ^{29}Si chemical shifts in X@$(HSiO_{3/2})_{12}$ (X = He, Ne and Ar) are almost the same as the ^1H and ^{29}Si chemical

shifts in the empty cage (Table 5.12). The ^{1}H and ^{29}Si chemical shifts in $F^{-}@(HSiO_{3/2})_{12}$ are shifted relative to $(HSiO_{3/2})_{12}$ by 0.3 and 2.1 ppm, respectively. In $Cl^{-}@(HSiO_{3/2})_{12}$ these shifts change by (0.2-0.2) and (2.3-2.2) ppm. Finally in $Br^{-}@(HSiO_{3/2})_{12}$ 4.5 ppm and (2.1-5.2) ppm, respectively, for ^{1}H and ^{29}Si nuclei. Therefore, ^{1}H and ^{29}Si NMR will be a useful tool to detect and identify $F^{-}@(HSiO_{3/2})_{12,}$ $Cl^{-}@(HSiO_{3/2})_{12}$ and $Br^{-}@(HSiO_{3/2})_{12}$.

Presence of a Counterion

Alkali metals would most likely be inserted into $(HSiO_{3/2})_{12}$ cage as cations. This raises the question of what effect a counter ion would play in this process. One could envision incorporating both the cation and anion into the cage. Alternatively, one ion could be incorporated endohedrally while the other becomes exohedrally coordinated to the cage. A preliminary study of the effect of a counterion was investigated using LiF. Initially structures were generated by placing both Li^{+} and F^{-} ion 1 Å apart inside both the D_{2d} and D_{6h} isomers of $(HSiO_{3/2})_{12}$. A second approach was to generate structures by placing F^{-} inside the cage and Li^{+} on a line from the center of the cage to outside of the center of the D5R surface of the D_{2d} isomer (or outside the D6R surface of the D_{6h} isomer). This inside/outside initial geometry was reminiscent of the ammonium $F^{-}@(HSiO_{3/2})_{12}$ salt synthesized and characterized by Taylor.[80] The structures were optimized at the B3LYP/6-311G(d, p) level. Table 5.14 summarizes total energies, zero-point energies, zero-point corrected binding energies and natural charges. The optimized structures are given in Figures 5.9a, 5.9b, and 5.9c.

When both ions are placed inside the D_{2d} cage, optimization gives a structure where both Li^+ and F^- ions remained inside the cage (5.9a). The Li^+ ion coordinates to four of the cage oxygen atoms. The F^- ion moves from the cage center towards two of the cage silicon atoms and is associated with these two Si atoms and with the Li^+ ion. The inclusion energy is still negative by –35.9 kcal/mol, despite the presence of two endohedral guests. This $LiF@(HSiO_{3/2})_{12}$ complex is energetically less stable than $F^-@(HSiO_{3/2})_{12}$ or $Li^+@(HSiO_{3/2})_{12}$ by 53.5 kcal/mol or 17.1 kcal/mol, respectively. The counterion destabilizes both the $F^-@(HSiO_{3/2})_{12}$ and $Li^+@(HSiO_{3/2})_{12}$ complexes. However the $LiF@(HSiO_{3/2})_{12}$ complex is still thermodynamically favorable. The nearest neighbor distance between Li^+ and oxygen in this complex is 2.259 Å while that between F^- and Si is 2.450 Å. The distance between Li^+ and F^- in gaseous LiF calculated at the B3LYP/6-311G(d, p) level is 1.550 Å. Hence the distance between Li^+ and F^- in the $LiF@(HSiO_{3/2})_{12}$ complex 1.665 Å is elongated compared to this distance in free LiF.

The optimization of the endohedral fluoride/exohedral lithium species geometry (generated from the D_{2d} isomer) gives the structure as shown in Figure 5.9(b). The F^- ion remained inside the cage while the Li^+ ion moved inwards towards one of the D5R surfaces, essentially becoming part of the cage surface. Part of the optimized structure's shape looks like a mushroom (Figure 5.9(b)). The binding energy of the $F^-@Li^+(HSiO_{3/2})_{12}$ calculated as the difference between the energy of $F^-@Li^+(HSiO_{3/2})_{12}$ and the sum of energy of $(HSiO_{3/2})_{12}$ and LiF is –33.5 kcal/mol (-254.5 kcal/mol if we considered both Li^+ and F^- energies as isolated atoms). The $F^-@Li^+(HSiO_{3/2})_{12}$ complex (with counter ion) is energetically less stable than $F^-@(HSiO_{3/2})_{12}$ or $Li^+@(HSiO_{3/2})_{12}$

(complexes without counter ion) by 55.9 kcal/mol or 19.5 kcal/mol, respectively. Despite this counterion destabilization, $F^-@Li^+(HSiO_{3/2})_{12}$ is still thermodynamically favorable. The nearest neighbor distance between Li^+ and oxygen is 2.471 Å and that between Li^+ and Si is 2.680 Å. The distance between Li^+ and F^- in the $Li^+@F^-(HSiO_{3/2})_{12}$ complex is only 1.681 Å which remarkably close to the optimized "inside-inside", $LiF@(HSiO_{3/2})_{12}$ structure's Li-F distance of 1.665 Å. For comparison, the distance between Li^+ and F^- in gaseous LiF calculated at the B3LYP/6-311G(d, p) level is 1.55 Å.

The "inside-inside" and F^- inside/Li^+ outside D_{6h}-cage species were both optimized. Both of these optimized structures are identical and is shown in Figure 5.9(c). In this structure 5.9(c) the F^- ion remained inside the cage while the Li^+ ion appeared to interact with two silicons and four oxygen atoms on the D6R cage surface. The F^- ion moved from the cage center towards the lithium ion. The shape of the optimized structures look like a mushroom (Figure 5.9c). The binding energy of this structure is –40.36 kcal/mol (–255.4 kcal/mol). The $F^-@Li^+(HSiO_{3/2})_{12}$ complex is less energetically stable than $F^-@(HSiO_{3/2})_{12}$ or $Li^+@(HSiO_{3/2})_{12}$ by 44.7 kcal/mol or 18.9 kcal/mol respectively. Thus the Li^+ counterion destabilizes the $F^-@(HSiO_{3/2})_{12}$ or F^- counter ion $Li^+@(HSiO_{3/2})_{12}$ complex. However, the $Li^+@F^-(HSiO_{3/2})_{12}$ complex is still thermodynamically favorable. The distance between Li^+ and F^- in the $F^-@Li^+(HSiO_{3/2})_{12}$ complex is 1.693 Å, slightly longer than the analogous complex generated starting from the D_{2d} cage isomer and substantially longer than the 1.550 Å the gas phase distance calculated at the B3LYP/6-311G(d, p) level.

The distance between Li^+ and F^- is elongated in both the $LiF@(HSiO_{3/2})_{12}$ and $F^-@Li^+(HSiO_{3/2})_{12}$ complexes compared to that in free LiF. Attractive interactions between both ions and the large $(HSiO_{3/2})_{12}$ cage (both D_{2d} and D_{6h} isomers) help reduce the columbic contraction of the LiF distance, thereby elongating this distance. In gaseous LiF the charges on Li^+ and F^- are +0.90 and –0.90, respectively. The atomic charges on Li^+ and F^- in $LiF@(HSiO_{3/2})_{12}$ and $F^-@Li^{+(}HSiO_{3/2})_{12}$ obtained from D_{2d} isomer are smaller than those in gaseous Li^+F^-. In $LiF@(HSiO_{3/2})_{12}$ the charge on Li^+ is +0.89 while that on F^- is - 0. 81. Furthermore, in $F^-@Li^+(HSiO_{3/2})_{12}$, the charge on Li^+ is 0.87 while that on F^- is –0.87. In contrast, atomic charge on Li^+ in $F^-@Li^+(HSiO_{3/2})_{12}$ complexes obtained from D_{6h} isomer are larger than those in gaseous LiF and smaller on F^-.

Conclusions

The following conclusions can be drawn from these theoretical calculations.The formation of the endohedral complexes $Li^+@(HSiO_{3/2})_{12}$, $Na^+@(HSiO_{3/2})_{12}$, $K^+@(HSiO_{3/2})_{12}$, $F^-@(HSiO_{3/2})_{12}$, $Cl^-@(HSiO_{3/2})_{12}$, $Br^-@(HSiO_{3/2})_{12}$, $He@(HSiO_{3/2})_{12}$, and $Ne@(HSiO_{3/2})_{12}$ from their isolated components is energetically favorable. These ions are thermodynamically stable within the $(HSiO_{3/2})_{12}$ cage. Encapsulation of Ar is thermodynamically unfavorable. The exohedral $X(HSiO_{3/2})_{12}$ ($X=Li^+$, Na^+, K^+, Ne, Cl^- and Br^-) complexes obtained from the initial D_{2d} cage isomer are energetically more favorable compared to their endohedral counterparts except for X = He and Ar. The exohedral $X(HSiO_{3/2})_{12}$ ($X=Li^+$, Na^+, K^+, He, Ne, Cl^- and Br^-) complexes obtained from the initial D_{6h} cage isomer are energetically more favorable than their endohedral

counterpart, except for X = F^-. Instead of forming an exohedral complex, the F^- ion penetrates into the cage center with no energy barrier.

Endohedral X@ $(HSiO_{3/2})_{12}$ compounds (X=Li^0, Na^0, K^0) have smaller first ionization potentials (IP) than the IP of atomic Cesium and can thus they can be considered " superalkalis ".

Upon encapsulations of an alkali metal cation, halide or noble gases into the center of the $(SiHO_{3/2})_{12}$, the framework properties changed distinctly. The electron density was transferred from the F^-, Cl^- and Br^- onto the silicon atoms in $X(HSiO_{3/2})_{10}$ (X = F^-, Cl^- and Br^-).

Upon inclusion of cations, the silicon atoms donate electron density to the cations. Encapsulation of noble gases generates negligible charge transfer.

The NICS value computed at the $(HSiO_{3/2})_{12}$ cage center shows no evidence for any aromaticity or antiaromaticity in the cage molecule.

In summary, the present work represents a new direction in the investigation of T_{12}-POSS clusters via accurate theoretical calculations. Subtle aspects of the structure and bonding were investigated for systems of considerable complexity. Among the salient points of this work is the significant amount of charge redistribution around the cage framework and at the incorporated ionic and atomic species. This effect is subtly different for anions, cations and noble gases. The framework silicon atoms act as an electron density sink, which can easily be changed depending on the nature of the particle incorporated.

References

(1) Li, G.; Wang, L.; Ni, H.; Pittman, C. U., Jr. *J. Inorg. Organomet. Polym.* **2002**, *11*, 123.

(2) Agaskar, P. A.; Klemperer, W. G. *Inorg. Chim. Acta* **1995**, *229*, 355.

(3) Brown, J. F., Jr.; Vogt, L. H., Jr. *J. Am. Chem. Soc.* **1965**, *87*, 4313.

(4) Dance, B. *Semiconduct. Int.* **2001**, *24*, 46.

(5) Feher, F. J.; Wyndham, K. D. *Chem. Commun.* **1998**, 323

(6) Li, G. Z.; Wang, L.; Toghiani, H.; Daulton, T. L.; Koyama, K.; Pittman, C. U., Jr. *Macromolecules* **2001**, *34*, 8686.

(7) Li, G. Z.; Wang, L.; Toghiani, H.; Daulton, T. L.; Pittman, C. U. *Polymer* **2002**, *43*, 4167.

(8) Li, H.; Eddaouddi, M.; Richardson, D. A.; Yaghi, O. M. *J. Am. Chem. Soc.* **1998**, *120*, 8567.

(9) Maxim, N.; Abbenhuis, H. C. L.; Stobbelaar, P. J.; Mojet, B. L.; van Santen, R. A. *Phys. Chem. Chem. Phys.* **1999**, *18*, 4473.

(10) Maxim, N.; Magusin, P. C. M. M.; Kooyman, P. J.; van Wolput, J. H. M. C.; van Santen, R. A.; Abbenhuis, H. C. L. *Chem. Materials* **2001**, *13*, 2958.

(11) Wada, K.; Yamada, K.; Kondo, T.; Mitsudo, T.-A. *Chem. Lett.* **2001**, 12.

(12) Lamm, M. H.; Chen, T.; Glotzer, S. C. *Nano Lett.* **2003**, *3*, 989.

(13) Fu, B. X.; Hsiao, B. S.; Pagola, S.; Stephens, P.; White, H.; Rafailovich, M.; Sokolov, J.; Mather, P. T.; Jeon, H. G.; Philips, S.; Lichtenhan, J.; Schwab, J. *Polymer* **2001**, *42*, 599.

(14) Romo-Uribe, A.; Mather, P. T.; Haddad, T. S.; Lichtenhan, J. D. *J. Polym. Sci. B-Polym. Phys.* **1998**, *36*, 18571872.

(15) Fu, B. X.; Hsiao, B. S.; White, H.; Rafailovich, M.; Mather, P. T.; Jeon, H. G.; Phillips, S.; Lichtenhan, J.; Schwab, J. *Polym. Int.* **2000**, *49*, 437.

(16) Lee, A.; Lichtenhan, J. D. *J. Appl. Polym. Sci.* **1999**, *73*, 1993.

(17) Haddad, T. S.; Lichtenhan, J. D. *Macromolecules* **1996**, *29*, 7302.

(18) Schwab, J. J.; Lichtenhan, J. D. *Appl. Orga. Chem.* **1998**, *12*, 707.

(19) Raj, R.; Riedel, R.; Soraru, G. D. *J. Am. Ceram. Soc.* **2001**, *84*, 2158.

(20) Abbenhuis, H. C. L. *Chem. Eur. J.* **2000**, *6*, 25.

(21) Ducateau, R.; Cremer, U.; Harmsen, R. J.; Mohamud, S. I.; C. L. Abbenhuis, C. L.; Avan Saten, R.; Meetsma, A.; Thiele, S. K.-H.; F. F. H. van Tol, F. F. H.; Kranenburg, M. *Organomet.* **1999**, *18*, 5447.

(22) Klunduk, M. C.; Maschmeyer, T.; Thomas, J. M.; Johnson, F. G. *Chem. Eur. J.* **1999**, *5*, 1481.

(23) Pescarmona, P. P.; Waal, J. C. v. d.; Maxwell, I. E.; Maschmeyer, T. *Angew. Chem., Int. Ed.* **2000**, *40*, 740.

(24) Xiao, F. S.; Han, Y.; Yu, Y.; Meng, X.; Yang, M.; Wu, S. *J. Am. Chem. Soc.* **2002**, *124*, 888.

(25) Liu, J. C. *Appl. Organomet. Chem.* **1999**, *13*, 295.

(26) Coupar, P. e. a. *J. Chem. Soc., Dalton Trans.* **1999**, 2183.

(27) Murfee, H. J. e. a. *Inorg. Chem.* **2000**, *39*, 5209.

(28) Saez, I. M. e.; al. Chemistry (Weinheim an Der Bergstrasse, G., 7, 2758. *Chemistry (Weinheim an Der Bergstrasse, Germany)* **2001**, *7*, 2758.

(29) de Vos, R. M.; Verweij, H. *J. Membr. Sci.* **1998**, *143*, 37.

(30) Suzuki, F.; Nakane, K.; Yasuo, H. *J. Mem. Sci.* **1995**, *104*, 183.

(31) Shanbhag, P. V.; Sirkar, K. K. *J. Appl. Polym. Sci.* **1998**, *69*, 1263.

(32) X. Feng; P. Shao; R. Y. M. Huang; G. Jiang; R. -X, X. *Seperation and Purification Technology*, **2002**, *27*, 211.

(33) McCusker, C.; Carroll, J. B.; Rotello, V. M. *Chem. Commun. (Cambridge, United Kingdom)* **2005**, 996.

(34) Xiang, K.-H.; Pandey, R.; Pernisz, U. C.; Freeman, J. *J. Phys. Chem. B* **1998**, *102*, 8704.

(35) Cheng, W.-D.; Xiang, K.-H.; Pandey, R.; Pernisz, U. C. *J. Phys. Chem.* **2000**, *104*, 6737.

(36) Päch, M.; Stösser, R. *J. Phys. Chem. A* **1997**, *101*, 8360.

(37) George, A. R.; Catlow, C. R. A. *Chem. Phys. Lett.* **1995**, *247*, 408.

(38) Charkin, O. P.; Klimenko, N. M.; Moran, D.; Mebel, A. M.; Charkin, D. O.Schleyer, P. v. R. *Inorg. Chem.* **2001**, *40*, 6913.

(39) Moran, D.; Stahl, F.; Jemmis, E. D.; Schaefer, H. F., III;; Schleyer, P. v. R. *J. Phys. Chem. A* **2002**, *106*, 5144.

(40) Chen, Z.; Jiao, H.; Moran, D.; Hirsch, A.; Thiel, W.; Schleyer, P. v. R. *J. Phys. Chem. A* **2003**, *107*, 2075.

(41) Schleyer, P. v. R.; Najafian, K.; Mebel, A. M. *Inorg. Chem.***1998**, *37*, 6765.

(42) Jemmis, E. D.; Balakrishnarajan, M. M. *J. Am. Chem. Soc.* **2000**, *122*, 7392.

(43) Jemmis, E. D.; Jayasree, E. G. *Collect. Czech. Chem. Commun.* **2002**, *67*, 965.

(44) Weiske, T.; Schwarz, H.; Hirsch, A.; Groesser, T. *Chem. Phys. Lett.* **1992**, *199*, 640.

(45) Rose, H. R.; Dance, I. G.; Fisher, K. J.; Smith, D. R.; Willett, G. D.; Wilson, M. A. *Orga. Mass Spectrom.* **1994**, *29*, 470.

(46) Buhl, M.; Thiel, W.; Jiao, H.; Schleyer, P. v. R.; Saunders, M.; Anet, F. A. L. *J. Am. Chem. Soc.* **1994**, *116*, 6005.

(47) Saunders, M.; Jimenez-Vazquez, H. A.; Cross, R. J.; Mroczkowski, S.; Gross, M. L.; Giblin, D. E.; Poreda, R. J. *J. Am. Chem. Soc.* **1994**, *116*, 2193.

(48) Shinohara, H. *Rep. Prog. Phys.* **2000**, *63*, 843.

(49) Irle, S.; Rubin, Y.; Morokuma, K. *J. Phys. Chem. A* **2002**, *106*, 680.

(50) Saunders, M.; Cross, R. J.; Jimenez-Vazquez, H. A.; Shimshi, R.; Khong, A. *Science (Washington, D. C.)* **1996**, *271*, 1693.

(51) Bassindale, A. R.; Pourny, M.; Taylor, P. G.; Hursthouse, M. B.; Light, M. E. *Angew. Chem., Int. Ed.* **2003**, *42*, 3488.

(52) Tejerina, B.; Gordon, M. S. *J. Phys. Chem. B* **2002**, *106*, 11764.

(53) Allen, E. C.,; Beers, K. J. *Polymer* **2005**, *46*, 569.

(54) Park, S. S.; Xiao, C.; Hagelberg, F.; Hossain, D.; Pittman, C. U., Jr.; Saebo, S. *J. Phys. Chem. A* **2004**, *108*, 11260.

(55) Tejerina, B.; Gordon, M. S. *J. Phys. Chem. B* **2002**, *106*, 11764.

(56) Earley, C. W. *J. Phys. Chem.* **1994**, *98*, 8693.

(57) Toernroos, K. W.; Buergi, H.-B.; Calzaferri, G.; Buergy, H. *Acta Crystallogr., Section B: Struct. Sci.* **1995**, *B51*, 155.

(58) Agaskar, P. A.; Day, V. W.; Klemperer, W. G. *J. Am. Chem. Soc.* **1987**, *109*, 5554.

(59) Feher, F. J.; Budzichowski, T. A. *J. Organometallics* **1989**, *153*, 373.

(60) Lee, C.; Yang, W.; Parr, R. G. *Phys. Rev. B: Condens. Matter and Materials Phys.* **1988**, *37*, 785.

(61) Becke, A. D. *J. Chem. Phys.* **1993**, *98*, 5648.

(62) Jimenez-Vazquez, H. A.; Tamariz, J.; Cross, R. J. *J. Phy. Chem. A* **2001**, *105*, 1315.

(63) Frisch, M. J. T., G. W.; Schlegel, H. B.; Scuseria, G. E.; Robb, M. A.; Cheeseman, J. R.; Montgomery, Jr., J. A.; Vreven, T.; Kudin, K. N.; Burant, J. C.; Millam, J. M.; Iyengar, S. S.; Tomasi, J.; Barone, V.; Mennucci, B.; Cossi, M.; Scalmani, G.; Rega, N.; Petersson, G. A.; Nakatsuji, H.; Hada, M.; Ehara, M.; Toyota, K.; Fukuda, R.; Hasegawa, J.; Ishida, M.; Nakajima, T.; Honda, Y.; Kitao, O.; Nakai, H.; Klene, M.; Li, X.; Knox, J. E.; Hratchian, H. P.; Cross, J. B.; Bakken, V.; Adamo, C.; Jaramillo, J.; Gomperts, R.; Stratmann, R. E.; Yazyev, O.; Austin, A. J.; Cammi, R.; Pomelli, C.; Ochterski, J. W.; Ayala, P. Y.; Morokuma, K.; Voth, G. A.; Salvador, P.; Dannenberg, J. J.; Zakrzewski, V. G.; Dapprich, S.; Daniels, A. D.; Strain, M. C.; Farkas, O.; Malick, D. K.; Rabuck, A. D.; Raghavachari, K.; Foresman, J. B.; Ortiz, J. V.; Cui, Q.; Baboul, A. G.;

Clifford, S.; Cioslowski, J.; Stefanov, B. B.; Liu, G.; Liashenko, A.; Piskorz, P.; Komaromi, I.; Martin, R. L.; Fox, D. J.; Keith, T.; Al-Laham, M. A.; Peng, C. Y.; Nanayakkara, A.; Challacombe, M.; Gill, P. M. W.; Johnson, B.; Chen, W.; Wong, M. W.; Gonzalez, C.; and Pople, J. A.Gaussian, Inc., Wallingford CT, 2004. Gaussian 03; Gaussian 03 ed., 2004.

(64) PQS version 3.1, P. Q. S., 2013 Green Acres Road, Fayetteville, AR 72703.

(65) Wolinski, K.; Hinton, J. F.; Pulay, P. *J. Am. Chem. Soc.* **1990**, *112*, 8251.

(66) Schreckkenbach, G.,; Ziegler, T. *J. Phys. Chem.* **1995**, *99*, 606.

(67) Ditchfield, R. *J. Chem. Phys.* **1976**, *65*, 3123.

(68) Cheeseman, J. R.; Trucks, G. W.; Keith, T.; Frisch, M. J. *J. Phys. Chem.* **1996**, *104*, 5497.

(69) Glendening, E. D.; Reed, A. E.; Carpenter, J. E.; Weinhold, F. *NBO 4.M University of Wisconson: Madison* **1993**.

(70) Boys, S. F.; Bernardi, F. *Mol. Phys.* **1970**, *19*, 553.

(71) Heyde, T. P. E.; Burgi, H., -B.; Burgi, H.; Tornroos, K. W. *Chimia* **1991**, *45*, 38.

(72) de Man, A. J. M.; Sauer, J. *J. Phys. Chem.* **1996**, *100*, 5025.

(73) Tossell, J. A. *J. Phys. Chem.* **1996**, *100*, 5025.

(74) Pasquarello, A.; Hybertsen, M. S.; Car, R. *Phys. Rev. B* **1996**, *54*, R2339.

(75) Cross, R. J.; Saunders, M.; Prinzbach, H. *Org. Lett.* **1999**, *1*, 1479.

(76) Sun, Q.; Wang, Q.; Yu, J. Z.; Ohno, K.; Kawazoe, Y. *J. Phys.: Condens. Matter* **2001**, *13*, 1931.

(77) Rehm, E.; Boldyrev, A. I.; Schleyer, P. v. R. *Inorg. Chem.* **1992**, *31*, 4831.

(78) Gutsev, G. L.; Boldyrev, A. I. *Chem. Phys. Lett.* **1982**, *92*, 262.

(79) Gutsev, G. L.; Boldyrev, A. I. *Adv. Chem. Phys.* **1985**, *61*, 169.

(80) Bassindale, A. R.; Baukov, Y. I.; Borbaruah, M.; Glynn, S. J.; Negrebetsky, V. V.; Parker, D. J.; Taylor, P. G.; Turtle, R. *J. Organomet. Chem.* **2003**, *669*, 154.

(81) Jiao, H.; Nagelkerke, R.; Kurtz, H. A.; Williams, R. V.; Borden, W. T.; Schleyer, P. v. R. *J. Am. Chem. Soc.* **1997**, *119*, 5921.

(82) Huheey, E. J.; Keiter, A. E.; Keiter , L. R. *Inorganic Chemistry : Principles of Structure and Reactivity*; HarperCollins,: New York, USA, 1993.

(83) James, M. A.; Lord, P. M. *Macmillan's Chemical and Physical Data*; Macmillan: London, UK, 1992.

Table 5.1 Selected Bond Lengths (in Å) and Bond Angles (in Degrees) of the D_{2d} $(HSiO_{3/2})_{12}$ Isomer Cage and its Endohedral $X@(HSiO_{3/2})_{10}$ Complexes at the B3LYP/6-311G(d,p) Level.

X	X-Si	X-Si	X-Si	X-O	X-O_b	Si-O	Si-O_b	Si-O	Si-H	OSiO	OSiO	SiOSi	OSiO	OSiO
Pure						1.636	1.642	1.637	1.643	109.3	107.4	150.9	109.6	109.2
Li^+	3.893	3.192	3.276	2.169	3.338	1.648	1.640	1.630	1.456	107.0	106.8	155.2	104.9	108.0
Na^+	3.877	3.276	3.276	2.410	3.326	1.646	1.640	1.632	1.457	107**.1**	106.1	152.	105.4	108.0
K^+	3.808	3.388	3.888	2.874	3.325	1.644	1.643	1.637	1.457	106.6	106.1	146.4	106.2	108.0
F^-	3.689	3.348	3.348	3.240	3.182	1.630	1.634	1.635	1.470	112.7	111.4	148.4	113.9	110.5
Cl^-	3.680	3.365	3.365	3.260	3.216	1.638	1.641	1.644	1.470	113.7	111.1	147.7	114.8	110.3
Br^-	3.675	3.373	3.373	3.279	3.229	1.627	1.632	1.636	1.470	113.9	110.9	149.1	114.9	110.2
He	3.732	3.380	3.716	3.153	3.121	1.636	1.642	1.637	1.643	109.7	109.4	150.2	109.7	109.2
Ne	3.731	3.382	3.395	3.150	3.124	1.636	1.642	1.631	1.643	109.8	109.4	150.2	109.7	109.2
Ar	3.716	3.382	3.395	3.391	3.156	1.639	1.643	1.635	1.643	110.2	109.0	148.6	110.4	109.0

Table 5.2 Selected Bond Lengths (Å) and Bond Angles (in Degrees) of the D_{6h} Isomer of $(HSiO_{3/2})_{12}$ Cage and its Endohedral $X@(HSiO_{3/2})_{12}$ Complexs at the B3LYP/6-311G(d,p) Level.

X	X-Si	X-O	Si-O	Si-H	OSO
Pure	3.570	3.293	1.635	1.164	109.3
Li^+	3.584	3.076	1.643	1.459	104.0
Na^+	3.587	3.086	1.643	1.456	104.1
K^+	3.594	3.117	1.646	1.459	104.8
F^-	3.521	3.401	1.632	1.472	112.7
Cl^-	3.536	3.410	1.637	1.472	113.2
Br^-	3.542	3.417	1.638	1.472	113.6
He	3.570	3.295	1.636	1.464	109.3
Ne	3.570	3.298	1.636	1.464	109.4
Ar	3.574	3.315	1.638	1.464	109.7

Table 5.3 Total Energies (in Hartrees), Zero-point Energies (ZPE), Molecular point Groups, Lowest Vibrational Frequencies ω_1 (cm^{-1}), Zero-point Corrected Inclusion Energies (kcal/mol) and Isomerization Energies (E_{iso}, kcal/mol) for Endohedral Complexes of $X@(HSiO_{3/2})_{12}$ with D_{2d} Symmetries at the B3LYP/6-311G(d,p) Level.

X	Energy	ZPE	*Sym.*	ω_1[a]	E_{inc}	E_{iso}
Pure	-4837.718917	132.1	D_{2d}	18.60		
Li^+	-4845.090379	133.4	D_{2d}	51.23	-53.0	13.2
Li^0	-4845.192860	132.0	C_1	60.10	10.9	
Li^-	-4845.167900	130.0	C_1	i352.97(1)	34.3	
Na^+	-4999.863635	132.7	D_{2d}	24.73	-35.3	-9.0
Na^0	-4999.965445	131.1	C_1	27.06	24.2	
Na^-	-4999.963537	129.6	D_{2d}	65.0798	34.2	
K^+	-5437.498981	131.6	D_{2d}	i42.57(4)	-12.4	-16.1
K^0	-5437.586331	130.1	D_{2d}	i38.75(4)	34.9	
K^-	-5437.543600	126.5	D_{2d}	i339.11(3)	68.2	
F^-	-4937.684574	133.1	D_{2d}	i69.28(1)	-89.5	-7.2
Cl^-	-5298.067730	133.4	D_{2d}	56.28	-28.9	-11.7
Br^-	-7411.975875	133.1	D_{2d}	65.57	-17.2	11.7
He	-4840.629883	132.9	D_{2d}	29.14	2.1	-1.9
Ne	-4966.674149	132.7	D_{2d}	38.21	-2.0	0.2
Ar	-5365.247881	133.1	D_{2d}	55.78	16.2	16.3

[a] Number in the bracket indicates the total number of imaginary frequency.

Table 5.4 Total Energies (in Hartrees), Zero-point Energies (ZPE), Molecular point Groups, Lowest Vibrational Frequencies ω_1 (cm^{-1}), Zero-point Corrected Binding Energies (kcal/mol), and Optimized Bond Lengths (Å) for endohedral complexes of $X@(HSiO_{3/2})_{12}$ with D_{2d} symmetry at the B3LYP/6-311++G(2d,2p).Level.

X	Energy	ZPE	*Sym.*	ω_1[a]	BE_{endo}	r_{X-Si}	r_{x-o}	$^{*}r_{si-O5R}$	r_{Si-O4R}	r_{Si-H}
Pure	-4837.756480	131.3	D_{2d}	25.16				1.639,1.638, 1.637, 1.632	1.643,1.639 1.638	1.646 1.463
Li^+	-4845.124772	132.8	D_{2d}	54.27	-50.8	3.891,3.334, 3.191	3.525 2.163	1.683, 1.641	1.649,1.641	1.460 1.456
Na^+	-4999.897330	132.0	D_{2d}	20.83	-32.8	3.877,3.277	3.494 3.323 2.404	1.648, 1.634	1.648, 1.642	1.459 1.457
K^+	-5437.532677	130.8	D_{2d}	i45.18(4)	-18.7	3.390,3.812 3.212	3.400 3.212 2.878	1.6471.646 1.638	1.646, 1.643	1.459 1.458
F^-	-4937.731728	132.2	D_{2d} D_{2d}	i74.07(1)	-50.3	3.695, 3.352 3.184	3.452 3.323 3.184	1.640, 1.632,1.628	1.643, 1.632	1.472 1.470
Cl^-	-5298.107363	132.5	D_{2d}	52.55	-28.4	3.684,3.368 3.214	3.454 3.264	1.695,1.643, 1.641, 1.634	1.643, 1.635	1.472 1.470
Br^-	-7412.015862	132.2	D_{2d}	62.26	-12.6	3.376,3680	3.280 3.231	1.638.1.646 1.637	1.643 1.637	1.472 1.471
He	-4840.667809	132.0	D_{2d}	27.01	-2.9	3.805, 3.383	3.418 3.157 3.126	1.463,1.639 1.638,1.632	1.643 1.638	1.464 1.462
Ne	-4966.714586	131.8	D_{2d}	34.33	2.0	3.736,3.385	3.418 3.159 3.127	1.644,1.639, 1.638	1.644 1.638	1.464 1.463

[a] Number in the bracket indicates the total number of imaginary frequencies.

$^{*}r_{si-O5R}$ and r_{Si-O4R} represents the distance between silicon and oxygen in five member and four member rings respectively.

Table 5.5 Total Energies (in Hartree), Zero-point Energies (ZPE), Molecular point Groups, Lowest Vibrational Frequencies ω_1 (cm^{-1}), Zero-point Corrected, Incusion Energies (kcal/mol) and Isomerization Energies (E_{iso}, kcal/mol) for Endohedral Complexesof $X@(HSiO_{3/2})_{12}$ with D_{6h} Symmetry at the B3LYP/ 6-311G(d,p) Level.

X	Energy	ZPE	*Sym.*	ω_1	E_{inc}	E_{iso}
Pure	-4837.711108	132.2	D_{6h}	25.30		
Li^+	-4845.114091	131.3	D_{6h}	i210.54(9)	-59.21	-13.3
Na^+	-4999.463714	129.3	C_1	23.70	-40.83	-12.0
K^+	-5437.498981	131.8	D_{6h}	i48.56(3)	-16.85	-20.9
F^-	-4937.669380	133.0	D_{6h}	i87.09(2)	-85.09	
Cl^-	-5298.061030	133.3	D_{6h}	66.07	-29.81	
Br^-	-7411.973890	133.0	D_{6h}	74.68	-21.08	9.4
He	-4840.622380	132.4	D_{6h}	1219.32	1.31	-16.0
Ne	-4966.667593	132.5	D_{6h}	28.49	-3.17	1.0
Ar	-5365.247240	132.8	D_{2h}	58.20	11.35	11.6

Table 5.6 Total Energies (in Hartrees), Zero-point Energies (ZPE), Molecular point Groups, Lowest Vibrational Frequencies ω_1 (cm^{-1}), Zero-point Corrected Inclusion Energies (kcal/mol), and Optimized Bond Lengths (Å) for endohedral complex of $X@(HSiO_{3/2})_{12}$ with D_{6h} symmetry at the B3LYP/ 6-311++G(2d,2p) Level.

X	Energy	ZPE	*Sym*	ω_1[a]	BE_{incl}	r_{X-Si}	r_{Si-O}	r_{Si-O}	r_{Si-H}
pure	-4837.750649	131.4	D_{6h}	23.59				1.643 1.637	1.464
Li^+	-4845.086999	130.6	D_{6h}	i209.59(9)	-32.3	3.586	3.869 3.077	1.647 1.644	1.459
Na^+	-4999.885951	130.7	D_{6h}	i105.93(7)	-30.0	3.589	3.859 3.087	1.647 1.645	1.459
K^+	-5437.541388	131.1	D_{6h}	i55.54(3)	-18.7	3.586	4.811 3.124	1.647 1.646	1.459
F^-	-4937.719277	132.4	D_{6h}	**i**76.33(2)	-50.3	3.490	3.490 3.401	1.640 1.634	1.472
Cl^-	-5298.103421	132.6	C_{2h}	64.07	-30.9	3.540	3.413 3.506	1.642 1.638	1.471
Br^-	-7412.016749	132.4	D_{6h}	75.17	-17.8	3.545	3.471 3.524	1.644 1.640	1.471
He	-4840.662673	131.4	D_{6h}	20.65	1.0	3.572	3.594 3.299	1.644 1.637	1.464
Ne	-4966.710366	131.7	D_{6h}	28.55	0.4	3.73	3.599 3.303	1.644 1.638	1.464
Ar	-5365.287852	132.1	D_{2h}	56.29	10.4	3.576	3.571 3.320	1.645 1.640	1.464

[a] Number in the bracket indicates number of imaginary frequencies.

Table 5.7 Natural Charge Analysis of X@ X@$(HSiO_{3/2})_{12}$ with D_{2d} symmetry at the B3LYP/6-311G(d,p) Level.

X	Q_X[a]	Q_{Si}	Q_{Si1}	Q_o	Q_{o1}	Q_{o1}	Q_{H1}	Q_{H1}
Pure		2.14	2.15	-1.27	-1.27	-1.27	-0.24	-0.20
Li^+	0.89	2.12	2.10	-1.25	-1.27	-1.31	-0.20	-0.20
Na^+	0.90	2.12	2.11	-1.26	-1.26	-1.30	-0.20	-0.20
K^+	0.89	2.12	2.12	-1.26	-1.27	-1.27	-0.21	-0.20
F^-	-0.85	2.15	2.17	-1.27	-1.27	-1.27	-0.27	-0.28
Cl^-	-0.88	2.16	2.17	-1.27	-1.27	-1.27	-0.27	-0.27
Br^-	-0.83	2.15	2.16	-1.27	-1.27	-1.27	-0.27	-0.27
He	0.00	2.14	2.15	-1.27	-1.27	-1.27	-0.24	-0.24
Ne	0.02	2.14	2.15	-1.27	-1.27	-1.27	-0.24	-0.24
Ar	0.03	2.14	2.15	-1.27	-1.27	-1.27	-0.24	-0.24

[a]Q_X = Charge on impurity X. The symbols Q_{Si}, Q_H and Q_O are defined analogously.

Table 5.8 Natural Charge Analysis of X@ X@$(HSiO_{3/2})_{12}$ with D_{2h} symmetry at the B3LYP/6-311G(d,p) Level.

X	Q_X[a]	Q_{Si}	Q_o	Q_{o1}	Q_{H1}
Pure		2.14	-1.26	-1.27	-0.24
Li^+	0.89	2.12/2.01	-1.24	-1.24	-0.20
Na^+	0.86	2.10/2.01	-1.26	-1.24	-0.22
K^+	0.91	2.11	-1.28	-1.24	-0.20
F^-	-0.86	2.16	-1.25	-1.28	-0.28
Cl^-	-0.90	2.16	-1.26	-1.28	-0.27
Br^-	-0.86	2.15	-1.26	-1.28	-0.27
He	0.00	2.14	-1.27	-1.27	-0.24
Ne	0.01	2.14	-1.27	-1.27	-0.24
Ar	0.03	2.14	-1.27	-1.27	-0.24

Table 5.9 Total Energies (in Hartree), Lowest Frequencies ω_1 (cm^{-1}), Molecular point Groups, Binding Energies (kcal/mol), and Optimized Bond Lengths (Å)for Exohedral Complexes of $X@(HSiO_{3/2})_{12}$ (D_{2d}) Calculated at the B3LYP/6-311G(d,p) Level.

X	Energy	ZPE	ω_1[a]	Sym.	E_{exo}	[b] $r_{X\text{-}si}$	$r_{X\text{-}O}$	r_1	r_2	r_3
Li^+	-4845 .108197	133.5	i29.59(1)	C_1	-39.8	2.954	2.581	1.643	1.608	1.459 1460
Na^+	-4999.878148	132.8	35.34	*Cs*	-44.3	3.148	2.453	1.613	1.614	1.459
K^+	-5437.526102	132.6	30.37	*Cs*	-28.5	3.536	2.888	1.654	1.615	1.459 1.461
F^-	-4937.695899	133.1	24.00	C_1	-96.7	1.721	2.411	1.653	1.644	1.467 1.469
Cl^-	-5298.047466	132.3	28.63	C_1	-17.2	3.313	3.681	1.636	1.676	1.469 1.463
Br^-	-7409.355366	158.2	37.17	C_1		2.735	2.958	1.616	1.674	1.422 1.427
He	-4840.631939	132.3	18.27	C_1	0.2	3.854	3.593	1.630	1.637	1.462, 1.464
Ne	-4966.6 73165	132.3	20.23	*Cs*	-1.9	3.702	3.303	1.630	1.637	1.462 1.464
Ar	-5365.272169	132.2	i4.28(1)	C_1	0.1	4.810	3.896	1.638	1.637	1.462 1.464

[a]Values in the bracet indicates the number of imaginary frequency.
[b] the sign used to indicated bond lengths are illustrated in Figure 5.7.

Table 5.10 Total Energies (in Hartree), Lowest Frequencies ω_1 (cm^{-1}), Molecular point Groups, Binding Energies (kcal/mol) and Optimized Bond Lengths (Å) for Exohedral Minima of Complexes of $X@(HSiO_{3/2})_{12}$ (D_{6h}) Calculated at the B3LYP/6-311G(d,p) Level.

X	Energy	Zero	ω_1	Sym.	E_{exo}	$r_{X\text{-}si}$	$r_{X\text{-}O}$	r_1	r_2	r_3	r_4
Li^+	-4845.113950	133.7	30.49	C_1	-72.6	2.781	2.088/2.091	1.689	1.626	1.632	1.459
Na^+	-4999.884060	132.8	-73.03 (3i)	C_{6V}	-52.8	3.341	2.619	1.656	1.624	1.657	1.633
K^+	-5437.534122	132.0	30.92	C_{6V}	-37.8	3.633	2.909/2.911	1.656/1.657	1.622	1.622	1.460
Cl^-	-5298.033958	132.0	20.60	C_1	-14.4	4.380	3.868	1.622	1.663	1.638	1.464/1.468
Br^-	-7411.956850	132.1	11.08	C_1	-11.6	3.418-4.856	1.623	1.615/1.662	1.636	1.638	1.464/1.468
He	-4840.624126	132.2	9.71	C_1	-0.3	5.076	4.880	1.635	1.642	1.635	1.464
Ne	-4966.665033	132.2	21.25	C_{6V}	-2.2	4.901	4.303	1.636	1.642	1.636	1.464
Ar	-5365.264229	132.2	10.27	C_{6V}	-0.2	3.861	3.236	1.635	1.642	1.636	1.464

[a]values in the bracket indicates the number ot totalimaginary frequencies.
[b] the sign used to indicated bond lengths are illustrated in Figure 5.8.

Table 5.11 Ionization and Reduction Potentials (IP, kcal/mol) of Free Atoms and Metal Encapsulated $X@(HSiO_{3/2})_{12}$ Complexes Calculated at B3LYP/6-311G(d,p) Level.

Ionization process			IP adiabatic	exptIP[a]	ΔIP
Li^-	→	$Li + e^-$	11.6		
$Li^-@H_{12}Si_{12}O_{18}$	→	$Li @H_{12}Si_{12}O_{18} + e^-$	13.7		20.9
Li	→	$Li^+ + e^-$	129.5	124.3	
$Li @H_{12}Si_{12}O_{18}$	→	$Li^+@(HSi_{3/2})_{10} + e^-$	65.7		195.2
Na^-	→	$Na + e^-$	10.3		
$Na^-@H_{12}Si_{12}O_{18}$	→	$Na@H_{12}Si_{12}O_{18} + e^-$	0.3		0.4
Na	→	$Na^+ + e^-$	125.0	118.5	
$Na@H_{12}Si_{12}O_{18}$	→	$Na^+@ H_{12}Si_{12}O_{18} + e^-$	65.5		331.1
K^-	→	$K + e^-$	10.1		
$K^-@H_{12}Si_{12}O_{18}$	→	$K@ H_{12}Si_{12}O_{18} + e^-$	23.2		-13.1
K	→	$K^+ + e^-$	113.7	100.1	
$K@H_{12}Si_{12}O_{18}$	→	$K^+@ H_{12}Si_{12}O_{18} + e^-$	56.3		160.0

[a] References 82, 83

Table 5.12 Chemical Shifts (δ ppm) for Nuclei in T-$_{12}$POSS and T_{12}-POSS Endohedral Complexes with D_{2d} Isomer Calculated at the B3LYP/6-311G(d,p) Level.

System	Si (δ)	H (δ)	X (δ ppm)
$(HSiO_{3/2})_{12}$ and NICS at D5R ring	-93.23, -89.65	4.82,4.72	-0.24 (0.24)
$(HSiO_{3/2})_{12}$ and NICS at the center	-93.23, -89.65	4.82, 4.72	-0.56 (0.56)
$He@(HSiO_{3/2})_{12}$	-103.35, -98.36	4.83, 4.73	0.79
$Ne@(HSiO_{3/2})_{12}$	438.97	5.59, 5.59	31.92
$Ar@(HSiO_{3/2})_{12}$	429.12, 424.98	4.88, 4.73	136.28
$Li^{+}@(HSiO_{3/2})_{12}$	-77.85, -88.20	5.14, 4.95	4.48
$Na^{+}@(HSiO_{3/2})_{12}$	-84.21	5.02, 5.15	72.04
$F^{-}@(HSiO_{3/2})_{12}$	-94.40, -90.91	4.55, 4.48	138.72
$Cl^{-}@(HSiO_{3/2})_{12}$	-99.51, 94.54	4.61, 4.49	274.71
$Br^{-}@(HSiO_{3/2})_{12}$	-94.55, -99.15	4.62, 4.06	762.49

Table 5.13 Chemical Shifts (δ ppm) for Nuclei inT-$_{12}$POSS and T_{12}-POSS Endohedral Complexes with D_{6h} Isomer Calculated at the B3LYP/6-311G(d,p) Level.

System	Si (δ)	H (δ)	X (δ ppm)
T_{12}-POSS Cage	433.70, 433.60	4.84	
$(HSiO_{3/2})_{12}$ and NICS at the center	433.70, 433.60	4.84	-0.68 (-0.68)
$He@(HSiO_{3/2})_{12}$	-93.05, -92.95	4.84,	0.87
$Ne@(HSiO_{3/2})_{12}$	-93.07, 92.97	4.84	28.5
$Ar@(HSiO_{3/2})_{12}$	93.07, -92.97	4.86	107.08
$F^{-}@(HSiO_{3/2})_{12}$	-95.15, -95.13	4.58, 4.59	123.67
$Cl^{-}@(HSiO_{3/2})_{12}$	-95.27, -95.23	4.61, 4.63	885.33 263.83
$Br^{-}@(HSiO_{3/2})_{12}$	-95.16, -95.19, -87.83	4.62, 9.28, 9.24	673.76

Table 5.14 B3LYP/6-311G(d,p) Calculated Properties of Counterion Li^+ and F^- with T_{10}-POSS. Total energies (Hatrees) Zero Point Energies (ZPE in kca/mol), Binding Energies (E_b in kcal/mol) and Natural Charge on Li^+ and F^- in the T_{12}-POSS.

System	Energy	ZPE	E_{bind}	Charge on X
$LiF@(HSiO_{3/2})_{12}$ (D_{2d})	-4945.220566	135.1	-35.9	L^+ = 0.89 F^- = -0.81
$F^-@Li^+(HSiO_{3/2})_{12}$ (D_{2d})	-4945.230697	135.2	-33.5	L^+ = 0.87 F^- = -0.87
$F^-@Li^+(HSiO_{3/2})_{12}$ (D_{6h})	-4945.233752	135.1	-40.4	L^+ = 0.91 F^- = -0.88
$F^-@Li^+(HSiO_{3/2})_{12}$ (D_{6h})	-4945.233674	134.8	-40.4	L^+ = 0.90 F^- = -0.88

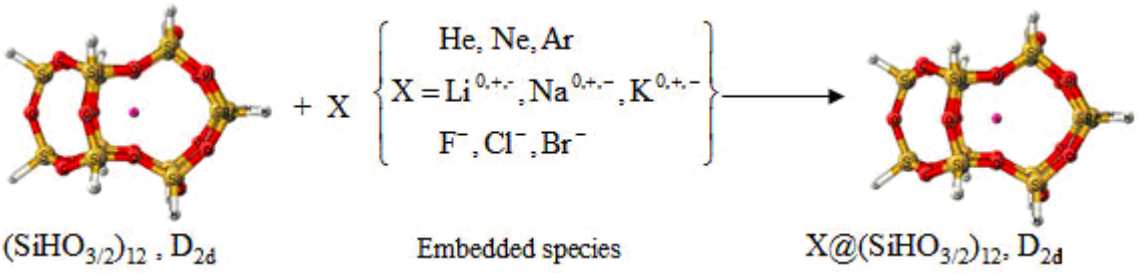

Figure 5.1 Schematic Representations of the Host Cage Species $(SiHO_{3/2})_{10}$ with D5R units and Impurities; (a) Host Cage with D_{5h} Symmetry (b) Identity of X (c) Endohedral Species of $X@(SiHO_{3/2})_{12}$.

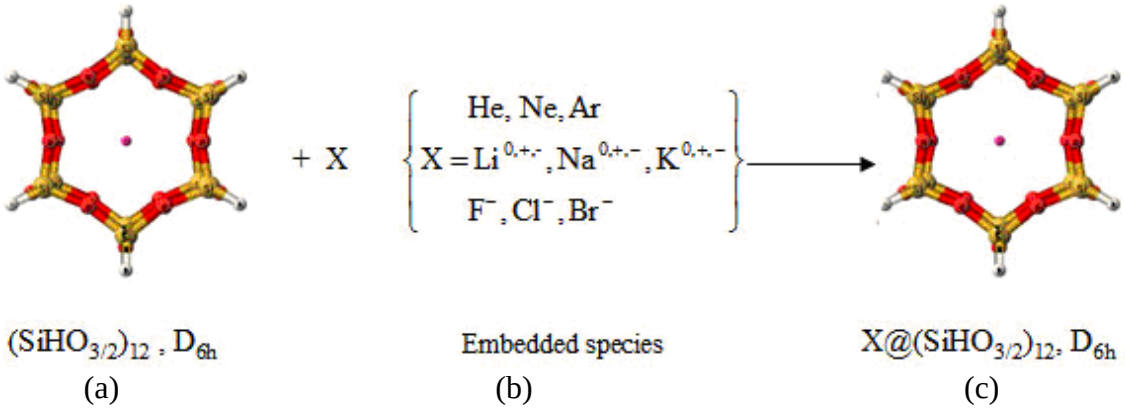

Figure 5.2 Schematic Representations of the Host Cage Species $(SiHO_{3/2})_{10}$ with D5R units and Impurities; (a) Host Cage with D_{6h} Symmetry (b) Identity of X (c) Endohedral Species of $X@(SiHO_{3/2})_{12}$.

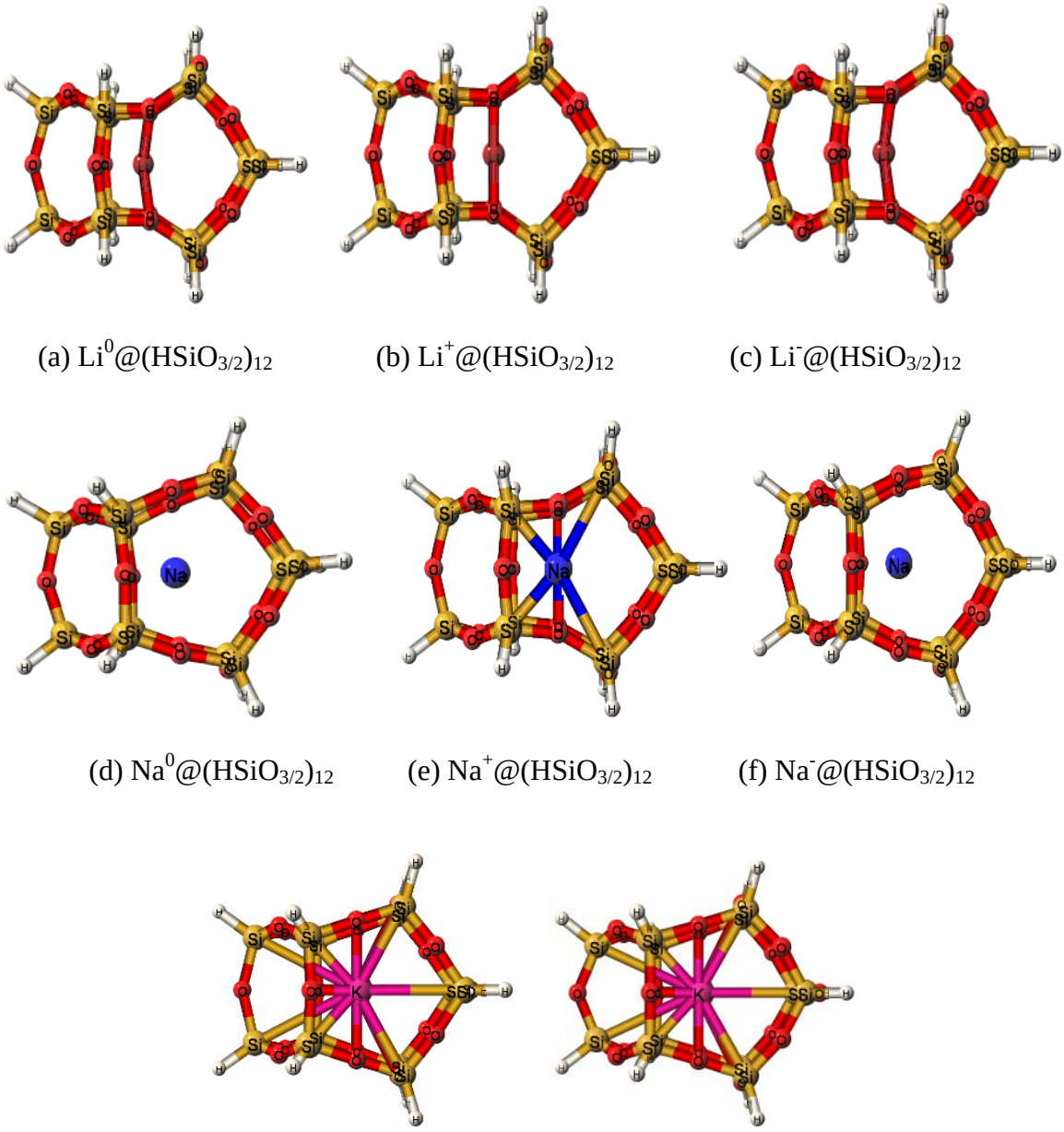

(a) $Li^0@(HSiO_{3/2})_{12}$ (b) $Li^+@(HSiO_{3/2})_{12}$ (c) $Li^-@(HSiO_{3/2})_{12}$

(d) $Na^0@(HSiO_{3/2})_{12}$ (e) $Na^+@(HSiO_{3/2})_{12}$ (f) $Na^-@(HSiO_{3/2})_{12}$

(g) $K^0@(HSiO_{3/2})_{12}$ (h) $K^+@(HSiO_{3/2})_{12}$

Figure 5.3 Optimized Geometries of Endohedral $X@(HSiO_{3/2})_{12}$ Complexes at the B3LYP/6-311G(d,p) Level with D_{2d} Symmetry.

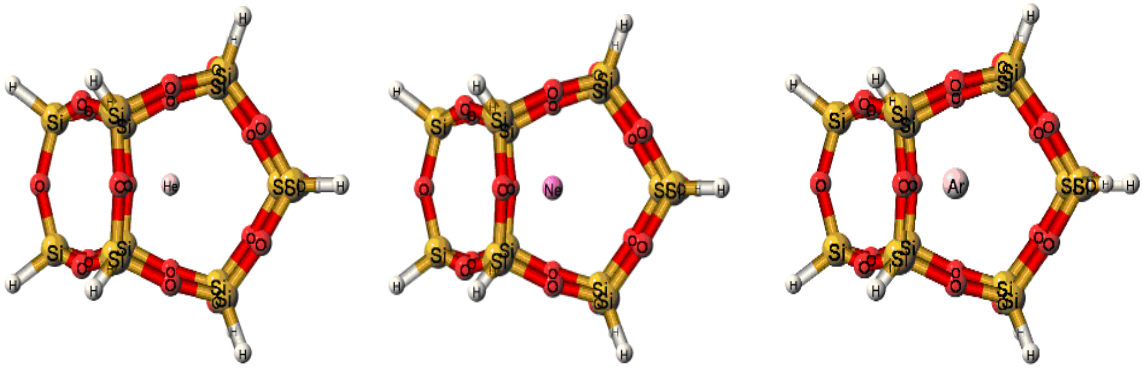

(j) $He@(HSiO_{3/2})_{12}$ (k) $Ne@(HSiO_{3/2})_{12}$ (l) $Ar@(HSiO_{3/2})_{12}$

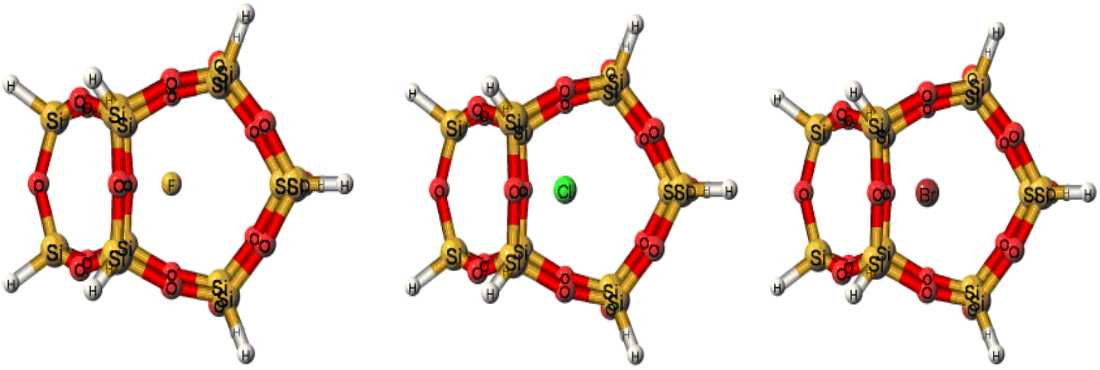

(l) $F^{-}@(HSiO_{3/2})_{12}$ (m) $Cl^{-}@(HSiO_{3/2})_{12}$ (n) $Br^{-}@(HSiO_{3/2})_{12}$

Figure 5.3 (continued).

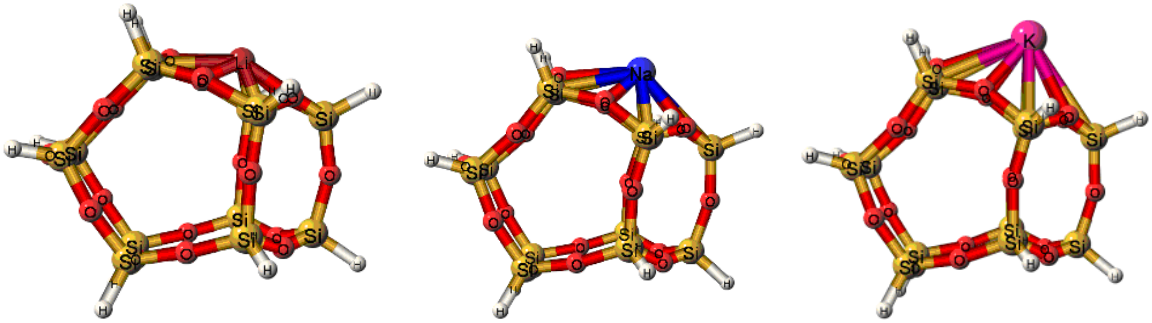

(a) $Li^{+}(HSiO_{3/2})_{12}$ (b) $Na^{+}(HSiO_{3/2})_{12}$ (g) $K^{+}(HSiO_{3/2})_{12}$

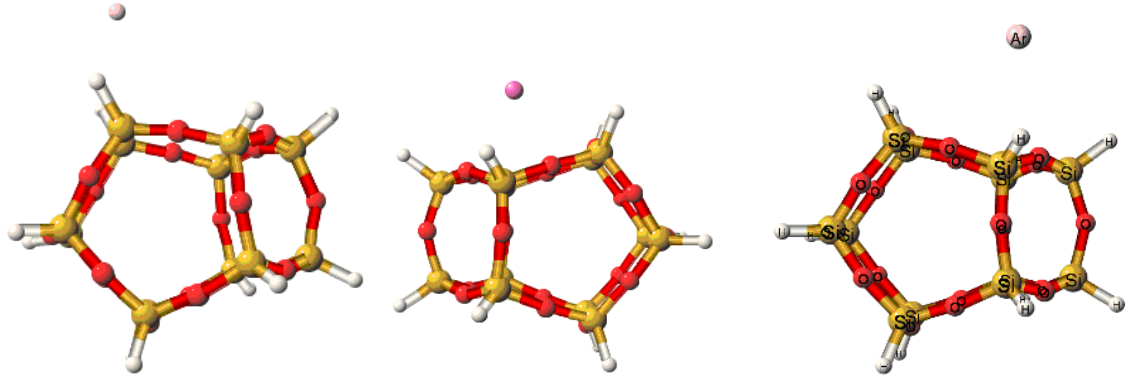

(c) $He(HSiO_{3/2})_{12}$ (d) $Ne(HSiO_{3/2})_{12}$ (e) $Ar(HSiO_{3/2})_{12}$

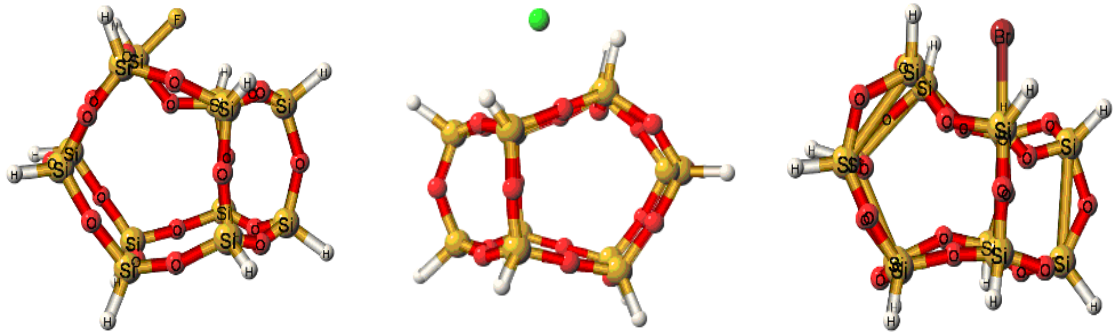

(d) $F^{-}(HSiO_{3/2})_{12}$ (e) $Cl^{-}(HSiO_{3/2})_{12}$ (g) $Br^{-}(HSiO_{3/2})_{12}$

Figure 5.4 Optimized Geometries of Exohedral $X(HSiO_{3/2})_{12}$ with D_{2d} Symmetry at the B3LYP/6-311G(d,p) Level.

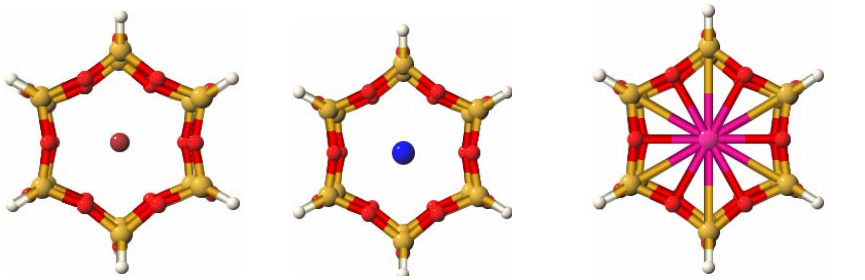

(a) $Li^{+}@(HSiO_{3/2})_{12}$ (b) $Na^{+}@(HSiO_{3/2})_{12}$ (c) $K^{+}@(HSiO_{3/2})_{12}$

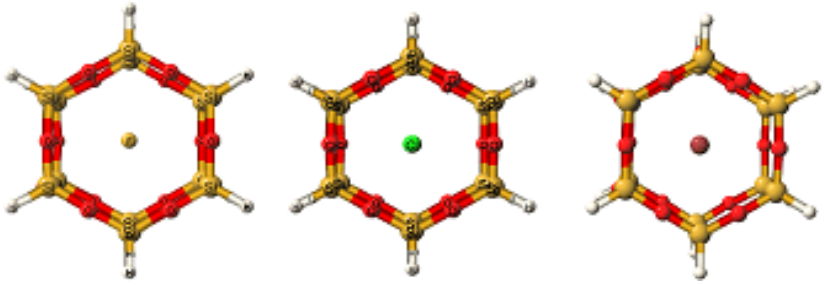

(d) $F^{-}@(HSiO_{3/2})_{12}$ (f) $Cl^{-}@(HSiO_{3/2})_{12}$ (g) $Br^{-}@(HSiO_{3/2})_{12}$

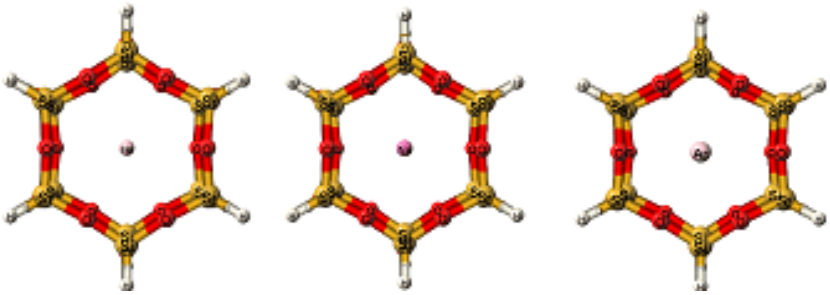

(h) $He@(HSiO_{3/2})_{12}$ (i) $Ne@(HSiO_{3/2})_{12}$ (j) $Ar@(HSiO_{3/2})_{12}$

Figure 5.5 Optimized Geometries of Endohedral $X@(HSiO_{3/2})_{12}$ Complexes at the B3LYP/6-311G(d,p) Level with D_{6h} Symmetry.

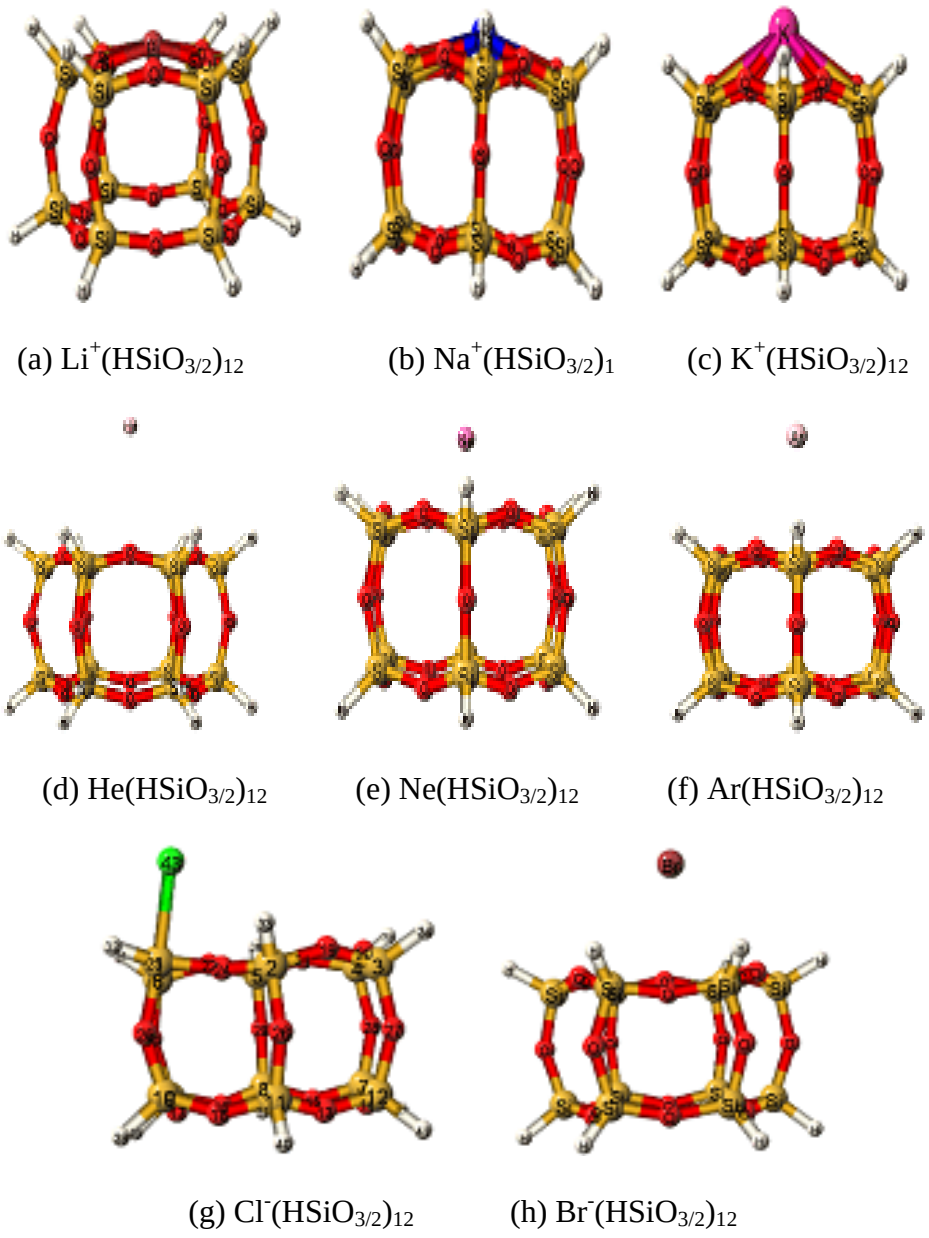

(a) $Li^{+}(HSiO_{3/2})_{12}$ (b) $Na^{+}(HSiO_{3/2})_{1}$ (c) $K^{+}(HSiO_{3/2})_{12}$

(d) $He(HSiO_{3/2})_{12}$ (e) $Ne(HSiO_{3/2})_{12}$ (f) $Ar(HSiO_{3/2})_{12}$

(g) $Cl^{-}(HSiO_{3/2})_{12}$ (h) $Br^{-}(HSiO_{3/2})_{12}$

Figure 5.6 Optimized Geometry of Exohedral $X(HSiO_{3/2})_{12}$ with D_{6h} Symmetry at the B3LYP/6-311G(d,p) Level.

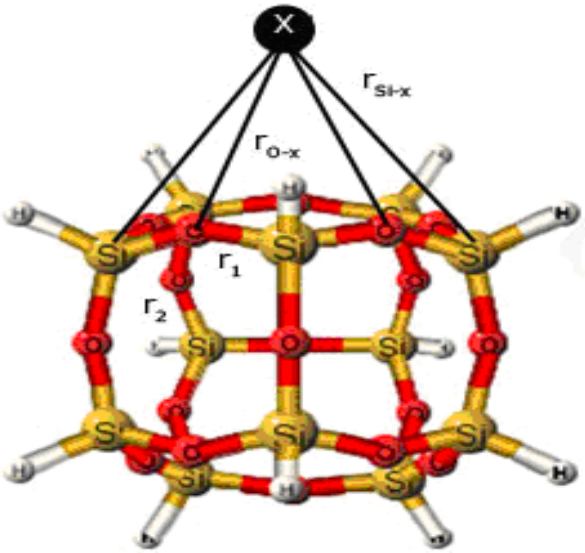

Figure 5.7 Schematic Geometry for the Exohedral $X^+(HSiO_{3/2})_{12}$ Complexes (D_{2d} isomer). X = Alkali Metal Species, Noble Gases and Halide Ions.

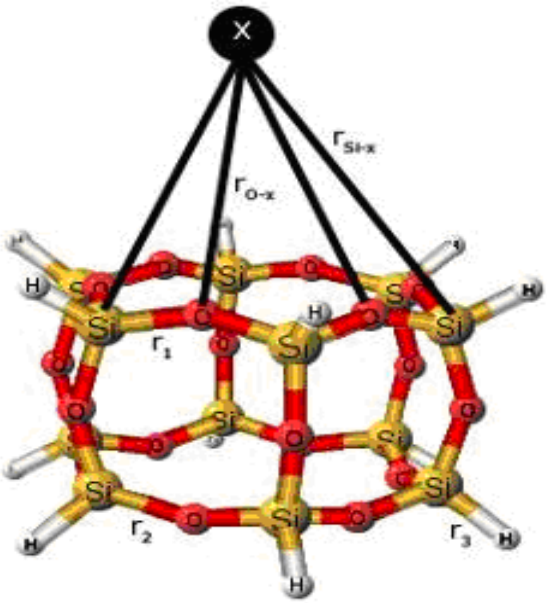

Figure 5.8 Schematic Geometry for the Exohedral $X^+(HSiO_{3/2})_{12}$ Complexes (D_{6h} isomer). X = Alkali Metal Species, Noble Gases and Halide Ions.

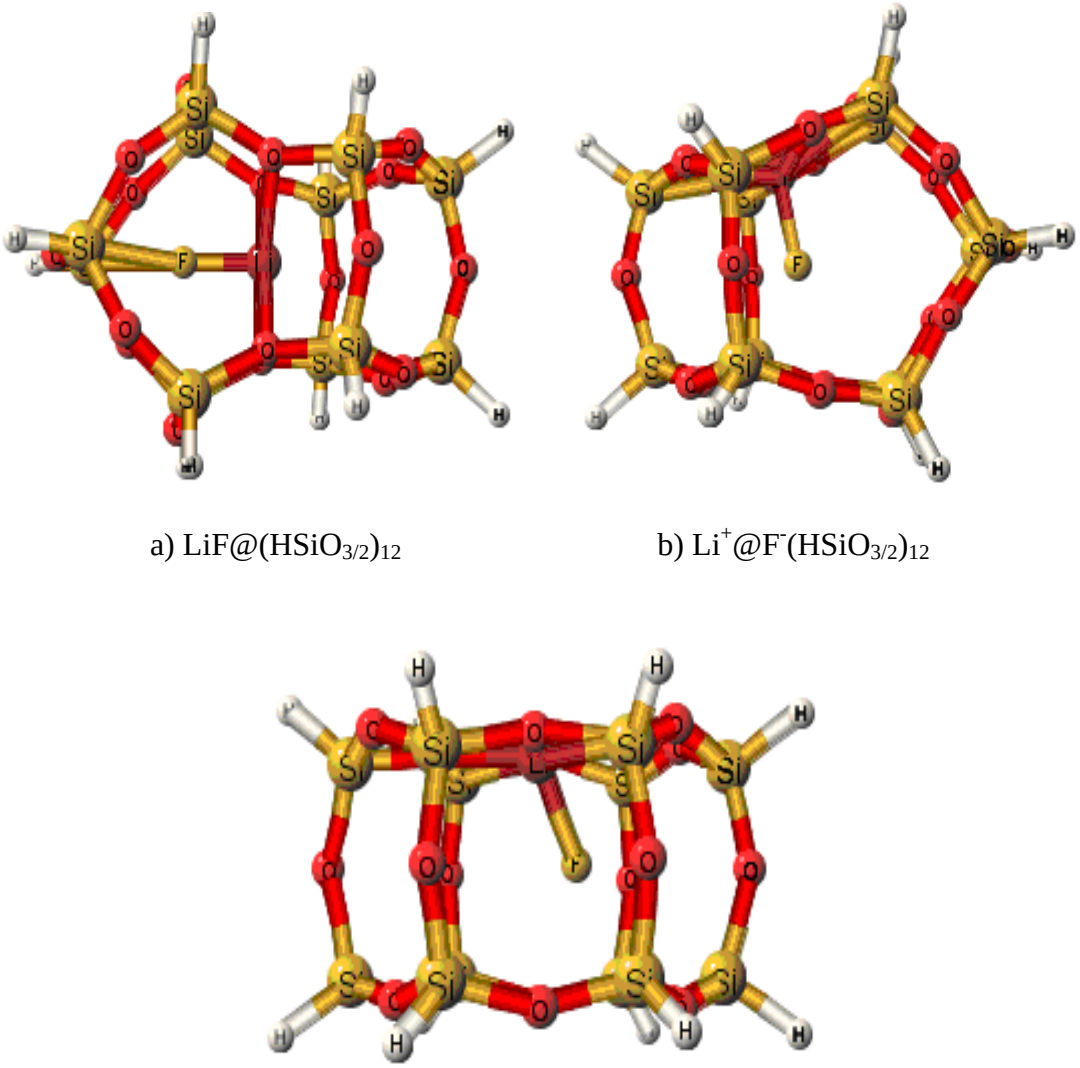

a) $LiF@(HSiO_{3/2})_{12}$ b) $Li^{+}@F^{-}(HSiO_{3/2})_{12}$

c) $Li^{+}@F^{-}(HSiO_{3/2})_{12}$

Figure 5.9 Optimized Geometries of $F^{-}@\ Li^{+}(HSiO_{3/2})_{12}$ Ion pair at the B3LYP/6-311(d,p) Level. (a) $F^{-}@\ Li^{+}(HSiO_{3/2})_{10}$, Placing both Li^{+} and F^{-} Inside the CageCenter. (b) $F^{-}@\ Li^{+}(HSiO_{3/2})_{12}$, Placing Li^{+} on D5R Surface and F^{-} Inside the Cage Center. (c) Placing Li^{+} on D6R Surface and F^{-} Inside the Cage Center and both Li^{+} and F^{-} Inside the Cage Center.

CHAPTER VI

STRUCTURES AND STABILITIES OF ENDO- AND EXO-DODECAHEDRAL SILSESQUIOXANE (T_{12}-POSS) COMPLEXES WITH TRANSITION METALS ATOMS AND IONS

Introduction

The polyhedral oligomeric silsesquioxanes (POSSs) are important nanostructured hybrid inorganic-organic chemicals. The H-silsesquioxane building block is the ($HSiO_{3/2}$) unit, designated by the letter T. The structures of POSS compounds are based on siloxane-containing cages that are formed from ($HSiO_{3/2}$) or ($RSiO_{3/2}$). Dodecasilsesquoixane, $(HSiO)_{12}$, (denoted as T_{12}-POSS) consists of 12 silicon atoms that are connected to each other through intermediate oxygen atoms and a hydrogen atom attached to each silicon. The synthesis, applications and theoretical studies of POSS derivatives were already reviewed very recently by Li et al.[1] These studies were limited with T_8-POSS cages.

Since their discovery in 1946[2], POSS compounds have drawn a great deal of attention because of their applications in material sciences and catalysis.[1,3-27] POSS compounds are cage molecules. The cavity sizes of these cages are big enough to act as a

host for atoms or ions. Bassindale *et al*[28] recently reported the synthesis of the endoheral fluoride-ion T_8-silsequioxane complex. After publishing this exciting result, the possibility of discovering of other endohedral POSS complexes has become more realistic. The majority of theoretical studies[29-34] have been devoted to pure cages and studies of endohedral complexes with POSS cages are very rare. So far, the only theoretical investigations of endohedral T_8-POSS complexes have been done by Geroge et al[35], Park et al (our group)[36] and Gordon and Tejerina.[37] Gordon and Tejerina[37] studied the insertion mechanism of O_2/N_2 into the T_8, T_{10} and T_{12} cages. Mattori et al[38] studied the trapping and detrapping of H-atom into the T_8-POSS cage. No reports exist on the insertion of transition metals into the POSS cages. Transition metal encapsulation into the POSS cages might produce different important endohedral complexes. Transition metal encapsulation may tune the electronic band gaps of POSS and hence alter their light emitting properties. In this section we report the results of our investigation of endohedral T_{12}-POSS complexes with transition metal atoms and ions (Figure 6.1). Their structures, stabilities, electronic properties, ionization potentials and NMR chemical shifts were discussed.

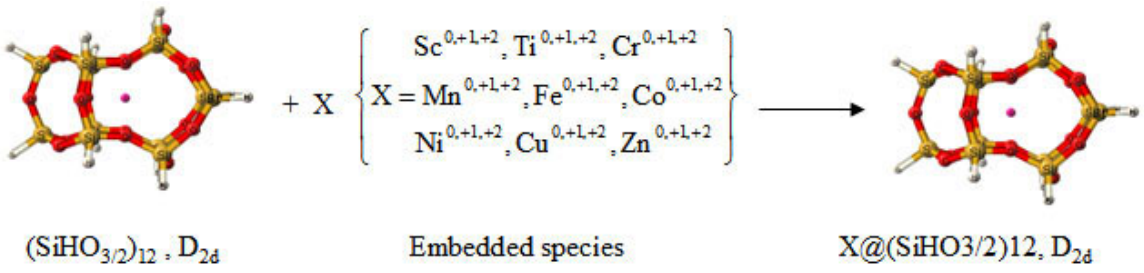

Figure 6.1 Schematic Representations of Host Cage, Embedded Species and Endohedral Complex.

T_{12}-POSS compounds could exist as twelve different isomers. Tejerina et al[37] investigated theoretically all of these possible T_{12}-POSS structures. The most stable isomers have D_{2d}, D_{6h} and T_d symmetries. The D_{2d}, D_{6h} and T_d structures are designated as $\{4^55^4\}$, $\{4^66^2\}$ and $\{3^46^4\}$ topologies, respectively. The T_d isomer contains three member rings and was predicted to be unstable.[29] Hence the possible stable isomers for T_{12}-POSS are D_{2d} and D_{6h}. The energy difference between D_{2d} symmetry with $\{4^55^4\}$ topology and D_{5h} and T_d isomers, with $\{4^66^2\}$ and $\{3^46^4\}$ topologies, obtained using HF theory are 4.7 kcal/mole and 16.3 kcal/mole respectively.[38] Earley[29] estimated the energy difference between D_{2d} and D_{6h} isomers to be 2.6 kcal/mole using HF theory. The D_{2d} isomer was found to be 1 kcal/mol stable than that of D_{6h} isomer using MP2 theory. The only experimental structure of T_{12}-POSS has D_{2d} symmetry, determined by X-ray diffraction.[39] The only isomer detected in solution had D_{2d} symmetry (with $\{4^55^4\}$ topology) based on ^{1}H and ^{29}Si-NMR studies.[40-42]

The D_{6h} isomer can be described as a double six-member ring and is observed as a secondary building block in solid-state geolites. Herein, the D_{2d} isomer is predicted to be 5.3 kcal/mol more stable than the D_{6h} isomer at the B3LYP/6-311G(d,p) level of theory, in agreement with previous experiments and theoretical predictions. The D_{2d} symmetry with $\{4^55^4\}$ topology is taken, herein, as the basis for all the model calculations. Further computations on the D_{6h} symmetry with $\{4^66^2\}$ topology were performed for comparison.

Computational Details

All calculations were performed using density functional theory (DFT/B3LYP).[43,44] The 6-311G(d,p) basis set was used to optimize the geometry and frequency calculations for the T_{12}-POSS system. This basis set was also used for the geometry optimization and frequency calculation of the endohedral X@T_{12}-POSS complexes (X= $Sc^{0,+1,+,2}$, $Ti^{0,+2}$, $Cr^{0,+1,+2}$, $Mn^{0,+1,+2}$ $Fe^{0,+1,+2}$, $Co^{0,+1+,2}$, $Ni^{0,+1,+2}$, $Cu^{0,+1,+2}$, $Zn^{0,+1,+2}$). The basis set LanL2DZ is used for the calculation of endohedral complexes of T_{12}-POSS with Mo^0, $W^{0,+1,+2}$. The Gaussian 03 program was used to perform these calculations.

The endohedral atoms or ions were introduced into the center of T_{12}-POSS cage (Figure 6.1) and geometry optimizations were then performed. The atoms and ions were situated outside of the 5DR (D_{2d}) faces and along an axis passing from the cage center through the geometric center of the 5DR rings as the starting point for optimizations of the exohedral complexes geometries. The natural bond orbital (NBO) calculations[48] were performed to obtain the electronic properties. The relative energies E_{inc}, E_{bind}, and E_{isom} were calculated according to the equations:

$$E_{inc} = E_{endo} - (E_{cage} + E_x)$$

$$E_{bind} = E_{exo} - (E_{cage} + E_x)$$

$$\Delta E_{isom} = E_{exo} - E_{endo}$$

All energies were corrected using the unscaled zero point energies.

The vibrational harmonic frequencies for $(HSiO_{3/2})_{12}$ and X@$(HSiO_{3/2})_{12}$ were computed for all optimized structures using the same levels of theory, to characterize the

stationary points as minima (zero imaginary frequencies) or saddle points. The NMR shielding tensors for selected systems were calculated using B3LYP/6-311G (d,p) and GIAO methods.[46,47]

Results and Discussions

Geometries of POSS cage

Table 6.1 summarizes the geometries, the optimized bond lengths and bond angles for the D_{2d} isomer of T_{12}-POSS and its endohedral X@T_{12}-POSS complexes. All of these were calculated at the B3LYP/6-311(d,p) level. The accuracy of the calculated geometries of $(HSiO_{3/2})_{12}$ can be assessed by comparison to the X-ray crystal structure of the D_{2d} isomer.[39,50] The X-ray crystal structure of this molecule was found to have approximate D_{2d} symmetry, with Si-O bond lengths ranging 1.582-1.617 Å. *In the calculations conducted herein, the Si-O bond lengths range from 1.630 to 1.642 Å.*

Comparison of the calculated structure of the D_{6h} $(HSiO_{3/2})_{12}$ isomer with experimental results is not possible because D_{6h} isomer has never been isolated. However, the calculated structures of both D_{2d} and D_{6h} isomers can be compared with other theoretical results. The bond lengths and angles obtained here agree well with previous experimental[51] and theoretical[38,30] results. de Man and Sauer calculated a Si-O distance of 1.64 Å using the HF method and a split-valence plus polarization basis set.[30] Tossell predicted an Si-O distance of 1.64 Å using HF/6-31G* calculations.[31] Xiang *et al*. have studied the molecular and electronic structure of the T_n-POSS compounds (n even, 4-16) using DFT with a double-ζ basis set and predicted a Si-O distance of 1.64.[33] Using LDA-DFT with an effective core potential (ECP), Pasquarello et al[32] obtained a Si-O distance

of 1.62 Å, the same as experimental X-ray diffraction values (Si-O, 1.62 Å). The Si-O distances in both D_{2d} and D_{6h} isomers (Table 6.1) obtained in this dissertation by the B3LYP/6-311G (d,p) method are agree with previous experimental and calculated values.

Endohedral T_{12}-POSS complexes

The transition metals or their ions were placed at center of the D_{2d} isomer of $(HSiO_{3/2})_{12}$ and then optimized under D_{2d} symmetry constraints. All optimized geometries were minima except for the Sc^0, Co^0, Ni^0 and Cu^0 endohedral complexes. The optimized D_{2d} structures are shown in Figures 6.2, 6.3 and 6.4. Each of these four complexes has one imaginary frequency indicating that these complexes are saddle points or transition states on the potential energy surfaces. No attempts were made to find the minima for the complexes.

The endohedral neutral complexes $X@(HSiO_{3/2})_{12}$ ($X=Sc^0$, Cr^0, Fe^0, Co^0, $Ni^{0,}$, $Cu^{0,}$, Zn^0, Mo^0, W^0), have different guest to-cage oxygen (X-O) and guest to-silicon (X-Si) internuclear distances. Tables 6.1 show selected X-Si and X-O distances for the Sc^0, Cr^0, Fe^0, Co^0, $Ni^{0,}$, $Cu^{0,}$, Zn^0, Mo^0, W^0 D_{2d} encapsulated complexes. The X-O distances decrease between the embedded atom, or its ion, and its nearest neighbor oxygen in the order $M>M^{+1}>M^{+2}$ (Table 6.1). The changes in bond distances and angles depend on the endohedral cation's size. The cage size contracts upon cation insertion because of the attractive interaction between cage framework atoms and embedded cations. The Si-H bond lengths shorten when hosting a metal cation versus its corresponding neutral metal. For example, The Si-H bond lengths in endohedral $Ni^0@(HSiO)_{12}$ are 1.462Å while those of $Ni^+@(HSiO)_{12}$ (1.450 Å) and $Ni^{+2}@(HSiO)_{12}$ (1.452Å) are shortened. The Si-H bond

shortens in $Ni^{+}@(HSiO)_{12}$ and $Ni^{+2}@(HSiO)_{12}$ because electron donation from cage atoms to metal cation causes an increase in *s* character in the Si-H bonds.

Inclusion Energies

The total energy and the ZPE-corrected endohedral inclusion energies (E_{inc}) for $X@(HSiO_{3/2})_{12}$ (X= $Sc^{0,+1,+2}$, Cr^{0}, $Fe^{0,+1,+2}$, $Co^{0,+1,+2}$, $Ni^{0,+1,+2}$, $Cu^{0,+1,+2}$, $Zn^{0,+1,+2}$, Mo, $W^{0,+1,+2}$) complexes constructed from the D_{2d} isomer are reported in Table 6.2. The inclusion energies obtained from the B3LYP/6-311G(d,p) level calculations reveal that all these complexes are more stable than the corresponding separated ions and the empty cage, except for three cases: $X@(HSiO_{3/2})_{12}$ (X=Cr^{0}, Ni^{0} and Zn^{0}) . The inclusion energies for the endohedral neutral atoms and their cations follows the trend $M^{+2} > M^{+1} > M^{0}$. This indicates that the size and charge of the embedded species are important factors influencing the stability of the endohedral transition metal complexes. The strain energy increases with increasing the size of the embedding species. The values of E_{inc} in Table 6.2, increase (negative value) as the atomic number (hence size) of X decreases within its periodic table group. Other factors in addition to guest size impact the endohedral binding energies. Large differences exist between the natural charges of similar sized guests and these are shown in Table 6.3. This suggests that charge transfer from the encapsulated species to the host cage determines the magnitude of E_{inc} in the absence of size effects.

Electronic properties

Table 6.3 summarizes the charge on different endoheral transition metals and their +1 ions. These are important because electronic properties depend on both the nature and charge of the metal atom embedded inside the T_{12}-POSS cage The endohedral metal atoms Sc^0, Mn^0 and Co^0 acquire electron density from the T_{12}-POSS cage. In contrast, endohedral Cr^0, Ni^0, Cu^0, and Zn^0 atoms provide electron density to the host cage. Electron donation occurs from endohedral Cr^0, Co^0, Ni^0, Cu^0, and Zn^0 metal atoms into the Si–O bonds. All of the transition metal cations in the endorheral cationic complexes gain electron density from the cage framework atoms.

The HOMO-LUMO gaps for different endohedral complexes are presented in Table 6.5. The HOMO-LUMO gap of $(HSiO_{3/2})_{12}$ is very large (8.12 eV). Hence the pure T_{12}-POSS cage is not suitable for an optoelectronic material. However, inclusion of metal atoms into the cage reduces these gaps and optoelectronic properties appear in different regions of the absorption spectrum. The HOMO-LUMO gaps for these endohedral zero-valent transition metal complexes vary over the range of 1.67-6.66 eV. These large HOMO-LUMO gaps indicate that the endohedral complexes $X@(SiHO_{3/2})_{12}$ are stable.

Ionization Potentials

The ionization potentials for $X@(SiHO_{3/2})_8$ (X= Sc^0, Fe^0,Co^0, Ni^0, Cu^0, Zn^0), calculated at the B3LYP/6-311G(d,p) level, are summarized in Table 6.4. For Ca and Zn the calculated ionization potentials are with 3% of the experimental values. However, for other transition metals the errors are large up to ~40%. The ionization potentials of encapsulated Sc^0, Fe^0, Co^0, Ni^0, Cu^0, and Zn^0, are all considerably lower than those of the

free metal. Table 6.4 also summarizes the ΔIP values. The ΔIP values (versus the free metal) range from 0.8 to 123.7 kcal/mol. This is consistent with the computational predictions for alkali metals encapsulated by the T_{10}-POSS cages and with dodecahedrane endohedral complexes of alkali and alkaline earth metals.[49]

Boldyrev and coworkers[51-53] defined species with first a ionization potential less than that of atomic Cs (90.0kcal/mol; 3.9 eV) to be "superalkalies". The first ionization potentials for T_8-POSS encapsulated Sc^0, Fe^0, Co^0, Cu^0 and Zn^0, range from 96.6 kcal/mol to 158.3 kcal/mol. These values are significantly higher than that of cesium. Thus these complexes do not qualify as "superalkalies". This contrasts with the predicted ionization potentials endohedral alkali metal complexes of T_{10}-POSS, T_{12}-POSS and dodecahedrane[49] which were "superalkalies". The ionization potential for Ni is 66.5 kcal/mol.

NMR Chemical Shifts

Chemical shielding tensors was calculated for the empty cage and the endohedral complexes at the B3LYP level using GIAO method. The chemical shifts are summarized in Table 6.5. ^{29}Si and ^{1}H are referenced against TMS while the shifts for transition metals are the difference between the isotropic shielding of the cage metal and that of the pure metal. The values are given in ppm. The computed chemical shifts for the Si atoms of the pure T_{12}-POSS cage are –89.65 and –93.23 and for H are 4.82 and 4.72 ppm respectively. These values are in excellent agreement with the experimental values (Si = -85.78, -87.76; H = 4.26, 4.29 ppm).[40]

The chemical shifts values indicate that the $(HSiO_{3/2})_{12}$ cage deshields the encapsulated atomic and ionic species. As the size of the ions or atom increases the deshielding becomes more pronounced (Table 6.5). The NICS at the center of the $(HSiO_{3/2})_{12}$ cage is –0.56 ppm. The NICS calculated at the D5R ring center is –0.24 ppm. These two values may be compared to the NICS value at the center of benzene (-11.5 ppm) or cyclohexane (-2.1 ppm),[54] to illustrate the lack of cyclic electron delocalization in the T_{12}-POSS cage. Since the NICS value of $(HSiO_{3/2})_{12}$ at the center of cage or D5R ring center is small, no evidence exists for either aromaticity or antiaromaticity in the empty T_{12}-POSS cage.

Upon encapsulation of Sc^0,Ti^0, Cr^0, Mn^0, Fe^0, Co^0, Ni^0, Cu^0 or Zn^0 into the $(HSiO)_{12}$ (D_{2d}) cage, the ^{29}Si chemical shifts in $X@(HSiO_{3/2})_{12}$ are shifted significantly relative to the ^{29}Si chemical shifts of $(HSiO_{3/2})_{12}$ pure cage (Table 6.5). These ^{29}Si chemical shifts are isolated from each other and can be easily identified. The predicted ^{1}H chemical shifts in Sc^0,Ti^0, Cr^0, Mn^0, Fe^0, Co^0, Ni^0, Cu^0 and Zn^0 are displaced relative to the ^{1}H chemical shifts in $(HSiO_{3/2})_{12}$. The change of ^{1}H chemical shifts in $X@(HSiO_{3/2})_{12}$ is highest for Cr encapsulation and lowest for Cu relative to the proton chemical shift of $(HSiO_{3/2})_{12}$. Both ^{1}H and ^{29}Si NMR are predicted to be useful in detecting all endohedral complexes $X@(HSiO_{3/2})_{12}$ obtained from D_{2d} isomer.

Conclusions

These *ab intio* calculations predicted that the cavity of the T_{12}-POSS cage is sufficiently large to accommodate many transition metal atoms or their cations. Several endohedral host-guest combinations were observed where inclusion of the metal or its

cation was energetically favorable. The zero-point corrected inclusion energies of the endohedral $X@(SiHO_{3/2})_8$ ($X = Sc^{0,+1,+2,}$ $Mn^{0,+1,+2}$, $Fe^{0,+1,+2}$, $Co^{0,+1,+2}$, $Ni^{+1,+2}$, $Cu^{0,+1,+2}$, Mo^0, $W^{0,+1,+2}$) are exothermic so these complexes are more stable than their isolated components except for ($X = Cr^0$, Ni^0 and Zn^0) complexes, which are formed endothermically. The inclusion energies for the neutral atoms and their cations follows the trend $M^{+2} > M^{+1} > M^0$.

The Si-O and Si-H bond lengths were shortened when hosting a cation versus their corresponding neutral transition metal atoms. This is due to the donation of electron density from the cage framework to the metal cation.

The cage properties changed quite distinctly upon encapsulating a transition metal atom or ion. For example, upon encapsulation of Ti^0, Cr^0, Fe^0, Ni^0, Cu^0, Zn^0 and W^0 into the T_{12}-POSS cage, electron density is transferred from the metal to the cage. In contrast, encapsulation of Sc^0, Mn^0 and Co^0 leads to donation of electron density from the cage to the encapsulated metal.

The ionization potentials of endohedral $X@(SiHO_{3/2})_{10}$ ($X = Sc^0$, Fe^0, Co^0, Ni^0, Cu^0, Zn^0) species are lower than those of the isolated metal. However, the drop in ionization potential is not sufficient to classify any of these species as superalkalis.

The HOMO-LUMO gaps of the endohedral transition metal T_{12}-POSS complexes are smaller than that of the pure cage. The predicted HOMO-LUMO gaps suggest that various endohedral transition metal complexes can be used to tune the HOMO-LUMO gaps and to absorb light over wide range of absorption bands.

Both ^{1}H and ^{29}Si NMR chemical shifts are predicted to be useful in detecting all endohedral transition metal complexes $X@(HSiO_{3/2})_{12}$ obtained from D_{2d} isomer.

Overall, the present work suggests a new research direction. The transition metal T_{12}-POSS complexes are unknown experimentally. All the endohedral cage complexes $X@(SiHO_{3/2})_{12}$ that were predicted to be more stable than their isolated components appear to be viable synthetic targets.

References

(1) Li, G.; Wang, L.; Ni, H.; Pittman, C. U., Jr. *J. Inorg. Organomet. Polym.* **2002**, *11*, 123.

(2) Scott, D. W. *J. Am. Chem. Soc.* **1946**, *68*, 356.

(3) Brown, J. F., Jr.; Vogt, L. H., Jr. *J. Am. Chem. Soc.* **1965**, *87*, 4313.

(4) Feher, F. J.; Wyndham, K. D. *Chem. Commun.* **1998**, 323

(5) Li, G. Z.; Wang, L.; Toghiani, H.; Daulton, T. L.; Koyama, K.; Pittman, C. U., Jr. *Macromolecules* **2001**, *34*, 8686.

(6) Li, G. Z.; Wang, L.; Toghiani, H.; Daulton, T. L.; Pittman, C. U. *Polymer* **2002**, *43*, 4167.

(7) Maxim, N.; Abbenhuis, H. C. L.; Stobbelaar, P. J.; Mojet, B. L.; van Santen, R. A. *Phys. Chem. Chem. Phys.* **1999**, *18*, 4473.

(8) Maxim, N.; Magusin, P. C. M. M.; Kooyman, P. J.; van Wolput, J. H. M. C.; van Santen, R. A.; Abbenhuis, H. C. L. *Chem. Materials* **2001**, *13*, 2958.

(9) Zheng, L.; Waddon, A. J.; Farris, R. J.; Coughlin, E. B. *Macromolecules* **2002**, *35*, 2375.

(10) Wada, K.; Yamada, K.; Kondo, T.; Mitsudo, T.-A. *Chem. Lett.* **2001**, 12.

(11) Dance, B. *Semiconduct. Int.* **2001**, *24*, 46.

(12) Lamm, M. H.; Chen, T.; Glotzer, S. C. *Nano Lett.* **2003**, *3*, 989.

(13) Abbenhuis, H. C. L. *Chem. Eur. J.* **2000**, *6*, 25.

(14) Ducateau, R.; Cremer, U.; Harmsen, R. J.; Mohamud, S. I.; C. L. Abbenhuis, C. L.; Avan Saten, R.; Meetsma, A.; Thiele, S. K.-H.; F. F. H. van Tol, F. F. H.; Kranenburg, M. *Organomet.* **1999**, *18*, 5447.

(15) Klunduk, M. C.; Maschmeyer, T.; Thomas, J. M.; Johnson, F. G. *Chem. Eur. J.* **1999**, *5*, 1481.

(16) Pescarmona, P. P.; Waal, J. C. v. d.; Maxwell, I. E.; Maschmeyer, T. *Angew. Chem., Int. Ed.* **2000**, *40*, 740.

(17) Xiao, F. S.; Han, Y.; Yu, Y.; Meng, X.; Yang, M.; Wu, S. *J. Am. Chem. Soc.* **2002**, *124*, 888.

(18) Fu, B. X.; Hsiao, B. S.; Pagola, S.; Stephens, P.; White, H.; Rafailovich, M.; Sokolov, J.; Mather, P. T.; Jeon, H. G.; Philips, S.; Lichtenhan, J.; Schwab, J. *Polymer* **2001**, *42*, 599.

(19) Romo-Uribe, A.; Mather, P. T.; Haddad, T. S.; Lichtenhan, J. D. *J. Polym. Sci. B-Polym. Phys.* **1998**, *36*, 18571872.

(20) Fu, B. X.; Hsiao, B. S.; White, H.; Rafailovich, M.; Mather, P. T.; Jeon, H. G.; Phillips, S.; Lichtenhan, J.; Schwab, J. *Polym. Int.* **2000**, *49*, 437.

(21) Lee, A.; Lichtenhan, J. D. *J. Appl. Polym. Sci.* **1999**, *73*, 1993.

(22) Haddad, T. S.; Lichtenhan, J. D. *Macromolecules* **1996**, *29*, 7302.

(23) Schwab, J. J.; Lichtenhan, J. D. *Appl. Orga. Chem.* **1998**, *12*, 707.

(24) Raj, R.; Riedel, R.; Soraru, G. D. *J. Am. Ceram. Soc.* **2001**, *84*, 2158.

(25) Liu, J. C. *Appl. Organomet. Chem.* **1999**, *13*, 295.

(26) de Vos, R. M.; Verweij, H. *J. Membr. Sci.* **1998**, *143*, 37.

(27) Suzuki, F.; Nakane, K.; Yasuo, H. *J. Mem. Sci.* **1995**, *104*, 183.

(28) Bassindale, A. R.; Pourny, M.; Taylor, P. G.; Hursthouse, M. B.; Light, M. E. *Angew. Chem., Int. Ed.* **2003**, *42*, 3488.

(29) Earley, C. W. *J. Phys. Chem.* **1994**, *98*, 8693.

(30) de Man, A. J. M.; Sauer, J. *J. Phys. Chem.* **1996**, *100*, 5025.

(31) Tossell, J. A. *J. Phys. Chem.* **1996**, *100*, 5025.

(32) Pasquarello, A.; Hybertsen, M. S.; Car, R. *Phys. Rev. B* **1996**, *54*, R2339.

(33) Xiang, K.-H.; Pandey, R.; Pernisz, U. C.; Freeman, J. *J. Phys. Chem. B* **1998**, *102*, 8704.

(34) Cheng, W.-D.; Xiang, K.-H.; Pandey, R.; Pernisz, U. C. *J. Phys. Chem.* **2000**, *104*, 6737.

(35) George, A. R.; Catlow, C. R. A. *Chem. Phys. Lett.* **1995**, *247*, 408.

(36) Park, S. S.; Xiao, C.; Hagelberg, F.; Hossain, D.; Pittman, C. U., Jr.; Saebo, S. *J. Phys. Chem. A* **2004**, *108*, 11260.

(37) Mattori, M.; Mogi, K.; Sakai, Y.; Isobe, T. *J. Phys. Chem. A* **2000**, *104*, 10868.

(38) Tejerina, B.; Gordon, M. S. *J. Phys. Chem. B* **2002**, *106*, 11764.

(39) Toernroos, K. W.; Buergi, H.-B.; Calzaferri, G.; Buergy, H. *Acta Crystallographica, Section B: Structural Science* **1995**, *B51*, 155.

(40) Agaskar, P. A.; Klemperer, W. G. *Inorg. Chim. Acta* **1995**, *229*, 355.

(41) Agaskar, P. A.; Day, V. W.; Klemperer, W. G. *J. Am. Chem. Soc.* **1987**, *109*, 5554.

(42) Feher, F. J.; Budzichowski, T. A. *J. Organomet.* **1989**, *153*, 373.

(43) Lee, C.; Yang, W.; Parr, R. G. *Phys. Rev. B: Condens. Matter and Materials Phys.* **1988**, *37*, 785.

(44) Becke, A. D. *J. Che.l Phys.* **1993**, *98*, 5648.

(45) Jimenez-Vazquez, H. A.; Tamariz, J.; Cross, R. J. *J. Phy. Chem. A* **2001**, *105*, 1315.

(46) Cheeseman, J. R.; Trucks, G. W.; Keith, T.; Frisch, M. J. *J. Phys. Chem.* **1996**, *104*, 5497.

(47) Schreckkenbach, G., ; Ziegler, T. *J. Phys. Chem.* **1995**, *99*, 606.

(48) Glendening, E. D.; Reed, A. E.; Carpenter, J. E.; Weinhold, F. *NBO 4.M University of Wisconson: Madison* **1993**.

(49) Moran, D.; Stahl, F.; Jemmis, E. D.; Schaefer, H. F., III;; Schleyer, P. v. R. *J. Phys. Chem. A* **2002**, *106*, 5144.

(50) Heyde, T. P. E.; Burgi, H., -B.; Burgi, H.; Tornroos, K. W. *Chimia* **1991**, *45*, 38.

(51) Rehm, E.; Boldyrev, A. I.; Schleyer, P. v. R. *Inorg. Chem.* **1992**, *31*, 4831.

(52) Gutsev, G. L.; Boldyrev, A. I. *Chem. Phys. Lett.* **1982**, *92*, 262.

(53) Gutsev, G. L.; Boldyrev, A. I. *Adv. Chem. Phys.* **1985**, *61*, 169.

(54) Jiao, H.; Nagelkerke, R.; Kurtz, H. A.; Williams, R. V.; Borden, W. T.; Schleyer, P. v. R. *J. Am. Chem. Soc.* **1997**, *119*, 5921.

Table 6.1 Selected Bond Lengths (Å) and Bond Angles (in Degrees) of the $(HSiO_{3/2})_{12}$ Cage and Endohedral $X@(HSiO_{3/2})_{12}$ Complexes at B3LYP/6-311G(d,p) Level.

X	X-Si	X-Si	X-O	Si-O	Si-O	$Si-O_b$	Si-O	Si-O	Si-H	Si-H	OSiO	OSiO	SiOSi	OSiO	OSiO
Pure	3.374	3.752	3.085	1.630	1.642	1.636	1.637	1.636	1.463	1.464	150.9	109.7	109.4	109.6	156.8
Sc	3.107	3.754	2.110	1.671	1.610	1.624	1.605	1.629	1.425	1.423	146.5	112.4	111.2	107.1	138.4
Ti	3.286	3.967	2.349	1.711	1.673	1.680	1.669	1.681	1.670	1.673	151.8	110.1	109.2	106.4	150.1
Cr	3.188	4.028	2.130	1.727	1.667	1.674	1.660	1.675	1.464	1.468	155.7	108.3	112.8	109.0	146.4
Mn	3.133	3.924	2.116	1.683	1.640	1.645	1.635	1.649	1.461	1.465	154.2	109.8	111.9	107.2	143.2
Fe	3.130	3.908	2.112	1.676	1.640	1.644	1.635	1.648	1.461	1.465	154.3	109.8	111.3	107.3	143.7
Co	3.169	3.798	2.243	1.638	1.637	1.652	1.642	1.641	1.479	1.478	146.6	112.5	110.3	109.0	149.8
Ni	3.555	3.832	2.350	1.654	1.639	1.642	1.636	1.643	1.461	1.465	154.0	110.4	109.2	108.0	148.1
Cu	3.389	3.710	3.202	1.633	1.644	1.640	1.638	1.637	1.462	1.464	150.8	110.3	109.2	110.2	157.0
Zn	3.398	3.712	3.200	1.636	1.642	1.643	1.640	1.639	1.462	1.463	150.0	110.8	109.1	110.5	158.0
Mo	3.274	3.939	2.888	1.716	1.664	1.674	1.659	1.673	1.464	1.467	155.4	109.3	110.5	105.2	146.1
W	3.216	4.008	2.185	1.736	1.664	1.678	1.659	1.675	1.464	1.468	156.6	109.4	105.5	109.3	145.6

Table 6.2 Total Energies (in Hartrees), Zero-point Energies (ZPE, kcal/mol), Molecular point Groups, Lowest Vibrational Frequencies ω_1 (cm^{-1}), Zero-point Corrected Encapsulation Energies (kcal/mol), and Optimized Bond Lengths (Å) for Endohedral Complex of $X@(HSiO_{3/2})_{12}$ with D_{2d} Symmetry.

X	Energy	Zero	[a]ω_1	Sym.	E_{inc}
Sc^{+}	-5598.175845	132.3	86.87	D_{2d}	-113.2
Sc^{+2}	-5597.909366	132.2	51.96	D_{2d}	-182.9
Ti	-5686.063962	127.2	73.27	D_{2d}	578.9
Ti^{+2}	-5686.590457	132.8	82.21	D_{2d}	
Cr	-1495.381800	129.2	71.50	D_{2d}	2.8
Mn	-5988.510751	131.9	72.75	D_{2d}	-19.1
Mn^{+}	-5988.299203	134.0	83.11	D_{2d}	-62.9
Mn^{+2}	-5988.0110 93	133.7	68.76	D_{2d}	-240.9
Fe	-6101.248887	132.7	71.63	D_{2d}	-27.0
Fe^{+}	-6101.096260	134.3	80.10	D_{2d}	-91.0
Fe^{+2}	-6100.746454	133.5	46.71	D_{2d}	-267.7
Co	-6220.350889	131.5	i105.54(1)	D_{2d}	-15.8
Co^{+}	-6220.189656	134.4	76.11	D_{2d}	-127.4
Co^{+2}	-6220.189657	134.4	76.41	D_{2d}	-521.9
Ni	-6345.880751	131.9	i299.77(1)	D_{2d}	-358.8
Ni^{+}	-6345.777344	133.6	69.09	D_{2d}	-102.0
Ni^{+2}	-6345.383844	134.1	69.21	D_{2d}	-325.7
Cu	-6478.121053	132.5	41.40	D_{2d}	-14.6
Cu^{+}	-6477.960974	133.0	i111.80(1)	D_{2d}	-87.0
Cu^{+2}	-6477.960974	133.0	i111.80(1)	D_{2d}	-528.7
Zn	-6617.004668	132.7	56.41	D_{2d}	17.1
Zn^{+}	-6616.751468	132.1	55.65	D_{2d}	-34.3
Zn^{+2}	-6616.432561	132.0	55.08	D_{2d}	-249.2
Mo	-1476.620700	123.4	74.81	*Cs*	-42.5
W	-1476.873414	128.4	52.04	D_{2d}	-23.7
W^{+}	-1476.776706	131.1	89.16	D_{2d}	-140.1
W^{+2}	-1476.776706	131.1	89.16	D_{2d}	-507.5

[a] Value in the brackets indicates the number of imaginary frequencies in cm^{-1}.

Table 6.3 Natural Charge Analysis of $X@(HSiO_{3/2})_{12}$ with D_{2d} symmetry at the B3LYP/6-311G(d,p) Level of Theory.

X	Q_X[a]	Q_{Si}	Q_{Si1}	Q_o	Q_{o1}	Q_{o1}	Q_{H1}	Q_{H1}
Cage		2.14	2.15	-1.27	-1.27	-1.27	-0.24	-0.24
Sc	-0.25	1.04	1.02	-0.62	-0.62	-0.63	-0.13	-0.12
Sc^+	0.89	2.11	2.08	-1.25	-1.26	-1.28	-0.20	-0.19
Ti	0.41	2.10	2.07	-1.26	-1.26	-1.28	-0.22	-0.22
Cr	0.19	2.12	2.11	-1.26	-1.27	-1.25	-0.23	-0.24
Mn	-0.23	2.11	2.07	-1.25	-1.26	-1.27	-0.23	-0.23
Mn^+	0.72	2.11	2.08	-1.25	-1.26	-1.25	-0.20	-0.20
Fe	0.27	2.05	2.01	-1.23	-1.25	-1.25	-0.19	-0.19
Fe^+	0.76	2.12	2.08	-1.25	-1.26	-1.26	-0.20	-0.20
Co	-0.53	1.06	1.06	-0.63	-0.63	-0.63	-0.12	-0.12
Co^+	0.78	2.12	2.07	-1.25	-1.26	-1.27	-0.20	-0.20
Ni	0.22	2.12	2.10	-1.25	-1.26	-1.28	-0.23	-0.23
Ni^+	0.92	1.06	1.05	-0.63	-0.63	-0.64	-0.10	-0.10
Cu	0.08	2.12	2.13	-1.26	-1.27	-1.26	-0.24	-0.24
Cu^+	0.93	2.12	2.09	-1.25	-1.26	-1.31	-0.20	-0.20
Zn	0.11	2.13	2.13	-1.27	-1.26	-1.27	-0.24	-0.24
Zn^+	0.85	2.12	2.11	-1.27	-1.26	2.11	-0.20	-1.29
W	0.92	2.17	2.12	-1.26	-1.30	-1.24	-0.18	-0.17
W^+	0.41	2.21	2.17	-1.30	-1.31	-1.25	-0.21	-0.21

Table 6.4 Ionization Potentials (IP in kcal/mol) of the Free Atoms and the Corresponding Endohedral Metal Atoms of $X@T_{12}$-POSS Complexes at the B3LYP/6-311G(d,p) Level of Theory.

Ionization process	IP adiabatic	expt IP	ΔIP
$Sc \rightarrow Sc^{+} + e$	212.4	156.1	
$Sc@(SiHO_{3/2})_{12} \rightarrow Sc^{+}@(SiHO_{3/2})_{12} + e^-$	116.5		0.8
$Fe \rightarrow Fe^{+} + e$	149.2	182.2	
$Fe@(SiHO_{3/2})_{12} \rightarrow Fe^{+}@(SiHO_{3/2})_{12} + e^-$	96.6		52.6
$Co \rightarrow Co^{+} + e^-$	215.7	187.7	
$Co@(SiHO_{3/2})_{12} \rightarrow Co^{+}@(SiHO_{3/2})_{12} + e^-$	104.0		111.7
$Ni \rightarrow Ni^{+} + e^-$	190.2	176.2	
$Ni@(SiHO_{3/2})_{12} \rightarrow Ni^{+}@(SiHO_{3/2})_{12} + e^-$	66.5		123.7
$Cu \rightarrow Cu^{+} + e^-$	173.3	178.1	
$Cu@(SiHO_{3/2})_{12} \rightarrow Cu^{+}@(SiHO_{3/2})_{12} + e^-$	100.9		72.4
$Zn \rightarrow Zn^{+} + e^-$	209.7	216.6	
$Zn@(SiHO_{3/2})_{12} \rightarrow Zn^{+}@(SiHO_{3/2})_{12} + e^-$	158.3		51.4

[a] ΔIP = Ionzation potential of M - ionization potental of $M@(SiHO_{3/2})_{12}$.

Table 6.5 B3LYP/6-311G(d,p) Level Calculations of the HOMO-LUMO Gaps (in eV), and Chemical Shifts (δ ppm) for T_{12}-POSS Cage Nuclei and X@T_{12}-POSS Endohedral Complexes using D_{2d} isomer.

System	Si (δ)	H (δ)	(HOMO-LUMO) gaps
T_{12}-POSS Cage	-93.23, -89.65	4.82, 4.72	
Sc@$(HSiO_{3/2})_{12}$	-79.12, -63.39, 20.51, 32.82	3.80, 4.00, 4.39, 4.43	1.67
Ti@$(HSiO_{3/2})_{12}$	-6.39, -7.97, -8.00, -8.21	2.50, 3.16, 5.06, 7.84	1.88
Cr@$(HSiO_{3/2})_{12}$	-24.25, -2.39	2.36, 10.97	3.57
Mn@$(HSiO_{3/2})_{12}$	-8.14, -4.04	6.93, 2.43	3.56
Fe@$(HSiO_{3/2})_{12}$	-16.61, -16.98	3.58, 6.14	3.16
Co@$(HSiO_{3/2})_{12}$	-10.18, -9.33	4.74, 4.90	3.61
Ni@$(HSiO_{3/2})_{12}$	-9.49, -14.77	5.35, 4.18	2.40
Cu@$(HSiO_{3/2})_{12}$	-6.41, -2.00	4.83, 4.71	3.35
Zn@$(HSiO_{3/2})_{12}$	-6.53, -2.53	4.86, 4.73	6.66

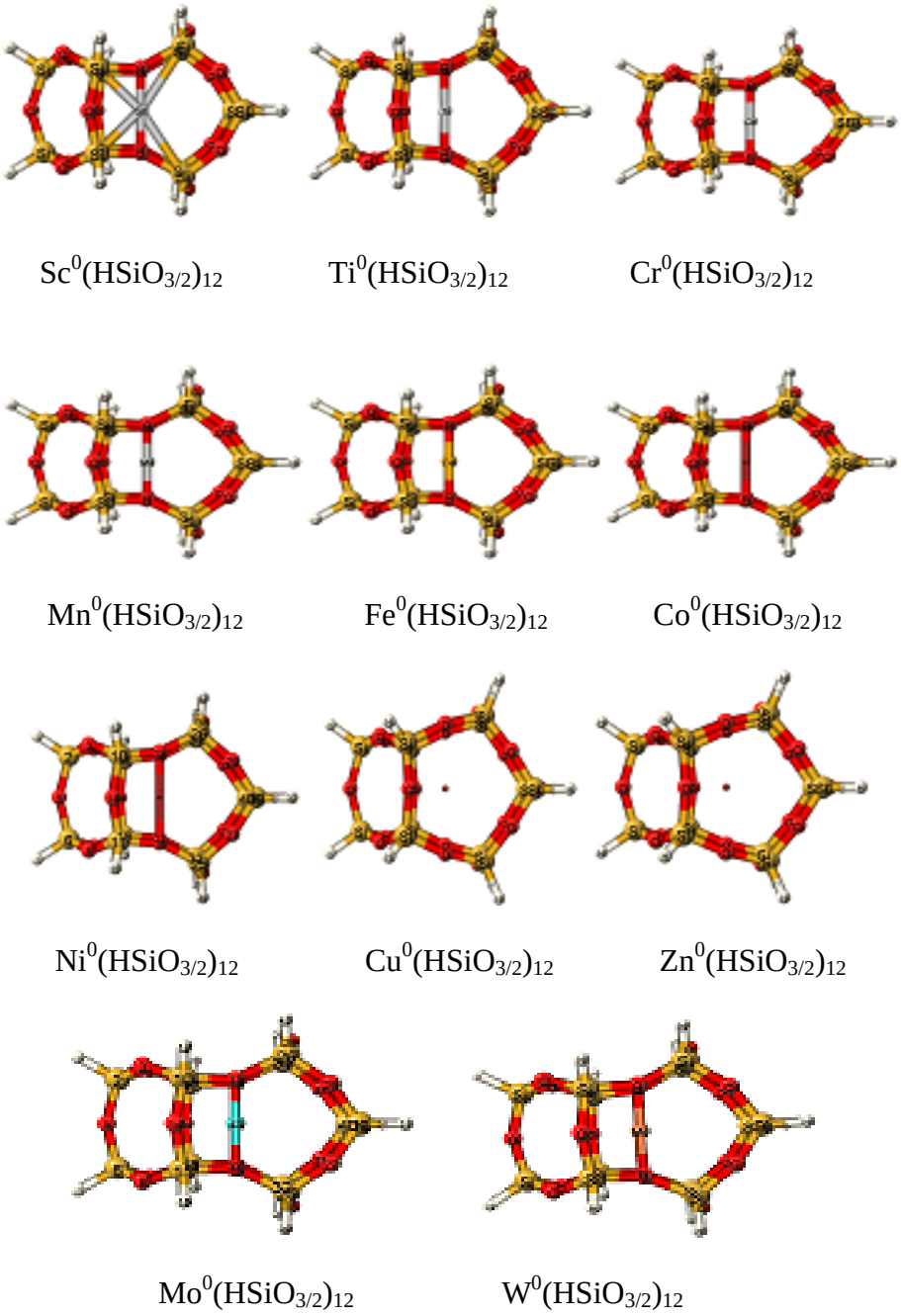

Figure 6.2 Optimized Geometries of Endohedral Complexes of $(HSiO_{3/2})_{12}$ with Neutral Transition Metal Atom at the B3LYP/6311G(d,p) Level.

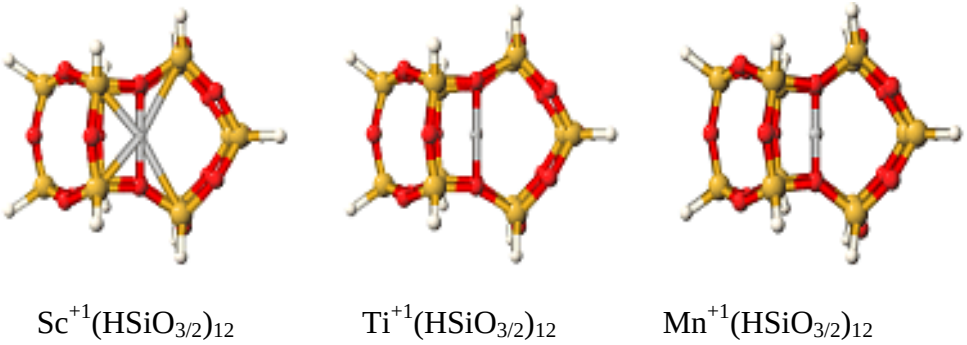

$Sc^{+1}(HSiO_{3/2})_{12}$ $Ti^{+1}(HSiO_{3/2})_{12}$ $Mn^{+1}(HSiO_{3/2})_{12}$

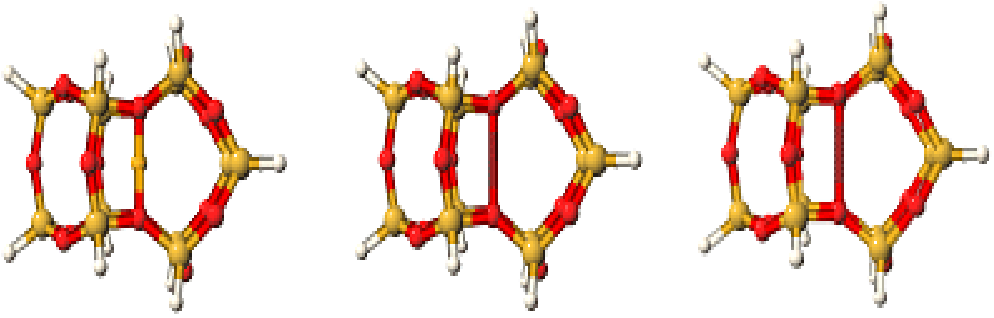

$Fe^{+1}(HSiO_{3/2})_{12}$ $Co^{+1}(HSiO_{3/2})_{12}$ $Ni^{+1}(HSiO_{3/2})_{12}$

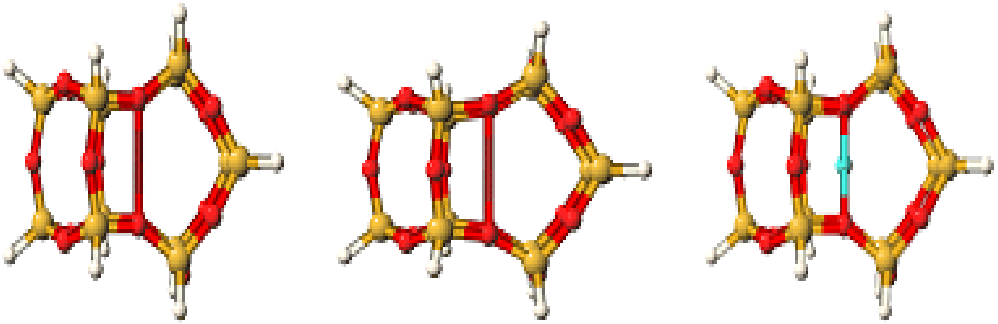

$Cu^{+1}(HSiO_{3/2})_{12}$ $Zn^{+1}(HSiO_{3/2})_{12}$ $W^{+1}(HSiO_{3/2})_{12}$

Figure 6.3 Optimized Geometries of Endohedral Complexes of $(HSiO_{3/2})_{12}$ with +1 Transition Metal Cation at the B3LYP/6311G(d,p) Level.

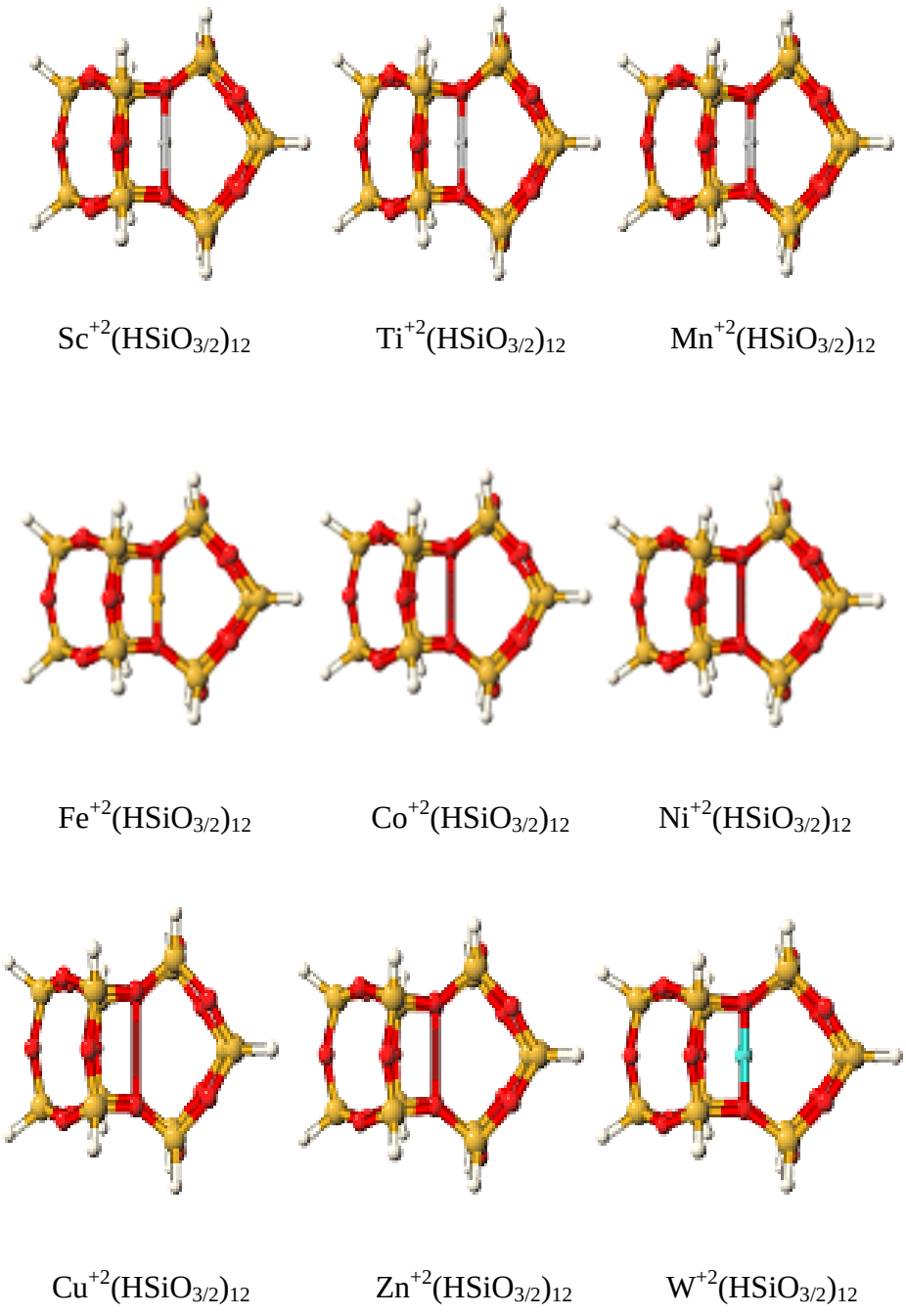

Figure 6.4 Optimized Geometries of Endohedral Complexes of $(HSiO_{3/2})_{12}$ with +2 Transition Metal Cation.at the B3LYP/6-311G(d,p) Level.

CHAPTR VII

ENDOHEDRAL SILICON CLUSTERS: $X@Si_{12}$ ($X=Li^{0,1,-1}$, $Na^{0,1,-1}$, K^+, He, F^- AND Cl^-), $Li_2@Si_{18}$, $Li_{20}@Si_{20}$ AND Na_2Si_{18}. STRUCTURE AND STABILITY

Introduction

Nanoclusters are particularly interesting building blocks for large self-assembled or consolidated materials. The properties of nanoclusters can be manipulated by changing their size, shape, and composition. Since silicon is the most widely used material in the semiconductor and microelectronic industries, extensive recent theoretical and experimental studies have been carried out on pure Si clusters as well as metal doped Si[1-5] to understand their structures and properties. The well-known stable carbon cage, fullerene, exhibits unusual stability due to the sp^2 hybridization of the carbon atoms and the extended surface conjugation. Even though Si is isovalent to the C atom in the periodic table, Si sp^2 hybridization is less favorable than for C and silicon double bonds are rare. Since silicon sp^2 hybridization is less favorable than for carbon, the fullerene like Si clusters are considered to be unstable.[6]

Recent experimental[4] and theoretical research[1-3,5-15] suggests that introducing guest atoms into the Si cages can stabilize Si clusters. Extensive theoretical studies of

metal-encapsulated silicon clusters led to the discovery of novel fullerene-like (f), cubic(c) Fran-Kasper (FK) polyhedral, isohedral(I_h) and other cluster geometric forms.[2,3,7-12,15] Hiura et al[4] reacted silane with different transition metals and found that the $Si_{12}W$ cluster is stabilized as a hexagonal prism structure where the W atom is located at the cage center. Theoretical studies predicted a similar structure for endohedral $Cr@Si_{12}$ and $Cu@Si_{12}$ clusters.[15,16] These studies demonstrated that Si clusters with endohedral metals have stabilities, which depend on the filling factor of the encapsulated transition metal's d band, the number of transition metal d bands and the number of Si atoms in the cage. Although it is believed that small clusters of Si tend to have close-packed structures, clusters with 14-25 atoms have porlate structures in which Si_9 and Si_{10} units are the building blocks.[13,17] Jackson et al[18] studied the dodecahedral Si_{20} cage with a Zr atom at the center. However, this result differed from Kumar and Kawazoe's predictions where the cage is distorted such that Si atoms were ejected leading to cage shrinkage.[3] Beck et al[19-21] generated metal-silicon clusters MSi_n (where M = Cu, Cr, Mo and W) by laser vaporization. MSi_{15} and MSi_{16} clusters (M=Cr, W, and Mo) were observed significantly greater abundance than any other metal-doped silicon clusters. The mass spectra of $CuSi_n$ ($6<n<12$) demonstrated that the endohedral cluster, $Cu@Si_{10}$, is exceptionally stable. Schere and co-workers experimentally produced metal clusters $M@Si_n$ (M = Cu, Ag and Au).[22-24] Combined experimental and theoretical studies of $SiNa_n^-$($n<7$) found that Na atom acts as an electron donor to Si_n framework.[25] Na adsorption left the original Si_n cluster's framework nearly unchanged in $NaSi_n$. The

electronic structure silicon based semiconductor surfaces is changed dramatically by alkali metal adsorption.

Silicon clusters containg encapsulated alkali metals, halides and noble gases has drawn a little attention despite the extensive studies of transition metal atoms encapsulated silicon clusters. Essential questions about alkali metals, halides and noble gas encapsulated clusters that must be addressed include: (1) Can alkali metals, halides or noble gases atoms be successfully encapsulated into the Si_n cluster? (2) Is this endohedral element always located at the center of the Si_n cluster? (3) How does the size of the encapsulated species affect on the size of Si_{12} cluster? (4) How do the electronic properties change after encapsulation of these elements or ions? (5) Are alkali metal-doped silicon nanotubes stable?

To address the these questions, *ab initio* calculations were conducted herein to predict the structural and electronic properties of endohedral alkali metals and their ions, halides and noble gases within the Si_{12} cluster; ($M@Si_{12}$ M = Li^+ Li^0, Li^-, Na^+, Na^0, Na^-, K^+, K^0, K^-, F^-,Cl^-, Br^-,He, Ne). We also investigated $Li_2@Si_{18}$, $Li_2@Si_{20}$ and Na_2Si_{20}.

Computational Methods

All calculations were performed using spin-unrestricted hybrid density functional theory with the B3LYP [26,34] exchange correlation functional and the triple split polarized basis set as 6-311+G(d,p). D_{6h} (hexagonal), I_h (icosahedral) and D_{2d} (derived from the Si_{16} fullerene-like structure) isomers of the Si_{12} cage were used to construct initial structures of endohedral $M@Si_{12}$ clusters. Harmonic vibrational frequencies were calculated for all optimized structures at the same level of theory to characterize the

stationary points as minima or as transition states. The embedding energies (EE) and binding energies (BE) of endohedral metal Si_{12} clusters were calculated using the equations:

$$EE = E(X_x@Si_n) - E(Si_n) - xE(X)$$

$$BE = -[E(X_x@Si_n) - nE(Si) - xE(X)]1/(n+1)$$

where, $E(X_x@Si_n)$, $E(Si_n)$, xE(X) and nE(Si) denote the calculated total energies for the endohedral silicon clusters, the silicon clusters, the embedding atoms and the total energy of the silicon atom respectively for a given system. Electronic properties were analyzed using the NBO 4 program.[35]

Results and Discussion

Si_{12} cages

The calculated embedding energies, binding energies, HOMO-LUMO gaps of $M@Si_{12}$ and the charge of the embedded atoms or ions obtained from the natural population analysis (NPA) are summarized in Table 7.1. Table 7.1 also contains binding energies HOMO-LUMO gaps for the pure Si_{12} clusters. The shape of the optimized structures of the Si_{12} cluster and endohedral $M@Si_{12}$ clusters obtained from different isomers of Si_{12} cage are shown in Figures 7.1-7.4. The geometries of $Li_2@Si_{18}$, $Li_2@Si_{20}$ and Na_2Si_{18} clusters are shown in Figure 7.5.

Initial structures of D_{6h}, D_{2d} and I_h isomers of the Si_{12} cage were optimized at the B3LYP/6-311+G(d) level. Three distinct cage-like structures were found for the empty Si_{12} clusters. A cyclohexane boat-like structure with C_{2h} symmetry was obtained from initial D_{6h} Si_{12} isomer. Upon optimization the initial D_{2d} Si_{12} isomer completely changed

to a C_1 symmetry structure. However, optimization of the initial I_h (icosahedral) Si_{12} isomer is distorted slightly from its initial and the final optimized structure has C_1 symmetry. These three structures are shown in Figure 7.1 (a), (b) and (c) respectively. The same structure was also obtained by Lee et al. [27] The binding energy of these three clusters are –3.55, -3.60 and –4.07 eV/atom, respectively. The Si_{12} cluster with C_1 symmetry obtained after optimization of the initial I_h isomer is more stable than the clusters obtained after optimization of the initial D_{2d} and D_{6h} Si_{12} isomers. Among all the three optimized clusters, the cluster with C_{2h} symmetry obtained from the initial D_{6h} Si_{12} isomer is the least stable.

Endohedral X@Si_{12} Complexes

Upon insertion of Li, Li^+, Li^-, Na, Na^+,or He into the initial Si_{12} D_{6h} cage transforms to a shape closely related to a double chair cyclohexane ring (Figure 7.2). In the $Li^{0,1,-1}@Si_{12}$, $Na^{0,1}@Si_{12}$ and $He@Si_{12}$ clusters, Li, Na or He are surrounded by twelve Si atoms. The Si-Li bond distances in $Li^+@Si_{12}$ vary over a range of 2.520-2.827 Å and the Si-Si distance is 2.417 Å. Insertion of He into the D_{6h} Si_{12} isomer gives the $He@Si_{12}$ cluster, which has a shape resembling the endohedral Li or Na clusters. The He-Si and Si-Si bond distances span the ranges of 2.440-2.944 Å and 2.361-2.362 Å, respectively. Insertion of Na^- inside Si_{12} (D_{6h}) is energetically unfavorable. In the optimized structure, Na^- spontaneously moves outside through the hexagonal surface and finally bond with one of the Si atoms of the D6 rings.

Upon inserting Li, Li^+, or Li^- into an initial Si_{12} icosahedron (I_h), the shapes of the optimized $M@Si_{12}$ (X = Li, Li^+, Li^-) structure are distorted slightly from its initial

shape and has C_1 symmetry. Insertion of Na, Na^+ or Na^- into the Si_{12} I_h isomer cage gives the cluster structure shown in Figure 7.4. Insertions of either Li or Na into the D_{2d} Si_{12} cage produce the C_1 symmetry structure shown in Figure 7.3. Its shape is almost the same as the initial the D_{2d} structure. Insertion of a K atom is energetically unfavorable and in all cases the cage structures are destroyed completely giving a new shape as shown in Figure 7.2 (c), and Figure 7.4 (c). Insertion of Ne into the D_{6h} isomer distorts the cage and Ne escapes from the cage. Insertions of halides into the cage are completely unfavorable. In each case the cage ruptured completely and new geometries are formed as shown in Figurs 7.2 and 7.3.

The clusters containing endohedral Li^- are energetically more favorable than those containg Li^0 starting from all three initial Si_{12} (D_{6h}, D_{2d}, I_h) cage geometries (Table 7.1). Similarly, all three endohedral Li^0 clusters are more stable than their corresponding Li^+ analogs.

Encapsulation of Li^+ into either the D_{6h} or D_{2d} the isomer of Si_{12} gives endohedral clusters, which have a higher energy than the sum of the Li^+ and Si_{12} initial energies. However, encapsulation of Li^+ in the I_h isomer gives a cluster which has a lower energy than the separated species. The embedding and binding energies for the D_{2d} $Li^+@Si_{12}$ cluster are 0.39 eV and –3.29eV/atom respectively.. For the I_h clusters these values are –0.62 eV and –3.81 eV/atom. The binding energies for $Li^+@Si_{12}$ are smaller than the respective empty cages by 0.31 eV, 0.26 eV and 0.21 eV/atom respectively.

Encapsulation of Li^0 into the D_{6h}, D_{2d} or I_h Si_{12} cage isomers are energetically favorable. The embedding energies of these clusters are –1.69 eV, -0.92eV and –1.95

eV, respectively. The cluster binding energies for the clusters generated from D_{6h} and I_h isomers are smaller than the corresponding binding energies of the empty Si_{12} cages. However, the binding energy for the Li^0 encapsulated cluster generated from the Si_{12} D_{2d} isomer is higher than the binding energy of the precursor Si_{12} (D_{2d}) cage, indicating that this cluster is more stable.

Each of the endohedral clusters formed by inserting Li^- into the D_{6h}, D_{2d} and I_h isomer of Si_{12} have lower energies than the corresponding isolated species. The embedding energies of these clusters are –4.71 eV, -3.42 eV and –4.94 eV, respectively. Li^0, Li^+, and Li^- encapsulated clusters obtained from I_h isomer of Si_{12} (icosahedral shape) cage are more stable in each case than corresponding clusters obtained from the other two (D_{6h} and D_{2d}) Si_{12} isomers. These $Li^-@Si_{12}$ clusters are exceptionally energetically favorable. The binding energies of each of the three $Li^-@Si_{12}$ clusters are higher than those of their corresponding empty Si_{12} precursor.

Encapsulation of Na^+ or Na^0 into the D_{6h} or D_{2d} or I_h isomer of Si_{12} cages gives energetically unfavorable endohedral clusters. The embedding energies of these three Na^+ encapsulated clusters are 2.10 eV, 3.53 eV and 0.63 eV, respectively. Furthermore, their binding energies are less than the corresponding binding energies of the Si_{12} empty cages (see Table 7.1). In contrast, encapsulations of Na^- into all these Si_{12} isomers are energetically favorable. Their embedding energies are, -3.99 eV, 2.65 eV and –0.96 eV respectively. The binding energy of the $Na^-@Si_{12}$ cluster (–3.58 eV/atom) obtained from D_{6h} isomer is almost the same as that of the empty cage (-3.55 eV/atom). The stability order ($Na^-@Si_{12} > Na^0@Si_{12} > Na^+@Si_{12}$) for the sodium series parallels that observed

for lithium series. The encapsulation of Na^- is energetically more favorable than the Na^+ and Na encapsulated clusters (Table 7.1). The Na^0 and Na^- endohedral cluster obtained from the initial D_{6h} Si_{12} isomer are energetically more favorable than those of the clusters obtained from the I_h and D_{2d} Si_{12} isomers. The endohedral Na^+ cluster obtained from the I_h isomer of Si_{12} is energetically more favorable than the clusters obtained from the other two isomers.

He encapsulation into the D_{6h}, D_{2d} and I_h Si_{12} isomers generate endohedral He@Si_{12} clusters. These clusters are thermodynamically unfavorable. The endohedral He@Si_{12} clusters obtained upon insertion of He into the D_{6h} and I_h Si_{12} isomers are energetically more favorable than the cluster obtained upon insertion of He into the D_{2d} Si_{12} isomer.

Upon insertion of a metal atom into Si_{12} cages, electron transfer is expected to occur between the metal atoms and the Si_{12} frame. The amount of charge on the encapsulated atom was calculated from NBO analysis (Table 7.1). Since Si is more electronegative than the alkali metals, electron transfer is expected to occur from neutral or anionic alkali metals to the Si_{12} cluster. Our calculations agreed with this expectation. The encapsulation of both alkali metal atom and their anion into the Si_{12} cage induces charge transfer from the alkali species to the cage. In contrast to the neutral alkali metal or their anions, the endohedral metal cations actually gain electron density from the cage. The average charge transferred from the cage to the alkali metal cations depends on which cation is encapsulated and the S_{12} cage's symmetry. The charge calculated on the

endohedral alkali metals and their ions indicates that the Si_{12} cage acts like electron sink. No charge transfer occurs between the endoheral He atom to the Si_{12} cage or vice versa.

The orbital pictures (isosurface plots) for the HOMO and LUMO of selected clusters are shown in Figure 7.6. The HOMO of the Si_{12} cage is a pure silicon *p* orbital. However, both in the HOMO and LUMO, a pentagonal donunt-shaped electron cloud is formed along the middle of the cage involving ten Si atoms. The HOMO and LUMO gaps listed in Table 7.1 for different clusters are very large indicating that these clusters are stable.

The Kohn-Sham orbital energies of selected doped and undoped clusters are shown in Figure 7.7 to help understand the cluster bonding. It is clear that all of the occupied and unoccupied orbitals of the endohedral $Li^0@Si_{12}$, $Li^+@Si_{12}$, $Li^-@Si_{12}$, $Na^0@Si_{12}$, $Na^+@Si_{12}$, $Na^-@Si_{12}$ and $He@Si_{12}$ clusters are shifted to higher energies except for those of $Li^+@Si_{12}$. The HOMO and LUMO energy levels are increased significantly in the $Li^0@Si_{12}$, $Li^-@Si_{12}$ and $Na^-@Si_{12}$ clusters. The LUMO's energy increase is greater than that of the HOMO producing a relatively large HOMO-LUMO gap these three clusters. Encapsulated Li^- and Na^- raise the inner electronic energy levels significantly. In $Li^+@Si_{12}$, the energy level of the LUMO is slightly lowered.

$Li_2@Si_{18}$, $Li_2@Si_{20}$ and Na_2Si_{18} Clusters

The Si_{18} cluster with D_{6h} symmetry may be considered a combination of two Si_{12} units in where one Si_6 hexagon unit is common. The fully relaxed ground state structure was obtained from the $Li_2@Si_{18}$ cluster derived by inserting two lithium atoms into D_{6h}

Si_{18} is shown in Figur 7.5(a). The optimized structure has C_{2h} symmetry and resembles the $Li@Si_{12}$ unit. Li atoms are shifted toward the end Si_6 units of Si_{18} cage. The Li-Li distance in $Li_2@Si_{18}$ is 2.787 Å. This bond length of free Li_2 is 2.075 Å. This elongated Li-Li distance in the optimized $Li_2@Si_{18}$ structure is due, in part, to bonding of each of the Li atoms with two Si_6 layers. In $Li_2@Si_{18}$ twelve silicon atoms surrounded each Li atom. The relaxed structure has C_{2h} symmetry. The shape of each Si_6 unit resembles the boat configuration of a cyclohexane ring. The Si-Si distances in the end Si_6 units range between 2.460-2.614 Å and these in middle Si_6 unit are 2.463A°. The Si-Li lengths vary from 2.502 to 2.902 Å.

The embedding and the binding energies of $Li_2@Si_{18}$ cluster are -1.85 eV and –3.36 eV/atom, respectively. The binding energy of $Li_2@Si_{18}$ (–3.36 eV/atom) is less than the binding energy of the Si_{18} (–3.65 eV/atom) cage, indicating that $Li_2@Si_{18}$ cluster is less stable than Si_{18}. The difference between highest occupied and the lowest unoccupied molecular orbitals is 1.44 eV. Hagelberg et al[28] studied the $M_2@Si_{18}$ (M = Mo, W) clusters. They predicted that the inclusion of W and Mo, changes the original D_{6h} symmetry to D_{3h} symmetry in the ground state optimized structure. In contrast to $Li_2@Si_{18}$, the Mo or W atoms did not bond to the middle Si_6 ring.

When two Na atoms are placed inside the Si_{18} (D_{6h}) cage, an exohedral cluster is formed rather than an endohedral cluster like that with $Li_2@Si_{18}$. The optimized structure of Na_2Si_{18} is fundamentally different from the $Li_2@Si_{18}$ cluster. The Na atoms moved along the central axis of Si_{18} and they become the end capping atoms in the optimized structure. Each Na atom caps a chair-like Si_6 unit at the opposite ends of the cluster. Na

atoms are larger than lithium, making their encapsulation energetically unfavorable inside the Si_{18} tube. Secondly, the Na-Na interactions might be repulsive, like those exerted by Li-Li and K-K within a carbon nanotube.[29] Yang et al.[27] predicted that that the Li atom prefers to occupy sites along the tube axis in (6,0) and (5,0) inside a carbon nanotubes. These interactions are exothermic. Inserting K atoms into carbon nanotubes was unfavorable due to their large radii. The repulsive force between two sodium atoms may be strong enough to overcome any favorable embedding energy. Hence, the repulsive sodium-sodium interaction probably contributes to why the endohedral cluster of $Na_2@Si_{18}$ is not formed. The Si-Na distances are 2.544 and 2.511 Å. The Si-Si distances in the central Si_6 unit are 2.544 and 2.438 Å. The distance between the terminal and central Si_6 units are 2.940 and 2.990 Å and the Si-Si distances in the end Si_6 units are 2.544 and 2.511 Å. The embedding and binding energy of Na_2Si_{18} cluster are –0.73 eV and –3.32 eV/atom respectively and the HOMO-LUMO gap of this cluster is 1.20 eV.

We also investigated the $Li_2@Si_{20}$ cluster generated from Si_{20} (D_{6h}) cage. Each of the end Si_6 units of the Si_{20} cage was capped with a Si atom. The ground state optimized structure is shown in Figure 7.5(c). The endohedral Li-Li distance is 2.391 Å. This is shorter than the Li-Li distance (2.787 Å) in the $Li_2@Si_{18}$ cluster. The Li-Si distances vary from 3.204 to 2.708 Å. The Si-Si distances between the middle Si_6 and the edge Si_6 units range from 2.383 to 2.607 Å. The Si-Si distances in the central Si_6 unit is 2.555 Å. The Si-Si distances in the end Si_6 units and between these Si_6 units and the capping atoms vary from 2.487 to 2.706Å. The embedding energy of $Li_2@Si_{18}$ is -4.77 eV. Examination of the structures in Figure 7.2(a) and Figure 7.5(a) shows that the Li atoms fit into the

extended cage. This suggests that a string of Li atoms might be encapsulated by extended Si nanotubes.

The implication of this finding is intriguing. It is now widely accepted that cage and or nanotube configurations of Si cannot in general be stable.[30] [30] However, recent investigations show that a transition metal suitably positioned inside a silicon nanotube can stabilize these structure.[31] Our calculations demonstrate for the first time, that properly positioned Li atoms inside a silicon nanotube can stabilize slightly distorted tube structures. Recently, Si nanowires were prepared by a laser ablation method.[32,33] However, their surfaces were coated with oxygen. The silicon atoms in $Li_2@Si_{18}$ are highly coordinated with the encapsulated lithium atoms. Hence, endohedral Li atoms within the nanotubes may make silicon nanotubes less reactive towards oxygen. The stability of the Li encapsulated nanotube might be promising for advanced applications.

Conclusions

We have presented results of our investigations of the structural and electronic properties on $M@Si_{12}$ (M = 12, 18, 20) clusters. The results presented can be summarized as follows:

Encapsulation of atoms and ions by the Si_{12} cage strictly depends on the size of the encapsulated atoms or ions. Encapsulation of Li, Na and He by Si cages leads to endohedral clusters. The larger K, Ne and halide destroy the cage and favor formation of the corresponding exohedral clusters.

Charge transfer occurs from Si to Li^{+} and Na^{+} in cationic endohedral clusters. Conversely, charge transfer occurs from $Li^{0,-1}$ and $Na^{0,-1}$ to the Si_{12} cage. No charge transfer occurs between the Si_{12} cage and He.

All observed clusters are stable and have large HUMO-LUMO gaps (>1eV). The anionic endohedral clusters are more stable than the neutral and cationic endohedral clusters. The stability order is anionic cluster > neutral clusters> cationic cluster.

Li-encapsulated all silicon nanotubes may be stabilized in a way that is analogous to stabilization by endohedral Mn, V and Ni atomic chains inside the Si-nanotubes.[31] In particular, the $Si_{12}Li$ cluster unit can be used as a building block to form nanotubes of the type $Si_{6n}Li_{n-1}$. Further investigations are in progress.

References

(1) Q. Sun; Q. Wang; P. Jena; B.K. Rao; Y. Kawazoe. *Phys. Rev. Lett.* **2003**, *90*, 135503.

(2) Kumar, V.; Y. Kawazoe. *Phys. Rev. B* **2002**, *65*, 073404.

(3) Kumar, V.; Y. Kawazoe. *Phys. Rev. Lett.* **2001**, *87*, 045503.

(4) H. Hiura; T. Miyazaki; T. Kanayama. *Phys. Rev. Lett.* **2001**, *86*, 1733.

(5) A. N. Andriotis, A. N.; Mpourmpakis, G.; Froudakis, G.; Menon, M. *New J. Phys.* **2002**, *4*, 78.

(6) Menon, M.; Subbaswamy, K. R. *Chem. Phys. Lett.* **1994**, *219*, 219.

(7) Kumar, V.; Majumder, C.; Kawazoe, Y. *Chem. Phys. Lett.* **2002**, *363*, 319.

(8) Kumar, V.; Kawazoe, Y. *Appl. Phys. Lett.* **2002**, *80*.

(9) Kumar, V.; Kawazoe, Y. *Rev. Modern Quantum Chem.* **2002**, *2*, 1421.

(10) Kumar, V.; Kawazoe, Y. *Phys Rev Lett* **2003**, *90*, 05550.

(11) Kumar, V. *Computational Materials Science* **2004**, *30*,, 260.

(12) Kumar, V.; Singh, A. K.; Kawazoe, Y. *Nano Lett.* **2004**, *4*, 677.

(13) Mitas, L.; Grossman, J. C.; Stich, I.; Tobik, J. *Phys. Rev. Lett.* **2000**, *84*, 1479.

(14) Sun, Q.; Wang, Q.; Briere, T. M.; Kumar, V.; Kawazoe, Y.; Jena, P. *Phys Rev B* **2002**, *65*, 235417.

(15) Xiao, C.; Hagelberg, F.; Lesster, j., W. A. *Phys. Rev. B* **2002**, *66*, 075425.

(16) Khanna, S. N.; Rao, B. K.; Jena, P. *Phys. Rev. Lett.* **2002**, *89*, 016803.

(17) Ho, K.-M.; Shvartsburg, A. A.; Pan, B.; Lu, Z. Y.; Wang, C. Z.; G;, W. J.; L;, F. J.; F, J. M. *Nature* **1998**, *392*, 582.

(18) Jackson, K.; Nelleermore, B. *Chem. Phys. Lett.* **1996**, *254*, 249.

(19) Beck, S. M. *J. Chem. Phys.* **1989**, *90*, 6306.

(20) Beck, S. M. *J. Chem. Phys.* **1987**, *87*, 4233.

(21) Beck, S. M. *Adv. Met. Semicond. Clusters* **1993**, *1*, 241.

(22) Scherer, J. J.; Paul, J. B.; Collier, C. P.; O'Keefe, A.; Saykally, R. J. *J. Chem. Phys.* **1995**, *103*, 9187.

(23) Scherer, J. J.; Paul, J. B.; Collier, C. P.; Saykally, R. J. *J. Chem. Phys.* **1995**, *102*, 5190.

(24) Scherer, J. J.; Paul, J. B.; Collier, C. P.; Saykally, R. J. *J. Chem. Phys.* **1995**, *103*, 113.

(25) Kishi, R.; Iwata, S.; Nakajima, A.; Kaya, K. *J. Chem. Phys.* **1997**, *107*, 3056.

(26) Becke, A. D. *J. Chem. Phys.* **1993**, *98*, 5648.

(27) Lee, I. H.; Chang, K. J.; Lee, Y. H. *J. Phys: Condens. Matter* **1994**, *6*, 741.

(28) Hagelberg, F.; Xiao, C.; Lester, W. A. *Phys. Rev. B: Condens. Matter and Mater. Phys.* **2003**, *67*, 035426/1.

(29) Yang, J.; Liu, H. J.; Chan, C. T. *Physical Review B: Condens. Matter and Mater. Phys.* **2001**, *64*, 085420/1.

(30) Andriiotis, A. N.; Menon, M. *Phys Rev B* **1998**, *51*, 10069.

(31) Menon, M.; Andriotis, A. N.; Froudakis, G. *Nano Lett.* **2002**, *2*, 301.

(32) Zhang, Y. F.; Tang, Y. H.; Wang, N.; Yu, D. P.; Lee, C. S.; Bello, I.; Lee, S. T. *Appl. Phys. Lett.* **1998**, *72*, 1835.

(33) Morales, A. M. L., C. M. *Science* **1998**, *279*, 208.

(34) Lee, C.; Yang, W.; Parr, R. G. *Phys. Rev. B: Condens. Matter and Materials Phys.* **1988**, *37*, 785.

(35) Glendening, E. D.; Reed, A. E.; Carpenter, J. E.; Weinhold, F. *NBO 4.M University of Wisconson: Madison* **1993**.

TABLE 7.1 Total Energies (in Hartree), Molecular Point Groups, Lowest Vibrational Frequencies (ω cm^{-1}), Embedding Energies (EE, eV/mol), Binding Energies (BE, eV/atom), HOMO-LUMO gaps (eV), and Natural Electronic Charge on Embedding Species

Cluster[a]	Energy	Sym.	ω	EE (eV)	BE (eV/atom)	HOMO-LUMO (eV)	Charge on X
Si_{12} (D_{6h})	-3474.077226	C_{2h}	97.27		-3.60	1.94	
Si_{12} (D_{2d})	-3474.107561	C_1	73.28		-3.55	1.72	
Si_{12} (I_h)	-3474.032818	C_1	38.04		-4.70	1.91	
$Li^+@Si_{12}$ (D_{6h})	-3481.407221	C_1	36.77	3.80	-3.34	2.15	0.79
$Li^0@Si_{12}$ (D_{6h})	-3481.645523	C_1	62.71	-1.69	-3.40	2.43	-0.58
$Li^-@Si_{12}$ (D_{6h})	-3481.770001	C_s	105.80	-4.71	-3.59	2.64	0.61
$Na^+@Si_{12}$ (D_{6h})	-3636.077274	C_1	12.08	2.10	-3.12	2.20	0.79
$Na^0@Si_{12}$ (D_{6h})	-3636.441967	C_1	82.49	-2.12	-4.02	2.61	0.90
$Na^-@Si_{12}$ (D_{6h})	-3636.561922	C_1	108.41	-3.99	-3.58	2.49	0.87
$Li^+@Si_{12}$ (D_{2d})	-3481.375558	C_1	43.10	0.39	-3.29	1.79	0.41
$Li^0@Si_{12}$ (D_{2d})	-3481.632728	C_1	86.05	-0.92	-3.99	1.79	0.50
$Li^-@Si_{12}$ (D_{2d})	-3481.767744	Cs	99.09	-3.42	-3.58	1.73	0.70
$Na^+@Si_{12}$ (D_{2d})	-3636.042128	C_1	15.38	3.53	-3.01	1.64	0.50
$Na^0@Si_{12}$ (D_{2d})	-3636.275094	C_1	23.49	3.25	-3.67	1.55	0.53
$Na^-@Si_{12}$ (D_{2d})	-3636.530649	C_1	72.76	-2.65	-3.56	1.81	0.74
$Li^+@Si_{12}$ (I_h)	-3481.340633	C_1	86.94	-0.62	-3.81	2.60	0.25
$Li^0@Si_{12}$ (I_h)	-3481.594503	C_1	122.54	-1.95	-3.91	2.62	0.27
$Li^-@Si_{12}$ (I_h)	-3481.726059	C_I	136.15	-4.94	-4.14	2.01	0.35
$Na^+@Si_{12}$ (I_h)	-3636.0840894	C_s	54.83	0.63	-3.71	2.19	0.57
$Na^0@Si_{12}$ (I_h)	-3636.424859	C_1	39.89	-2.86	-3.98	1.72	0.88
$Na^-@Si_{12}$ (I_h)	-3636.376284	C_1	57.45	-0.96	-3.61	2.33	0.36
$He@Si_{12}$ (D_{6h})	-3476.913009	C_2	17.08	1.96	-3.13	0.38	0.02
$He@Si_{12}$ (D_{2d})	-3476.878471	C_1	47.93	3.28	-3.34	1.93	0.00
$He@Si_{12}$ (I_h)	-3476.854141	C_1	103.93	2.48	-3.46	1.66	0.01
$K@Si_{12}$ (D_{6h})	-4073.846885	C_2	16.09	-0.02	-3.28	2.14	0.97
$K@Si_{12}$ (D_{2d})	-4073.765270	C_1	3.86	2.38	-3.10	2.45	0.80
$F^-@Si_{12}$ (D_{6h})	-3574.1290598	C_1	53.08	-3.27	-4.57	1.93	-0.71
$Cl^-@Si_{12}$ (D_{6h})	-3934.491378	C_1	49.38	-2.36	-3.46	2.43	-0.02
$Cl^-@Si_{12}$ (D_{2d})	-3934.458643	C_1	40.01	-1.09	-3.37	1.88	-0.41

[a]Symmetry in the brackets indicates the initial symmetry of the Si_{12} clusters.

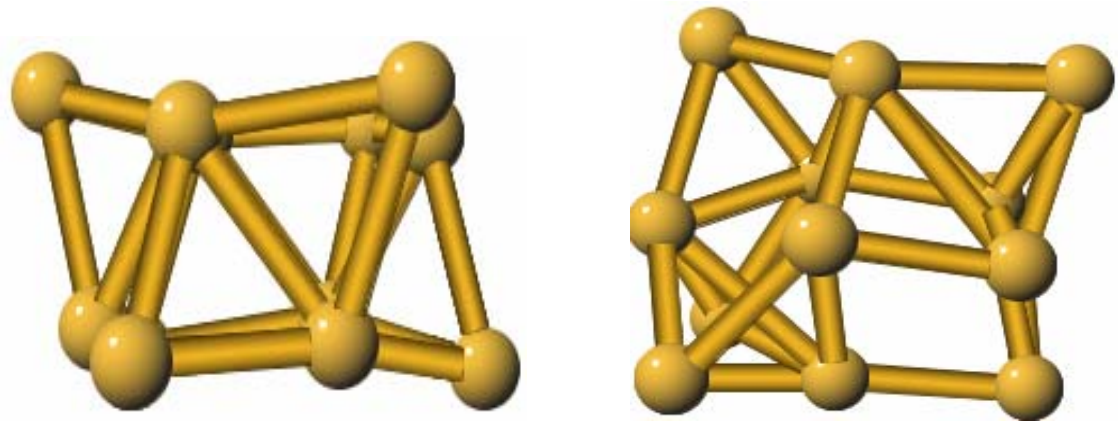

(a) Si_{12} (C_{2h})

(b) Si_{12} (C_1)

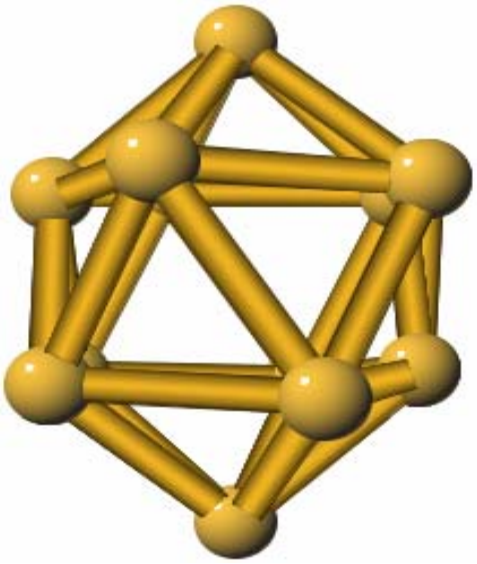

(c) Si_{12} (C_1)

Figure 7.1 Optimized Structures of Si_{12} Clusters.(a) Structure Obtained from D_{6h} Isomer (b) Structure Obtained from D_{2d} Isomer and (c) Structure Obtained from I_h Isomer.

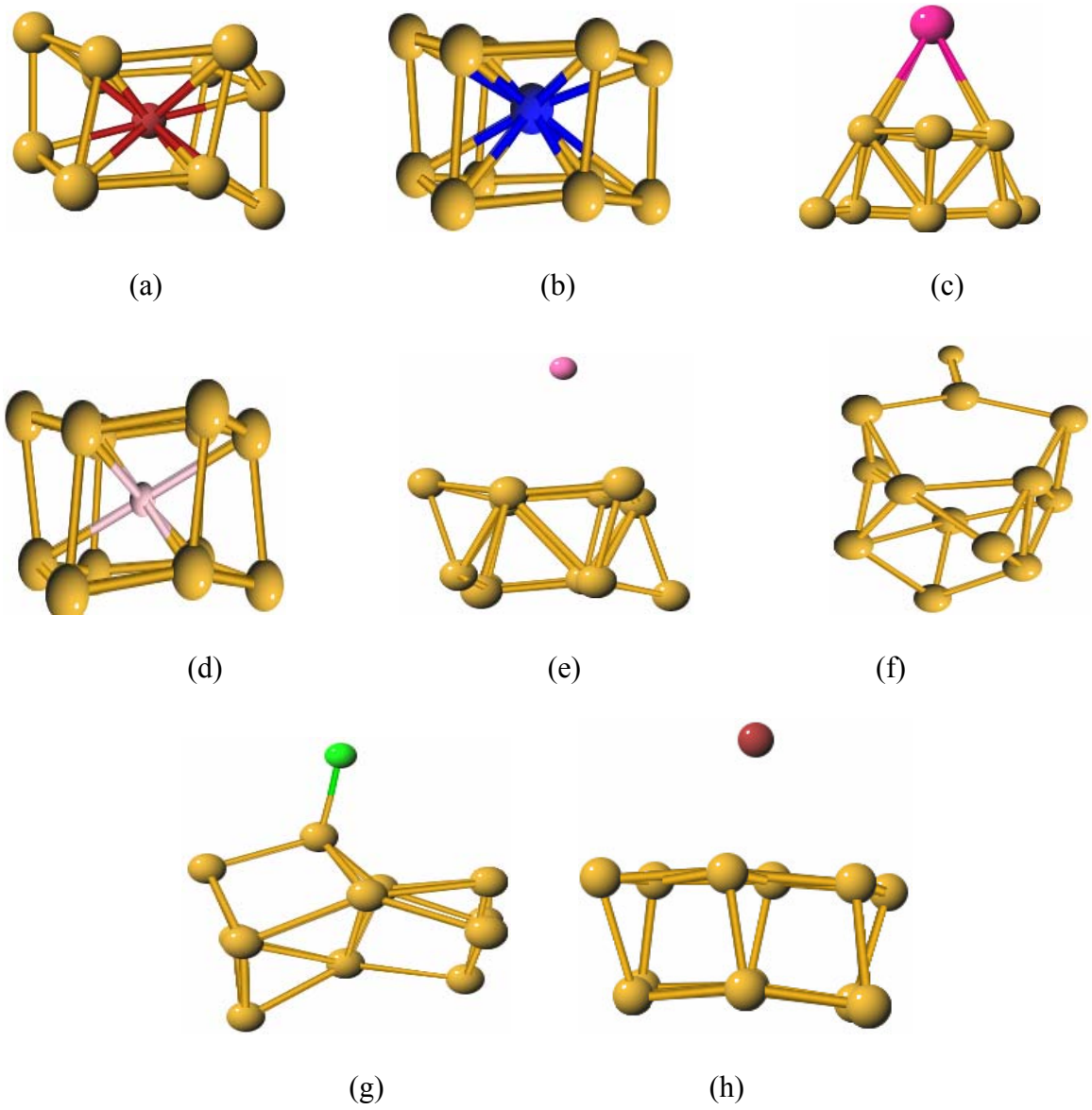

Figure 7.2 Lowest Energy Structure of Endroheral Clusters Obtained from Si_{12} D_{6h} Isomer.(a) $Li^{+}@Si_{12}$ (b) $Na^{+}@Si_{12}$ (c) $K^{+}@Si_{12}$ (d) $He@Si_{12}$ (e) $Ne@Si_{12}$ (f) $F^{-}@Si_{12}$ (g) $Cl^{-}@Si_{12}$ (h) $Br^{-}@Si_{12}$

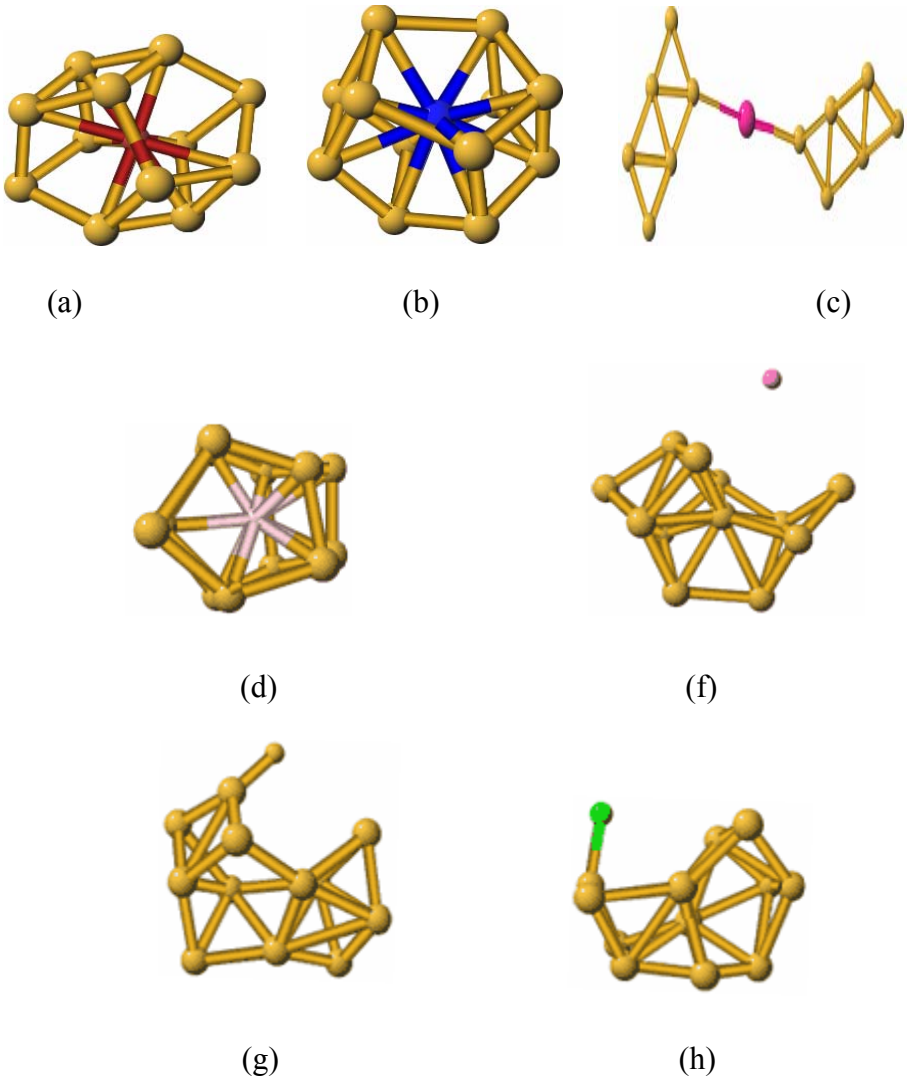

Figure 7.3 Lowest Energy Structure of Endohedral Clusters Obtained from Si_{12} D_{2d} Isomer.(a) $Li^{+}@Si_{12}$ (b) $Na^{+}@Si_{12}$ (c) $K^{+}@Si_{12}$ (d) $He@Si_{12}$ (e) $Ne@Si_{12}$ (f) $F^{-}@Si_{12}$ (g) $Cl^{-}@Si_{12}$

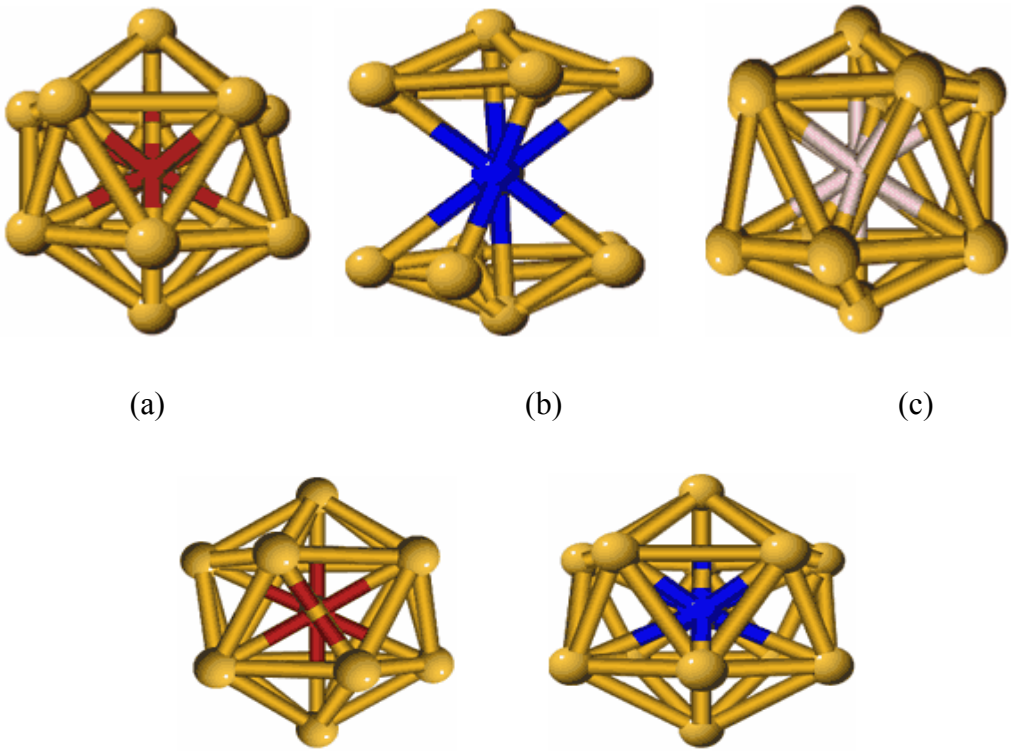

Figure 7.4 Lowest- Energy Structure of Endohedral Cluster Obtained From the Initial Si_{12} Structure with I_h Symmetry. (a) $Li@Si_{12}$ (b) $Na@Si_{12}$ (c) $He@Si_{12}$ (d) $Li^-@Si_{12}$ (f) $Na^-@Si_{12}$

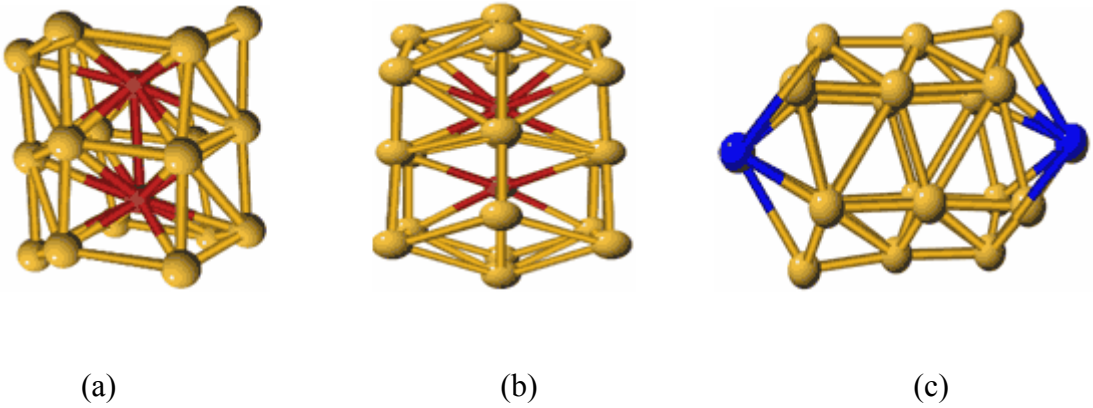

Figure 7.5.Lowest Energy Structure of Endohedral Clusters Obtained from the Initial Si_{18} and Si_{20} Structures with D_{6h} Symmetry. (a) $Li_2@Si_{18}$ (b) $Li_2@Si_{20}$ (c) Na_2Si_{18}.

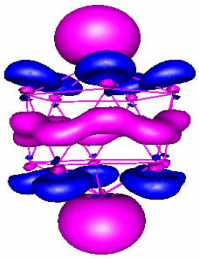

HOMO $Li^0@Si_{12}$

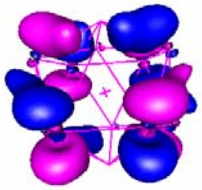

LUMO $Li^0@Si_{12}$

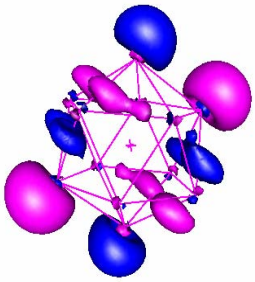

HOMO $Na^-@Si_{12}$

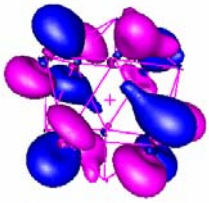

HOMO $Li^-@Si_{12}$

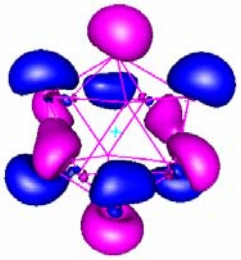

HOMO $He@Si_{12}$

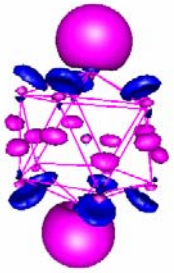

LUMO $He@Si_{12}$

Figure 7.6 Orbital Pictures of HOMOs and LUMOs for Selected Endohedral System (I_h symmetry).

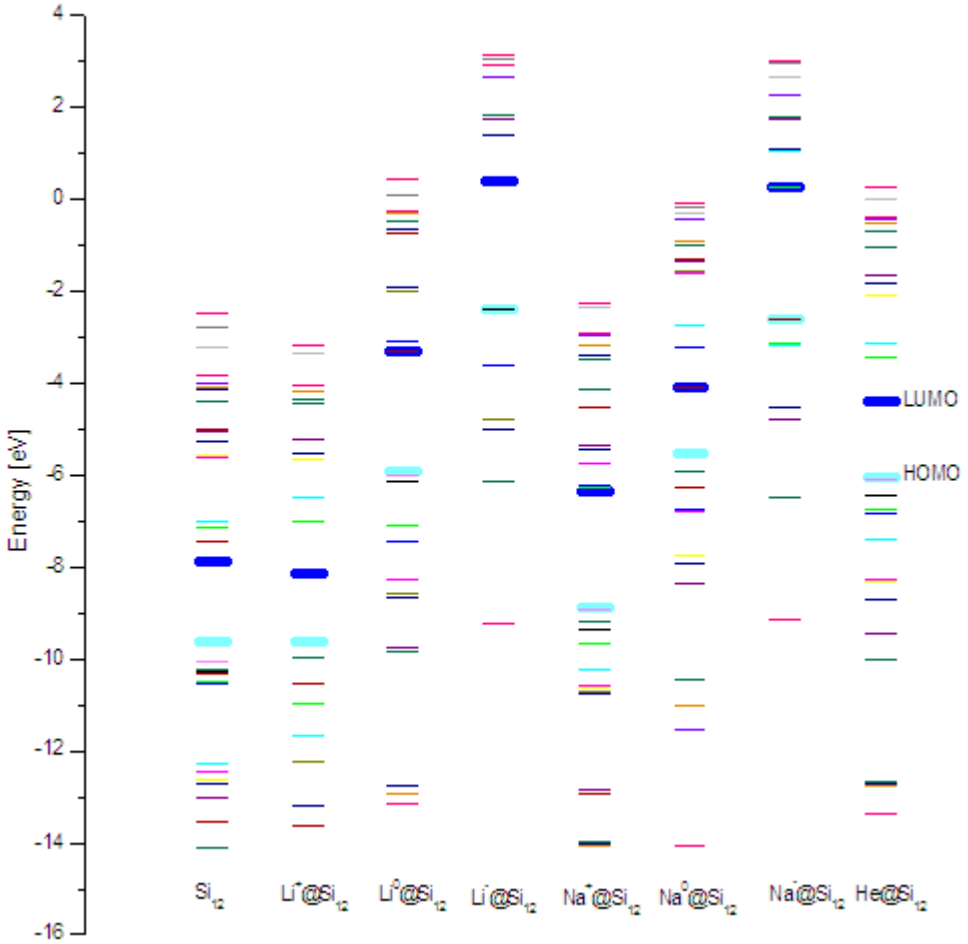

Figure 7.7 Kohn-Sham Orbital Energies for the $X@Si_{12}$ Cluster and for Si_{12} (I_h) Cage.

CHAPTER VIII

CONCLUSIONS

This dissertation presented *ab initio* electronic structure calculations for the endohedral X@T_n-POSS and the exohedral XT_n-POSS complexes. Three distinct polyhedral oligomeric silsesquioxane classes, T_8-POSS, T_{10}-POSS and T_{12}-POSS, were chosen as hosts. The guest atoms X were alkali metals and their ions, noble gases, halides and transition metals and their ions, respectively. The results of this study can be summarized as follows:

The encapsulation of the different atoms or ions into the POSS cage depends on size of the embedded atoms or ions as well as the host cage size. As the host cage size increased, the strain energy between the host and guest decreased. For all host cages interaction of some guest species were energetically favorable. Very large guest sizes created more repulsion, raising the energies of the complexes. However, with small host atoms or ions, the endohedral complexes oscillated along the potential energy surface. Encapsulation of atoms or ions was predicted to be more favorable with larger cages, following the stability order: T_{12}-POSS > T_{10}-POSS > T_8-POSS.

Alkali metal ion encapsulation into the POSS cage caused the cage to shrink. Electron transfer occurred from the cage atoms to the cations. However, encapsulation of

neutral alkali atoms and their negative ions caused electron density to transfer from the metal to the cage framework. Lithium and sodium ion caused the cage to deform. The cage deformation is greatest for Li^+ and smallest for K^+.

Encapsulation of halides always caused the cage to expand. This effect is more pronounced for the smaller T_8-POSS cage and smaller for larger T_{12}-POSS cage. Electron transfer occurred from halide ion to the cage framework.

The endohedral $F^-@T_n$-POSS (n = 8, 10, 12) complexes are exceptionally stable. The fluoride ion migrates into all POSS cages (except for the D2d T_{12}-POSS isomer without any predicted energy barrier. Hence, no exohedral complexes were predicted for F^- except in the case of the D_{2d} T_{12}-POSS isomer. In that case, the F^- ion attacked a cage Si atoms to form a pentacoordinated silicon.

Encapsulation of the noble gas He, Ne and Ar into the T_n-POSS cage caused the cage size to expand. No electronic interactions occurred between a encapsulated noble gas and cage framework atoms. Charge transfer between POSS cage framework atoms and endohedral noble gas is almost negligible.

Endohedral transition metal complexes were studied with T_8-POSS and T_{12}-POSS cages. The endohedral complexes are thermodynamically more stable than their precursors. The cationic complexes were more stable than their neutral counterparts. Transition metal encapsulation caused the endohedral complexes' HOMO-LUMO gaps to decrease compared to the HOMO-LUMO gap of the empty cages. Thus, using a suitable transition metal, the HOMO-LUMO gaps might be tuned to change the absorption and fluorescence properties of the POSS molecules.

Exohedral complexes are thermodynamically more stable than their endohedral counterparts. However, some atoms (usually noble gases) resided so far away from the cage surface that the existences of these exohedral complexes are questionable.

The ionization potentials for endohedral alkali and transition metal systems were smaller than those of the free metals. Alkali metals, when embedded in POSS cages, exhibit "superalkali" behavior. However, transition metals did not show this behavior.

In addition to the present endohedral and exohedral cluster calculations, there are many other directions for future work. The study of atomic and ionic Li clusters incorporated into the POSS cages is one interesting direction. POSS cages could probably hold several lithium atoms based on the results found in this dissertation. Specifically, investigations of endohedral interactions between clusters of compositions $(Li)_n^+$, n = 2, 3, …n and T_n-POSS cages with (n = 8, 10, 12) will be interesting. If each cage can hold a lithium cluster and if Li^+ ions can enter and leave the cages easily, then polymers of POSS could serve as storage sites for lithium in lithium ion batteries. Studies of this type should be quickly pursued with respect to the arrival of ABSL power solutions Inc. at Mississippi State University.

Endohedral transition metal complexes should be further studied. This dissertation predicted that appropriate transition metal atoms could tune the HOMO-LUMO gaps. Hence the light emitting (fluorescent) properties of the cage could be widely tuned. If endohedral POSS transition metal complexes can be prepared experimentally, these complexes can be used as pendant functions in polymerization and copolymerization. This would change the light emitting properties of the polymer or

films of M@POSS could be made to serve as pixels to generate colored emissions. Another application of transition metal endohedral POSS complexes might be in an oxidation and radiation-resistant space shuttle coating. The space shuttle's surfaces are under constant assault by singlet state oxygen, which destroys organic coatings. If a POSS polymer with an embedded transition metal could be made, the transition metal and the POSS cage will react with singlet oxygen to form SiO_2 /MO_x barriers to further oxidation. Certain metal may also generate radiation protection.

The properties of endohedral transition metals in all their traditional oxidation states need to be studded. For example, how do the structures and properties of T_n-POSS cages (n = 8, 10 and 12) change by varying the endohedral metal from Fe^0 to Fe^{2+} to Fe^{3+}. Some metals have high oxidation states (for example Mn^{7+} in MnO_4^-). These high oxidation states should also be examined.

Salts inside cages represent an interesting topic. LiF inside T_{10}-POSS and T_{12}-POSS were studied herein. Increasing the size of the alkali metal cation or the halide anion (LiCl, LiBr, LiI, KF, RbF, CsF, $LiNO_3$) should be examined. Many other interesting questions remain to be examined.

Overall, the present theoretical investigations should encourage future new research on POSS chemicals. The endo- and exohedral complexes studied are currently unknown experimentally. All the endohedral cage complexes, $X@(SiHO_{3/2})_{12}$, that were predicted to be more stable than their isolated components appear to be viable synthetic targets.